

# **Concrete Mechanics Applications**

TNO DIANA BV

**Concrete Mechanics Applications**

Edited by: Frits C. de Witte and Max A. N. Hendriks

Published by:

TNO DIANA BV

P.O. Box 49, 2600 AA Delft, The Netherlands.

Phone: +31 15 276 32 50

Fax: +31 15 276 30 19

E-mail: [info@tnodiana.com](mailto:info@tnodiana.com)

Web page: <http://www.tnodiana.com>

*Trademarks.*

DIANA is a registered trademark of TNO DIANA BV. FEMGV, FEMGEN and FEMVIEW are trademarks of Femsys Ltd. MARC is a registered trademark of MSC. ANSYS is a registered trademark of Ansys, Inc. ABAQUS is a registered trademark of Hibbitt, Karlsson & Sorensen, Inc. AUTOCAD is a registered trademark of Autodesk Inc.

*October 7, 2003.*

Copyright © 2003 by TNO DIANA BV, all rights reserved. No part of this publication may be reproduced in any form by print, photoprint, microfilm or any other means, without the prior written permission of the publisher.

The information in this document is subjected to change without notice and should not be construed as a commitment by TNO DIANA BV. TNO DIANA BV assumes no responsibility for any errors that may appear in this document.

This document was prepared with the L<sup>A</sup>T<sub>E</sub>X Document Preparation System.

# Contents at a Glance

Preface	xi
1 Concrete Mechanics for the Structural Engineer	1
2 Fracture of Concrete – Observations of Softening Behavior	5
3 Comparison of Concrete Models for Cyclic Loading	25
4 Bending, Shear, and Torsion of Prestressed HSC Beams	43
5 Joints in a Multi-beam Box Girder Bridge	61
6 Fire Analysis of an LNG Tank	75
7 Numerical Simulations of Tests on a Segmented Tunnel Lining	91
8 Nonlinear Behavior of Joints in Bored Tunnels	109
9 How to Avoid Cracking in Young Concrete	125
10 Design of Concrete Deep Beams	139
11 Restrengthening of Brickwork to Reduce Crack Width	149
12 FEM Models Applied for Unreinforced Underwater Concrete	161
13 Structural Safety of Concrete Structures	169
Bibliography	185
Index	193





# Contents

<b>Preface</b>	<b>xi</b>
<b>1 Concrete Mechanics for the Structural Engineer</b>	<b>1</b>
1.1 Structural Engineers Are Fond of Their Comforts . . . . .	1
1.2 From Research to Practice . . . . .	2
1.3 General-purpose Software . . . . .	2
1.4 Special-purpose Software . . . . .	3
1.5 Future Evolution . . . . .	4
<b>2 Fracture of Concrete – Observations of Softening Behavior</b>	<b>5</b>
2.1 Introduction . . . . .	5
2.2 Concrete Cracking under Uniaxial Tension . . . . .	6
2.2.1 Nonlinear Fracture Models for Concrete . . . . .	7
2.2.2 Experimental Validation . . . . .	10
2.2.3 Influence of Reinforcement . . . . .	14
2.3 Failure under Uniaxial Compression . . . . .	15
2.3.1 Experimental Validation . . . . .	15
2.3.2 Compression Damage Zone Model . . . . .	19
2.4 Multiaxial States of Stress . . . . .	20
2.5 Conclusions . . . . .	23
<b>3 Comparison of Concrete Models for Cyclic Loading</b>	<b>25</b>
3.1 Introduction . . . . .	25
3.2 Description of Constitutive Models for Concrete . . . . .	26
3.2.1 Multiple-Fixed Crack Model with Von Mises Crushing Model .	27
3.2.2 Rankine–Von Mises Plasticity Model . . . . .	31
3.2.3 Total Strain-based Models . . . . .	32
3.3 Application . . . . .	34
3.4 Analysis . . . . .	36
3.5 Discussion . . . . .	38

<b>4</b>	<b>Bending, Shear, and Torsion of Prestressed HSC Beams</b>	<b>43</b>
4.1	Introduction . . . . .	43
4.2	Experimental Tests . . . . .	43
4.2.1	Problem Description . . . . .	44
4.2.2	Set-up . . . . .	45
4.2.3	Test Results . . . . .	46
4.2.4	Conclusion . . . . .	54
4.3	Numerical Analysis . . . . .	55
4.3.1	Finite Element Model . . . . .	55
4.3.2	Analysis Results . . . . .	57
4.4	Conclusions . . . . .	59
4.4.1	Experimental . . . . .	59
4.4.2	Numerical . . . . .	59
<b>5</b>	<b>Joints in a Multi-beam Box Girder Bridge</b>	<b>61</b>
5.1	Introduction . . . . .	61
5.1.1	Multi-beam Box Girder Bridges . . . . .	61
5.1.2	Current Design Practice . . . . .	62
5.1.3	Design Considerations . . . . .	63
5.1.4	Approach . . . . .	63
5.2	Case Study – Box Girder Bridge ‘Heultsedreef’ . . . . .	64
5.2.1	Geometry . . . . .	64
5.2.2	Materials and other Properties . . . . .	65
5.2.3	Design Loads . . . . .	65
5.3	Linear Analysis . . . . .	66
5.3.1	Volume Model . . . . .	67
5.3.2	Shell Model . . . . .	67
5.3.3	Orthotropic Plate Model . . . . .	68
5.3.4	Results and Justification . . . . .	69
5.3.5	Influence Fields . . . . .	69
5.4	Nonlinear Analysis . . . . .	69
5.4.1	Analysis Phases and Load Steps . . . . .	70
5.4.2	Material Modeling . . . . .	71
5.4.3	Results for Construction Phases 1 and 2 . . . . .	71
5.5	Conclusion . . . . .	73
<b>6</b>	<b>Fire Analysis of an LNG Tank</b>	<b>75</b>
6.1	Introduction . . . . .	75
6.2	LNG Tank of 120,000 m <sup>3</sup> Capacity . . . . .	76
6.3	Purpose and Principles of the Analysis . . . . .	77
6.3.1	Temperature Distribution . . . . .	77
6.3.2	Material Properties . . . . .	78
6.4	Analysis of the Structure . . . . .	79
6.4.1	Phased Construction and Analysis . . . . .	80
6.4.2	Finite Element Model . . . . .	80

6.4.3	Performance of the Analysis . . . . .	83
6.4.4	Why DIANA's Module NONLIN was not Applied . . . . .	85
6.5	Analysis Results vs. Design Criteria . . . . .	85
6.5.1	Maximum Compression Strain of Concrete . . . . .	86
6.5.2	Maximum Tensile Strain of Reinforcement Steel . . . . .	87
6.5.3	Corrective Prestress Load . . . . .	88
6.6	Conclusions . . . . .	89
<b>7</b>	<b>Numerical Simulations of Tests on a Segmented Tunnel Lining</b>	<b>91</b>
7.1	Introduction . . . . .	91
7.2	Experiments . . . . .	92
7.2.1	Set-up . . . . .	92
7.2.2	Loading . . . . .	93
7.2.3	Measurements . . . . .	94
7.3	Numerical Analyses . . . . .	95
7.3.1	Finite Element Model . . . . .	95
7.3.2	Material Properties . . . . .	96
7.3.3	Boundary Conditions . . . . .	99
7.3.4	Performed Analyses . . . . .	99
7.4	Results . . . . .	100
7.4.1	Introduction . . . . .	100
7.4.2	Deformations . . . . .	101
7.4.3	Axial Strains and Stresses . . . . .	102
7.4.4	Tangential Strains and Bending Moments . . . . .	104
7.4.5	Principal Strains . . . . .	107
7.5	Conclusions . . . . .	107
<b>8</b>	<b>Nonlinear Behavior of Joints in Bored Tunnels</b>	<b>109</b>
8.1	Introduction . . . . .	109
8.1.1	The Amsterdam North–South Metroline . . . . .	109
8.1.2	Innovative Design of the Bored Tunnels . . . . .	110
8.1.3	Numerical Modeling of the Behavior of the Tunnel Lining and its Components . . . . .	111
8.2	Conceptual Numerical Model of the Bored Tunnel . . . . .	112
8.2.1	General . . . . .	112
8.2.2	Designing the Numerical Model . . . . .	112
8.3	Validation of the Numerical Model . . . . .	114
8.3.1	Simplified Spring Model – 2D Joint . . . . .	115
8.3.2	Macro Model of the Lining – Simple Load Cases . . . . .	116
8.3.3	Simplified Spring Model – Results of Physical Model . . . . .	118
8.4	Application of the Model in Practice . . . . .	119
8.4.1	Modeling of the Construction Phase . . . . .	119
8.4.2	Modeling of the Serviceability Phase . . . . .	120
8.4.3	Parameter Study . . . . .	121
8.5	Detailed Modeling of the Elastomer Profile . . . . .	123

8.5.1	General . . . . .	123
8.5.2	Modeling of the Elastomer Profile . . . . .	124
8.6	Conclusions . . . . .	124
<b>9</b>	<b>How to Avoid Cracking in Young Concrete</b>	<b>125</b>
9.1	Introduction . . . . .	125
9.2	Problem Description . . . . .	126
9.3	Required Analysis Data . . . . .	127
9.3.1	Geometry and Phasing of the Structure . . . . .	127
9.3.2	Material Properties of the Concrete . . . . .	127
9.3.3	Kinematic Boundary Conditions . . . . .	128
9.3.4	Physical Boundary Conditions . . . . .	129
9.4	Analysis for Situation Without Precautions . . . . .	130
9.5	Analysis for Situation With Cooling . . . . .	132
9.5.1	Design of the Cooling Plan . . . . .	132
9.5.2	Analysis Results . . . . .	133
9.5.3	Protocol for the Western Scheldt Tunnel Access Roads . . . . .	135
9.6	Conclusions . . . . .	137
<b>10</b>	<b>Design of Concrete Deep Beams</b>	<b>139</b>
10.1	Focus on D-Regions . . . . .	139
10.1.1	Pro's and Con's of Existing Methods . . . . .	140
10.1.2	An Alternative: SPanCAD . . . . .	140
10.2	Stringer-Panel Theory . . . . .	141
10.3	A Three-step Design Procedure . . . . .	142
10.3.1	Step One: Elastic Analysis . . . . .	142
10.3.2	Second Step: Nonlinear . . . . .	142
10.3.3	Third Step: Final Simulation . . . . .	143
10.3.4	Classical Cases Covered . . . . .	143
10.4	Design Example . . . . .	144
10.4.1	First Step . . . . .	145
10.4.2	Second Step . . . . .	145
10.4.3	Third Step . . . . .	146
<b>11</b>	<b>Restrengthening of Brickwork to Reduce Crack Width</b>	<b>149</b>
11.1	Mixed Building Techniques: 'De Adelaar' . . . . .	149
11.2	The Main Problem . . . . .	150
11.3	Basic Interventions . . . . .	151
11.3.1	Insulation on the Inside . . . . .	151
11.3.2	Adding a Climate Façade on the Inside . . . . .	151
11.3.3	Dilatation Joints in the Outside Wall . . . . .	152
11.3.4	Reinforcement . . . . .	152
11.4	Numerical Simulation of Interventions . . . . .	152
11.4.1	Modeling Strategy . . . . .	153
11.4.2	Results without Restrengthening . . . . .	154

11.4.3	Brickwork with CFRP-Sheet Reinforcement . . . . .	155
11.4.4	Conclusions . . . . .	157
11.5	The Laboratory Test . . . . .	157
11.5.1	Numerical Analysis Results . . . . .	159
11.5.2	Epilogue . . . . .	160
<b>12</b>	<b>FEM Models Applied for Unreinforced Underwater Concrete</b>	<b>161</b>
12.1	Introduction . . . . .	161
12.1.1	Flow of Forces . . . . .	162
12.2	Case Study . . . . .	163
12.3	Linear Elastic Calculations . . . . .	164
12.3.1	Beam Model . . . . .	164
12.3.2	Advanced Shell Model . . . . .	165
12.3.3	Three-dimensional Model . . . . .	166
12.4	Nonlinear Analysis . . . . .	167
12.5	Conclusions . . . . .	168
<b>13</b>	<b>Structural Safety of Concrete Structures</b>	<b>169</b>
13.1	Introduction . . . . .	169
13.1.1	Probabilistic Methods . . . . .	170
13.1.2	DARS Method . . . . .	170
13.2	Example Analysis – Underwater Concrete . . . . .	171
13.2.1	Finite Element Model . . . . .	172
13.2.2	Choosing the Number of Stochastic Variables . . . . .	174
13.2.3	Probabilistic Analysis . . . . .	176
13.2.4	Choosing the Limit States . . . . .	177
13.2.5	Parameters for Probabilistic Analysis . . . . .	178
13.2.6	Probabilistic Results Based on Linear Elastic Analysis . . . . .	178
13.2.7	Probabilistic Results Based on Nonlinear Analysis . . . . .	181
13.3	Conclusions . . . . .	183
	<b>Bibliography</b>	<b>185</b>
	<b>Index</b>	<b>193</b>



# Preface

In 1987 the CUR report nr.134 was published within the scope of the project ‘Betonmechanica’ and supervised by the CUR Research Committee A26. Report nr.134 [15]<sup>1</sup> describes the analysis of eight real-life concrete structures with the finite element program DIANA. At that time a number of material models had already been developed which could describe cracking, plasticity of concrete and reinforcement, and the attachment between concrete and reinforcement. Since 1987 many more material models have become available and the know-how of the material concrete and the performance of nonlinear analyses has been increased considerably. Moreover, there has been a trend from one-dimensional toward two-dimensional and three-dimensional models and new classes of concrete have been applied, not only in the familiar structures like buildings and bridges, but also in other types of structures such as bored tunnels.

In the world of science, considerable progress has been made with respect to nonlinear material models. The researchers have gained an insight into the applicability, and its restrictions, of the theory of plasticity for concrete. The influence of cracking on the reduction of the stiffness of unreinforced and reinforced concrete has become well-known. New contact and interface elements have been developed to model joints in masonry, bridges and tunnels. Much of the knowledge has been formatted in software codes, of which the Dutch DIANA code is a distinct representative. Via these codes the new knowledge becomes available to structural design engineers.

The present publication aims to be a sample selection of the current possibilities of concrete mechanics applications. The presented numerical elaborations may help the structural engineer to create models, based on the current state of knowledge, that have a competitive and practically-oriented nature and yield fail-safe structures.

**Acknowledgment.** This publication has been compiled by the CUR Research Committee A36 ‘Concrete Mechanics’. The DIANA User’s Association (DOV) initiated Committee A36 in 2000 and commissioned it to transform the subjects brought up by the DOV into examples for the engineering practice.

The CUR gratefully acknowledges the authors, and the companies and organizations as listed below, who donated their efforts in the compilation of this report. Finally the CUR expresses its gratitude to the Bouwdienst Rijkswaterstaat and to

---

<sup>1</sup>Please refer to the Bibliography on page 185.

Ballast Nedam Engineering for their financial support which enabled the project supervision and the publication of the Dutch version of this report [18]. The English version at hand has been edited and published by TNO DIANA BV.

September 2003

The CUR Administration



Adviesbureau voor Bouwtechniek ABT  
[www.abt-consult.nl](http://www.abt-consult.nl)



Royal Haskoning – Engineers, Architects & Consultants  
[www.royalhaskoning.com](http://www.royalhaskoning.com)



TNO Building and Construction Research  
[www.bouw.tno.nl](http://www.bouw.tno.nl)



Swiss Federal Institute of Technology Zurich  
[www.ethz.ch](http://www.ethz.ch)



Witteveen+Bos Consultants  
[www.witteveenbos.com](http://www.witteveenbos.com)



FEMMASSE BV  
[www.femmasse.nl](http://www.femmasse.nl)



DIANA User's Association  
[www.dianausers.nl](http://www.dianausers.nl)



Ballast Nedam Engineering  
[www.ballast-nedam.com](http://www.ballast-nedam.com)



Ministry of Transport, Public Works and Water Management  
– The Netherlands  
[www.rijkswaterstaat.nl](http://www.rijkswaterstaat.nl)



Delft University of Technology  
[www.tudelft.nl](http://www.tudelft.nl)



TNO DIANA BV  
[www.tnodiana.com](http://www.tnodiana.com)



**CUR A36 Committee.** At the moment of publication CUR Committee A36 was composed as follows.

dr. ir. C. van der Veen (chair)  
*Delft University of Technology*

ir. A. de Boer  
*Ministry of Transport, Public Works and Water Management (Bouwdienst RWS) – The Netherlands*

ir. S. W. H. Droste  
*Adviesbureau voor Bouwtechniek ABT*

ir. W. H. N. C. van Empel  
*Adviesbureau Noord/Zuidlijn*

ir. C. M. P. 't Hart  
*TNO DIANA BV*

dr. ir. M. A. N. Hendriks  
*TNO DIANA BV*

ir. F. J. Kaalberg  
*Adviesbureau Noord/Zuidlijn*

prof. ir. C. S. Kleinman  
*Eindhoven University of Technology*

prof. dr. ir. J. G. M. van Mier  
*ETH Hönggerberg, Institute for Building Materials, Zürich*

dr. ir. P. Roelfstra  
*Roelfstra Consultants BV*

prof. dr. ir. J. G. Rots  
*Delft University of Technology*

ir. A. Rijswijk  
*Royal Haskoning*

dr. ir. G. M. A. Schreppers  
*TNO DIANA BV*

ir. M. H. Verwoerd  
*INFRA Consult + Engineering*

dr. ir. P. H. Waarts  
*TNO Building and Construction Research*

ing. A. W. van den Thoorn (editor)  
*CUR*

ing. M. J. van der Vliet (coordinator)  
*CUR*

prof. dr. ir. J. Blaauwendraad (supervisor)  
*CUR*



# Chapter 1

## Concrete Mechanics for the Structural Engineer

J. Blaauwendraad

*Delft University of Technology, Faculty of Civil Engineering and Geosciences*

### 1.1 Structural Engineers Are Fond of Their Comforts

Designers in the structural engineering world like taking things easy. They simplify the physical reality such that the design problem is addressable with the existing knowledge and the analysis tools that are available. Structural engineers do know that real nature is highly nonlinear but in determining stresses and deformations they (have to) idealize structures to a high extent. Either they really account for the nonlinear nature, however do it in a simplified way, or they are prepared to make sophisticated types of analysis indeed, but stick to the assumption that the structure behaves elastically.

An example of the first approach is the application of the Strut-and-Tie method. In this method a continuous structure or structural part is replaced by a well-chosen truss-type of structure in which the force flow can be determined by equilibrium considerations. This means that redistribution of stresses is presupposed, so plasticity considerations are in the game. An example of the latter approach is the application of the Finite Element Method. Now the continuous nature of the structure is fully respected and thousands of equations may be solved, but the material is supposed to behave elastically for all load cases and all load levels.

## 1.2 From Research to Practice

In research circles analysis methods are in use already for many years, which account for nonlinear material behavior and gross deformations. The majority of general-purpose FEM packages offer such options, be it in a larger variety for metal structures than for brittle material structures like concrete and masonry. Gradually more such nonlinear software starts playing a role in practice as a design tool. This chapter intends to give in a nutshell an overview of nowadays possibilities, both for general-purpose packages and special-purpose programs.

Nonlinearity can be related to actions as well. Deviations from linearity due to gravity loads are different from deviations due to fire, and these are different from the cyclic nonlinearity at earthquake excitations. A fire application is part of this book [Ch. 6]. Material nonlinearity can have several reasons: the concrete can be cracked under tension, can become plastic in compression, aging creep can be the source, or swell and shrinkage may occur. Failure will occur due to passage of strength limits or by fatigue. A modern trend is not to speak in terms of cracks and plasticity, but to use the concept of damage for the loss of structural integrity.

Another category of nonlinear behavior consists of contact problems. The material itself can stay elastic, but the geometry of the structure may change. This can be found in tunnel linings and box girder bridges, which are built up from pre-cast concrete elements. The elements itself are considered to stay elastic, but the joints have nonlinear characteristics. Both examples, a tunnel and a bridge, will be discussed hereafter.

Undeniably an immense effort has been made in research circles to achieve at the state-of-art of today. Particularly big progress has been made for the modeling of the nonlinear characteristics of the material. If compared to a couple of decades ago much insight was gained about the applicability of the theory of plasticity and its limits, about the influence of cracking on the reduction of stiffness in plain and reinforced concrete, which curiously enough in the first case is called tension-softening and in the latter case tension-stiffening. Thanks to much experimental work in Canada and Japan we now do understand in which way the compression strength of concrete panels is influenced by the tensile strain in transverse direction. And we master the art to replace the designer-oriented formulation of creep in codes of practice by Maxwell chains of springs and dashpots. We also have at disposal a new family of contact and interface elements to model the behavior of joints between structural elements of concrete or masonry. And so we have much more functionality at our disposal.

## 1.3 General-purpose Software

To day there are various general-purpose FEM packages available, for instance DIANA, MARC, ANSYS and ABAQUS. Most of them have a USA origin and started from aeronautics applications. So they offer a varied library for metal nonlinearity but have a limited functionality for the nonlinear analysis of concrete structures. However the user can adapt the general-purpose software to his needs by means of user-supplied

subroutines. In this way a firm can tune a general-purpose system to its own needs. There are exceptions like the Dutch system DIANA, which particularly was developed for civil engineering purposes with a focus on structural concrete.

All general-purpose packages may have the disadvantage that user-friendliness is not a particular goal. It is software to *check* a design, not to *make* a design. The design has to be done in one way or another without use of the number-crunching software and from this design approach reinforcement schemes can be determined. Only when this is finished a nonlinear FEM analysis can be started, which will give indications about cracking and deformations in the serviceability state and about the ultimate load, which can be carried. Many universities have developed software packages, which have functionality for concrete structures to be compared with DIANA. Well-known examples, among others, are Bochum, Stuttgart, Vienna and Tokyo.

## 1.4 Special-purpose Software

It is hard to find designer oriented software, which will cover all possible sources of nonlinearity. In practice special kinds of software exist for different applications. In this way one can tune software to particular needs of interest. Here we will mention a few.

- A special class of nonlinear analysis consists of the modeling of hydration processes in young hardening concrete. This is done to control the tensile stresses during the temperature development in the curing process in order to prevent early cracking. An example of such application, the HEAT program of FEM-MASSE BV, is included in this book [Ch.9]. The results of this program help to decide on the number of hours after which the formwork can be removed and whether or not cooling is needed. And the effect of cooling can be studied.
- Special FEM software has come into being, which was developed for a special class of structure, say shear walls. Now special attention can be paid to user-friendliness and nicely visualizing results. The Czech 2D-program SBETA has been a clear example of this type of software. Agreed, it is still software for checking purposes, but it can easily be used in an iteration procedure. The author of this program has announced new generation 3D-software going under the name ATENA which is supposed to replace the 2D-version. This means a shift into the direction of general-purpose software.
- The design of structural concrete with the Strut-and-Tie method can be supported by software, which accounts for the stiffness of tensile members in a cracked state. In this way information about crack widths and deformations in the serviceability state is received and the method can be extended to truss models, which are statically indeterminate. An example of such software is the CAD-program as was developed in the University of Stuttgart.
- An attempt to write by purpose design-oriented software is the 2D-program SPANCAD. This software is intended to support the designer of concrete deep

beams and shear walls and helps to choose a proper reinforcement scheme. The Dutch authors aim to combine advantages of the Strut-and-Tie method and the Finite Element Method [Ch. 10]. The structural designer improves in an interactive way the dimensions of the concrete parts and the reinforcement, starting from an elastic analysis and allowing after that for redistribution of stresses due to cracking and yielding.

- A class of programs, which has not yet been made widely available is based on the classic theory of plasticity and optimization techniques. The universities of Zürich and Copenhagen/Esbjerg have done interesting work in this field. It is a special application of the Finite Element Method which results in an automatic design of reinforcement schemes. Nice results can be achieved along these lines.
- Some programs are in circulation in which assemblages of rigid parts and lumped masses, springs and dashpots are applied, sometimes in combination with a limited set of standard continuous finite elements. An example is the New Zealand package RUAUMOKO for inelastic dynamic analysis as developed in the Canterbury University at Christchurch. Such programs can easily include nonlinear cyclic spring characteristics as a result of laboratory testing for the behavior of components and connections. A less well-known example is the (not widely spread) research-oriented program TILLY of the of Delft University of Technology in The Netherlands.

## 1.5 Future Evolution

If use is made of non-linear analysis in the design of a structure it is a separate question whether or not the partial safety factors still do apply which have been chosen in the code of practice. Arguments can be raised that other probabilistic considerations should be made in such cases. Incorporation of stochastic features in FEM packages will be an interesting development in the years to come. A probabilistic structural safety study is included in Chapter 13.

A number of the special cases of software mentioned before have taken a powerful position as long as the general-purpose programs have been moderate user-friendly. This position may be subject to change since the general-purpose programs increasingly more offer highly user-friendly options. One such option has been the release of software versions, which can run on personal computers and make use of top-of-the-bill visualizing software. Another option is the development of ‘specials’, which are derived from the general-purpose program and use that software in a way hidden to the user. The DIANA system is clearly developing in this direction. The end-user believes he has a program, which has been tuned to his particular needs. This evolution may in the long run mean that less room is left for special-purpose software like the above-mentioned 2D-programs for the analysis of concrete structures. Unless the FEM packages keep on being used for checking purposes only and not for design. Let us hope that software suppliers accept the challenge to make special-purpose software superfluous in future.

## Chapter 2

# Fracture of Concrete – Observations of Softening Behavior

J. G. M. van Mier

*ETH Hönggerberg, Institute for Building Materials, Switzerland*

**Summary.** Since the development of numerical methods to analyze reinforced concrete structures, fracture models for concrete have received a lot of attention. The application of an appropriate model enables computer-based design and detailing of a reinforced concrete structure. The attempts to gain a correct understanding of the failure of concrete are based on fracture mechanics. The first attempts to model fracture were rather elementary, and, when viewed from the perspective of modern developments, primitive. Despite modern developments, the quest for a correct fracture criterion is still a timely topic. In this contribution an overview is given of the fracture models for concrete subjected to tensile and compressive load. Experimental evidence that underscores the various theoretical models is given.

### 2.1 Introduction

The development of a fracture criterion depends to a large extent on the size-scale at which crack phenomena occur. In the other chapters concrete structures are analyzed at the macroscopic level. That is to say, it is assumed that concrete and steel have the same ‘smeared’ properties from point to point. The materials are considered to be isotropic continua. For materials like steel and other metals a continuum approach can last very long due to the tiny dimensions of the material structure. For concrete with individual grains up to 32 mm, and in some cases even

larger, the material structure may affect the behavior under certain circumstances. This is particularly true when the dimension of the structure becomes less than the so-called ‘representative volume’. It is generally assumed that a material volume with dimensions of at least five times the largest heterogeneity is sufficiently large to determine continuum properties like stress and strain. However, it is questionable whether a continuum description is still appropriate when fracture occurs. Under tension as well as under compression, fracture causes a material volume or a structure to break into two or more parts, and the material or the structure loses its integrity. The cracks (or shear bands) that develop in the material or the structure are discrete displacements (in applied mechanics often denoted as ‘localization of deformations’), which likely may not be ‘smeared-out’ in the same way as the strains are obtained.

In 1976 Hillerborg and co-workers published a new approach to model cracking in concrete [37]. It concerns a discrete crack model; Bažant & Oh developed a ‘smeared’ version a few years later [6]. These models will be broadly outlined in §2.2. The Crack Band Model of Bažant & Oh underlies the crack model in the DIANA finite element code. We will also discuss the experimental verification. It will turn out that in experiments not all boundary conditions can be met, which are, however, assumed in these models.

For uniaxial compression Van Mier demonstrated in 1984 that localization of deformations occur, despite the apparently distributed crack pattern observed in experiments [75]. This means that ultimately failure must be described with a discrete model, like for uniaxial tension. Such a model was developed by Markeset [49]. Failure under compression was handled like crack formation in the Hillerborg model. At first sight the model seems to perform fairly good, but also here there are indications that theory and experiments do not correspond sufficiently well.

In numerical analysis of reinforced concrete structures, uniaxial stress states are the exception rather than the rule. In most cases two-dimensional simulations are performed, which of course require a two-dimensional model. In §2.4 we will outline the behavior of concrete under bi- and triaxial loading. DIANA offers models which describe multiaxial failure surfaces, applied in the constitutive model. In §2.4 we will also outline the experiments that underlie this modeling. Besides, the various failure models will be discussed.

## 2.2 Concrete Cracking under Uniaxial Tension

Generally it is assumed that concrete will crack when the uniaxial tensile strength is exceeded. From the point of view of application of the Finite Element Method and continuum constitutive models this is a suitable assumption, easily incorporated in bi- and triaxial models. Literature provides some other failure criteria, for instance based on exceeding a critical deformation, or an energy criterion. Hillerborg’s model is also based on a strength criterion for crack initiation; for crack propagation an energy criterion is applied. In §2.2.1 we will first describe the ‘Fictitious Crack Model’ of Hillerborg and the ‘Crack Band Model’ as developed by Bažant & Oh. After that the experimental determination of the various model parameters will be



described, based on the results from uniaxial tensile tests.

### 2.2.1 Nonlinear Fracture Models for Concrete

In 1968 it turned out that, when concrete is loaded in tension, and redistribution of stresses is possible in the experiment, an additional amount of energy is needed to break the material completely into two pieces (see for instance the stable displacement-controlled tension tests of Evans & Marathe [25], where a softening branch was measured beyond maximum stress). If it is assumed, like in the Rankine criterion, that the tensile strength is the critical parameter for concrete in tension, then the energy dissipation is partly neglected. In the 1960's it was attempted to describe the cracking behavior of concrete based on Linear Elastic Fracture Mechanics (LEFM). This theory was developed successfully for the fracture of glass and brittle materials like cast iron. For concrete, and earlier for plastic metals, matters appear to be more complicated.

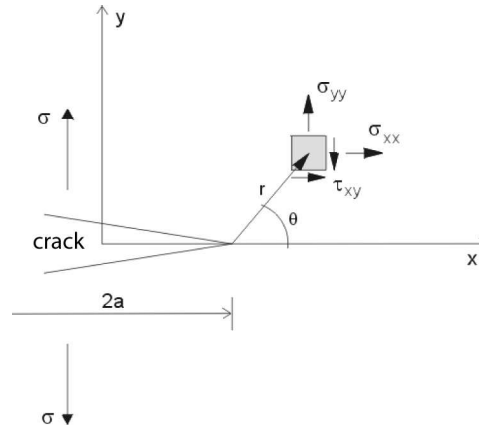


Figure 2.1: Stress components at the tip of a crack with length  $2a$  in a uniaxial stress field

Figure 2.1 shows the stress components near a crack tip in an isotropic continuum. The stress  $\sigma_{yy}$  at the tip is most important under tensile load, and is described by the following equation.

$$\sigma_{yy} = \frac{\sigma\sqrt{\pi a}}{\sqrt{2\pi r}} \cos \frac{1}{2}\theta \left(1 - \sin \frac{1}{2}\theta \sin \frac{3}{2}\theta\right) = \frac{K_I}{\sqrt{2\pi r}} f_{ij}(\theta) \quad (2.1)$$

The stress at the tip approaches infinity (if  $r \rightarrow 0$ ), which means that cracking occurs for any external load, i.e., irrespective of the value of this load. This definitely does not correspond to reality. The problem is overcome by choosing a new criterion for crack propagation, namely the so-called stress intensity factor  $K$ , instead of the classical strength criterion. The factor  $K$  indicates how critical the situation is at the crack tip; it not only depends on the externally applied stress but is also proportional

to the square root of the crack length (2.1). This introduces a scale-dependency which normally does not exist in continuum models. Furthermore, the equation for  $K$  holds a shape factor. The propagation of a crack in an arbitrary geometry depends on the boundary conditions, which is expressed by this shape factor. The linear fracture model performs well for brittle materials. In metals, and also in ‘rock-like’ materials (concrete, natural rock, ceramics, but also ice), numerous processes appear before cracks actually appear. This means that the original linear model must be adapted.

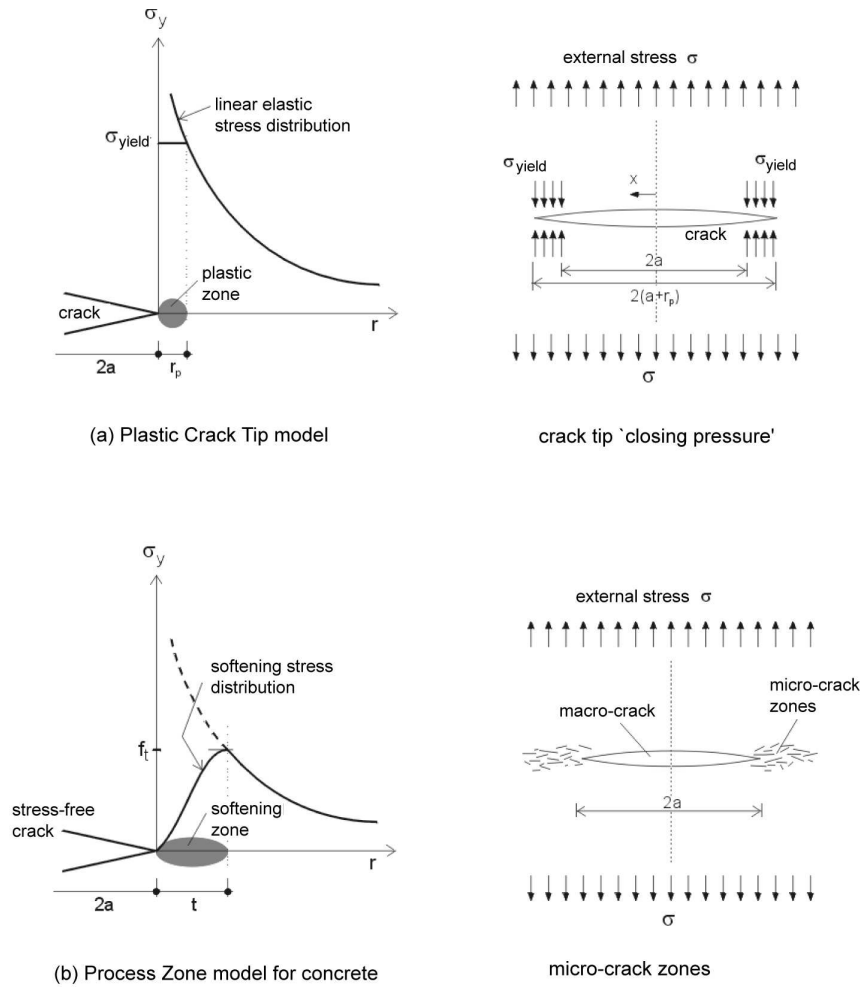


Figure 2.2: Plastic Crack Tip model (a) and analogous model for cracking in concrete (b). Due to the lower acceptable stress for concrete, the process zone of the plastic crack tip for concrete will be many times larger than for metals (after Van Mier [78]).

For plastic metals a process zone at the crack tip was introduced in the beginning of the 1960's. It was hypothesized that, regarding the high stress at the crack tip and the possible occurrence of plasticity for these materials, plastic deformations should occur prior to fracture. In literature these models are known as 'Dugdale–Barenblatt' models [23, 5]. As indicated in Figure 2.2, yielding occurs at the tip. For this model it is assumed that the crack length in the calculations is equal to the original crack length  $a$  plus the length of the plastic crack tip zone  $r_p$ . Next it is assumed that pressure equal to the yield stress  $\sigma_y$  along the length of the plastic zone, closes the crack at the tip, and thus simulates plasticity.

The Fictitious Crack Model for concrete has been developed in analogy to the Plastic Crack Tip model. The argumentation is identical to the one outlined for plastic metals. Concrete can only cope with a tensile stress of 3 to 5 MPa, which is far less than the infinitely high stress as found in the Linear Elastic Fracture Mechanics solution. However, prior to fracture nonlinear processes occur like micro-crack propagation. Hillerborg assumed that the stress profile over the 'plastic zone' in concrete would take the shape of the softening curve as observed in a uniaxial tensile test. Figure 2.2b shows the equivalent model for concrete, placed next to the Plastic Crack Tip model. The analogy is obvious. Figure 2.3a shows the Fictitious Crack Model as it was published originally.

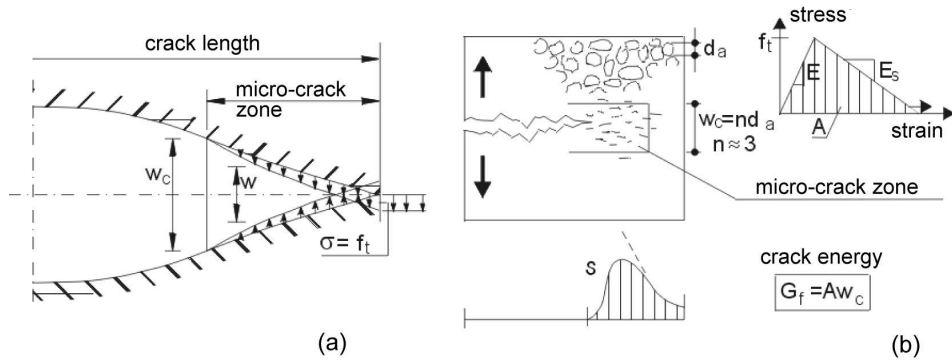


Figure 2.3: Fictitious Crack Model (a) and Crack Band Model (b), reprinted from Van Mier [78].

In the Crack Band Model, developed by Bažant & Oh [6], a similar approach is followed. However, instead of a line crack, it is now assumed that a crack band of a certain width is present [Fig. 2.3b]. This assumption has the advantage that the model can be implemented in normal finite element codes without the necessity to specify additional interface elements, as required for the Fictitious Crack Model. However, the 'smeared' Crack Band Model requires an additional parameter: the width of the band over which the cracks have been 'smeared-out'. Bažant & Oh based the Crack Band Model on the assumption that a crack in concrete normally is not a straight line, but that it follows a tortuous path due to the presence of aggregate particles in concrete. This causes the energy to dissipate along a volume

with distinct dimensions, instead of along a surface as assumed in Hillerborg's model.

### 2.2.2 Experimental Validation

To determine the parameters in the Fictitious Crack Model it was originally proposed to perform a uniaxial tensile test between non-rotating loading platens. Because the model requires knowledge about softening, the experiment should be carried-out in deformation-control. In such an experiment a regulation amplifier is used to continuously adjust the loading (i.e., force) while the deformation increases linearly. The force may either increase or decrease. An example of results is shown in Figure 2.4.

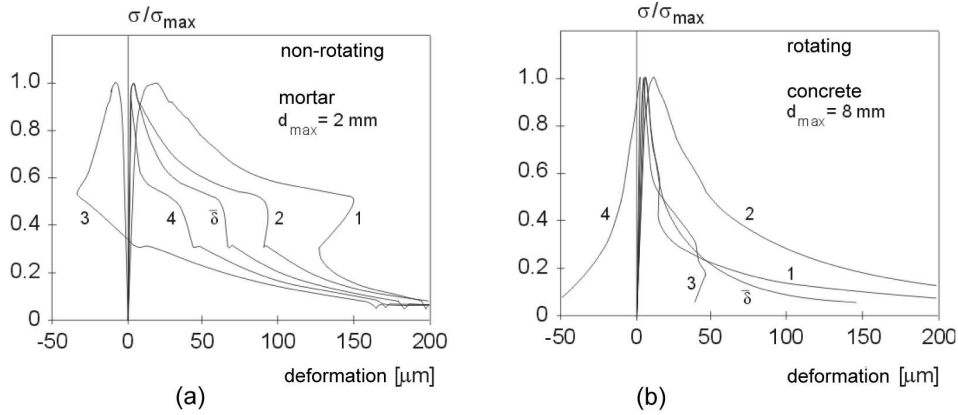


Figure 2.4: Result of a deformation-controlled uniaxial tension experiment between fixed (non-rotating) loading platens (a) and between rotating platens (b) (after Van Mier [78]).

Figure 2.4a gives a result conform the original proposal of Hillerborg. The test specimen (a cylinder with a diameter of 100 mm and a 5 mm deep groove halfway along the height) is loaded between platens, which cannot rotate during the entire experiment. The deformations have been measured around the test specimen and the bold solid line (with the symbol  $\bar{\delta}$ ) is the average of the four measurements around the specimen's circumference. After a maximum load has been recorded, the load decreases quickly. Then a plateau is observed, followed by a long tail.

Figure 2.4b shows the result of a tensile test between freely rotating loading platens. The dimensions of the specimen, and all other variables of the experiment, were the same as for the non-rotating test [Fig. 2.4a]. The only difference is the composition of the concrete, but this does not affect the fracture mechanism. Like for the experiment with non-rotating platens, the four individual measurements around the specimen are indicated (enumerated 1 to 4), together with the average of these four measurements.

Both experiments are completely comparable, the only difference being the allowed rotation of the loading platens. There is a minor difference in crack initiation.

The experiments showed that a (macroscopic) crack always nucleates when the maximum tensile stress is reached. It was also observed that the maximum tensile stress was a little bit smaller in the case with rotating loading platens. Evidently, the fixed platens allow for some redistribution of stresses after the appearance of the first micro-cracks. For this purpose, the cylindrical test specimens are perfect: crack initiation is possible from any weak spot around the circumference. Prismatic specimens generally show a stress concentration at the corners, which influences crack initiation, as confirmed by numerous tensile tests on prismatic specimens. However, the big difference is in the crack propagation phase. Photo-elastic investigations have proved that a macroscopic crack propagates while the stress–deformation diagram describes a descending branch (see Van Mier & Nooru-Mohamed [80]). Moiré interferometry gives similar results (see Raiss et al. [56]). In a test with fixed loading platens, propagation of a macro crack induces a load-eccentricity. Because the platens are fixed, a counteracting bending moment will arise which temporarily restrains crack propagation, or sometimes may even completely stop it. From Figure 2.4a this restrained crack propagation can be derived: it causes the plateau in the stress–displacement diagram. At a certain point the local stress at the other side of the test specimen rises to the level that a second crack develops which causes a steep drop of the global stress, as can be seen from Figure 2.4a.

Fixed loading platens allow for redistribution of stresses in the cracked cross-section. As a consequence, multiple cracks may arise and the stress–deformation diagram shows a curious ‘bump’. Figure 2.5 shows this behavior as well as the crack pattern that develops.

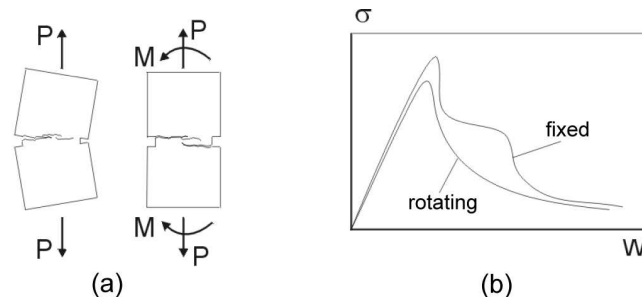


Figure 2.5: Difference in crack mechanism in a uniaxial tension test between freely rotating and fixed loading platens (a), and schematic stress–crack-opening diagrams (b) (after Van Mier [78]).

For a test with freely rotating loading platens the behavior is totally different. In this case stresses can not be redistributed during the propagation phase; after initiation the crack will simply grow from one side of the specimen to the opposite side. The result is a nice, smoothly falling softening branch as depicted in Figure 2.4b. The crack mechanism is shown in Figure 2.5. Actually, the smooth decrease of the global stress indicates a gradually decreasing cross-sectional area. Figure 2.4b also shows that during opening of the crack larger deformations occur at one side of

the specimen, while a compressive zone develops at the opposite side of the specimen. This justifies the conclusion that internal bending occurs in the uniaxial tensile test.

The long tail of the stress–displacement diagrams can be explained from the so-called ‘crack bridges’ that develop in the growing macro crack. The crack is not immediately stress-free. The development of crack bridges has been convincingly shown by Van Mier [80, 77, 76]. The size of the largest aggregate particles in the concrete influences the size of the crack bridges, and with that the stress that can be transferred in the tail of the diagram. Comparing the average stress–deformation diagrams in Figure 2.4a-b shows the relatively small difference in the tail of the diagrams, caused by the different dimensions of the aggregate particles.

Usually the area below the softening branch is related to the total amount of energy required for the fracture process,

$$G_f = \int \sigma(w) dw \quad (2.2)$$

Generally a linear stress–strain behavior until peak (the tensile strength) is assumed. Beyond the peak, the localization of deformations in a crack justifies the term ‘stress–crack-opening diagram’. The fracture energy is equal to the area below this falling trajectory and is expressed in newton per meter [N/m]. The fracture energy is influenced by the composition of the concrete (like the water–cement ratio, the largest aggregate size), as well as by the maturity (age), the loading rate, and many other parameters. Going into details about this would lead too far afield here; for further reading see Van Mier [78]. Here we limit ourselves by mentioning that the tensile strength of concrete may vary between 0.5 and 15 MPa, and the fracture energy between 30 and 20000 N/m. These are very extreme values: for concrete with low compressive strength ( $f_c \leq 10$  MPa) to materials with large amounts of fibers incorporated. The tensile strength for normal construction concrete ranges from 3 to 6 MPa and the fracture energy from 80 to 150 N/m.

We once more emphasize that the fracture energy may *not* be considered as a material property. The parameter depends on the boundary conditions in the experiment, and on the dimensions of the test specimen (size-effect). In the Fictitious Crack Model the fracture energy is a major parameter, but the physical basis is very weak. Unfortunately, the area of application of the model is not generally mentioned, but it is obvious that for very low concrete qualities, as well as for extremely high-performance materials, the model should at least be adapted.

A parameter derived from the Fictitious Crack Model is the characteristic length  $l_{ch}$ . This parameter exclusively comprises material parameters like the modulus of elasticity  $E$ , the tensile strength  $f_t$ , and the fracture energy  $G_f$ .

$$l_{ch} = \frac{E G_f}{f_t^2} \quad (2.3)$$

The lower the value of  $l_{ch}$ , the more brittle the material will behave. The various materials may only be compared if the dimensions of the test specimen or structure do not change. The only correct approach is to take the characteristic dimension of the particular test specimen or structure into consideration. This characteristic

dimension can be the smallest dimension of the cross-section where the crack arises. The brittle behavior can then be analyzed by determining the quotient of two parameters: the surface energy required to form the crack, and the elastic energy as released in the specimen or structure (see Elfgren [24]):

$$\frac{\text{elastic energy}}{\text{fracture energy}} = \frac{\frac{L^3 f_t^2}{E}}{L^2 G_f} = \frac{L f_t^2}{E G_f} \quad (2.4)$$

It appears that the brittle behavior does not exclusively depend on the material properties, but also on the dimensions of the structure. Equation (2.4) clearly demonstrates the close relation between material behavior and the structural behavior. The greatest problem with fracture experiments is to separate the effects caused by the material and by the structure itself.

The results of the uniaxial tensile experiment in Figure 2.4 and Figure 2.5 clearly prove that it is not easy to simply and directly measure the tensile strength and the fracture behavior. The fracture energy measured in the test with freely rotating platens was 30 to 40% lower than the value from the test with fixed platens. Moreover, both the tensile strength and the fracture energy are scale dependent [Fig. 2.6]. In a series of stable deformation-controlled uniaxial tensile tests between freely rotating loading platens, the complete stress–crack opening diagram of concrete has been measured in a scale range of 1:32 (see Van Vliet & Van Mier [81]).

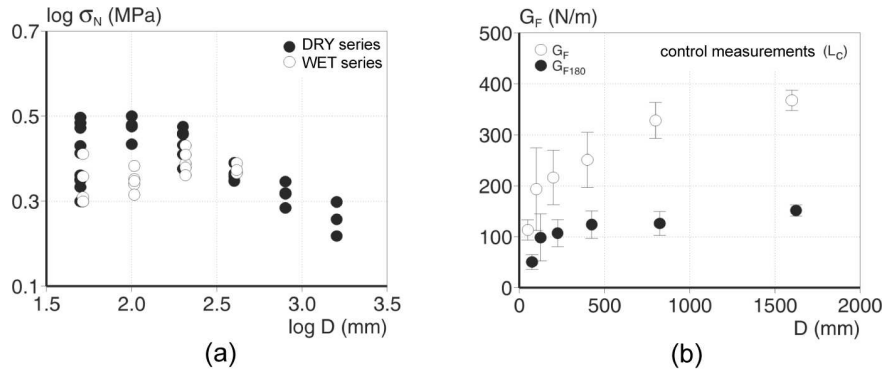


Figure 2.6: Scale dependency of tensile strength (a) and fracture energy (b) measured in uniaxial tension (after Van Vliet & Van Mier [81]).

Figure 2.6a shows the results of tensile tests on specimens where the moisture content was in equilibrium with the environment (solid circles), and of tests where a large moisture gradient was present (open circles). For the latter type of specimen, i.e., *wet* specimen, only the four smallest dimensions have been tested because of restrictions in the storage of larger specimen in a fog-room ( $RH \approx 95\%$ ). Note that the largest specimens were 2.40 m long. All specimens were made of plain concrete, which required handling with great care to prevent premature cracking.

The influence of the various humidity conditions is particularly visible for the smaller specimens. The ‘dry’ tests show, after a small increase of the tensile strength, a gradual decrease of the strength with increasing specimen dimensions. The slope seems to become constant beyond the third specimen size. Investigations have shown that the strength of the dry tests, i.e., the constant slope for the four largest dimensions, can be described by a Weibull model (Weakest Link model). Problems arise for the smallest dimensions. The largest aggregates in the concrete had a size of only 8 mm but the smallest dimension of the two smallest specimens was 37.5 and 75 mm. This comes very close to the so-called representative volume. The results of the smallest specimens show a large scatter, which possibly justifies the conclusion that a representative volume of  $5\times$  the largest aggregate particle in the concrete mixture is inappropriate. Therefore, the smallest specimen can only be analyzed with a micro-mechanical model.

For the smallest specimen, the results for strength are particularly affected when high moisture gradients are present. In applied mechanics, phenomena other than mechanical, are generally incorporated via phenomenology. An example of such a phenomenon is drying, and the related shrinkage, which probably extends over a zone of constant depth, is independent of the original specimen size. The results of Figure 2.6 show that the influence of non-uniform drying is not trivial: sizes that are found in real structural applications are significantly affected by these physical processes.

### 2.2.3 Influence of Reinforcement

In the previous sections we have shown that in a uniaxial tensile test, depending on the boundary conditions, redistributions of stress may appear which change the shape of the softening curve. Apart from the boundary conditions also the bending stiffness of the test specimen influences this ‘bump’. In reinforced concrete structures the stresses may be redistributed because after cracking the stress, as originally carried in the full concrete cross-section, is concentrated in the reinforcement across the crack. This reinforcement may be internally or externally applied, but also (on a lower material level) steel or synthetic fibers maybe as mixed into the concrete. The shear stress–slip behavior between the bar or fiber and the surrounding concrete is of importance to the bridging of the cracks by the reinforcement. Finite element codes like DIANA facilitate the simulation of this shear stress–slip behavior via interface elements.

A variation on the interface model is the so-called Tension Stiffening Model. In this model the behavior of reinforcement and concrete is considered entirely at the level of the constitutive models. With such a ‘smeared’ approach, the stiffness of the elements must be estimated correctly, considering the reinforcement/concrete ratio. We will not enter into details on this subject, which as such can become very complex for various reinforcement configurations.



## 2.3 Failure under Uniaxial Compression

In addition to the previously described failure under uniaxial tension, fundamental failure of concrete can also be studied under uniaxial compression. The compression situation is more complex because apart from cracking<sup>1</sup> also shear will occur. Possibly, the compressive test is the most common test in concrete practice. Generally speaking, for reinforced concrete structures tensile cracking is the governing factor. However, in some situations compressive failure may occur, like, for instance, in the case where the rotation capacity of beams and plates is considered. In such situations a proper understanding of concrete failure, both in tension and compression, is essential. In this section we will treat the behavior of concrete under uniaxial compression in more detail.

With respect to compression, phenomenological descriptions of behavior have prevailed over the years. In the 1970's and 1980's general applicable constitutive equations for concrete under multiaxial stress were developed. The uniaxial compressive state of stress is a particular case. We will now first describe some important observations in experiments under uniaxial compression. After that, we will describe the model of Markeset [50] which elaborates on these experiments. In this case, the experiments have significantly pushed the development of models in the right direction.

### 2.3.1 Experimental Validation

In a standard compression test, a concrete cube of 150 mm is loaded between two stiff steel loading platens. Of course, the contact surfaces must be flat to ensure a proper transfer of the stresses from the loading platens to the test specimen. The loading apparatus has a ball hinge at one side to set off slight obliqueness of the specimen.

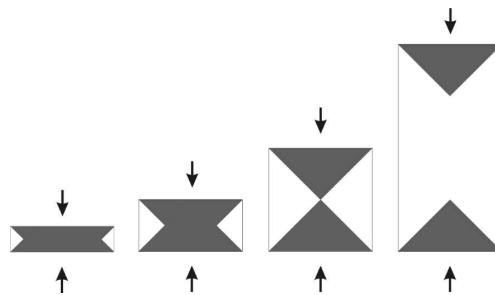


Figure 2.7: Triaxially confined influence zones in concrete prisms, loaded vertically between stiff steel loading platens (reprinted from Van Mier [78]).

The failure pattern is well-known: two pyramidal rest-parts and a crushed center zone are formed in a load-controlled test. Thus, the failure pattern is far more

<sup>1</sup>Cracking at grain level of the concrete; note that in continuum mechanics no tensile stresses are generated in a compression test.

complex than under uniaxial tension. The pyramidal parts are due to disturbance of the state of stress near the stiff loading platens.

During application of the loading, the difference in Young's modulus  $E$  and Poisson's ratio  $\nu$  for steel and concrete enables the development of inward directed frictional forces between the loading platens and specimen. The frictional forces appear in two mutually perpendicular directions. In combination with the axial pressure this yields a triaxial compressive state of stress in the end-zones of the specimen. The affected zones are of constant dimension: about half the diameter of the specimen. Tests on specimens of various slenderness (various lengths with equal cross-section), lead to the picture of Figure 2.7. For very slender specimens, the influence zones are clearly separated; for lower slenderness the zones may overlap.

The specimens strength becomes dependent on the slenderness due to these end-effects. Short specimens are in a state of triaxial compression, and yield a higher failure strength than more slender specimens where a larger part of the specimen volume is under a more-or-less uniaxial state of stress. The relation between failure strength and slenderness is shown in Figure 2.8. Immediately the question arises: "What is the uniaxial compressive strength of concrete?" For slender specimen ( $h/d = 2$  to 2.5), the curve approximates an asymptote. This value is generally assumed to represent the compressive strength of concrete.

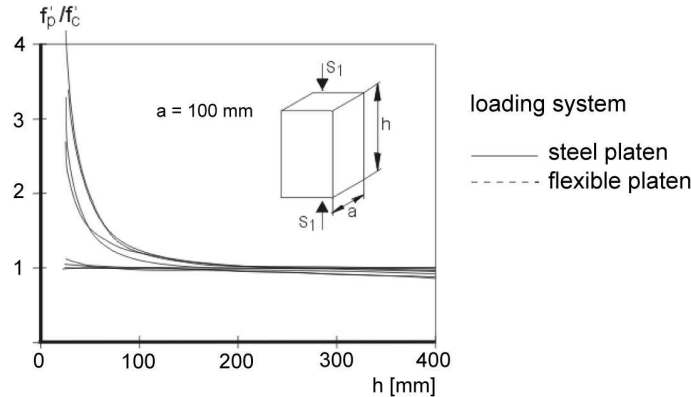


Figure 2.8: Influence of specimen slenderness on the uniaxial compressive strength of concrete (reprinted from Van Mier [78]).

When friction reducing layers are placed in between the steel loading platens and the concrete specimen, the observed strength is almost constant for varying slenderness. Such results are also depicted in Figure 2.8. They indicate that friction is the primary cause of the varying compressive strength. The 'flexible' loading platen, referred to in Figure 2.8, is a loading system with low friction, developed by Schickert [62]. The friction coefficient is a bit higher than for Teflon, but still considerably lower than for dry steel platens.

Figure 2.9 shows four diagrams of axial stress against axial strain, measured for test specimens of various slenderness, various concrete quality, and loaded between

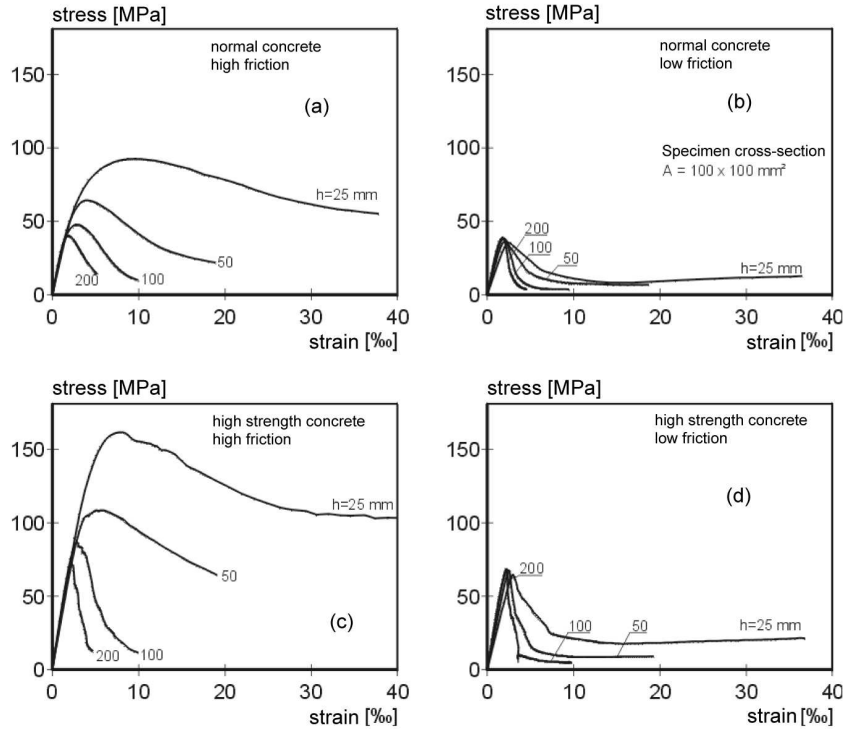


Figure 2.9: Influence of specimen slenderness and concrete quality on the uniaxial stress-strain diagram of normal concrete (a,b) and high strength concrete (c,d). Results have been obtained with specimen loaded between stiff steel platens (a,c) or between low friction platens (b,d) (reprinted from Van Mier [78]).

various types of loading platens. The two figures at the left (a,c) show the results obtained from specimen loaded between stiff platens; the two graphs at the right side (b,d) have been obtained with a friction-less interlayer. These results clearly show the differences in maximum stress. In addition, the deformations also increase when no friction-reducing interlayers are used. Most notable is the increasing ‘toughness’ in the softening zone when the friction between loading platens and specimen is at its maximum. This phenomenon has been observed previously by Kotsovos [44]. It induced him to conclude that the behavior beyond the peak could best be described by means of a purely brittle fracture model. He thought that the entire softening behavior could be explained from the boundary conditions during the experiment. This is a risky conclusion. Indeed, when the direction of the friction between loading platens and specimen changes, a splitting crack with a very brittle character may arise. However, this brittle behavior is most likely caused by an erroneously selected deformation parameter, which is used to control the experiment. Looking at the results in Figure 2.9, particularly the results with friction-reducing measures, it appears that for similar deformation in the softening regime the curve for the 100 mm

cubes shows stresses which are approximately  $2\times$  as high as for the 200 mm high prism.

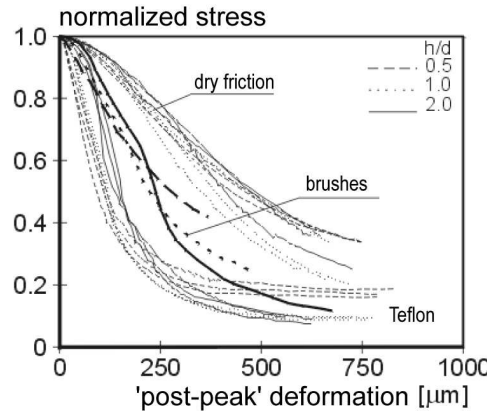


Figure 2.10: Localization of deformations in the softening regime for concrete loaded in uniaxial compression (reprinted from Van Mier [78]).

If only the deformations beyond the maximum stress are plotted against the stresses, then the diagram of Figure 2.10 is obtained. This figure shows the post-peak curves for measurements with specimens of various slenderness and between various loading platens: brushes, steel platens with Teflon interlayer, and massive steel platens. The stress-axis is shown in dimensionless form to enable comparison. For each type of loading platen the results for various slenderness come in a narrow bundle. In other words: the post-peak behavior seems to be independent of the specimens' slenderness when the deformations rather than the strains are plotted along the horizontal axis against the (dimensionless) stress. This proves that localization of deformations occurs beyond the peak, analogous to the failure of concrete under uniaxial tension. The difference is that for compressive experiments the actual failure pattern is obscured by the more distributed crack propagation.

The area below the stress-strain curve could be associated with the fracture energy of concrete under compression, as for the tensile experiment. By measuring the crack surface, Vonk has tried to compute the fracture energy under compression from the fracture energy under tension [93]. Microcracking is an important part of the fracture process under compression, but it does not account for the total energy dissipation. A similar conclusion was drawn earlier by Attigobe & Darwin [3]. In the next section we will describe a model where efforts have been made to separate the various mechanisms.

In conclusion, the following remarks are made. For compressive experiments, the rotations of the loading platens and the possible friction between loading platens and test specimen are of the utmost importance. Recently, the RILEM Technical Committee 148-SSC has proposed a standard experiment to determine the strain-softening curve under uniaxial compression [58]. The proposal is to load 200 mm high

prisms between platens with Teflon sandwich layers to reduce the friction. One of the most important reasons is that such experiments show considerably less scatter.

### 2.3.2 Compression Damage Zone Model

As discussed previously, localization of deformations occurs, which requires a fracture mechanics approach to correctly describe the behavior in compression. Recently two models have been developed: the CDZ model by Markeset [49], and the BDZ model by König et al. [43]. Basically both models are comparable, therefore we will restrict ourselves to a global description of Markeset's CDZ model. The Compression Damage Zone model is an elaboration of an earlier model by Hillerborg [36]. In analogy with the model for tension, Hillerborg's model discerns a localization zone when the material has reached the maximum compressive strength. In that case, the total deformations comprise an elastic part, and a nonlinear part which covers the localized deformations.

Considering that distributed crack formation occurs around the localized crack zone evidently induces some additional energy dissipation. Markeset introduced this energy dissipation from distributed cracking as a third component. Moreover, the linear elastic zone (before the peak) was converted into a nonlinear elastic behavior. The three types of behavior may then be described as follows [Fig. 2.11].

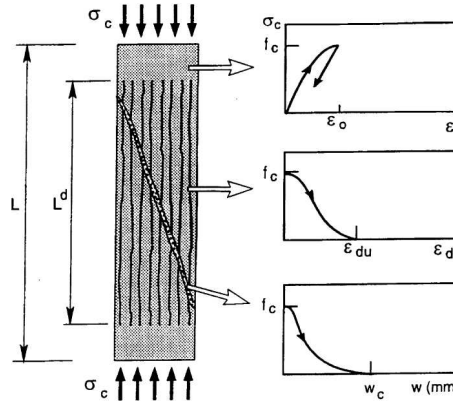


Figure 2.11: Compression Damage Zone model to describe concrete behavior under uniaxial compression (from Markeset [49]).

**Regime 1:** the material behaves nonlinearly elastic, i.e., it has not yet exceeded the maximum stress and remains (macroscopically) uncracked ( $\sigma$ - $\epsilon$ ).

**Regime 2:** describes the cracked material outside the localization zone with a relation between stress and additional strain ( $\sigma$ - $\epsilon_d$ ).

**Regime 3:** describes material in the localization zone ('shear band') with a stress-deformation relation ( $\sigma$ - $w$ ), which actually describes the transfer of friction in the shear band.

The model of Figure 2.11 shows an additional parameter: the localization length  $L^d$ . Generally this length is assumed to be two to three times the width of the test specimen. The total strain in the model is then described as

$$\varepsilon_m = \varepsilon + \varepsilon_d + \frac{w}{L} \quad (2.5)$$

The extension in relation to Hillerborg's 1990 model is the strain component  $\varepsilon_d$ . With Markeset's model the rotation capacity of beams can be described adequately.

It must be stated here that generally, localization causes problems in the Finite Element Method where a continuum model is applied to describe crack formation and localization. The definition of strain conflicts with the physically observed deformation and induces mesh dependency. To avoid this mesh dependency, generally higher order continuum models are introduced with an additional parameter to describe the average influence of microstructure. Possibly, here we reach the frontiers of applicability of continuum mechanics, albeit that the majority of applied mechanics experts will not accept this.

The fact remains that under tensile as well as under compressive loading the failure of concrete is a gradual process of microcrack propagation to localization of deformation in a single macroscopic crack, where the material has broken into two or more discrete pieces. Particularly the fracture phase has little to do with a continuum, and hence I am confident that here it would be better to follow the physics of the fracture process. It would lead too far afield for this chapter to go into more detail about this. For a more comprehensive discussion on this subject, the interested reader is referred to Van Mier [78].

## 2.4 Multiaxial States of Stress

In the previous sections we have described the complex behavior under uniaxial tension and uniaxial compression. Basically these are the most simple loadings. Generally speaking, reinforced concrete structures are subjected to multiaxial states of stress. For most of the applications a biaxial description is more than adequate. However, exceptional three-dimensional structures, like for instance components of off-shore platforms or nuclear reactors, may require a more general description in three dimensions.

In the 1970's and 1980's triaxial stress situations have been studied thoroughly. Models have been developed to describe the bi- and triaxial failure envelope as well as numerous constitutive models which more or less adequately describe the stress-deformation behavior. A triaxial failure envelope is an essential part of most of these models. This is a complex curved cone with the apex in the triaxial tensile domain; it is assumed that the cone is open-ended in the triaxial compressive domain. Mathematical description is complex; however, in the past a number of models has been developed that approximate the envelope reasonably well. It must be considered that, due to the complexity of triaxial experiments, the scatter is rather large. Especially in zones where the material is not only loaded in compression but also in tension,

in one or two directions, the experiments are extremely complex, demanding, and time-consuming.

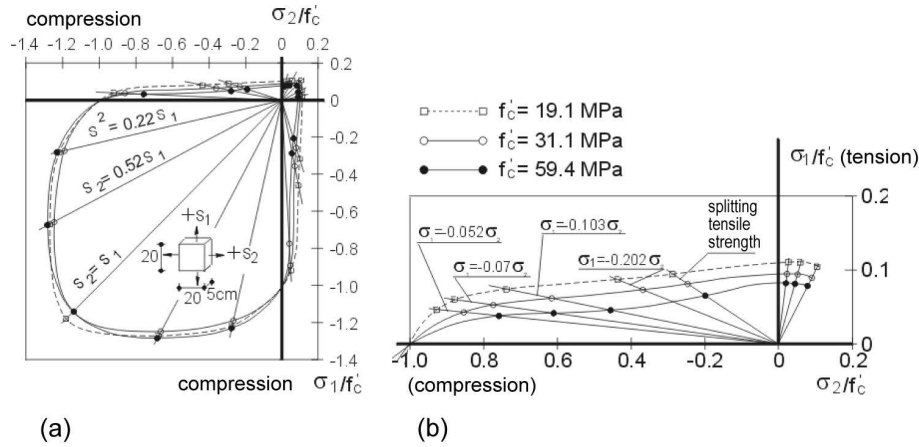


Figure 2.12: Biaxial failure envelope according to Kupfer [45]

Probably, the biaxial envelope has been best determined by Kupfer [45] [Fig. 2.12]. It is common knowledge that for biaxial compression the strength is about 20% higher than for uniaxial compression. The increase in biaxial strength appears to be independent of concrete quality. As soon as the loading is compressive in one direction and tensile in the other direction, then the strength decreases considerably compared to the uniaxial compressive strength. The effect of the tensile component is disastrous: the microcrack processes, which normally are very stable in a compressive stress field, are accelerated considerably. This causes failure at substantially lower levels of loading.

Here we do not describe the triaxial failure envelope. Again, the interested reader is referred to Van Mier [78], who gives a comprehensive overview. Chen [14] also gives an excellent overview of the various mathematical descriptions of the failure envelopes for concrete; the models are presented in order of increasing number of parameters. It is no surprise that the accuracy of the 'fit' increases with the number of parameters. The five-parameter model, developed by William & Warnke [95], seems to be quite optimal. It comprises five parameters that can be derived from the strength under certain loading combinations in the triaxial tensile and compressive domain. It turned out that the parameter set determined on a data set by Schickert & Winkler [62] also reasonably satisfied the experiments by Van Mier [75].

It would lead too far to repeat every detail. However, the following is of importance. Depending on the loading situation, various failure shapes may occur. Generally, the material will show cracks at right angles to the least loaded direction. For instance for biaxial compression this means that failure occurs due to splitting of the concrete in the plane through the two principal loading directions. This type of cracking is rather brittle, hence special control methods are required to maintain stability during the entire test. In case of a third compressive stress, failure will occur

in the least compressed direction. However, when the third compressive stress becomes too high, the material can behave as plastic metal and huge deformations may occur. Due to this observation a model for triaxially loaded concrete is often based on the theory of plasticity. However, in most triaxial stress states the deformations will localize as well. This is obvious when a tensile component is present. If, on the other hand, triaxial compression is concerned, a distinct shear band appears as shown in Figure 2.13. The width of the shear band depends, among other things, on the

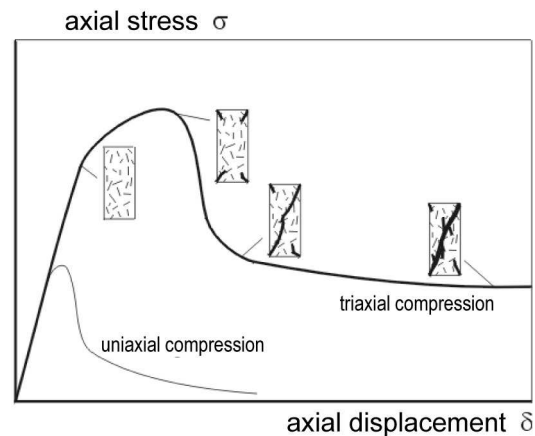


Figure 2.13: Shear-band formation under triaxial compression (reprinted from Van Mier [79]).

compressive state of stress and on the material structure (for example the maximum aggregate size). As stated previously, an increasing of the minor compressive stress, will lead to plastic material behavior. At a particular value of the minor compressive stress, depending on the material structure, the fracture will change from brittle into plastic. More fine-grained materials show this transition at a higher value of the minor stress. In case of plastic behavior a shear-band will still appear, however with a considerably larger width.

The above description is qualitative, but indicates that localization is problematic under virtually all stress situations. As stated earlier, for me it looks quite senseless to try to describe a jump in the displacement (which always accompanies the localization) by means of a continuum model. The physics of fracture and cracking must form an integral part of the model, otherwise no crack analysis whatsoever will be of predictive value. This is exactly what has always been the challenge in the Concrete Mechanics project. It is now on the model developers to develop more realistic, physically based models for fracture of concrete. This is just what they have managed to avoid in recent decades. Fortunately, the majority of the analyses as performed until now have not proceeded up to the failure limit. However, for rotation capacity predictions this is absolutely required and therefore a thorough adaptation of the models must be considered.



## 2.5 Conclusions

This chapter has described the behavior of concrete under uniaxial tension, uniaxial compression and under multiaxial states of stress. The overview is as restricted and global as can be outlined in limited available space. To describe the concrete behavior under uniaxial tension and uniaxial compression, in recent decades fracture mechanics theories have been applied. However, these theories have been adapted such that a continuum approach remains feasible. In my opinion this adaptation does no justice to the physics of crack formation, and therefore the models can never lead to correct predictions.

The major conclusion to be drawn from the above observations and descriptions are the following:

1. Localization of deformations occurs under uniaxial tension. The softening diagram under tension, representing this localization, depends on the boundary conditions in the experiment and on the size of the test specimen. Hence, strictly speaking, softening is *not* a material property.
2. The same can be concluded for the behavior under uniaxial compression. Also here softening and localization are not properties of the material, but combined material/structural effects.
3. Also under multiaxial compressive states of stress localization occurs. However, for increasing values of the minor compressive stress the behavior will change from brittle to ductile. Beyond the brittle–ductile transition a continuum model seems to be useful. However, such situations will not be met often in common concrete structures.
4. Size/scale effects can not be neglected: structural as well as material influences on fracture properties must be considered. In recent decades valuable information about this has been obtained from experiments.
5. Until now, experiments have provided a good insight in the physics of fracture. It would be my wish that the modelers should take up the challenge to develop more physically based models in a finite element environment. The concrete mechanics approach would certainly benefit from such a model, and it is to be expected that the current ‘post-diction’, can be directed toward real ‘predictions’.

Finally I would like to emphasize that this chapter describes the failure behavior under uniaxial tensile and compressive loading only very globally. Also the behavior under multiaxial loading has been described very briefly. Phenomena like shear deformation in cracks, bond of steel and concrete, and others, are of equal importance, but these have been omitted here in view of the limited space. A more comprehensive overview can be found in Van Mier [78].



## Chapter 3

# Comparison of Concrete Models for Cyclic Loading

P. H. Feenstra  
*Cornell Theory Center*

J. G. Rots  
*Delft University of Technology, Faculty of Architecture*

**Abstract**<sup>1</sup>. We present four popular constitutive models for reinforced concrete and compare the models on their merits for monotonic and cyclic loading. Whereas the behavior for monotonic loading does not differ much between the different models, the behavior for cyclic loading shows dramatic differences.

### 3.1 Introduction

Failure assessment of concrete structures is mainly dependent on the proper modeling of the constitutive behavior. Concrete is a heterogeneous material that resists compressive stresses relatively well, but can only resist small tensile stresses with a fast reduction of the stress after the peak stress has been reached. This quasi-brittle cracking behavior is also known as tension softening which results in a full separation of the material. This phenomenon can be modeled with the finite element method in different ways but in this study we will consider the cracked material still as a continuum where the cracking is modeled in a more phenomenological sense. The latter approach is known as smeared cracking which models the quasi-brittle material with a reduction of the strength of the material as a function of the loading history.

Under compressive loading, concrete also shows a nonlinear behavior where under uniaxial loading the material behaves approximately linear until one third of the

---

<sup>1</sup>This chapter is a reprint of an article in the ASCE Special Publication [29].

compressive strength. After that the behavior is nonlinear until the compressive strength, after which a decrease in the allowable stress is observed. The failure mechanism in compression is mainly isotropic, distributed small-scale cracking. This crushing mechanism is modeled with a continuum approach similar to the model used for cracking in this study.

The cyclic behavior of concrete is more complicated because of the complex mechanisms that occur during crack closure and re-opening, either with the localized cracking in tension, or the distributed cracking in compression. However, we can observe a more secant type of unloading and reloading in tension, and more elastic unloading and reloading in compression. The shear capacity, necessary in seismic regions to resist the earthquake loading, is mainly due to increased shear strength because of the confinement of the concrete. The confinement is often obtained in structural elements by the hoop reinforcement in column and beams. However, in this study we will concentrate on the cyclic behavior by comparing a shear wall structure. In these types of structures confinement is more difficult to obtain and therefore we assume a plane stress situation. We model the reinforcement in the structure with embedded reinforcement assuming perfect bond. So in conclusion, we restrict our application area such that we can concentrate on the cyclic behavior of the constitutive models.

## 3.2 Description of Constitutive Models for Concrete

As discussed above, we assume that the damaged concrete can be described with a continuum approach. Two ways exist to model the cracked concrete as a continuum. The first is to decompose the strain into a part that represents the concrete between the cracks, and a part that represents the smeared cracks. Such ‘decomposed strain-based models’ are conceptually elegant as they allow for a separate treatment of softening for the cracks and elasticity and/or plasticity for the continuum in between the cracks. The second way is to start from the notion of a total strain for the cracked material. These ‘total strain-based models’ describe the material via stress–total strain relations. This gives less flexibility for incorporating sophisticated crack laws, but the idea is conceptually simple and appealing to practicing engineers who think in terms of stress–strain relations rather than sophisticated crack laws or abstract yield functions.

Examples of the decomposed strain model for the tensile regime are the Rankine plasticity model [27, 51] and the multiple-fixed crack model [20, 60]. A popular decomposed strain model for compressive crushing is a plasticity model, e.g. Drucker–Prager or in plane stress the Von Mises yield criterion. The models for tension and compression can be combined, so that we arrive either at a full Rankine–Von Mises plasticity model, or a combination of the multiple-fixed crack model for tension with Von Mises plasticity for compression. Regarding total strain-based models, both tension and compression are captured within the same framework, via the engineering stress–strain laws for tension and compression respectively. Here, two variants exist. The total strain-based fixed model is an extended fixed, orthogonal crack model, and

the total strain based-rotating model is an extended rotating, orthogonal crack model [30].

Another approach for modeling constitutive behavior in concrete is damage-based models. A theoretical comparison of an isotropic damage model and a plasticity-based decomposed-strain model is discussed by Feenstra and De Borst [28]. In that study the damage model has only been applied to an elementary example to show the basic behavior of the damage model. The study of Rots [61] showed that the isotropic damage model performs well in an analysis of a plain concrete notched beam under three-point bending because it avoids stress locking. The isotropic damage model is, however, not applicable to model the stress redistribution in reinforced concrete structures like shear walls, because isotropic reduction of the stiffness would limit the ability to create compressive struts that work together with the reinforcement in tension.

This study aims at a comparison of four different models (multiple-fixed crack model with Von Mises, Rankine–Von Mises, total strain-based fixed, and a total strain-based rotating model) to compare the behavior for large-scale analysis of reinforced concrete structures under cyclic loading.

### 3.2.1 Multiple-Fixed Crack Model with Von Mises Crushing Model

The first model we discuss in this study is the combination of the multiple-fixed crack model [20, 60] and the Von Mises plasticity model to describe the compressive regime. This model is based on strain decomposition according to

$$\boldsymbol{\varepsilon} = \boldsymbol{\varepsilon}^e + \boldsymbol{\varepsilon}^{\text{crk}} + \boldsymbol{\varepsilon}^{\text{cru}} \quad (3.1)$$

with the total strain vector  $\boldsymbol{\varepsilon}$ , decomposed into an elastic part  $\boldsymbol{\varepsilon}^e$ , a cracking part  $\boldsymbol{\varepsilon}^{\text{crk}}$ , and a crushing part  $\boldsymbol{\varepsilon}^{\text{cru}}$ . The stress vector is then given by the elastic stiffness matrix  $\mathbf{D}^e$ , and the elastic part of the strain vector according to

$$\boldsymbol{\sigma} = \mathbf{D}^e \{ \boldsymbol{\varepsilon} - \boldsymbol{\varepsilon}^{\text{crk}} - \boldsymbol{\varepsilon}^{\text{cru}} \} \quad (3.2)$$

In this study we assume an isotropic elastic constitutive relationship with the stiffness matrix defined in a plane stress case as

$$\mathbf{D}^e = \frac{E}{1 - \nu^2} \begin{bmatrix} 1 & \nu & 0 \\ \nu & 1 & 0 \\ 0 & 0 & \frac{1 - \nu}{2} \end{bmatrix} \quad (3.3)$$

The crack strain vector is given by the summation of the crack strain vectors over the number of cracks  $n_{\text{crk}}$

$$\boldsymbol{\varepsilon}^{\text{crk}} = \sum_{i=1}^{n_{\text{crk}}} \boldsymbol{\varepsilon}_{(i)}^{\text{crk}} \quad (3.4)$$

The crack strain vector of the  $i$ -th crack is given by the transformation

$$\boldsymbol{\varepsilon}_{(i)}^{\text{crk}} = \mathbf{N}_{(i)} \mathbf{e}_{(i)}^{\text{crk}} \quad (3.5)$$

with the strain transformation matrix

$$\mathbf{N}_{(i)} = \begin{bmatrix} \cos^2 \phi_{(i)} & +2 \sin \phi_{(i)} \cos \phi_{(i)} \\ \sin^2 \phi_{(i)} & -2 \sin \phi_{(i)} \cos \phi_{(i)} \\ \sin \phi_{(i)} \cos \phi_{(i)} & \cos^2 \phi_{(i)} - \sin^2 \phi_{(i)} \end{bmatrix} \quad (3.6)$$

See Figure 3.1 for the different coordinate systems where two cracks are depicted. Note that in this model two cracks are not necessarily orthogonal. The local crack

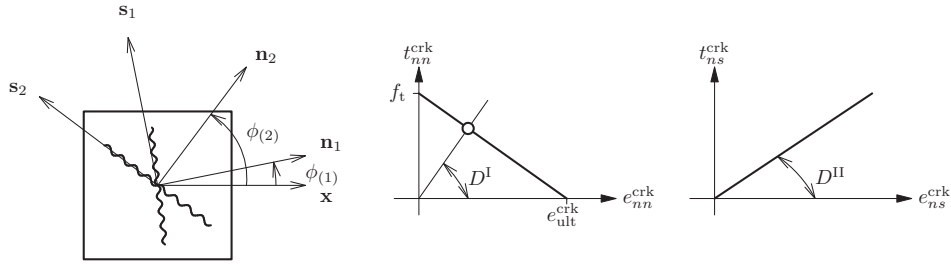


Figure 3.1: Multiple-fixed crack model

stress vector is determined by the static constraint

$$\mathbf{t}_{(i)}^{\text{crk}} = \mathbf{N}_{(i)}^T \boldsymbol{\sigma} = \mathbf{D}_{(i)}^{\text{crk}} \mathbf{e}_{(i)}^{\text{crk}} \quad (3.7)$$

The stiffness matrix  $\mathbf{D}_{(i)}^{\text{crk}}$  is the relationship between the crack strain and the crack stress of the  $i$ -th crack

$$\mathbf{D}_{(i)}^{\text{crk}} = \begin{bmatrix} D_{(i)}^I & 0 \\ 0 & D_{(i)}^{\text{II}} \end{bmatrix} \quad (3.8)$$

which can be elaborated for linear tension softening and a constant shear retention factor  $\beta$ , as

$$\mathbf{D}_{(i)}^{\text{crk}} = \begin{bmatrix} \frac{f_t}{e_{\text{ult}}^{\text{crk}}} \left( \frac{e_{\text{ult}}^{\text{crk}} - e_{nn}^{\text{crk}}}{e_{nn}^{\text{crk}}} \right) & 0 \\ 0 & \frac{\beta}{1 - \beta} G \end{bmatrix} \quad (3.9)$$

The stiffness terms in this matrix are schematically shown in Figure 3.1. The relationship between the stress and the strain vector for damaged concrete is now derived from the elastic stress update,

$$\boldsymbol{\sigma} = \mathbf{D}^e \boldsymbol{\varepsilon}^e = \mathbf{D}^e \left\{ \boldsymbol{\varepsilon} - \sum_{i=1}^{n_{\text{crk}}} \boldsymbol{\varepsilon}_{(i)}^{\text{crk}} - \boldsymbol{\varepsilon}^{\text{cru}} \right\} \quad (3.10)$$

To simplify the notation, we do not write the crack strain vector as the summation of the local crack strain vectors. Instead, we write [57],

$$\boldsymbol{\varepsilon}^{\text{crk}} = \mathbf{U} \mathbf{e}^{\text{crk}} \quad (3.11)$$

with the generalized transformation matrix

$$\mathbf{U} = [\mathbf{N}_{(1)}, \mathbf{N}_{(2)}, \dots, \mathbf{N}_{(n_{\text{crk}})}] \quad (3.12)$$

Furthermore we have the generalized local crack stress vector and generalized local crack strain vector,

$$\mathbf{t}^{\text{crk}} = \begin{Bmatrix} \mathbf{t}_{(1)}^{\text{crk}} \\ \mathbf{t}_{(2)}^{\text{crk}} \\ \vdots \\ \mathbf{t}_{(n_{\text{crk}})}^{\text{crk}} \end{Bmatrix} \quad \mathbf{e}^{\text{crk}} = \begin{Bmatrix} \mathbf{e}_{(1)}^{\text{crk}} \\ \mathbf{e}_{(2)}^{\text{crk}} \\ \vdots \\ \mathbf{e}_{(n_{\text{crk}})}^{\text{crk}} \end{Bmatrix} \quad (3.13)$$

and the local crack stress-strain relationship given by

$$\mathbf{D}^{\text{crk}} = \begin{bmatrix} \mathbf{D}_{(1)}^{\text{crk}} & \mathbf{0} & \dots & \mathbf{0} \\ \mathbf{0} & \mathbf{D}_{(2)}^{\text{crk}} & \dots & \mathbf{0} \\ \vdots & \vdots & \ddots & \vdots \\ \mathbf{0} & \mathbf{0} & \dots & \mathbf{D}_{(n_{\text{crk}})}^{\text{crk}} \end{bmatrix} \quad (3.14)$$

assuming no direct interaction between the different cracks.

The generalized local crack strain can be found by pre-multiplication with  $\mathbf{U}^T$  which results in

$$\mathbf{U}^T \boldsymbol{\sigma} = \mathbf{U}^T \mathbf{D}^e \boldsymbol{\varepsilon} - \mathbf{U}^T \mathbf{D}^e \mathbf{U} \mathbf{e}^{\text{crk}} - \mathbf{U}^T \mathbf{D}^e \boldsymbol{\varepsilon}^{\text{cru}} = \mathbf{t}^{\text{crk}} = \mathbf{D}^{\text{crk}} \mathbf{e}^{\text{crk}} \quad (3.15)$$

so it follows that

$$\mathbf{e}^{\text{crk}} = [\mathbf{D}^{\text{crk}} + \mathbf{U}^T \mathbf{D}^e \mathbf{U}]^{-1} \mathbf{U}^T \mathbf{D}^e \{\boldsymbol{\varepsilon} - \boldsymbol{\varepsilon}^{\text{cru}}\} \quad (3.16)$$

The updated stress vector is finally given by

$$\begin{aligned} \boldsymbol{\sigma} &= \mathbf{D}^e \{\boldsymbol{\varepsilon} - \mathbf{U} \mathbf{e}^{\text{crk}} - \boldsymbol{\varepsilon}^{\text{cru}}\} \\ &= [\mathbf{D}^e - \mathbf{D}^e \mathbf{U} [\mathbf{D}^{\text{crk}} + \mathbf{U}^T \mathbf{D}^e \mathbf{U}]^{-1} \mathbf{U}^T \mathbf{D}^e] \{\boldsymbol{\varepsilon} - \boldsymbol{\varepsilon}^{\text{cru}}\} \\ &= \mathbf{D}^{\text{crco}} \{\boldsymbol{\varepsilon} - \boldsymbol{\varepsilon}^{\text{cru}}\} \end{aligned} \quad (3.17)$$

With which the update of the stress vector solely depends on the updated crushing strain vector  $\boldsymbol{\varepsilon}^{\text{cru}}$ . See for more details about the multiple-fixed crack model [60].

The crushing strain vector is governed by a flow theory of plasticity where we assume the Von Mises yield surface as the failure surface and the potential surface. The crushing strain rate vector is then given by the following relationship,

$$\dot{\boldsymbol{\varepsilon}}^{\text{cru}} = \dot{\lambda}_{\text{vm}} \frac{\partial f_{\text{vm}}}{\partial \boldsymbol{\sigma}} \quad (3.18)$$

with the complementary Kuhn–Tucker conditions

$$\dot{\lambda}_{\text{vm}} \geq 0 \quad f_{\text{vm}} \leq 0 \quad \dot{\lambda}_{\text{vm}} f_{\text{vm}} = 0 \quad (3.19)$$

The Von Mises yield surface is here defined in the square root form,

$$f_{\text{vm}} = \sqrt{\frac{1}{2} \boldsymbol{\sigma}^T \mathbf{P}_{\text{vm}} \boldsymbol{\sigma}} - f_c \quad (3.20)$$

with the projection matrix

$$\mathbf{P}_{\text{vm}} = \frac{1}{3} \begin{bmatrix} 2 & -1 & 0 \\ -1 & 2 & 0 \\ 0 & 0 & 6 \end{bmatrix} \quad (3.21)$$

It is tacitly assumed that the compressive behavior is modeled elastic-perfectly plastic. The updated crushing strain is now determined by

$$\boldsymbol{\varepsilon}^{\text{cru}} = \boldsymbol{\varepsilon}^{\text{cru}} + \Delta \boldsymbol{\varepsilon}^{\text{cru}} \quad (3.22)$$

so that the updated stress is given by

$$\boldsymbol{\sigma} = \mathbf{D}^{\text{crco}} \{ \boldsymbol{\varepsilon} - \boldsymbol{\varepsilon}^{\text{cru}} - \Delta \boldsymbol{\varepsilon}^{\text{cru}} \} \quad (3.23)$$

Substituting the crushing strain increment,

$$\Delta \boldsymbol{\varepsilon}^{\text{cru}} = \Delta \lambda_{\text{vm}} \frac{\mathbf{P}_{\text{vm}} \boldsymbol{\sigma}}{2 \Psi_{\text{vm}}} \quad (3.24)$$

with  $\Psi_{\text{vm}} = \sqrt{\frac{1}{2} \boldsymbol{\sigma}^T \mathbf{P}_{\text{vm}} \boldsymbol{\sigma}}$  finally gives the updated stress vector,

$$\boldsymbol{\sigma} = \left[ \mathbf{I} + \frac{\Delta \lambda_{\text{vm}}}{2 \Psi_{\text{vm}}} \mathbf{D}^{\text{crco}} \mathbf{P}_{\text{vm}} \right]^{-1} \boldsymbol{\sigma}^E \quad (3.25)$$

with the elastic trial stress given by

$$\boldsymbol{\sigma}^E = \mathbf{D}^{\text{crco}} \{ \boldsymbol{\varepsilon} - \boldsymbol{\varepsilon}^{\text{cru}} \} \quad (3.26)$$

If the elastic trial stress does not violate the yield condition in (3.20), the updated stress is given by the elastic trial stress, otherwise the return-mapping procedure presented in (3.25) should be applied. The relationships presented in (3.17) and (3.26) are in general nonlinear and need an iterative solution to solve the system such that the resulting stress situation both complies with the cracking model and with the plasticity model. For a more comprehensive discussion about smeared cracking and plasticity see [19].



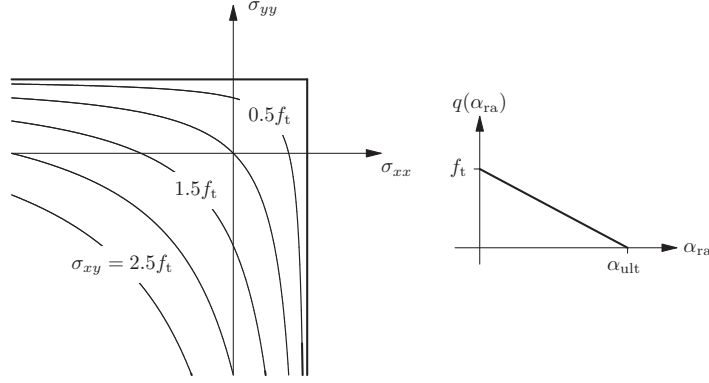


Figure 3.2: Rankine plasticity model

### 3.2.2 Rankine–Von Mises Plasticity Model

This plasticity-based model is also defined in terms of strain decomposition according to (3.1) and the stress vector is again given by (3.2). The plasticity model that describes the tensile failure surface governs now the crack strain rate vector,

$$\dot{\epsilon}^{\text{crk}} = \dot{\lambda}_{\text{ra}} \frac{\partial f_{\text{ra}}}{\partial \sigma} \quad (3.27)$$

and the crushing strain vector by the plasticity model describing the compressive failure surface,

$$\dot{\epsilon}^{\text{cru}} = \dot{\lambda}_{\text{vm}} \frac{\partial f_{\text{vm}}}{\partial \sigma} \quad (3.28)$$

with the conditions

$$\begin{aligned} \dot{\lambda}_{\text{ra}} &\geq 0 & f_{\text{ra}} &\leq 0 & \dot{\lambda}_{\text{ra}} f_{\text{ra}} &= 0 \\ \dot{\lambda}_{\text{vm}} &\geq 0 & f_{\text{vm}} &\leq 0 & \dot{\lambda}_{\text{vm}} f_{\text{vm}} &= 0 \end{aligned} \quad (3.29)$$

The failure surface for tensile failure [Fig. 3.2] is given by the Rankine yield condition,

$$f_{\text{ra}} = \sqrt{\frac{1}{2} \sigma^T \mathbf{P}_{\text{ra}} \sigma} + \frac{1}{2} \pi^T \sigma - q(\alpha_{\text{ra}}) \quad (3.30)$$

The projection matrix of the Rankine criterion is given by

$$\mathbf{P}_{\text{ra}} = \frac{1}{2} \begin{bmatrix} 1 & -1 & 0 \\ -1 & 1 & 0 \\ 0 & 0 & 4 \end{bmatrix} \quad (3.31)$$

The failure surface for the compressive stresses is given by the Von Mises yield condition (3.20). The stress update is again dependent on the updated cracking and crushing strain which are now both given by the flow theory of plasticity,

$$\epsilon^{\text{crk}} = \epsilon^{\text{crk}} + \Delta \epsilon^{\text{crk}} \quad (3.32)$$

$$\epsilon^{\text{cru}} = \epsilon^{\text{cru}} + \Delta \epsilon^{\text{cru}} \quad (3.33)$$

so that the updated stress is given by

$$\boldsymbol{\sigma} = \mathbf{D}^e \{ \boldsymbol{\varepsilon} - \boldsymbol{\varepsilon}^{\text{crk}} - \boldsymbol{\varepsilon}^{\text{cru}} - \Delta \boldsymbol{\varepsilon}^{\text{crk}} - \Delta \boldsymbol{\varepsilon}^{\text{cru}} \} \quad (3.34)$$

Substituting the cracking and crushing strain increments,

$$\Delta \boldsymbol{\varepsilon}^{\text{crk}} = \Delta \lambda_{\text{ra}} \frac{\mathbf{P}_{\text{ra}} \boldsymbol{\sigma}}{2 \Psi_{\text{ra}}} + \Delta \lambda_{\text{ra}} \boldsymbol{\pi} \quad \text{and} \quad \Delta \boldsymbol{\varepsilon}^{\text{cru}} = \Delta \lambda_{\text{vm}} \frac{\mathbf{P}_{\text{vm}} \boldsymbol{\sigma}}{2 \Psi_{\text{vm}}} \quad (3.35)$$

with  $\Psi_{\text{ra}} = \sqrt{\frac{1}{2} \boldsymbol{\sigma}^T \mathbf{P}_{\text{ra}} \boldsymbol{\sigma}}$  and  $\Psi_{\text{vm}}$  defined earlier, this finally gives the updated strain vector,

$$\boldsymbol{\sigma} = \left[ \mathbf{I} + \frac{\Delta \lambda_{\text{ra}}}{2 \Psi_{\text{ra}}} \mathbf{D}^e \mathbf{P}_{\text{ra}} + \frac{\Delta \lambda_{\text{vm}}}{2 \Psi_{\text{vm}}} \mathbf{D}^e \mathbf{P}_{\text{vm}} \right]^{-1} \{ \boldsymbol{\sigma}^E - \frac{1}{2} \Delta \lambda_{\text{ra}} \mathbf{D}^e \boldsymbol{\pi} \} \quad (3.36)$$

with the elastic trial stress given by

$$\boldsymbol{\sigma}^E = \mathbf{D}^e \{ \boldsymbol{\varepsilon} - \boldsymbol{\varepsilon}^{\text{crk}} - \boldsymbol{\varepsilon}^{\text{cru}} \} \quad (3.37)$$

Again, if the elastic trial stress does not violate both yield conditions of (3.20) and (3.30), the updated stress is given by the elastic trial stress, otherwise the return-mapping procedure presented in (3.36) should be applied. The relationships presented in (3.36) are in general nonlinear and need an iterative solution to solve the system such that the resulting stress situation both complies with the Rankine failure condition and the Von Mises yield condition. For more details about the formulation and implementation details of the Rankine–Von Mises model see [26].

### 3.2.3 Total Strain-based Models

The constitutive models presented so far are both based on strain decomposition. The following class of models is based on total strain, i.e. the internal state is fully described by the components of the updated strain vector and the internal variables. The basic assumption in a total strain-based model is that the constitutive relationships are evaluated in a rotated, local coordinate system defined by an assumption for the crack initiation. The global strain update is given by

$$\boldsymbol{\varepsilon}_{xy} = \boldsymbol{\varepsilon}_{xy} + \Delta \boldsymbol{\varepsilon} \quad (3.38)$$

The local strain vector is now determined as

$$\boldsymbol{\varepsilon}_{ns} = \mathbf{T}(\tau \phi) \boldsymbol{\varepsilon}_{xy} \quad (3.39)$$

with  $\tau \phi$  the angle between the global coordinate system  $xy$  and the local coordinate system  $ns$ , determined at some time  $\tau$ . In a plane stress situation the angle is given by

$$\tau \phi = \frac{1}{2} \arctan \frac{\tau \gamma_{xy}}{\tau \varepsilon_{xx} - \tau \varepsilon_{yy}} \quad (3.40)$$

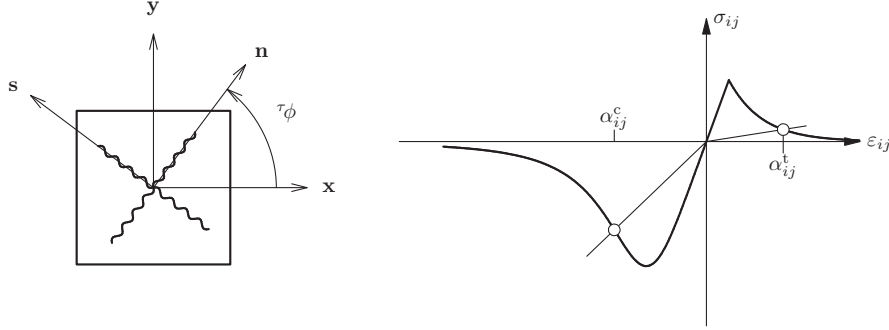


Figure 3.3: Total strain-based models

See Figure 3.3. Note that for the total strain-based model, two cracks are necessarily orthogonal. For a total strain-based fixed model the time  $\tau$  is given by the first occurrence of the violation of the failure condition in tension. For the total strain-based rotating model the time  $\tau$  is given by the current time  $t + \Delta t$ . Given the angle  $\phi$  between the local and the global coordinate system the strain transformation matrix is given by

$$\mathbf{T}(\phi) = \begin{bmatrix} \cos^2 \phi & \sin^2 \phi & +\sin \phi \cos \phi \\ \sin^2 \phi & \cos^2 \phi & -\sin \phi \cos \phi \\ -2 \sin \phi \cos \phi & +2 \sin \phi \cos \phi & \cos^2 \phi - \sin^2 \phi \end{bmatrix} \quad (3.41)$$

The stress vector in the local coordinate system is given by the general relationship

$$\boldsymbol{\sigma}_{ns} = \mathbf{D}(\boldsymbol{\varepsilon}_{ns}) \boldsymbol{\varepsilon}_{ns} \quad (3.42)$$

With the assumption of a co-rotational concept between the local strain vector and the local stress vector the updated stress vector in the global coordinate system is given by

$$\boldsymbol{\sigma}_{xy} = \mathbf{T}^T(\tau\phi) \boldsymbol{\sigma}_{ns} \quad (3.43)$$

With these equations the whole concept of total strain-based models is explained and we only need to specify the constitutive relationships in the local coordinate system (3.42). It is emphasized that these relationships are equal for the fixed and the rotating version of the total strain-based models. The formulation of the constitutive model in the local coordinate system is possible in a large number of ways. In this study we choose an equivalent uniaxial strain concept in which the stress in a certain direction is schematically given by

$$\sigma_{ij} = f_{ij}(\alpha_{ij}^s) \cdot g_{ij}(\alpha_{ij}^s, \varepsilon_{ij}) \quad (3.44)$$

with the subscript  $ij$  the direction under consideration, either  $nn$ ,  $ss$ , or  $ns$ . The general nonlinear function  $f_{ij}(\alpha_{ij}^s)$  is a function of an internal parameter  $\alpha_{ij}^s$ , which is here assumed to be determined by the maximum strain experienced in the direction  $ij$

either in tension,  $s$  equals ‘t’, and in compression,  $s$  equals ‘c’ [Fig. 3.3]. The loading–unloading function  $g_{ij}(\alpha_{ij}^s, \varepsilon_{ij})$  is assumed to be linear in tension and compression,

$$g_{ij}(\alpha_{ij}^s, \varepsilon_{ij}) = 1 - \frac{\alpha_{ij}^s - \varepsilon_{ij}}{\alpha_{ij}^s} \quad (3.45)$$

The model monitors the damage in the material with six different internal parameters, two in the normal tensile direction, two in the normal compressive direction, and in principal two in the shear direction. The implementation of the various functions can be quite complicated but there is no iteration involved in the stress update: as soon as the internal variables are updated from the updated strain, the stress can be determined directly. See [30] for more information.

### 3.3 Application

We will discuss the behavior of the different models under monotonic and cyclic loading with the failure assessment of a shear wall panel. The geometry, materials, and boundary conditions are chosen similar to the shear wall panels experimentally

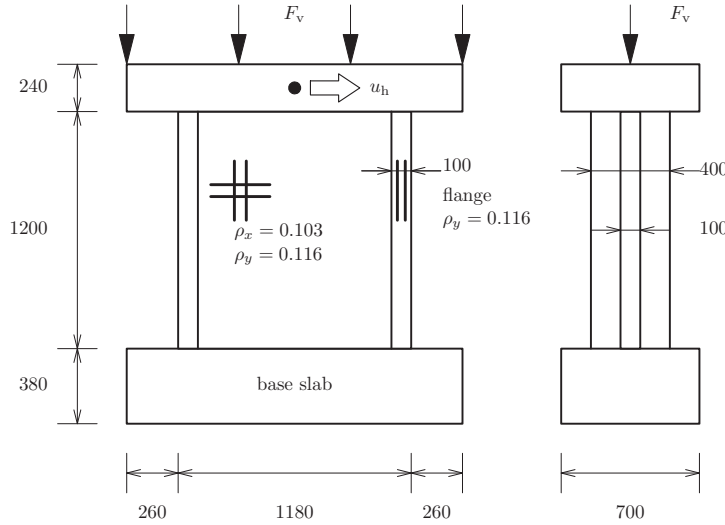


Figure 3.4: Shear wall panel – geometry and boundary conditions (measures in mm)

tested by Maier and Thürlimann [48] but we do not have the intention to model the observed failure mechanism in this study. For more information about simulation of these panels see [26]. Here we concentrate on the differences and similarities of the presented models under monotonic and cyclic loading.

The geometry and boundary conditions are shown in Figure 3.4. The web, flanges, and top slab are discretized with 204 four-node plane stress elements with full (four point Gauss) integration. The base slab is replaced by fixed boundary conditions in

Table 3.1: MATERIAL PROPERTIES FOR THE SHEAR WALL

Concrete			
Young's modulus	$E$	30000	[N/mm <sup>2</sup> ]
Poisson's ratio	$\nu$	0.15	[-]
tensile strength	$f_t$	2.2	[N/mm <sup>2</sup> ]
ultimate tensile strain	$\varepsilon_{ult}^{crk}$	0.0014	[-]
shear retention factor	$\beta$	0.05	[-]
compressive strength	$f_c$	27.5	[N/mm <sup>2</sup> ]

Reinforcement			
Young's modulus	$E$	200000	[N/mm <sup>2</sup> ]
yield strength	$f_{sy}$	574	[N/mm <sup>2</sup> ]
hardening modulus	$E_{sy}$	8000	[N/mm <sup>2</sup> ]

the horizontal and vertical directions. The reinforcement is modeled with embedded reinforcement grids in the web and the flanges. The structure is initially loaded with a total vertical load  $F_v$  equal to 433 kN resulting in an initial vertical stress in the web equal to approximately 2.5 N/mm<sup>2</sup>. The horizontal load is applied in the center of the top slab as a prescribed displacement  $u_h$ , monotonically increasing in the case of the monotonic comparison, and cyclic in the case of the cyclic comparison. The top slab is kept linear-elastic, i.e., no cracking or crushing is modeled. The flanges and the web are modeled with the different material models discussed previously. The material properties of the flanges and the web given in Table 3.1 are applied to all models, insofar these are appropriate. The reinforcement ratios of the flanges and the web are given in Figure 3.4 with the material properties given in Table 3.1. The uniaxial stress-strain curves of the concrete and steel models are shown in Figure 3.5.

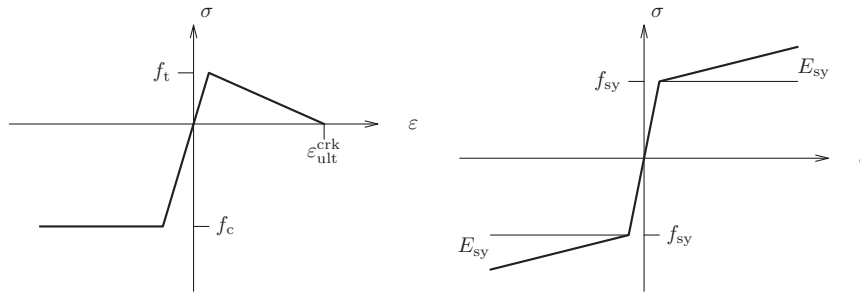


Figure 3.5: Uniaxial stress-strain relationship of concrete (left) and reinforcement (right)

For the fixed crack models, i.e., the multiple-fixed crack and the total strain-based fixed crack model, the choice of the shear retention factor  $\beta$  remains a subtle ques-

tion. Although physically speaking some non-zero shear retention factor, preferably decreasing with increasing normal crack strain  $\varepsilon_{nn}^{crk}$ , would be realistic, numerical studies show that a very low, almost zero, value yields the best results which is related to the issue of stress locking [60].

The compressive behavior is modeled with a constant compressive strength (elastic-perfectly plastic). A recent study [7] shows, however, that modeling of the softening behavior in compression is of utmost importance for accurate simulation of cyclic behavior. In this study we want to concentrate on the similarities and differences of the models for the unloading-reloading behavior and eliminate all other influences by assuming ideal behavior as much as possible. For a more realistic simulation of cyclic behavior of reinforced concrete, the compressive softening should be included, see [7].

The structure is analyzed for monotonic and cyclic loading for the four constitutive models described before:

1. multiple-fixed crack model with Von Mises to model the crushing (MFCMVM);
2. Rankine-Von Mises plasticity model (RANVMI);
3. total strain-based fixed model (TOTFIX); and
4. total strain-based rotating model (TOTROT).

In the next section the comparison for monotonic and cyclic loading is presented and in the final section [§ 3.5] we will discuss the results and explain the basic features underlying the similarities and the differences.

### 3.4 Analysis

The monotonic analysis is performed by first applying the vertical loading, followed by a monotonic increase of the prescribed displacement at the center of the top slab. Because we do not consider any inertia effects, the loading is considered being applied in the time domain where the concept of time is solely used to order the sequence of events. Figure 3.6 shows the loading function. The results are shown in Figure 3.7 where the push-off force is shown against the displacement of the center of the top.

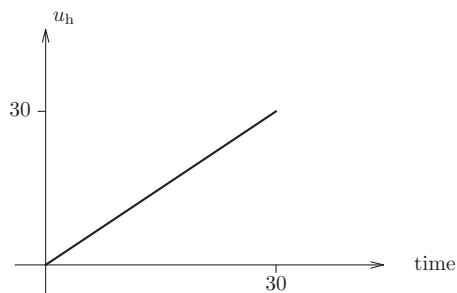


Figure 3.6: Monotonic loading history for shear wall

From these results it becomes clear that the differences between the various models are small. The differences are only present in the limit state where yielding of the

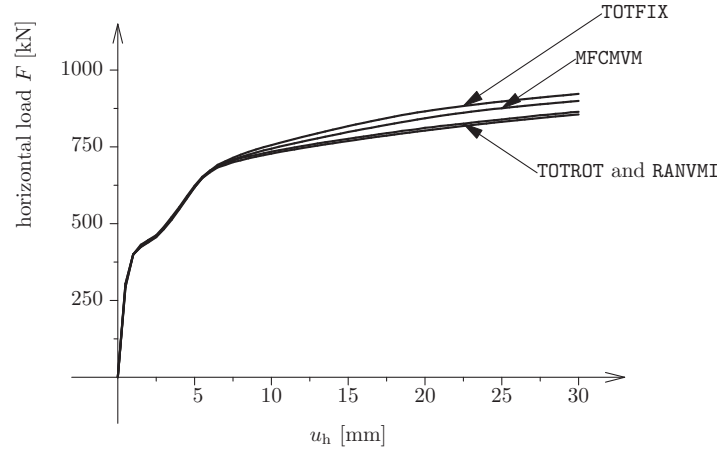


Figure 3.7: Load-displacement history for monotonic loading

embedded reinforcement dominates the global behavior. The total strain-based fixed model results in the highest ultimate load, followed by the multiple-fixed crack model with the Von Mises crushing model. The results of the Rankine-Von Mises model and the total strain-based rotating model are almost the same.

The structure is subjected to cyclic displacement of the center of the top according to the scheme presented in Figure 3.8. The loading is chosen such that the loading-unloading cycles are at the position where the crack patterns develop, see the load-displacement history for the monotonic loading in Figure 3.7: between zero and ten millimeters displacement. We apply five full cycles with increasing amplitude from 1.0, 2.5, 5.0, 7.5, and 10.0 mm. The results for all models are shown in Figure 3.9. It is clear that the results are quite dramatic for the Rankine-Von Mises model.

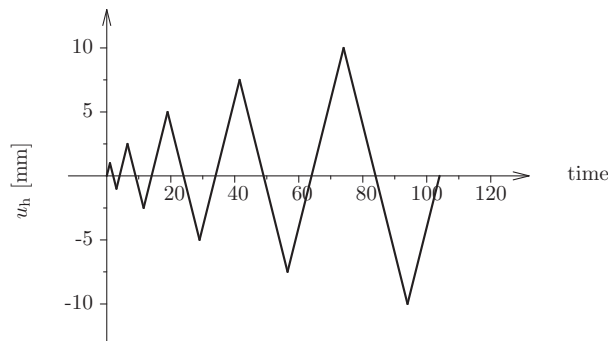


Figure 3.8: Cyclic loading history for shear wall

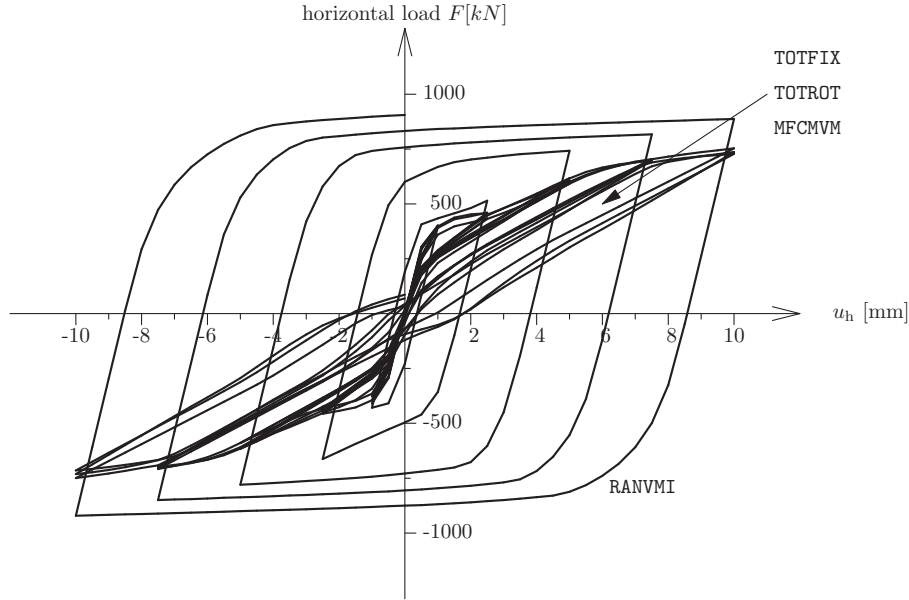


Figure 3.9: Load-displacement history for cyclic loading

The model dissipates too much energy in cyclic loading, resulting the model to be useless for earthquake simulations. The results of the other three models are more similar, although this is a little obscured by the results of the Rankine–Von Mises model. We will discuss the results in the next section and give an explanation for the pathological behavior of the Rankine–Von Mises model.

### 3.5 Discussion

The behavior of this type of structure under monotonic and cyclic loading is primarily caused by two different aspects of the constitutive models: firstly the allowable stress states defined by the failure surfaces, and secondly the unloading and reloading behavior. In the case of monotonic loading the failure surface and the evolution of the failure surface dominates the behavior. Although due to redistribution of the internal force in the structure unloading and reloading at the local level may occur, it is never dominating the response. In case of cyclic loading, the failure surface and the evolution are still important, but the unloading and reloading of the models will dominate the behavior. In other type of structures, for instance in shear-critical beams, other aspects can influence the results. Especially in case of high shear deformation along a discrete crack the rotating crack models perform poorly [88]. In these cases, however, one could argue the validity of the assumption of smeared cracking. For the current study we neither have dominant cracks nor large rotations of the principal strain directions and we can restrict ourselves to the discussion of the unloading–reloading



models.

The similarity in the monotonic response is primarily explained from the failure surfaces of each constitutive model. The allowable, elastic stress space in plane stress is shown in Figure 3.10 for the different models. In the shear wall, a tension–compression stress state prevails. In this regime the differences between the two models are small.

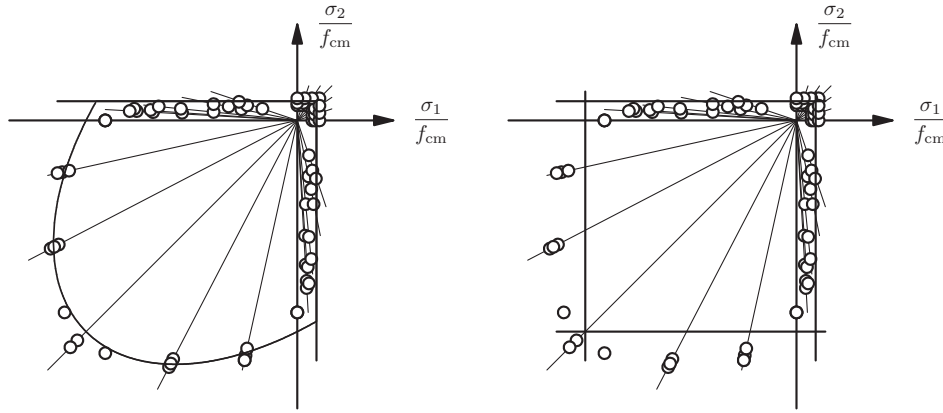


Figure 3.10: Failure surface for multiple-fixed crack model with Von Mises and for Rankine–Von Mises (left) and for the total strain-based models (right) compared to the biaxial data of Kupfer and Gerstle [46]

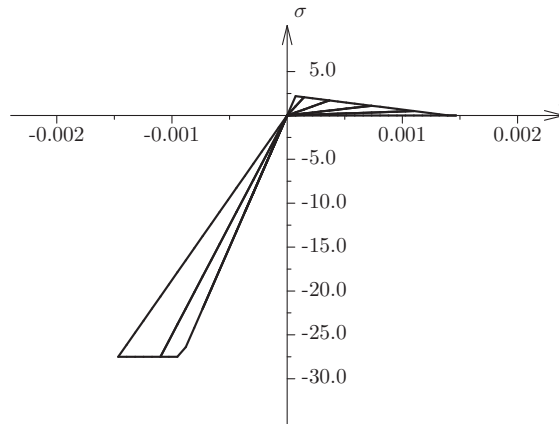


Figure 3.11: Total-strain models: cyclic uniaxial stress–strain behavior

In cyclic loading, the unloading–reloading model dominates the behavior. Especially in tension where the strain can be large at the point of unloading due to the redistribution to the reinforcement the behavior can be quite different. For the total strain-based models we have a secant-type of unloading–reloading model for

both tension and compression, see Figure 3.11 where we show the behavior of the total strain-based model for a loading history similar to the loading history of the shear wall. The multiple-fixed crack model with the Von Mises crushing model has

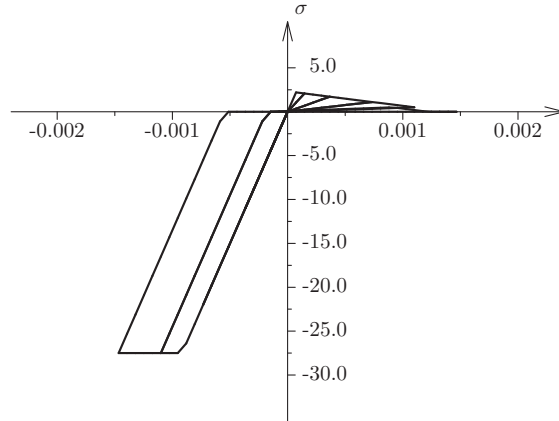


Figure 3.12: Multiple-fixed crack model with Von Mises: cyclic uniaxial behavior

a secant-type of unloading in tension and an elastic-type of unloading in compression [Fig. 3.12]. The puzzling behavior at the compressive reloading stage is due to the assumption of the strain decomposition. The Rankine–Von Mises model is fully plasticity-based which implies that both in tension as well as in compression the unloading–reloading behavior is elastic for the stress–strain response under the loading history [Fig. 3.13]. Because the multiple-fixed crack model with Von Mises

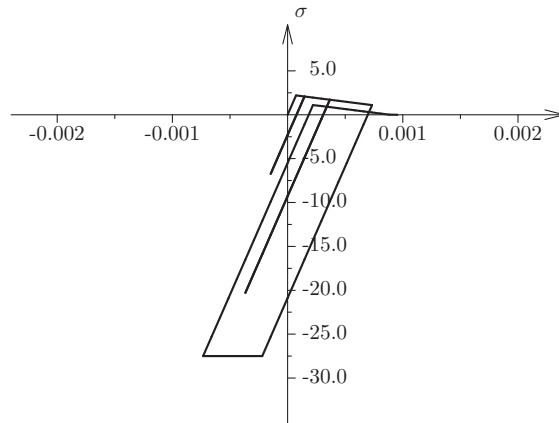


Figure 3.13: Rankine–Von Mises model: cyclic uniaxial behavior

has also elastic unloading in compression and is also based on strain decomposition, the cause of the pathological behavior of the Rankine–Von Mises model lies in the fact that the tensile regime has elastic unloading and reloading. In Figure 3.13 it is

clearly depicted that this results in increased energy dissipation, compare with Figure 3.12. The conclusion is that the elastic unloading as inherent to plasticity-based approaches in tension, may give rise to over-stiff, pathological behavior in case of cyclic loading, leading to an extreme overestimation of the energy dissipation. Models with a secant unloading–reloading model do not suffer from this deficiency. Future work should concentrate on extending the computationally elegant plasticity models with secant unloading–reloading options, for example a combination of damage models with plasticity models.

The choice of the structure, the reinforcement ratio, and the material parameters that are chosen, such as the constant maximum compressive strength, obviously influences the results presented in this study. Nevertheless, the conclusions are in accordance with a study of the cyclic behavior of pre-stressed beam–column connections [7] and are most likely valid for a wide range of reinforced and pre-stressed concrete structures. Furthermore, the conclusions are expected to hold not only for cyclic loading, but also for non-proportional loading and other cases whereby cracks undergo significant unloading or closing.

**Acknowledgements.** The authors appreciate the information and discussions about cyclic behavior with Professor Sarah L. Billington and Win-Ping Kwan at Cornell University. The calculations are performed with the DIANA finite element code, release 7.1. The first author acknowledges the financial support of MCEER through Program 4 under number 994201. The second author acknowledges the support of the Netherlands Technology Foundation (STW) under grant DCT 3683.



## Chapter 4

# Bending, Shear, and Torsion of Prestressed HSC Beams

S. W. H. Droste

*Adviesbureau voor Bouwtechniek ABT*

C. M. P. 't Hart and G. M. A. Schreppers

*TNO DIANA BV*

### 4.1 Introduction

The experimental part of the investigation, presented by the first author in §4.2, has been carried out to supplement the current knowledge of High Strength Concrete (HSC) and as reference for the Euro Lightcon project, i.e., European research to (high strength) light concrete. In § 4.3 on page 55 the other authors will present the numerical analysis of one part of the experimental research. Interesting analysis results are the deformation of the beam, the slope of the compression diagonals, and of course the shear force capacity of the beam.

### 4.2 Experimental Tests

The technical research report [22] presents the theoretical and experimental research to the behavior of prestressed HSC beams with a high proportion of transverse reinforcement braces. The aim of the research is threefold: to determine the shear force capacity at high proportions of transverse reinforcement braces, to determine the torsional capacity, and to determine the capacity of the cross-section against shear force and torsion.

The basis for the dimensioning of the test specimen is the collapse of the concrete compression diagonal. The capacity of this compression diagonal is assumed to be

$0.6 \times f'_{cm}$ . Figure 4.1 shows the dimensions of the beams in longitudinal direction.

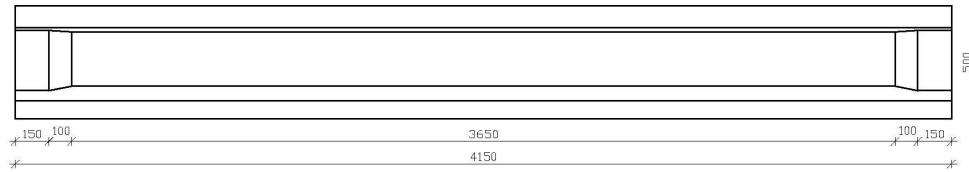


Figure 4.1: Beam longitudinal dimensions

Figure 4.2a shows the beam cross-section with its dimensions and the longitudinal prestressed steel tendons and reinforcement bars. Figure 4.2b shows the beam cross-section and the shape of the transverse steel braces. The proportion of these transverse braces is 3.51%.

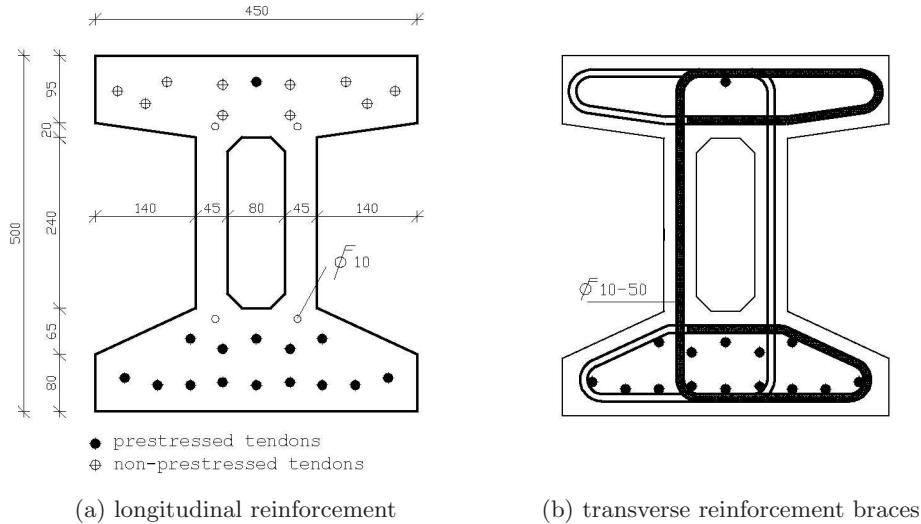


Figure 4.2: Beam cross-section

#### 4.2.1 Problem Description

The instructions regarding shear force and HSC, as presented in CUR Recommendation 37 [16], link up well with the Dutch norm NEN 6720 [54]. However, unlike the NEN norm, the CUR Recommendation gives an upper limit of  $\tau_2$  which is not directly proportional to the concrete quality, for qualities higher than B65. This should give a better fit with the more brittle failure behavior of HSC and with the declining redistribution capacity due to smoother cracking surfaces.

The approach in the CUR Recommendation is clearly more conservative. Furthermore, it assumes that the lower limit for the slope  $\theta$  of the compression diagonal

is proportional to the concrete quality:  $\theta = 30^\circ$  for quality B65 and  $45^\circ$  for quality B105. Following the CUR Recommendation for similar beams, with  $\alpha = 90^\circ$  and with equal shear force and equal  $\tau_1$ , the calculated proportion of transverse reinforcement braces for quality B105 is  $1.73\times$  the proportion for quality B65. Therefore, in addition to the determination of the ultimate capacity, the goal of the experimental laboratory tests is also to resolve the direction of the compression diagonal, i.e., the principal stress direction.

### 4.2.2 Set-up

Figure 4.3 shows the experimental set-up and measuring procedure.

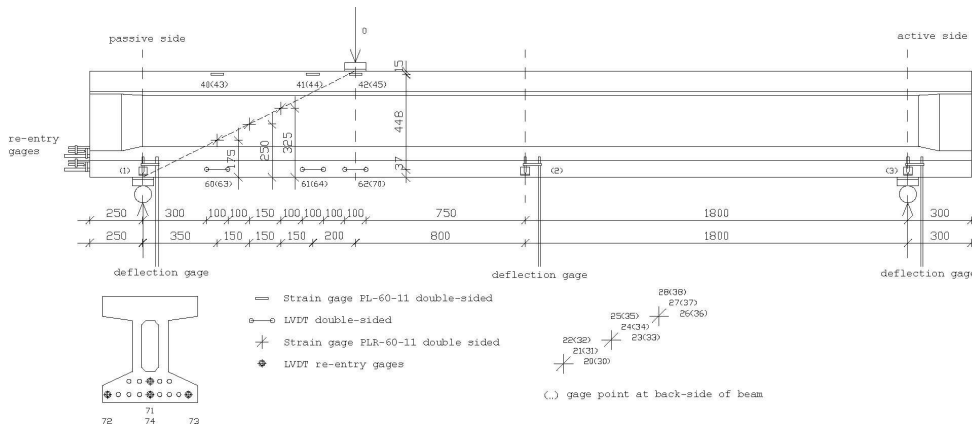


Figure 4.3: Measuring procedure for shear force tests

**Strain gages.** To determine the principal directions, the stresses in the web of the beams will be measured in three directions by means of special strain gages. The diagonal strain gage is applied in a direction of  $45^\circ$  with the longitudinal direction of the beam. Presumably this strain gage will not be damaged due to cracking of the web. The three measuring directions enable the calculation of the principal strains and the slope of the compression diagonal. The effect of the crack formation on the measured values should become clear during the test procedure.

**Loading and supports.** Two 100 tons jacks will supply the required force. A massive steel block and a 20 mm softboard plate of  $200 \times 300$  mm transfer this force onto the beams. Both supports are roll-shaped with a diameter of 80 mm. A 30 mm steel plate of  $120 \times 300$  mm rests on the roll. Between the steel plate and the beam a 10 mm softboard plate is applied.

**Measuring.** The deflection of the beam will be measured in the middle of the span, and corrected for the measured deflections of the supports. The re-entry will

be measured to detect any premature collapse due to fracture of the anchorage (slip of the tendons). The strains in the pretensioned bending-compression zone of the beam will be measured via strain gages. At the prestressed bending-tension zone so-called LVDT displacement detectors will be applied which enable the measuring of displacements, even beyond crack formation.

### 4.2.3 Test Results

#### 4.2.3.1 Crack Propagation

The photographs in Figure 4.4 show the crack patterns in the test specimen for various loading stages. The first cracks occur due to shear force in the web of the beams [Fig. 4.4a]. These cracks have a slope of approximately 25 to 30° with the

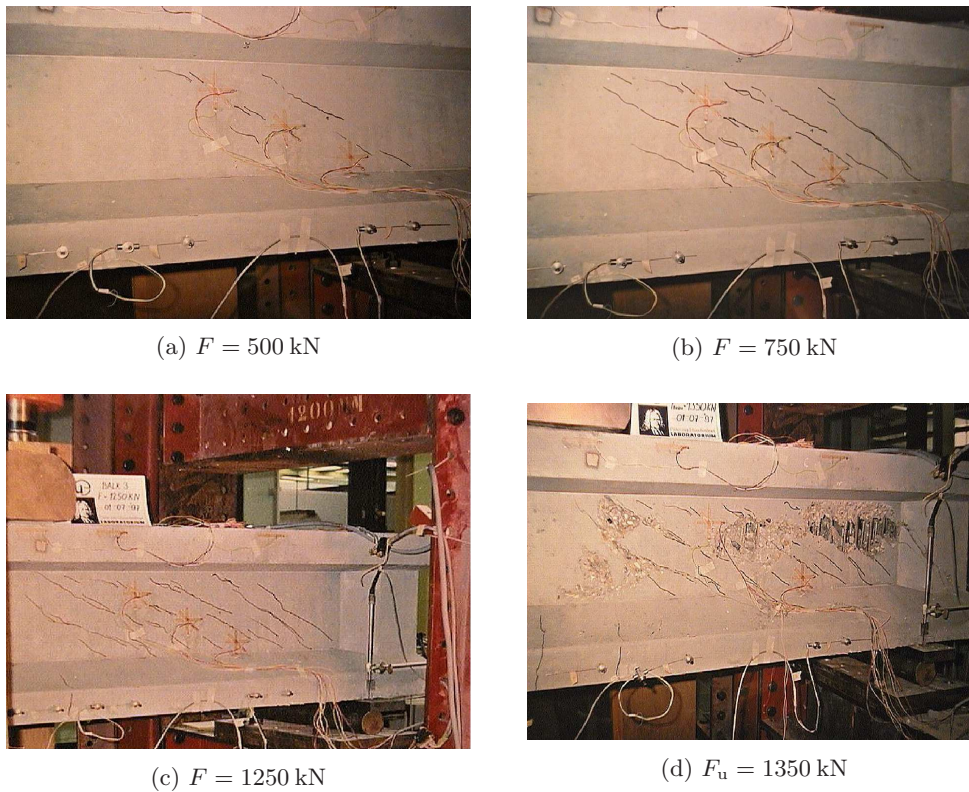


Figure 4.4: Crack patterns in test specimen

longitudinal axis of the beam. Subsequently more shear force cracks appear, while at a loading of 750 to 900 kN we can also observe bending-tension cracks in the lower flange of the beams [Fig. 4.4b]. With increasing loading the beam collapses



explosively. The concrete covering flews off the web, thus exposing the transverse reinforcement bracemnts [Fig. 4.4d].

#### 4.2.3.2 Deflection

The deflection of the beams has been measured in the middle of the span. As an example, the graph in Figure 4.5 shows the deflection of beam 3.

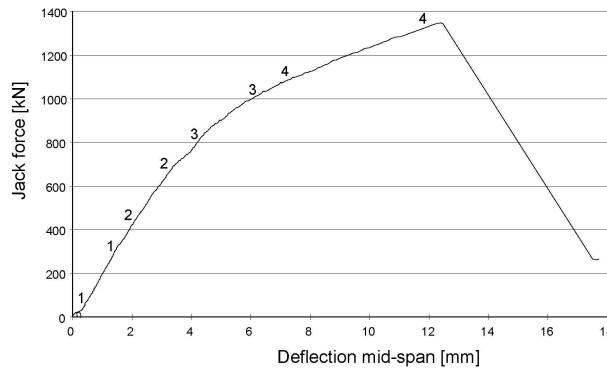


Figure 4.5: Measured deflection of beam 3

In the graphs four sections may be discerned.

1. In the first section no cracks appear in the cross-section as a result of which the bending stiffness is at its largest.
2. In the transition of the first section to the second, cracks appear in the web of the cross-section because the principal tension stresses exceed the tensile strength. These cracks only slightly reduce the bending stiffness.
3. In the third section bending-tension cracks appear gradually. Moreover, more cracks appear in the web.
4. In the fourth section the cross-section is cracked due to bending-tension cracks which may be observed with the naked eye. The bending stiffness has decreased considerably.

The following equation allows the determination of the average bending stiffness along the beam span ( $E'_b \times I_b$ ):

$$\delta_m = \frac{F a (3l^2 - 4a^2)}{48 E'_b I_b} \implies E'_b I_b = \frac{F a (3l^2 - 4a^2)}{48 \delta_m} \quad (4.1)$$

where  $F$  is the measured force and  $\delta_m$  the measured deflection. The bending stiffness for the uncracked beam is calculated from the Young's modulus of elasticity on the

Table 4.1: AVERAGE BENDING STIFFNESS OF THE BEAMS  $[\text{N} \cdot \text{mm}^2]$ 

Beam nr.:	1	2	3
$EI_{\text{uncr. (analytical)}}$	$1.74734 \times 10^{14}$	$1.73381 \times 10^{14}$	$1.82621 \times 10^{14}$
$EI_{\text{section1}}$	$1.72687 \times 10^{14}$ 98.8%	... <sup>†</sup>	$1.82031 \times 10^{14}$ 99.7%
$EI_{\text{section2}}$	$1.40392 \times 10^{14}$ 80.3%	$1.35978 \times 10^{14}$ 78.4%	$1.42820 \times 10^{14}$ 78.2%
$EI_{\text{section4}}$	$0.37125 \times 10^{14}$ 21.2%	$0.39152 \times 10^{14}$ 22.6%	$0.39464 \times 10^{14}$ 21.6%

<sup>†</sup>For beam 2 the bending stiffness in the uncracked section can not be determined.

day of performance of the experiments. The axial quadratic area moment of the composed cross-section is calculated assuming the same modulus of elasticity. Table 4.1 gives the results of these calculations.

Summarizing, it may be stated that the calculated average bending stiffness for the uncracked section accords very well with the measured bending stiffness. Due to cracking of the web, the bending stiffness reduces to about 80% and due to bending-tension cracks to about 22% of the value for the uncracked beam.

#### 4.2.3.3 Strains in Web

Because the strains have been measured in three directions, the principal stress directions may be determined based on linear elastic material behavior. The first strain gage is located 600 mm from the head-end of the beam. Therefore a linear elastic

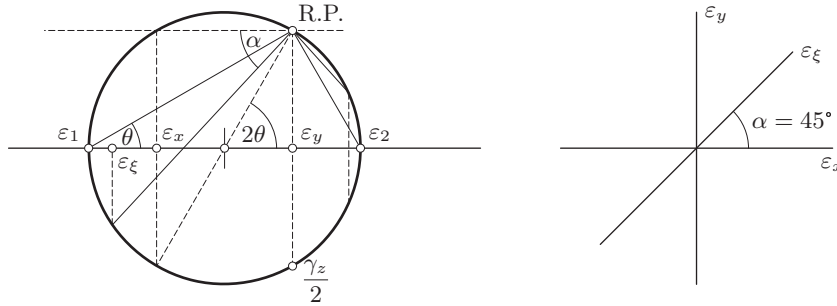


Figure 4.6: Mohr's circle and direction of the strain gages

stress situation may be assumed in the calculations. From the measured strains and Mohr's circle [Fig. 4.6] it follows that

$$\varepsilon_{\xi} = \frac{\varepsilon_x + \varepsilon_y}{2} + \left( \frac{\varepsilon_x - \varepsilon_y}{2} \right) \cos 2\alpha + \frac{\gamma_z}{2} \sin 2\alpha \quad (4.2)$$

With  $\alpha = 45^\circ$  this gives

$$\frac{\gamma_z}{2} = -\frac{\varepsilon_x + \varepsilon_y}{2} + \varepsilon_{\xi} \quad (4.3)$$

This allows the determination of the principal directions from

$$\tan 2\theta = \frac{\gamma_z}{2} \times \frac{2}{\varepsilon_x - \varepsilon_y} = \frac{\gamma_z}{\varepsilon_x - \varepsilon_y} \quad (4.4)$$

The influence of the strain due to the prestress is settled in the values of  $\varepsilon_x$  and  $\varepsilon_\xi$  in the following way [Fig. 4.7]

$$\begin{aligned} \varepsilon_x &= \varepsilon_{pw} + \varepsilon_{x,test} \\ \varepsilon_\xi &= \frac{\varepsilon_{pw}}{2} + \varepsilon_{\xi,test} \end{aligned} \quad (4.5)$$

where  $\varepsilon_{pw}$  can be determined from the working prestress, with the modulus of elasticity on the day of testing. From (4.5) directly follows that  $\gamma_z/2 = 0$  if the jack force is zero, i.e.,  $\varepsilon_{x,test} = 0$  and  $\varepsilon_{\xi,test} = 0$ . This means that  $\tan 2\theta = 0$  which gives

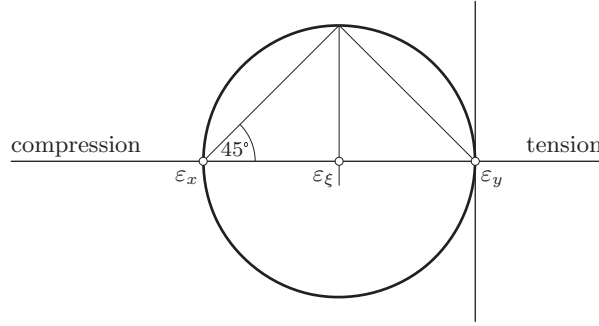


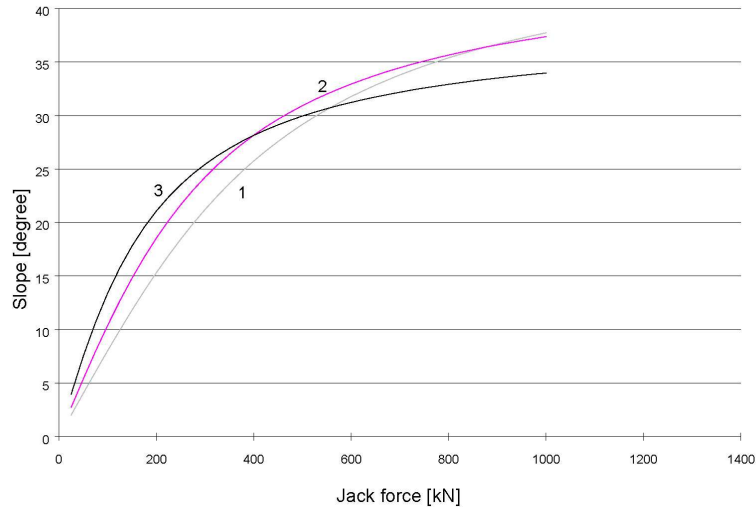
Figure 4.7: Mohr's circle for a one-dimensional stress situation

$\theta = 0$ . This situation corresponds to a one-dimensional stress state, prevailing in the beams as long as there is no external loading, aside from the transition sections.

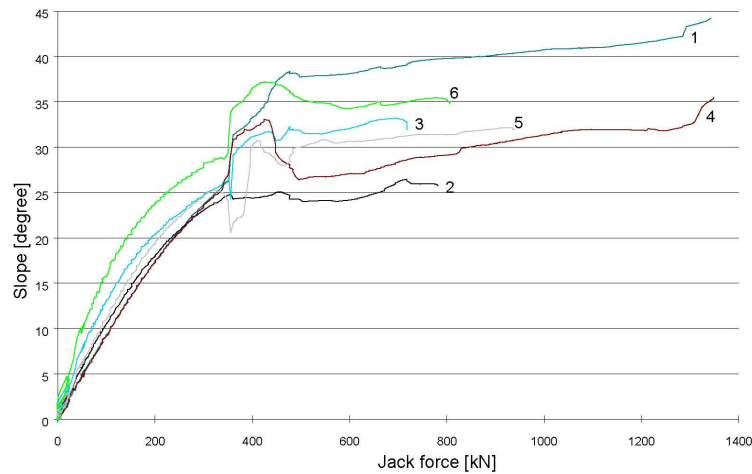
Figure 4.8 on the next page shows the measured slopes of the compression diagonal. The graphs have been drawn up to the jack force where all three strain gages that go together are still undamaged. As stated before, and confirmed by Figure 4.8,  $\theta = 0$  if  $F_{jack} = 0$ . Then the slope of the compression diagonal, with respect to the longitudinal beam axis, increases. Mutually there are minor differences between the calculated slopes. This is caused by minor mutual differences in the shear stress  $\sigma_z$ , and by bending which equalizes the differences in the horizontal stress.

For strain gage 20/21/22 the compression stress  $\sigma_x$  gradually decreases; the  $\sigma_x$  in strain gage 23/24/25 hardly changes because it is nearly at the median; for gage 26/27/28 the compression stress increases. All this causes the mutual differences in the stress of the strain gages to decrease. The increment of the slope of the compression diagonal is caused by the increasing influence of the shear stress over the normal stress.

As a first impression we may note the close match between calculated and measured slopes in the uncracked zone. At a load of 350 kN shear force cracks appear



(a) linear elastic calculation



(b) test results

Figure 4.8: Beam 3: slope of compression diagonals for increasing jack force

in the web. A sudden and fanciful course of the measured values characterizes this situation, however, by no means this indicates the location of the cracks. In the cracked zone, the trend of the linear elastic calculation is followed as well. Furthermore, the graphs in Figure 4.8 indicate that at the start of cracking the slope of the compression diagonal is about 25 to 30°. Similar slopes have been measured during

the experimental tests. This justifies the conclusion that the slope of the compression diagonals is directly related to the slope of the cracks. The graphs also indicate that the slope increases with increasing load. The crack pattern in the beam also follows this trend.

The upper limit of the slope of the compression diagonals is about 40°. However, the CUR Recommendation 37 gives a lower limit of 45° for this slope, while this value is more like an upper limit regarding the results of the present research with respect to prestressed beams. This justifies the conclusion that the lower limit from CUR Recommendation 37 is a safe lower limit for this research project.

#### 4.2.3.4 Ultimate Shear Force Capacity

The ultimate shear stress  $\tau_u$  can be derived from the jack force  $V_u$  at the moment of collapse from

$$\tau_u = \frac{V_u}{b_w d} \quad (4.6)$$

According to the Dutch VBC Model Code [54] the value for  $V_u$  can be converted to a shear stress in which

- $b_w$  is the width of the web ( $2 \times 45 = 90$  mm),
- $d$  is the useful height of the beam with respect to the center of gravity of the total bending-tension reinforcement ( $500 - 60 = 440$  mm).

The results of the experimental tests can be compared to the VBC and the relevant articles in CUR Recommendation 37.

**CUR Recommendation 37.** Instead of the values for the long-term now the short-term average values must be used in the calculations. For  $\tau_u = \tau_{2\text{CUR-37}}$  instead of

$$\tau_2 = 0.1(f'_b + 39) k_n k_\theta \leq 9.5 k_\theta \quad (4.7)$$

now holds

$$\tau_{2\text{CUR-37}}^* = 0.1 (0.85 f'_{\text{cm,B65}}) k_n k_\theta \leq 9.5 k_\theta \frac{\gamma_m}{0.85} \quad (4.8)$$

where

- 0.85 is the assumed factor for conversion from cube compression strength to one-axial pressure strength,
- $f'_{\text{cm,B65}} = 70$  N/mm<sup>2</sup> is the estimated average cube compression strength,
- $k_n = 1$ ,
- $k_\theta = 1$  (for  $\alpha = 90^\circ$ ),
- $\gamma_m = (0.72/0.68) \times 1.2 = 1.27$ .

From which follows

$$\tau_{2\text{CUR-37}}^*(\max) \leq 9.5 \times 1 \times \frac{1.27}{0.85} = 14.2 \text{ N/mm}^2 \quad (4.9)$$

Table 4.2 gives the values obtained according to the description above. From this table it may be concluded that the calculation method according to CUR Recommendation 37 gives an extra safety factor of about 1.6 to 1.7.

Table 4.2: SHEAR FORCE CAPACITY – MEASURED VERSUS CUR 37

Beam nr.:		1	2	3
$f'_{\text{cm}}$	[N/mm <sup>2</sup> ]	117.0	110.7	123.9
$F_{\text{u,jack}}$	[kN]	1353	1283	1348
$V_{\text{u}}$	[kN]	977	927	974
$\tau_{\text{u}}$	[N/mm <sup>2</sup> ]	$0.21 \times f'_{\text{cm}} = 24.7$	$0.21 \times f'_{\text{cm}} = 23.4$	$0.20 \times f'_{\text{cm}} = 24.6$
$\tau_{2\text{CUR-37}}^*$	[N/mm <sup>2</sup> ]	14.2	14.2	14.2
$\tau_{\text{u}}/\tau_{2\text{CUR-37}}^*$		1.74	1.65	1.73

**Dutch VBC Model Code.** The comparison can also be made by ignoring the instructions of CUR Recommendation 37 and only take the Dutch VBC Model code [54] for granted. For  $\tau_{\text{u}} = \tau_{2\text{VBC}}$  instead of

$$\tau_2 = 0.2 f'_b k_n k_\theta \quad (4.10)$$

now holds

$$\tau_{2\text{VBC}}^* = 0.2 \times 0.85 f'_{\text{cm,beam}} k_n k_\theta \quad (4.11)$$

where

0.85 is the assumed factor for conversion from cube compression strength to one-axial pressure strength,

$$k_n = 1,$$

$$k_\theta = 1 \text{ (for } \alpha = 90^\circ \text{)}.$$

This gives the values as shown in Table 4.3 on the next page. From this table it may be concluded that the calculation method according to the VBC gives an extra safety factor of about 1.2 to 1.3.

To obtain sufficient safety for the present research project it is not necessary to apply the rules in CUR Recommendation 37. We explicitly state that this only holds for the current test experiments where the proportion of the transverse steel braces is 3.51%.

**Other experiments.** To compare our results with those of the shear force experiments of the TU Delft [67] we give the graphs in Figure 4.9 on the facing page. The graphs show a close similarity between the two series of experiments, where it must be noted that the test specimen in Delft were not prestressed.

Table 4.3: SHEAR FORCE CAPACITY – MEASURED VERSUS VBC

Beam nr.:		1	2	3
$\tau_u$	[N/mm <sup>2</sup> ]	24.7	23.4	24.6
$\tau_{2VBC}^*$	[N/mm <sup>2</sup> ]	18.8	19.0	18.4
$\tau_u / \tau_{2VBC}^*$		1.31	1.23	1.34

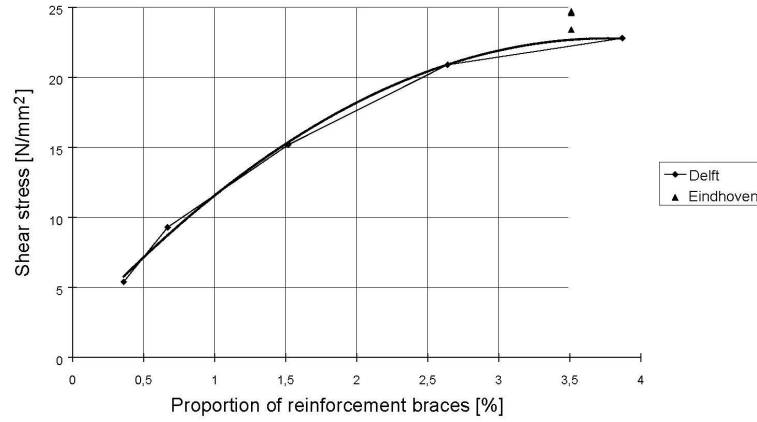


Figure 4.9: Results of shear force experiments in Delft and Eindhoven compared

**CEB-FIP Model Code 1990.** The shear force capacity may also be compared to the CEB-FIB Model Code 1990 [13]. For the calculation values for the ultimate compression strength of the concrete compression diagonals  $f_{cd2}$  instead of

$$f_{cd2} = 0.6 \left( 1 - \frac{f_{ck}}{250} \right) f_{cd} \quad (4.12)$$

now holds

$$f_{cm2} = \frac{0.60}{0.85} \left( 1 - \frac{0.85 f'_{cm}}{250} \right) 0.85 f'_{cm} \quad (4.13)$$

where

- $f_{ck}$  is the characteristic cylinder compression strength,
- $f_{cd}$  is the calculation value of the cylinder compression strength,
- $f'_{cm}$  is the average cube compression strength,
- $1/0.85$  is the conversion factor for the short-term strength,
- $0.85$  is the assumed factor for conversion from cube compression strength to one-axial pressure strength.

The shear force capacity can now be calculated from

$$V_{uMC-90}^* = f_{cm2} b_w z \cos \theta \sin \theta \quad (4.14)$$

where

$$\begin{aligned} b_w &= 2 \times 45 = 90 \text{ mm}, \\ z &= 0.9 \times d = 0.9 \times 440 \approx 400 \text{ mm}. \end{aligned}$$

Table 4.4 gives the values obtained from the above assumptions, where  $V_{uMC-90}^*$  is determined for  $\theta = 30^\circ$  and  $45^\circ$ . From this table it may be concluded that for  $\theta = 30^\circ$  the calculation method according to the CIB-FIP Model Code 1990 gives an extra safety factor of 1.4 to 1.5. For  $\theta = 45^\circ$  the extra safety factor is 1.2 to 1.3. This is

Table 4.4: SHEAR FORCE CAPACITY – MEASURED VERSUS MC 1990

Beam nr.:		1	2	3
$V_u$	[kN]	977	927	974
$V_{uMC-90}^*$	[kN]	659	646	671
$V_u/V_{uMC-90}^*$	(30°)	1.48	1.43	1.45
$V_{uMC-90}^*$	[kN]	761	746	774
$V_u/V_{uMC-90}^*$	(45°)	1.28	1.24	1.26

because the vertical component of the compression diagonals increases with  $\theta$ , which also increases the shear force capacity. For prestressed concrete the angle  $\theta = 45^\circ$  must be considered as an upper limit. The results obtained according to the CIB-FIP Model Code 1990 are a bit closer to the experimental results than those obtained according to the CUR Recommendation 37, compare Table 4.2 on page 52.

#### 4.2.4 Conclusion

Comparing the presented results we may conclude that a calculation according to the CUR Recommendation 37 underestimates the shear force capacity of the tested beams with a factor of 1.71. Furthermore, these recommendations ignore the influence of the slope  $\theta$  of the compression diagonals on the calculated ultimate shear force capacity if  $\alpha = 90^\circ$ , i.e., if the transverse steel braces are perpendicular to the beam axis. This seems a bit strange because the truss-analogy underlies the formulas, see also the shear force formula in the CIB-FIP Model Code 1990. However, the CUR Recommendations 37 give the following lower limit for the angle  $\theta$

$$\theta_{\min} = 30^\circ + \left( \frac{k_f - 65}{40} \right) \times 15^\circ \quad \text{with} \quad k_f = f'_{ck} \quad (4.15)$$

This limit aims at compensation for the more brittle failure behavior of High Strength Concrete and for the reduced redistribution capacity of the crack slopes caused by smoother crack surfaces.

For a B65 concrete quality  $\theta_{\min}$  is  $30^\circ$  and for B105 quality it is  $45^\circ$ . Hence, for similar beams with  $\alpha = 90^\circ$  and equal shear force and  $\tau_1$ , the calculated amount of transverse steel braces for a B105 concrete quality is  $1.73\times$  as much as for a B65 quality.



## 4.3 Numerical Analysis

In addition to the experiments and analytical models that have been presented in the previous section, a numerical model of beam number 3 has been defined and analyzed with the finite element program DIANA, release 8.1. Typical points of interest here are the deformation of the beam, the slope of the pressure diagonals, and, of course, the ultimate capacity of the beam.

### 4.3.1 Finite Element Model

The model comprises three parts: the concrete beam, the prestressed steel tendons, and the transverse steel braces. Because of symmetry of the material as well as loading and supports, only one half of the beam need to be taken into account in the numerical model. Figure 4.10 shows the finite element grid of the concrete model.

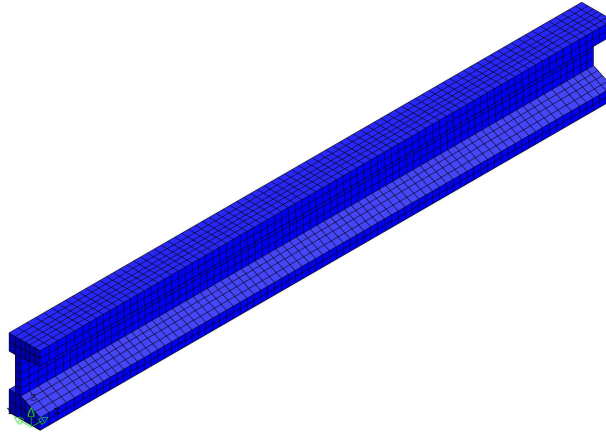


Figure 4.10: Finite element model of half of beam 3

This model contains 2378 brick elements (CHX60) with quadratic interpolation of the displacement field. In the longitudinal direction the elements are equally distributed but have different widths near the tail ends.

**Embedded reinforcement.** Both the prestressed steel tendons and the transverse steel braces are modeled as embedded reinforcement bars. That means that the user can specify the shape and location of the reinforcement independently of the finite element grid of the concrete components in which the reinforcement is embedded. The DIANA program finds out which concrete elements are intersected by reinforcements and the stresses in the reinforcement bar are added to the internal forces of the concrete element. Also the stiffness of the steel reinforcement is automatically added to the stiffness properties of the concrete.

Figure 4.11 on the following page shows the concrete beam with the prestressed steel tendons and longitudinal reinforcement bars (a) and the transverse steel braces

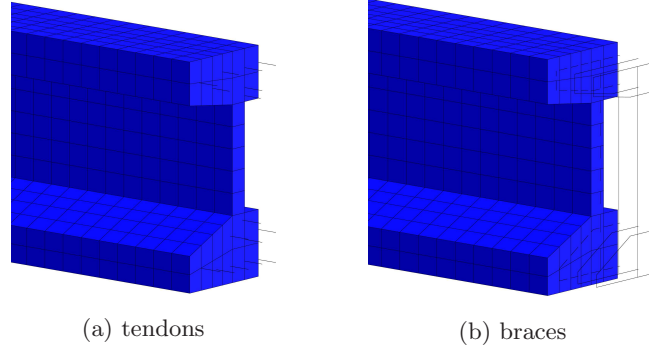


Figure 4.11: Finite element model with reinforcements

(b). In these figures the concrete elements at the end of the beam have been removed in order to make the reinforcements visible. The numerical model that has been analyzed contained both the transverse steel braces and the prestressed steel tendons. The three prestressed tendons, which are located in the plane of symmetry, have a cross-section of  $50 \text{ mm}^2$  whereas the other six tendons in the half model have a cross-section of  $100 \text{ mm}^2$ . The transverse steel braces have a constant cross-section of  $78.5 \text{ mm}^2$  each.

**Material properties.** For the concrete beam a fixed rotating crack model is applied in the tensile regime. The Von Mises plasticity model without hardening is applied in the compressive regime. The concrete as used in the experiment had a characteristic compressive strength of  $123.9 \text{ N/mm}^2$  [16]. Table 4.5 gives the parameters for this high strength concrete. For the transverse steel braces a Von Mises

Table 4.5: MATERIAL PROPERTIES FOR CONCRETE BEAM

		value	unit	DIANA input
Young's modulus	$E$	40856	$\text{N/mm}^2$	YOUNG
Poisson's ratio	$\nu$	0.2	-	POISON
Mass density	$\rho$	2400	$\text{kg/m}^3$	DENSIT
Tensile strength	$f_t$	5.7	$\text{N/mm}^2$	CRKVAL
Linear tension softening		1		TENSIO
Ultimate strain	$\varepsilon_u^{\text{cr}}$	0.005	mm	TENVAL
Constant shear retention		1		TAUCRI
Shear retention factor	$\beta$	0.01		BETA
Von Mises plasticity		VMISES		YIELD
Yield stress	$\sigma_y$	70	$\text{N/mm}^2$	YLDVAL

elastoplastic material model is used with a Young's modulus of  $200000 \text{ N/mm}^2$  and a yield stress of  $500 \text{ N/mm}^2$ . For the prestressed steel tendons only a linear elastic model is applied with a Young's modulus of  $200000 \text{ N/mm}^2$ .

**Supports.** The beam is supported at both ends in vertical direction at a distance of 250 mm from the end at the left-hand side and 300 mm at the right-hand side [Fig. 4.3]. All the nodes in the symmetry plane are supported in the normal direction. Moreover, the node on the first vertical support line located in the symmetry plane has a support in longitudinal direction in order to avoid rigid-body movements.

**Loading.** Three different loads apply to the model. The first is a dead-weight load as result of a vertical gravity acceleration of  $9.8 \text{ m/s}^2$ . The second load is a prestress of  $1000 \text{ N/mm}^2$  in each of the prestressed steel tendons, resulting in a prestress force of 100 kN per tendon. The third load models the incrementing hydraulic punch load as a distributed surface load at the location of the hydraulic punch. This surface load is applied instead of a point load in order to avoid unrealistic stress concentrations at the punch location.

In a first load step the dead weight load and the prestresses are applied. In the following load steps the punch load is incremented step by step.

### 4.3.2 Analysis Results

**Punch load.** The solid line in Figure 4.12 shows the calculated punch load as function of the deflection of the middle of the beam. The pink dots indicate the punch load measured in the experiment. In the analysis, the calculated punch load is

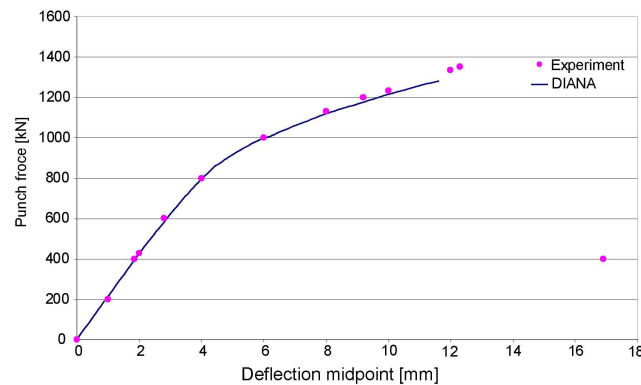


Figure 4.12: Punch load vs. deflection for beam mid-span

calibrated to zero after dead weight and prestresses have been applied. Analysis and experimental results seem to match within a range of 4%, which is very good. The DIANA model seems to be a little more stiff in the elastic regime whereas it is slightly weaker in the failure branch. The numerical analysis diverges at a maximum punch load of 1283 kN whereas in the experiment a load of 1348 kN could be reached.

**Formation of cracks.** Figure 4.13 on the next page shows a deformed normal view of the beam with small disks in the elements where a crack has been formed. The

orientation of the disk coincides with the orientation of the crack plane.

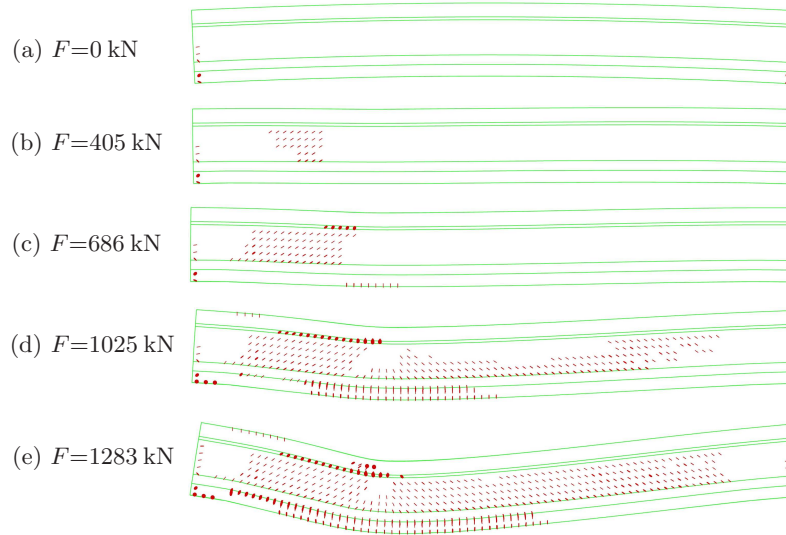


Figure 4.13: Crack pattern in deformed beam for increasing punch load  $F$

In the beginning only some cracks at the anchor points of the prestressed tendons can be noticed [Fig. 4.13a]. These cracks are oriented parallel to the direction of the tendons. At a punch load of 405 kN load the web is cracked in the area between loading and support at the left-hand side [Fig. 4.13b]. The cracks are oriented normal to the pressure diagonal between loading point and right-hand side support. At a punch load of 686 kN the lower flange starts to crack directly under the loading point, where the tensile forces are apparently maximal [Fig. 4.13c]. At the bottom of the upper flange cracks parallel to the symmetry plane are coming in under the point where the punch load attaches. At a load of 1025 kN the lower flange is cracked over its full thickness [Fig. 4.13d]. In the web now also the area between the point of loading and the right-hand side support is cracked. The cracks in this region are again oriented normal to the direction of the pressure diagonal. The top of the upper flange seems to be still intact at this loading. When the load has increased to 1283 kN [Fig. 4.13e], cracks have also arisen in the upper flange and the web has reached the plasticity limit at many places, the beam is falling apart.

**Compression angles.** Figure 4.14 on the facing page shows the orientation of the calculated maximum principal stresses in the model at the locations position 1 (20, 21 and 22), position 2 (23, 24 and 25) and position 3 (26, 27 and 28). The calculated maximum principal stresses are compared with the measured pressure diagonals in the experiments.

The orientations of the measured pressure diagonals and the calculated maximum principal stresses have reasonable agreement until cracking comes in at circa 400 kN.

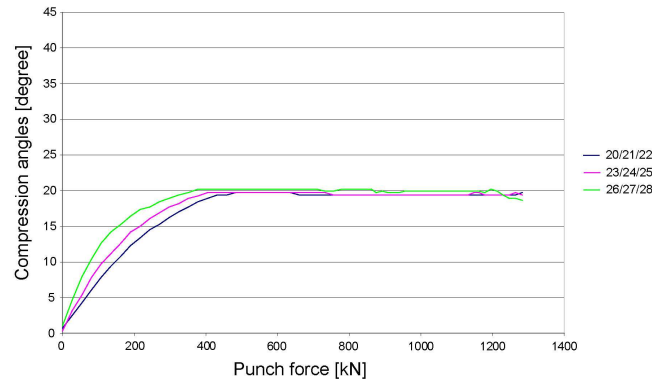


Figure 4.14: Calculated compression angles as function of punch load

From then on, the orientation of the calculated maximum principal stresses stays more or less constant, whereas the measured pressure diagonals keep increasing.

## 4.4 Conclusions

### 4.4.1 Experimental

From the strains, measured in three directions, the main compression directions have been derived. It turns out that cracks arise in the web at a slope of the compression diagonals of  $25^\circ$  to  $30^\circ$ . Afterward, this slope stabilizes at an angle of  $30^\circ$  to  $40^\circ$ . Also in cracked zones the trend for change of the slope remains fairly similar to the linear elastic calculations. The upper limit for the slope of the compression diagonals is found to be about  $40^\circ$ . Hence, the lower limit of  $45^\circ$  as incorporated in the CUR Recommendations 37 for a B105 concrete quality, is a safe lower limit. However, in comparison to B65 concrete quality, this lower limit causes a higher amount of transverse reinforcement braces to be required.

### 4.4.2 Numerical

The numerical analyses show that cracks appear at the beam tips. This cracking is caused by the prestress in the tendons and can also be proved via a calculation by hand. The cracks in question are not visible for the naked eye, but they do certainly exist. The crack propagation in the web at about 400 kN, due to exceeded tension strength, corresponds very well with the values found experimentally; this also is the case for crack propagation in the lower flange at about 700 kN. Also the calculated deformations of the beam are almost identical to the measured deformations. In the uncracked zones, the direction of the compression diagonal corresponds very well with the values obtained experimentally. In the numerical model the slope does not increase beyond cracking. This is probably due to the fact that the numerical model can not simulate redistribution beyond cracking. Furthermore, the capacity

obtained numerically does match the real failure capacity of the beams very close; the differences are merely 4%.

The overall conclusion is that the performed calculations correctly simulate the behavior of the beam in general, and the ultimate failure behavior in particular.

## Chapter 5

# Joints in a Multi-beam Box Girder Bridge

C. M. Frissen and M. A. N. Hendriks

*TNO DIANA BV*

N. Kaptijn, A. de Boer and H. Nosewicz

*Ministry of Transport, Public Works and Water Management – The Netherlands*

**Abstract.** Three finite element models have been developed to analyze the cross-sectional forces in the joints of multi-beam box girder bridges. A model based on shell elements is used in nonlinear analyses including two analysis phases. The analysis phases simulate the construction phases. For straight bridges current design methods based on orthotropic plate models give reasonable results compared to the results of the advanced model. For bridges with a skew or curved geometry plan orthotropic plate models give poor predictions for the forces and moments in the joints. Advanced modeling, as presented in this chapter, is then to be preferred.

### 5.1 Introduction

In this introductory section we will present a design question related to multi-beam box girder bridges. This question has lead to an intensive numerical study of a multi-beam box girder bridge. We will start with a general description.

#### 5.1.1 Multi-beam Box Girder Bridges

As indicated by the name, multi-beam box girder bridges consist of several box shaped girders. The topsides of the girders compose the car deck. Figure 5.1 is an illustrative sketch of a box girder bridge. Prefabricated girders are frequently used for bridges crossing highways where you do not want not disturb the traffic during

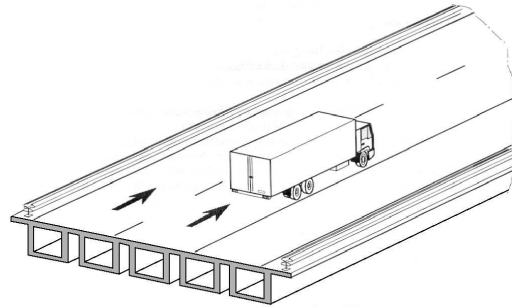


Figure 5.1: Sketch of a multi-beam box girder bridge

the construction phase. In the Netherlands multi-beam box girder bridges are not commonly applied. Because of the costs normally inverted prestressed T-beams are used. Multi-beam box girder bridges are regularly applied for spans up to forty meters.

Concrete multi-beam box girder bridges are always prestressed in longitudinal direction. The curved prestressed tendons or strands in the girder webs of the boxes result in an upward load, in the opposite direction of the gravity load. The greater the curvature of the tendons, the greater this effect is. The maximal curvature of the tendons depends on the ratio between the height of the boxes and the length of the span.

### 5.1.2 Current Design Practice

The design loads comprise the following.

- Dead weight of the girders and the joints between the girders.
- Prestress of the strands (tendons).
- Distributed loads of asphalt, rails, and mobile loads.
- Concentrated wheel loads, to be located on the most unfavorable position.

The force transmission of the loads through a multi-beam box girder bridge is a complex issue. The complexity increases even more when, instead of a straight plan arrangement, bridges of curved or skew plan geometry have to be analyzed. A popular methodology, based on the Finite Element Method, makes use of two-dimensional plate bending models.

For multi-beam box girder bridges the overall bending stiffness in longitudinal direction is substantial higher than the bending stiffness in transverse direction. In transverse direction the relatively soft joints between the box girders dominate the bending stiffness. In two-dimensional plate bending models this is modeled by applying plate models with geometrically orthotropic properties, where moment of inertia



$I_{xx}$  in longitudinal direction differs from the moment of inertia  $I_{yy}$  in transverse direction. The determination of  $I_{xx}$  and  $I_{yy}$  follows Timoshenko's theory for plates and shells [69] and reflects the cross-sectional shape of the box girder bridge. Linear static analyses are adopted where reduced stiffness moduli account for the cracks to be expected in the cross-section of the concrete.

### 5.1.3 Design Considerations

The design considerations that form the basis of the numerical study as presented in this study focus on the cross-sectional forces in the joints between the box girders. These girders are prefabricated boxes; the joints are casted after placement of the girders. These two construction phases cause the joints to be initially stress free, apart from the influence of the dead weight on the joints. After completing the viaduct with asphalt, and after introducing additional loads such as mobile loads and possible (wind) loads resulting from baffle boards, this situation has been changed.

The design of the reinforcements in the joints requires a good insight in the (shear) forces and bending moments in the joints. Furthermore, the question could be raised whether it is necessary to apply post-tensioned strands in the transverse direction. It is believed that the current design procedure does not give sufficient insight in the forces and bending moments in the joints. For this, a more advanced analysis is in its place. More generally, such an advanced analysis could serve as an assessment of the design method based on orthotropic plate models.

### 5.1.4 Approach

In this study we have selected a relatively small bridge which we will describe in detail in §5.2. The economic relevance of this case study is motivated by the popularity of such bridges. As a variation study, a wind load on baffle board was investigated. As a geometric variation study, a skew bridge was investigated. In each case the forces and moments in the joints are the primary concern.

An advanced analysis should include the construction phases as these have a crucial effect on the stresses in the joints. Also, such an analysis should include nonlinear effects, such as cracking of the concrete and plasticity of the reinforcements. Three models will be used: a full three-dimensional model with solid brick elements, a degenerated full three-dimensional model based on shell elements, and a two-dimensional plate bending model. From a geometrical viewpoint, the full three-dimensional model is the most accurate model. However, for the nonlinear analyses the three-dimensional solid model is not considered as a feasible option due to the very long computing time. For the nonlinear analyses the three-dimensional shell model will be adopted. The two-dimensional plate bending model will serve as a reference and represents the standard design practice.

In §5.2 we will give a more detailed description of the selected case. Subsequently, §5.3 and §5.4 respectively present linear and nonlinear analyses. The main purpose of the linear analyses is justification of the three models. Section §5.5 concludes this study by reverting to the design question.

## 5.2 Case Study – Box Girder Bridge ‘Heultsedreef’

As a case study we selected viaduct ‘KW 14 Heultsedreef’, a typical multi-beam box girder bridge, located near Boxtel in the south of the Netherlands, crossing the  $2 \times 2$  lanes highway ‘A2’. We will subsequently describe its geometry, the material properties and the design loads.

### 5.2.1 Geometry

The structure consists of five prestressed and prefabricated box girders. The bridge comprises two fields, each spanning two lanes. Because of symmetry we will consider one half of the structure with a span of 27225 mm. Each box is 1180 mm wide and

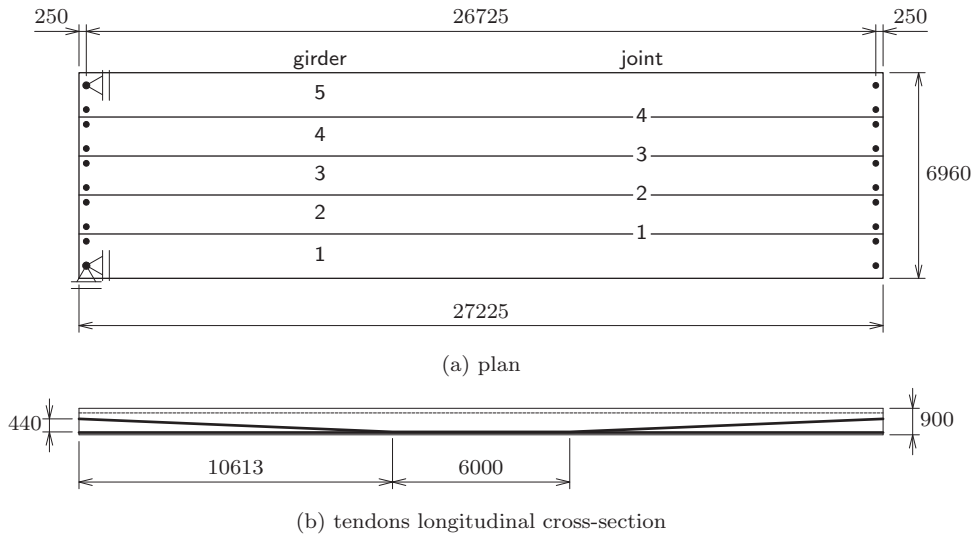


Figure 5.2: Viaduct ‘Heultsedreef’

900 mm high. The center to center distance between the boxes is 1320 mm. The top slabs are designed such that a strip of 230 mm wide and 160 mm thick will be casted on the site. We will refer to this strip as the ‘joint’. Figure 5.3 shows the drawing of the structure. The width of the deck is 6960 mm. Each girder is placed on four rubber supports, located 250 mm from the girder ends. Figure 5.2a illustrates the general configuration. This figure also indicates the horizontal supports, as how these will be schematized in the analyses.

The shape of the prestressed strands is illustrated in Figure 5.2b. The figure shows the strands in one of the ten webs. Each web includes twenty bended strands. Note that the course of the strands is such that they come down 440 mm from the girder end to the middle of the girder. Each of the bottom slabs includes twenty-four prestressed strands, which are straight.



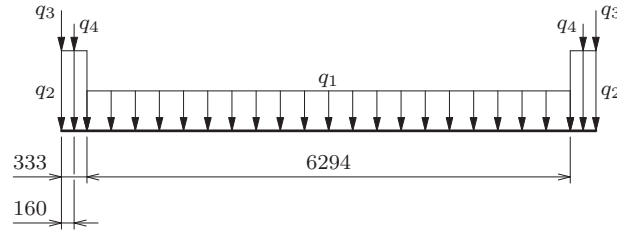


Figure 5.4: Distributed loads on the top slabs – cross-sectional view

4. A traffic load, as an equally distributed load acting on the same area as the weight of the asphalt layer  $q_1$ .
5. A wheel load composed of three axle loads [Fig. 5.5]: case 1 at the edge and case 2 in the middle of width. Each axle load is distributed over four wheels, resulting in  $3 \times 4$  wheel prints. The critical position of the wheel load, in transverse as well as in longitudinal direction, will be determined with an influence field analysis [§ 5.3].

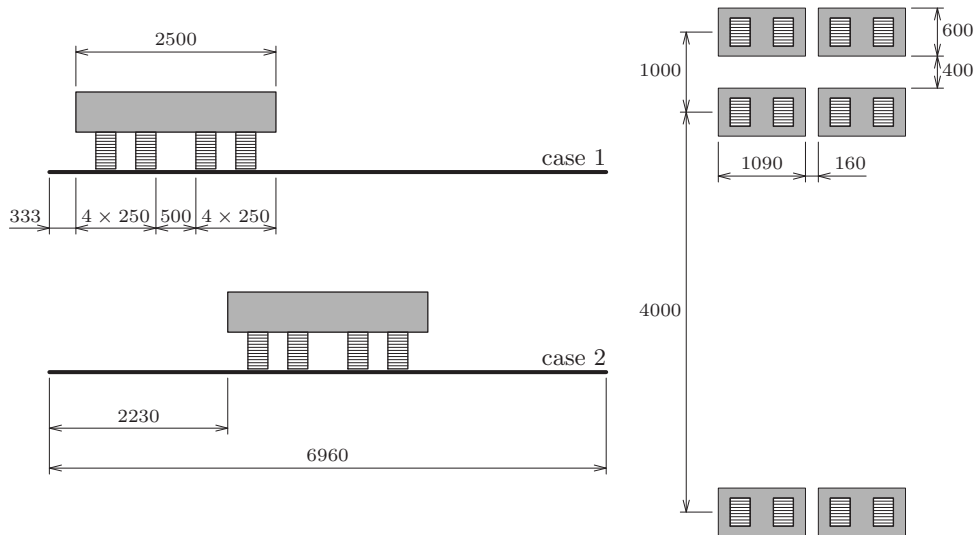


Figure 5.5: Wheel loads on the top slabs

### 5.3 Linear Analysis

In the next three sections we will subsequently present the element meshes for the full three-dimensional model [§ 5.3.1], the shell model [§ 5.3.1], and the orthotropic plate model [§ 5.3.3]. We will compare the major results [§ 5.3.4], and present an

influence field analysis to assess the most critical position of the wheel loads [§ 5.3.5]. For the influence analysis the shell model was adopted.

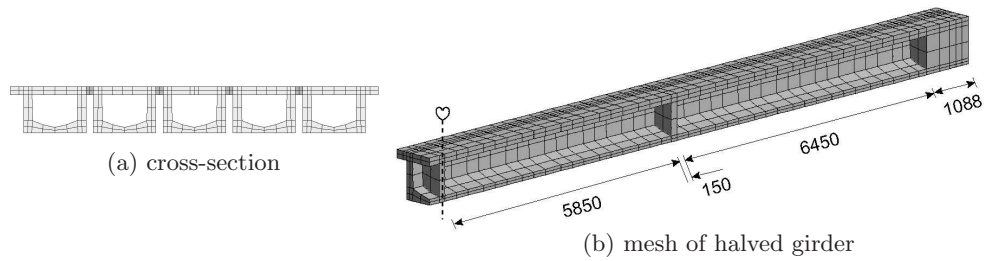


Figure 5.6: Volume model

### 5.3.1 Volume Model

The full three-dimensional volume model could be termed as a straightforward model, as it required the fewest geometrically simplifying assumptions. Figure 5.6 illustrates the mesh that comprises five girders. The mesh consists of twenty-node solid brick elements CHX60. There are two types of embedded reinforcements: bars for the strands [Fig. 5.7], and grids for the reinforcements.

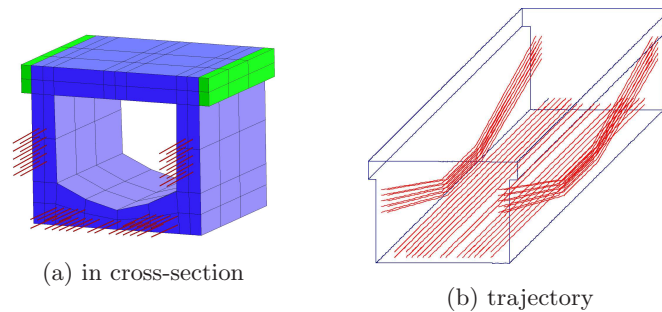


Figure 5.7: Locations of the strands in the volume model

### 5.3.2 Shell Model

The shell model consists of curved shell elements: eight-node quadrilaterals CQ40S and six-node triangles CT30S [Fig. 5.8]. These elements could be envisaged as degenerated solid elements, assuming the shell hypotheses of straight normals and zero normal stress. Compared to the volume model an additional point of concern is the geometric treatment of the corners in the model. As a guiding principle for the geometric discretization, the bulk concrete volume is preserved. The embedding of strand and reinforcements is analogous to that of the volume model.

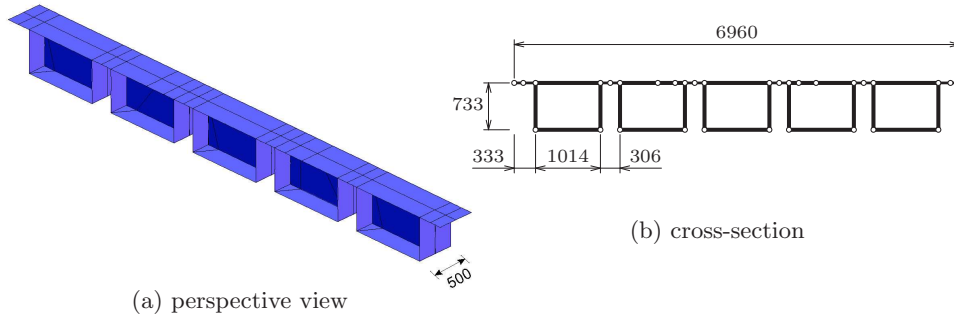


Figure 5.8: Shell model

### 5.3.3 Orthotropic Plate Model

The orthotropic plate model consists of eight-node quadrilateral plate bending elements CQ24P. The geometrically orthotropic properties of the two-dimensional plate elements reflect the actual geometry of the bridge, see for instance Timoshenko [69]. Two geometry groups are distinguished [Fig. 5.9]: one for the two edge girders (red) and one for the three girders in between (yellow).

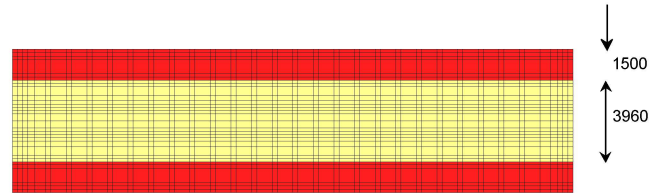


Figure 5.9: Two-dimensional orthotropic plate model – moments of inertia

Table 5.2 presents the moment of inertia  $I_{xx}$  in longitudinal direction, the moment of inertia  $I_{yy}$  in transverse direction and the moments of inertia  $I_{xy}$  and  $I_{yx}$ . To

Table 5.2: GEOMETRICAL ORTHOTROPIC PROPERTIES OF THE PLATE ELEMENTS

	$10^6 \text{ mm}^4/\text{mm}$		
	$I_{xx}$	$I_{yy}$	$I_{xy} = I_{yx}$
<b>Deck</b>	45.69	0.76	35.06
<b>Edge girders</b>	42.80	0.76	35.06

estimate the moments  $M_{xy}$  in the girders and in the joints, the calculated moments  $M_{xy}$  resulting from the analysis should be multiplied with respectively 2.0 and 0.02 (see Frissen [33]).

### 5.3.4 Results and Justification

The three finite element models have been analyzed with various load cases of which case 1 of the wheel loads is the most asymmetric one [Fig. 5.5]. The force transmission of the wheel loads could easily be demonstrated by plotting the reaction forces in the elastic supports. On each edge the bridge is supported by ten elastic supports, two per girder. Figure 5.10 shows the reaction forces on one edge of the bridge as

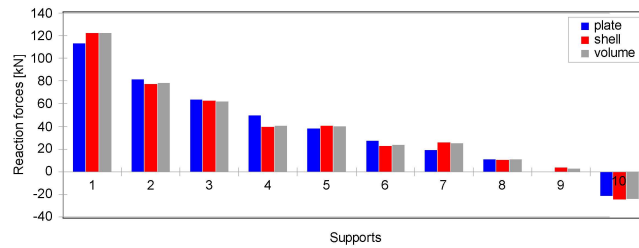


Figure 5.10: Reaction forces in elastic supports for wheel load

resulting from wheel load case 1 in the middle of the span [Fig. 5.5]. Compared to the reaction forces as obtained with the volume model, the shell model gives a difference of about 2% and the plate model gives a difference of about 10%.

### 5.3.5 Influence Fields

The shell model was adopted to calculate influence fields. Figure 5.11 shows the influence field of a wheel load. The colors indicate the transverse moment  $M_{yy}$  in joint 2 between box girders 2 and 3 at the middle of the span. Note that we selected a point in a joint as that is the focus of this study. Based on various influence field

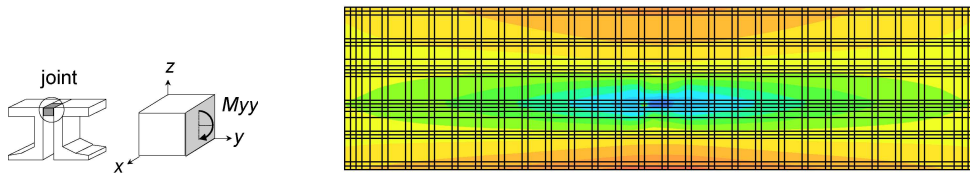


Figure 5.11: Influence field for  $M_{yy}$  in joint – mid-span between girder 2 and 3

analyses for several points and for both bending moments and shear forces, wheel load case 2 [Fig. 5.5] was selected as the normative wheel load.

## 5.4 Nonlinear Analysis

The linear analyses revealed that the differences between the results of the three models are small. For the assessment of the cross-sectional forces in the joint we

will proceed with nonlinear analyses, all performed with the shell model. In this section we will describe the analysis phases (construction phases), the load steps, the material properties and the analysis results. The nonlinear results are compared with results obtained from the orthotropic plate model.

### 5.4.1 Analysis Phases and Load Steps

The analysis comprises two phases. In the first phase the model consists of five girders, which are not yet connected with joints. The loads are the gravity and the prestress in the strands.

In the second analysis phase the joints are added to the model. The reason to distinguishing two phases is that the concrete in the joint is added free from strains, stresses and possible cracks. This also holds true for the reinforcements in the joints. As opposed to the joints, the initial state of the girders in the second phase equals the resulting state of the first analysis phase. The loads from the first phase are maintained in the second analysis phase. Next the permanent loads, the distributed traffic load, and the wheel load case 2 are applied.

In this way a viaduct modeled might be modeled too stiff. In reality, cracking due to the ongoing traffic loads on the viaduct might influence the transfer of loads. To simulate this in the analysis the viaduct will be pre-damaged by applying and subsequently removing wheel loads at ten locations. This is like moving a truck forth

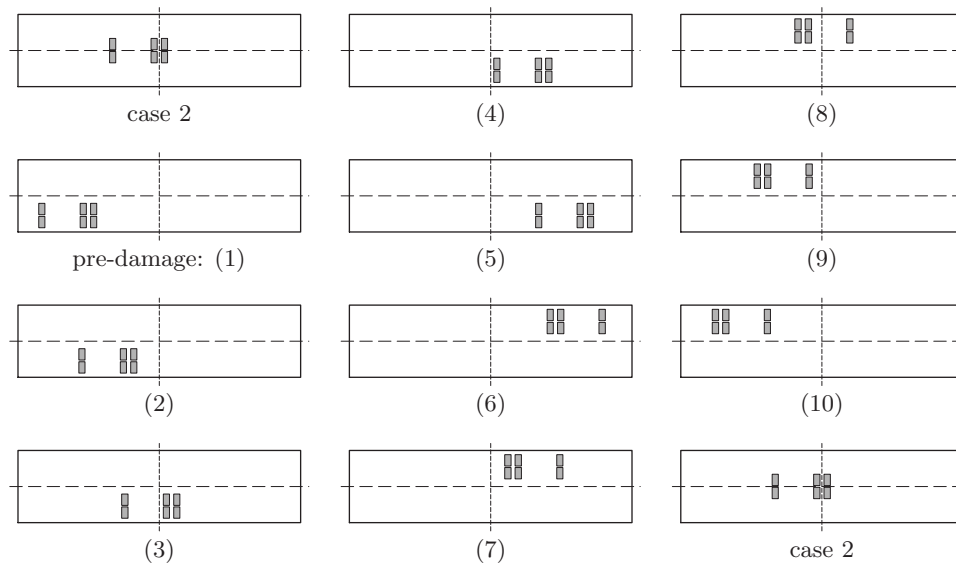


Figure 5.12: Load history of the twelve wheel loads

along one lane of the viaduct and back along the other lane. Figure 5.12 illustrates the initial loading and unloading of wheel load case 2, the subsequent loading and unloading of the ten pre-damaging wheel loads and finally the loading of wheel load



case 2.

### 5.4.2 Material Modeling

For the concrete DIANA's 'smeared crack' model is adopted, with tension stiffening. It is assumed that the tensile stress in the concrete decreases after the maximum tensile strength has been reached and that it becomes zero again when the reinforcement steel starts yielding. The compressive behavior is modeled with an ideal plastic Von Mises model. The reinforcements are modeled with Von Mises ideal plasticity. The strands are modeled with plasticity with minimum stiffness beyond yielding. Figure 5.13 shows the stress-strain diagrams.

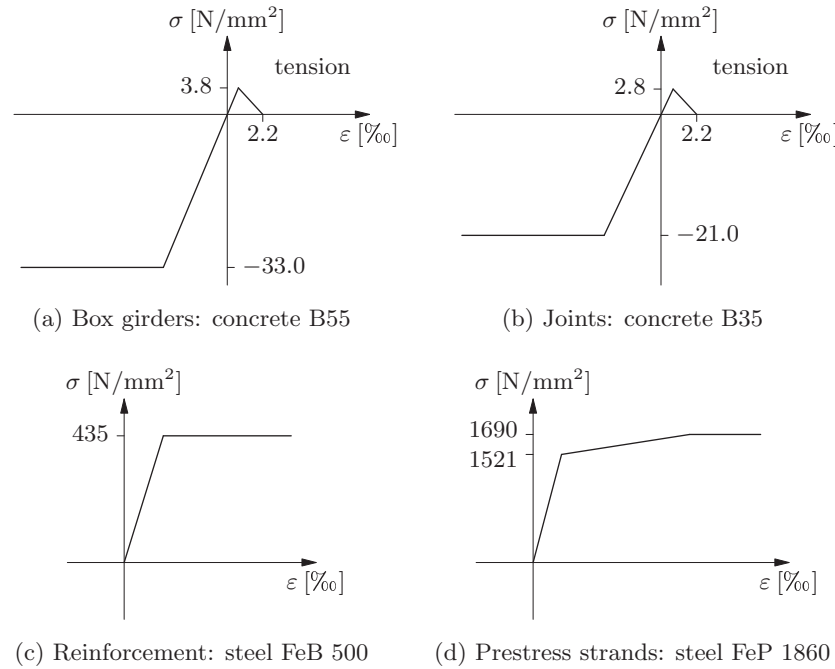


Figure 5.13: Stress-strain diagrams

### 5.4.3 Results for Construction Phases 1 and 2

In this section some exemplary results for the ultimate limit state analysis are presented. The nonlinear analysis comprises two analysis phases. Figure 5.14 gives the bending of the topsides of the girders due to dead weight and prestress for analysis phase 1. Note that the elements representing the joints are not active in this analysis phase. In the middle of the span the displacement is 38 mm in upward direction. Figure 5.15 shows the crack pattern for construction phase 2. Longitudinal cracks arise in the joints, whereas cracks in transverse direction could be observed in the

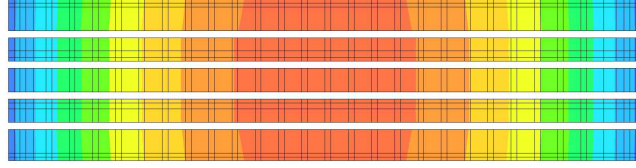


Figure 5.14: Phase 1: placement of the girders – bending of girder topsides due to dead weight and prestress

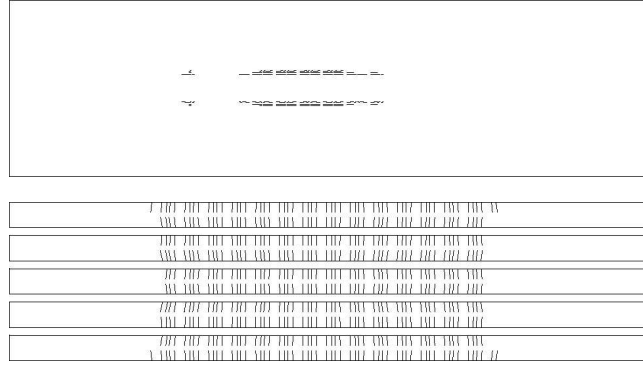


Figure 5.15: Phase 2 – crack pattern at bottom side of joints (top) and girders (bottom)

bottom sides of the girders. Figure 5.16 further illustrates the cross-sectional deformations at the middle of the span. The maximum vertical displacement is 220 mm.

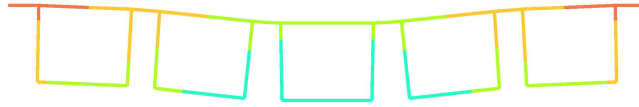


Figure 5.16: Phase 2 – vertical displacements at mid-span

A typical comparison between the nonlinear shell model and the plate model is given in Figure 5.17 on the next page. This graph presents the bending moment  $M_{yy}$  in joint 2, in the middle of the transverse direction, along the span. Bending moment  $M_{yy}$  is one of the many forces and moments that were compared in this study, but was considered as one of the most crucial ones for the joints. The lines distinguish between:

- shell models versus orthotropic plate models,
- reduced stiffness (red.),<sup>1</sup> to account for cracking, and non-reduced stiffness (for

<sup>1</sup>The reduced stiffness has been obtained by multiplication of the moments of inertia  $I_{xx}$  and

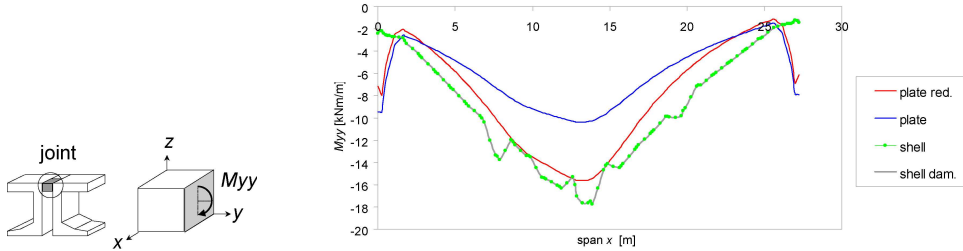


Figure 5.17: Phase 2 – bending moments in joint 2

the plate model),

- with (dam.) and without pre-damaging (for the shell model).

The lines of the shell model with and without pre-damage show that the effect of pre-damaging the shell elements could be neglected [Fig. 5.17]. Further, reducing the stiffness in the plate models yields reasonable results compared to the results of the shell model. The reduced plate model underestimates  $M_{yy}$  up to 7%. Non-reduced plate models underestimate  $M_{yy}$  up to 38%. Variation studies with skew viaducts [Fig. 5.18], revealed that also the reduced plate models fail to accurately predict  $M_{yy}$

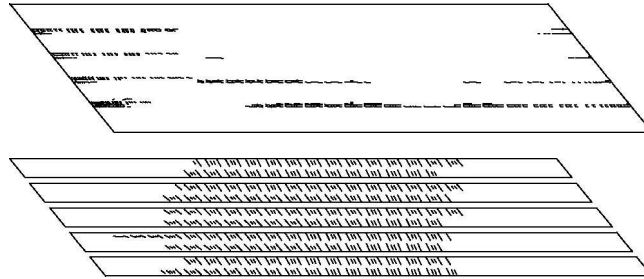


Figure 5.18: Skew viaduct phase 2 – crack pattern at bottom side of joints (top) and girders (bottom)

in the joints. Figure 5.19 on the following page shows the same results as Figure 5.17 but now for the skew viaduct. Although, in absolute sense, the maximum value of  $M_{yy}$  for the plate model with reduced stiffness is comparable with the maximum value for the shell model, we observe that the course is completely different.

## 5.5 Conclusion

It is feasible to perform a nonlinear analysis of box girder bridges taking into account the two main construction phases. The number of variation studies is still limited.

$I_{yy}$  from Table 5.2 with a factor 0.5, and the friction stiffnesses with a factor 0.2.

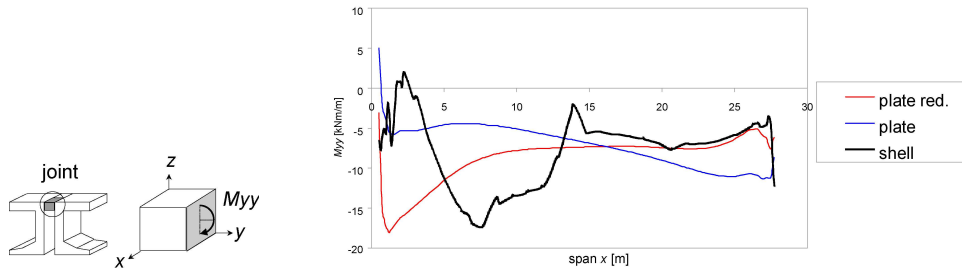


Figure 5.19: Phase 2 – bending moments in the joints for the skew viaduct

Based on the current variation studies, including the modeling of a skew viaduct, effect of the position of the wheel loads and the effect of wind loads on baffle boards, we concluded that nonlinear analyses have an added value above the orthotropic plate models. This holds especially true for the skew viaduct and will also hold true for bridges with a curved planar geometry. In this case plate models give bad predictions for the bending moments and forces. Nonlinear analysis is then to be preferred.

For the ‘Heultsedreef’ bridge, relatively high bending moments  $M_{yy}$  occur in the joints but it was not necessary to apply post-tensioning strands in transverse direction.

## Chapter 6

# Fire Analysis of an LNG Tank

A. Rijswijk

*Protected Storage Engineers (joint venture of Royal Haskoning and DHV-AIB)*

### 6.1 Introduction

Gases cooled down until liquidity are usually stored in vertical cylindrical tanks. Because the gas is cooled down until the boiling point it may be stored under atmospheric pressure. An isolated reservoir of 9% nickel steel is usually applied to store this liquefied gas. Safety regulations require the application of an additional concrete safety tank for capacities of more than 4000 m<sup>3</sup>. This concrete safety tank protects the steel inner tank against external influences, like explosions, fire and parts falling down from the installation around the tank.

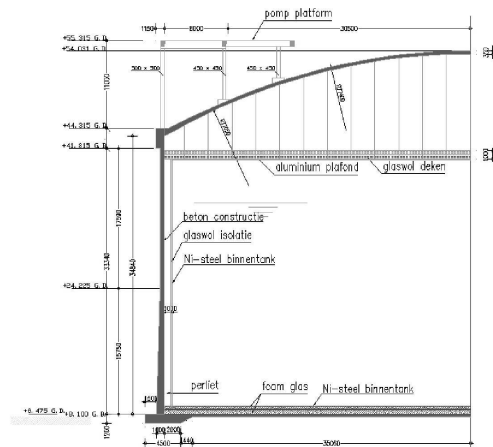


Figure 6.1: Cross-section of a ‘full containment’ tank

The safety tank comprises various parts [Fig. 6.1]. Firstly there is a floor, founded on the subsoil, which supports the steel inner tank. A prestressed wall surrounds the steel inner tank, resting on the outer edge of the floor. Above the steel tank a domed roof rests on the wall. To reduce the risk of leakage as much as possible, the connections between the various parts of the safety tank are usually made monolithic. A tank, constructed as such, is called a ‘full containment tank’.

Liquefied gases, stored under boiling point temperature, always show vaporization (*boil-off*) which causes an overpressure of the gas in the tank. Moreover, the filling of the tank may yield an overpressure as well. For the protection of the tank against overpressure so-called depressurization valves are applied. When these valves open, the surplus gas is blasted up via a chimney and burned at about ten meters above the tank.

This chapter discusses the effect of a fire temperature load on the domed roof, caused by blasting via a depressurization valve. CUR Report nr. 134 [15] presents calculations for a similar structure with respect to testing of the fluid density and the determination of the effects of a temperature load, caused by a nearby burning tank. These calculations were focused on the monolithic wall–floor connection in particular.

## 6.2 LNG Tank of 120,000 m<sup>3</sup> Capacity

The structure under consideration is a tank for storage of LNG (Liquefied Natural Gas) with a capacity of 120,000 m<sup>3</sup>, as has been built in 2001 in Malaysia. The tank structure is composed as follows.

- *Steel inner tank* with a diameter of 75 m and a height of 31 m.
- *Concrete floor* with a diameter of 82 m. The thickness is 0.40 m for the middle part and 1.20 m for the outer 4.50 m.
- *Concrete wall* with an inner diameter of 77 m. The wall is prestressed horizontally. At the connection to the floor, the wall is 1.00 m thick. The thickness decreases until 0.60 m at a height of 15.75 m above the floor. Further up the thickness is uniform until a height of 35.50 m.
- *Concrete edge beam* horizontally prestressed along the edge of the roof on the wall. The beam is 1.15 m wide and 2.50 m high.
- *Concrete platform* of 17.5 × 25 m resting on the edge beam and the roof via columns. To introduce the forces into the roof, 1.60 × 1.60 m concrete footings have been applied.
- *Concrete domed roof* with an inner radius of 77 m [Fig. 6.2]. The thickness in the center part is 0.35 m. Over the outer 7.5 m the thickness increases until 0.60 m along the edge of the dome. Below the platform the dome is at least 0.40 m thick.

The structure is built on a consolidated soil layer with a thickness of 0.30 to 4.00 m, applied on top of the natural sandstone formation. The structural design of the con-

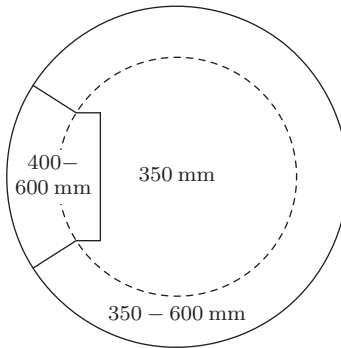


Figure 6.2: Overview geometry of the dome

crete safety tank is based on a combination of various regulations and specifications. In addition to the clients' specification the following publications are of interest.

- BS 7777 [10], for the general design;
- BS 8110 [11], for determination of reinforcement and prestress;
- UBC 1997 [1], for earthquake influences;
- ACI 318M [2], for specification of the reinforcement with respect to earthquakes;
- CEB-FIP Model Code 1990 [13, § 7.4.3], for calculation of crack widths;
- CEB-FIP Bulletin d'Information No. 208 [12], for material behavior in case of fire;
- The PhD thesis of C. van der Veen [72], for the bonding behavior of concrete to reinforcement at low temperatures.

The building materials for the concrete structure have been specified according to the British code [11]. Concrete with quality C45 is applied for the edge beam (cube compression strength  $45 \text{ N/mm}^2$ ). The other concrete parts are made of quality C40 (cube compression strength  $40 \text{ N/mm}^2$ ). The yield stress of the reinforcement steel has been taken as  $460 \text{ N/mm}^2$ . The temperature distribution that may occur during the life span of the tank has influenced the applied steel quality for the various parts. For the prestress steel a quality FeP 1860 has been applied.

## 6.3 Purpose and Principles of the Analysis

### 6.3.1 Temperature Distribution

The original design of the safety tank was based on the utilization of a sprinkler installation on the roof. This limits the temperature of the concrete, during a fire

caused by blasting via the depressurization valves, to at most 100 °C. This temperature will hardly do any harm to the quality of the concrete. During the construction phase of the project the question arose whether it would be possible to satisfy the client's specification without the utilization of a sprinkler installation.

In this case the normative design situation is the burning of the gas caused by blasting via the depressurization valves. The burning occurs via chimneys at ten meters above the domed roof which causes a temperature load on the roof. The

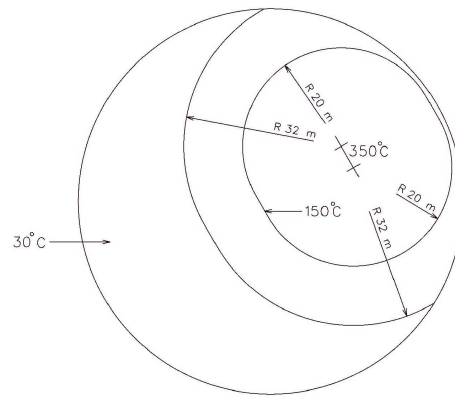


Figure 6.3: Roofs' outer temperature during fire in depressurization valve

specifications require the assumption of the temperature distribution on the outside of the dome after a burning time of six hours as indicated in Figure 6.3. The temperature of the wall inside the dome has been assumed to be 30 °C, followed by a linear increase over the thickness of the dome.

### 6.3.2 Material Properties

**Reinforcement steel.** Figure 6.4 shows the assumptions of the variation of the steel properties during fire.

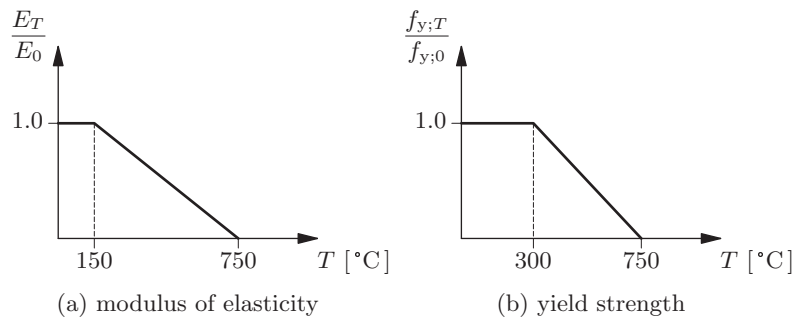


Figure 6.4: Influence of temperature on steel properties



**Concrete.** The temperature dependent creep of the concrete (transient creep) has been determined according to the CEB-FIP report “Methods and assessment of the fire resistance of concrete structural members” [32].

$$\varepsilon_{\text{cr}} = \beta_0 \frac{\sigma}{\sigma_u(T)} \left( \frac{t}{t_r} \right)^p e^{k_1(T-20)} \quad (6.1)$$

With

$$\beta_0 = -0.53 \times 10^{-3},$$

$\sigma_u(T)$  is the ultimate stress at the current temperature  $T$ ,

$t$  is time,

$$t_r = 3 \text{ hours},$$

$$p = 0.5,$$

$$k_1 = 3.04 \times 10^{-3} \text{ }^\circ\text{C}^{-1},$$

$T$  is temperature.

The compression strength of concrete for temperatures up to 350 °C is equal to the compression strength at normal temperatures according to BS 8110 [11] [Fig. 6.5].

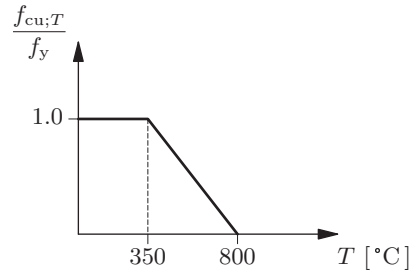


Figure 6.5: Influence of temperature on concrete compression strength

**Failure.** For the situation described above, the following verification criteria apply for the ultimate state of failure.

- Maximum strain of the concrete under pressure less than 3.5 ‰.
- Maximum strain of the reinforcement steel less than 1 ‰.

There are no further requirements on the serviceability of the structure. Any cracks, caused by a fire situation, must be examined and assessed after the fire. If the width of cracks seriously affect the durability of the structure, these cracks must be injected.

## 6.4 Analysis of the Structure

The analysis of the structure of the concrete safety tank has been carried out in two parts: a main calculation of the total structure followed by some calculations of

details of the various parts of the structure. The main calculation presents the basic assumptions, the phases in the building process, the analysis model, the loads and load combinations, and the analysis process. The detailed calculations determine the reinforcement and the prestressed steel for the various parts, based on the model of the main calculation.

### 6.4.1 Phased Construction and Analysis

The following building and operational phases are relevant for the design of the structure.

1. Construction of the tank up to the edge beam, including the first prestressing phase.
2. Construction of the domed roof, including the second phase of the prestressing.
3. Construction of the platform and field-testing of the structure.
4. Regular operational situations of the tank.
5. Emergency situation due to leakage of the steel inner tank.
6. Emergency situation during earthquakes.
7. Emergency situation during fire due to blasting via the depressurization valve.

The tank is being build in phases, which each have their typical influence on the behavior of the tank and the associated force distribution. Therefore separate models have been defined for each phase, where a subsequent phase is based on the previous one with the addition of the structural parts to be made and the possibly modified material parameters. The transition of the testing phase to the normal operational situation is characterized by the modification of the material parameters of the consolidated soil layer. Each change in the behavior of the tank in the emergency situations will be related to the material properties as defined for the normal operational situation.

Choices for the structural stiffness to be expected have been made for each phase, based on experience since 1970. Furthermore, separate load cases have been defined in the phase where they may appear for the first time, or may be supposed to appear for the first time. For instance the deadweight of the floor has been applied in phase 1 and the deadweight of the platform in phase 3. For a particular design situation the deformation and force distribution in the tank can be determined by combining analysis results of individual load cases. Then the compliance with the various design criteria can be tested, based on the locally applied amount of reinforcement and prestressed steel and on the calculated internal forces. Furthermore, the adequateness of the compatibility between deformation and force distribution can be checked.

### 6.4.2 Finite Element Model

The analysis has been performed with the DIANA computer program. Due to the asymmetry of the foundation and the platform, a full three-dimensional model has

been chosen. Figure 6.6 shows a bird's-eye view of the model for phase 2 up to and including phase 7. Note that the platform is not shown in this figure. In phase 1 the

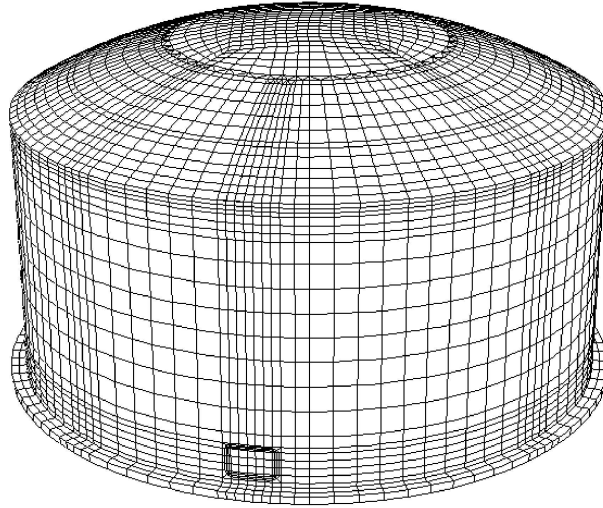


Figure 6.6: Finite element model for safety tank structure

domed roof is not present. Two types of shell elements (CQ40S and CT30S) and one type of interface element (CQ48I) have been applied in the three-dimensional model.

**CQ40S shell element.** The CQ40S element is an eight-node isoparametric shell element, curved in two directions [Fig. 6.7]. The element is applied in models where

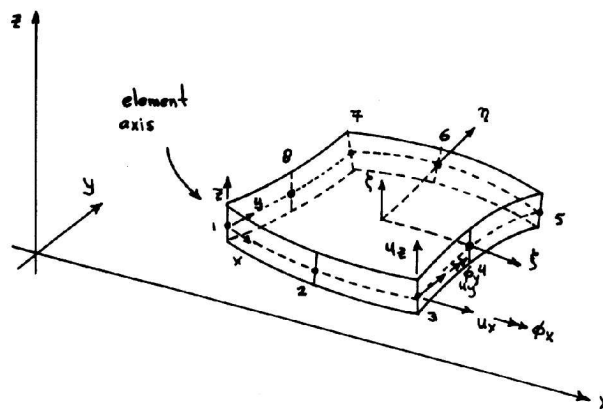


Figure 6.7: Geometry of the CQ40S element

the thickness of the structure is small compared to the other dimensions. The CQ40S element is very useful to model storage tanks.

Degrees of freedom:  $u_x, u_y, u_z, \phi_x, \phi_y$  in each node.

Output stresses:  $\sigma_x, \sigma_y, \sigma_z = 0, \sigma_{xy}, \sigma_{yz}, \sigma_{zx}$ .

Output displacements:  $u_x, u_y, u_z$ .

**CT30S shell element.** The CT30S element is a six-node isoparametric shell element, curved in two directions. It is applied in the same way as the CQ40S element.

Degrees of freedom:  $u_x, u_y, u_z, \phi_x, \phi_y$  in each node.

Output stresses:  $\sigma_x, \sigma_y, \sigma_z = 0, \sigma_{xy}, \sigma_{yz}, \sigma_{zx}$ .

Output displacements:  $u_x, u_y, u_z$ .

**CQ84I quadrilateral interface element.** The CQ48I element is an interface between two faces in a three-dimensional configuration [Fig. 6.8]. The basic variables

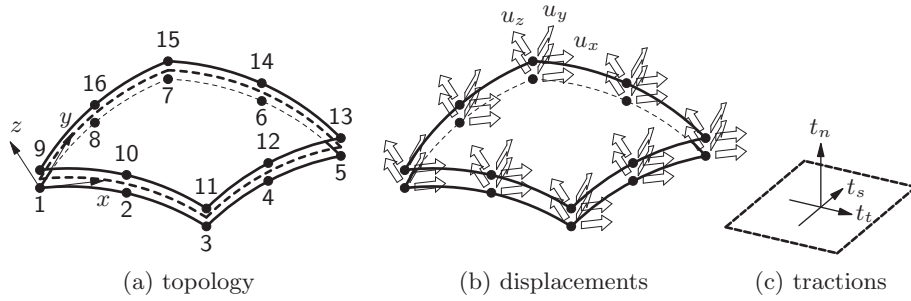


Figure 6.8: Geometry of the CQ48I element

are the nodal displacements  $\mathbf{u}$ , the relative displacements  $\Delta\mathbf{u}$  and the tractions  $\mathbf{t}$ .

$$\mathbf{u}_e = \begin{Bmatrix} u_x \\ u_y \\ u_z \end{Bmatrix} \quad \Delta\mathbf{u} = \begin{Bmatrix} \Delta u_x \\ \Delta u_y \\ \Delta u_z \end{Bmatrix} \quad \mathbf{t} = \begin{Bmatrix} t_n \\ t_s \\ t_t \end{Bmatrix} \quad (6.2)$$

The axes along the surface are  $nts$  with  $n$  perpendicular to the tangent plane and  $t$  and  $s$  in the tangent plane. The axes for the displacements are  $xyz$ . DIANA evaluates this axes system in the first node with  $z$  perpendicular to the tangent plane and  $x$  and  $y$  in the tangent plane. The element is based on quadratic interpolation.

**Element mesh.** Table 6.1 on the facing page gives the number and type of elements, applied in each structural part. Figure 6.9 on the next page shows the element mesh of the domed roof.

**Loading.** For the fire situation due to the blasting of the depressurization valve the following loadings on the domed roof are of major importance.

Table 6.1: ELEMENTS IN THE MODEL

Part	Element type	Nr. of elements
Domed roof	CQ40S & CT30S	1995
Edge beam	CQ40S	110
Wall	CQ40S & CT30S	2118
Floor	CQ40S & CT30S	1964
Foundation	CQ48I	1964
Total		8151

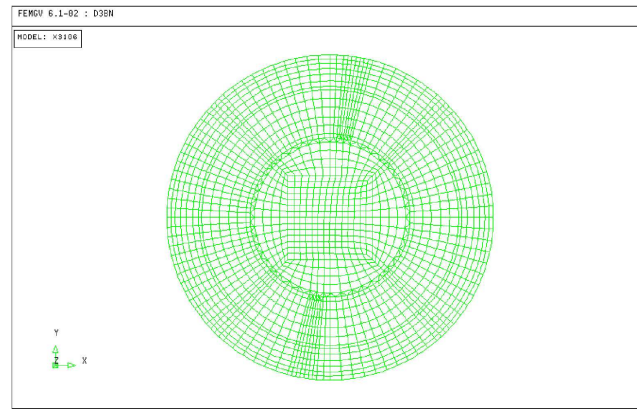


Figure 6.9: Bird's-eye view of element mesh for domed roof

- The permanent deadweight load of the roof; the load of the installation on the roof; the insulation package with supporting structure suspended from the roof; the deadweight and installation of the platform, resting in the roof via columns.
- The prestress of the edge beam and the upper part of the wall.
- The internal overpressure in the safety tank of  $7 \text{ kN/m}^2$ .
- The variable load on the insulation package, the domed roof and the platform.
- The temperature load as defined in §6.3.1.

### 6.4.3 Performance of the Analysis

The analysis procedure for the assessment of the fire situation above the domed roof has been performed as follows.

1. *Linear elastic DIANA analysis* — For each phase a linear elastic analysis has been performed and the results written to a file in FEMVIEW format. Subsequently, these individual files have been consolidated into one single large results file.

2. *Load case combination in FEMVIEW* — The results file has been read in FEMVIEW, where the results of the load cases have been combined into the design situation for the fire to be considered. The output results have been written to a combination file.
3. *Assessment of the calculated force distribution by means of a dedicated postprocessor* — The force distribution, as stored in the combination file, has been assessed by means of a dedicated postprocessor. For each element the effects of the force distribution have been examined with respect to the design criteria, based on the geometry of the structure and the locally applied materials. The algorithms applied comprise some parts which are specific for the project:
  - Cross-section checks based on the British regulations, including the non-linear temperature dependency of the materials.
  - Evaluation of the structural stiffness based on the CEB-FIP Model Code 1990 [13], including nonlinear temperature dependency of the material, crack propagation and tension stiffening. The statistical variation of the concrete tension strength and the crack distances have been incorporated in the evaluation. This defines a constant relation between the section forces (normal forces and moments) on the one hand, and the structural deformation (axial strains and curvatures) on the other hand.
  - Examination with respect to design criteria.
  - Determination of the differences in the linear elastic strains and curvatures obtained from the DIANA analysis with respect to the strains and curvatures determined with the dedicated postprocessor.
4. *Generation of an additional load* — Generally the deformation obtained from DIANA will deviate from the deformation as determined with the dedicated postprocessor. For large differences, the compatibility between force distribution and deformation will be lost. However, this can be mended easily by definition of an additional load case for nonlinear effects in the DIANA analysis. This load case applies the dissimilarity in the strains and curvatures per element, as determined in step 3, in opposite direction as a prestress, based on the  $E$ -modulus of the element. The additional load case is written from within the dedicated postprocessor to an ASCII text file.
5. *Re-analysis with DIANA* — The effect of the additional prestress can be determined from a repeated DIANA analysis. The prestress load relaxes if the construction can deform freely. In this situation the deformation within the DIANA analysis will be adapted. If the structure is not free to deform, then the prestress will be added to the internal forces, that is an adaptation of the force distribution. Generally, the result will be somewhere in between these two extremes. Like this, the effects of cracking and plasticity can be incorporated in the linear elastic DIANA analysis. By repeating the DIANA analysis with the additional prestress load until satisfactory convergence the compatibility between deformation and force distribution can be warranted.

6. *Presentation of the examination results* — After step 5 the examination results are written from within the dedicated postprocessor to a file in FEMVIEW format which enables their presentation via FEMVIEW.

#### 6.4.4 Why DIANA's Module NONLIN was not Applied

The DIANA package offers comprehensive modules for analysis of nonlinear behavior. However, we have not chosen to apply these possibilities within the package. Some considerations to do so were the following.

- For the majority of the load combinations a force distribution as resulting from a quasi-linear elastic analysis is sufficiently accurate. The reinforcement determined from such a force distribution is quite economic.
- The  $E$ -moduli to be chosen for the various parts are known, based on experience.
- For the remaining combinations, with important nonlinear effects, the relation between axial strain and curvature on the one hand, and the normal force and moment on the other hand, strongly depends on crack propagation. For instance, the axial deformation in circumferential direction of the tank wall influences the curvature in both the circumferential and the vertical direction. Therefore, it is not always easy to reach a converged solution for nonlinear analysis of a tank structure. The iteration process is prone to jump back and forth between two wrong solutions, generally caused by sudden changes in stiffness due to cracking.
- Application of a dedicated postprocessor simplifies the achievement of convergence, certainly when the design engineer knows a qualitative solution based on experience. For instance for the fire situation, a maximum crack propagation is expected to be located at the largest temperature gradient, and to decrease with a decreasing temperature gradient.
- Furthermore, the dedicated postprocessor, with its built-in testing of the reinforcement within the iteration process, has the advantage that the amount of reinforcement can be adapted even if a converged solution has not yet been reached. A visual assessment of the intermediate results of the iteration process readily clarifies whether the strain in the reinforcement exceeds its limit.

### 6.5 Analysis Results vs. Design Criteria

Figure 6.10 on the following page shows the axes as applied for presentation of results. In the model for DIANA analysis the local  $z$  axis of the domed roof points downwards. Consequently, the 'lower plane' is on the outside and the 'upper plane' on the inside of the safety tank. The results will be examined and presented with respect to the design criteria for a maximum strain of concrete under compression and a maximum strain of reinforcement steel under tension. Note that the color modulation in all contour plots is different for the two planes.

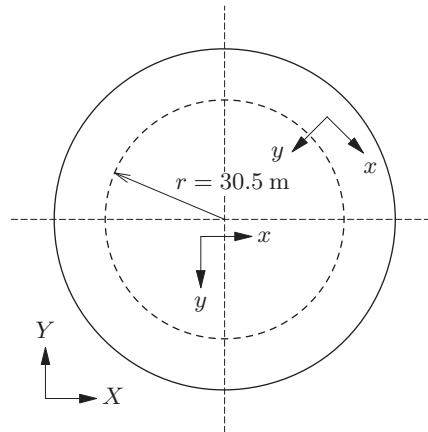


Figure 6.10: Global  $XY$  and local  $xy$  axes for analysis of the domed roof

### 6.5.1 Maximum Compression Strain of Concrete

The design criterion for concrete is that the strain under compression is at most 3.5‰. Figure 6.11 shows a contour plot of the concrete strain in local  $x$  direction. Figure 6.12 on the facing page shows the same strains in the local  $y$  direction. Both figures ignore the transient creep because this has been incorporated in the additional prestress load. See Figures 6.15 and 6.16 for this.

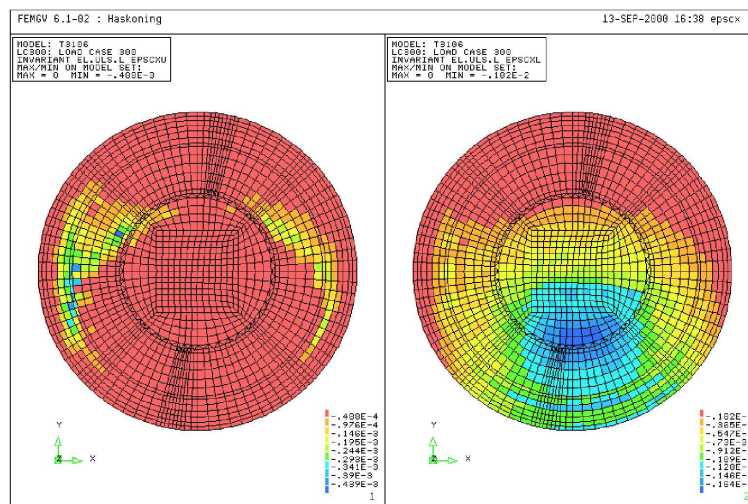
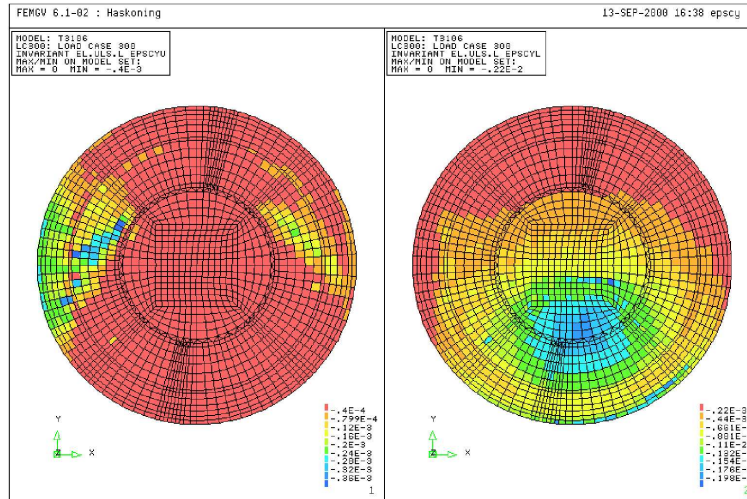


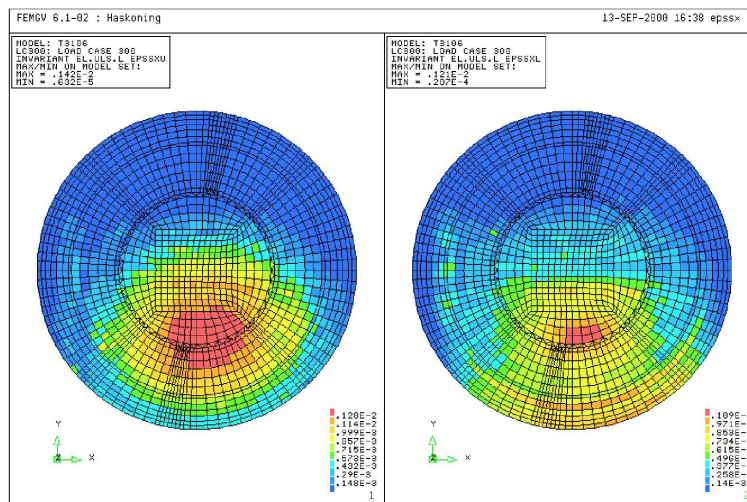
Figure 6.11: Strain of concrete in local  $x$  direction (upper and lower plane)



Figure 6.12: Strain of concrete in local  $y$  direction (upper and lower plane)

### 6.5.2 Maximum Tensile Strain of Reinforcement Steel

The design criterion for reinforcement steel is that the strain under tension is at most 1%. Figure 6.13 shows a contour plot of the reinforcement strain in local  $x$  direction. Figure 6.14 on the following page shows the same strains in the local  $y$  direction. Both figures ignore the stiffness of the reinforcement steel because this has been incorporated in the additional prestress load. See Figures 6.15 and 6.16 for this.

Figure 6.13: Strain of steel in local  $x$  direction (upper and lower plane)

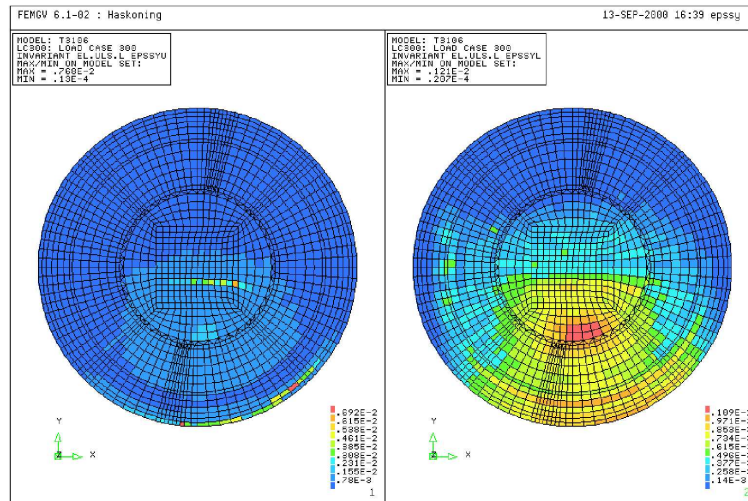


Figure 6.14: Strain of steel in local  $y$  direction (upper and lower plane)

### 6.5.3 Corrective Prestress Load

Figure 6.15 shows the bending moments of the additional prestress load for correction of cracking and nonlinear material behavior. Figure 6.16 on the facing page shows the normal forces of the same prestress load.

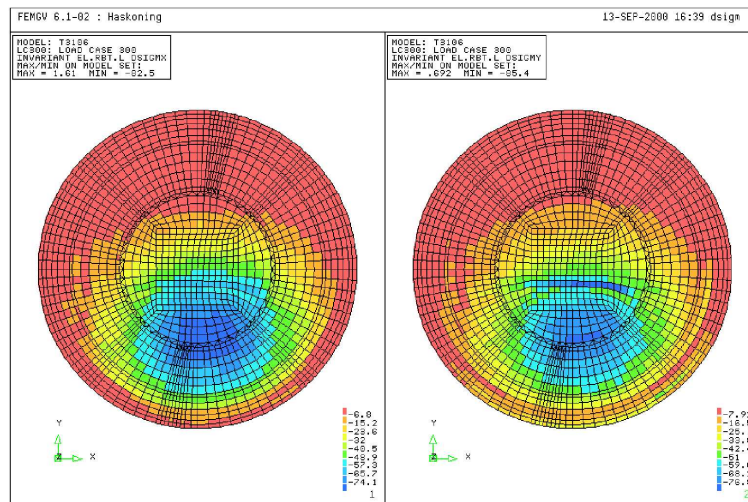


Figure 6.15: Corrective prestress moments ( $m_x$  and  $m_y$ )

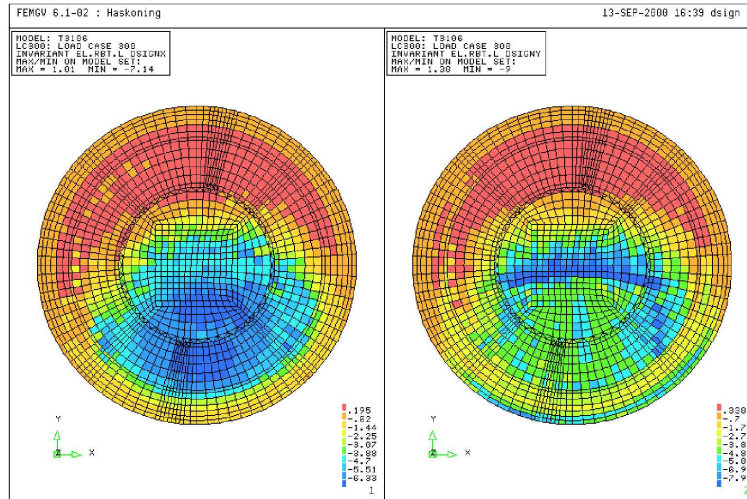


Figure 6.16: Corrective prestress normal forces ( $n_x$  and  $n_y$ )

## 6.6 Conclusions

The presented calculations establish the possibility to omit the sprinkler installation. However, this requires more reinforcement steel to prevent collapse of the domed roof due to fire.

The addition of a fictitious prestress load, to simulate the nonlinear material behavior, enables the iterative determination of the force distribution by means of a quasi-linear elastic analysis. An advantage of the reinforcement examination, built-in within the iteration process, is the possibility to adapt the amount of reinforcement during the iteration process without the necessity to reach a fully converged solution.



## Chapter 7

# Numerical Simulations of Tests on a Segmented Tunnel Lining

A. H. J. M. Vervuurt and F. B. J. Gijsbers

*TNO Building and Construction Research*

C. van der Veen and J. A. den Uijl

*Delft University of Technology, Faculty of Civil Engineering and Geosciences*

### 7.1 Introduction

From 1995 several projects involving shield driven segmented tunnels have been realized in the Netherlands. The first experiences have been gained with the Second Heijenoord Tunnel. In the lining of this tunnel two rings have been instrumented and measurements have been performed with respect to the strain distribution in the lining and the loads acting upon the lining. The results showed that the stresses that develop during the construction phase, are considerably higher than expected. Therefore, contrarily to conventional design, the construction loads can not be neglected.

In the Second Heijenoord Tunnel, the stresses in the construction phase led to damage to the construction. In shield driven tunnel projects carried out after 1995 similar problems were faced. Again damage of the construction was observed during the construction phase. In order to examine the observed aspect in more detail a research project was started by the Delft Cluster. Delft Cluster is a corporation of five research institutes in which, among others, Delft University of Technology and TNO participate. The research program was sponsored by the Delft Cluster, the Dutch Government and two project organizations which are involved in shield driven

tunnel projects (HSL-Zuid and Betuweroute).

The test model consists of a full scale tunnel lining containing three rings with 9.45 m external diameter and a segment thickness of 0.4 m (lining center radius  $r = 4.525$  m).

In the first tests with the full scale equipment, which were performed in 1999, the ring behavior under several loading conditions was emphasized. The results obtained from the evaluation of these tests are described described by van der Vliet et al. [73] yielded the following conclusions:

- For modeling the behavior of the lining correctly, the behavior of the joints between the segments and between the rings is crucial.
- Locally large differences were observed between the measured moments and forces and the numerically predicted values. No reasonable explanation could be given for this.
- From the experiments a significant effect was found of initial gaps in the joints during the construction phase.

The experiences in the first series of tests gave reason to perform a second series of tests with the full scale test facility. The numerical analyses performed on behalf of these additional tests are described in this chapter. The tests focus upon the behavior in the final stage (service loads) as well as in the construction phase. The effect of inaccurate positioning of the segments leading to possible damage of the construction is studied by applying initial gaps in the ring joints.

In §7.3 and §7.4 the numerical analyses carried out with the finite element program DIANA are outlined. Attention is focused upon the model and a comparison of the results with the experimental results. More specifically, attention has been paid to the modeling of the behavior of the segment joints. For this purpose a *user-supplied subroutine* was adopted. In the following section [§ 7.2] the full scale test facility which was used for performing the tests is outlined. A summary of the conclusions and a preview of the final tests is given at the end of the chapter [§ 7.5].

## 7.2 Experiments

### 7.2.1 Set-up

The full scale test facility adopted for the experiments is shown in Figure 7.1 on the next page. It can be seen from the photograph that the three rings are mounted in vertical direction, thereby denying the dead weight of the construction. The effect of the dead weight is significantly less than the effect of the active loads due to the grout and the Tunnel Boring Machine (TBM).

The photograph also shows that the lining is surrounded by a steel reaction frame for balancing the radial loads which are applied by twenty-eight hydraulic actuators per ring. The axial forces representing the loads from the TBM are applied by fourteen actuators placed at the top and connected by a closed frame to the bottom





Figure 7.1: Full-scale test facility in the Stevin Laboratory of Delft University

of the lining. In order to avoid friction at the bottom supports the bottom ring (ring 1) is mounted on Teflon layers. Moreover, the bottom ring is supported by four tangential active supports, whereas the reaction frame is prevented from rotating by four tangential pendulums.

### 7.2.2 Loading

As mentioned previously, radial as well as axial loads can be applied to the test specimen. For each actuator a different load can be applied, with the condition that

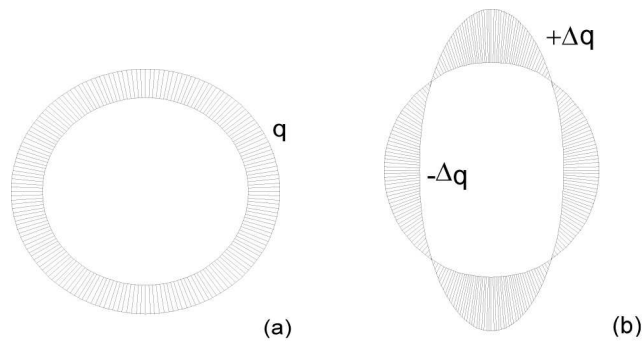


Figure 7.2: Uniform radial loads (a) and ovalization loads (b)

the radial actuators are diametrically coupled to ensure symmetry. The tested load scheme with respect to the radial hydraulic actuators is illustrated in Figure 7.2.

Based on the radial loads shown [Fig. 7.2a-b] the total radial load is given by:

$$p = q - \Delta q \cos 2\theta \quad (7.1)$$

The expected (radial) deformation due to the so-called ovalization load [Fig. 7.2b] is illustrated in Figure 7.3. The shape of the deformed tunnel is characterized by

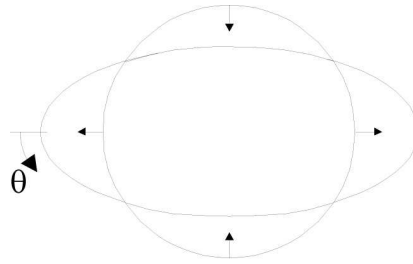


Figure 7.3: Shape of the expected ovalization of the lining

a positive horizontal ovalization and a negative vertical ovalization. The rotational angle  $\theta$  refers to the angle which is used for presenting the results [§ 7.4].

The axial loads in the tests described in this chapter are uniformly distributed along the circumference of the lining. However, in the set-up also a global bending moment may be applied to the lining, simulating the actual load distribution from the TBM.

### 7.2.3 Measurements

During testing the loads are applied in a number of steps. After each load step several measurements are performed that are used for the evaluation and for comparison to the results of the finite element calculations. During testing the following data are recorded:

- Oil pressure of the (axial and radial) hydraulic actuators.
- Radial forces by means of load cells.
- Radial displacements of the lining by means of laser measurements as well as Linear Variable Displacement Transducers (LVDT's).
- Radial displacements of the reaction frame.
- Axial, tangential and diagonal strains at the inner and outer side of the concrete segments. In total 312 strain gauges are used.
- Displacements at the (ring and segment) joints by means of 128 LVDT's.



## 7.3 Numerical Analyses

### 7.3.1 Finite Element Model

As mentioned earlier, two series of tests are performed. A full description of the two series is given by Vervuurt et al. [90, 91]. The results of each test are analyzed and compared to the results of calculations carried out with the finite element program DIANA.

An overview of the outlines of the model is given in Figure 7.4. As can be seen from the figure a shell model was used for modeling the specimen, using eight-node quadrilateral isoparametric curved shell elements (type CQ40S) with  $2 \times 2$  integration points. Because the material behavior of the elements is assumed linear elastic, three

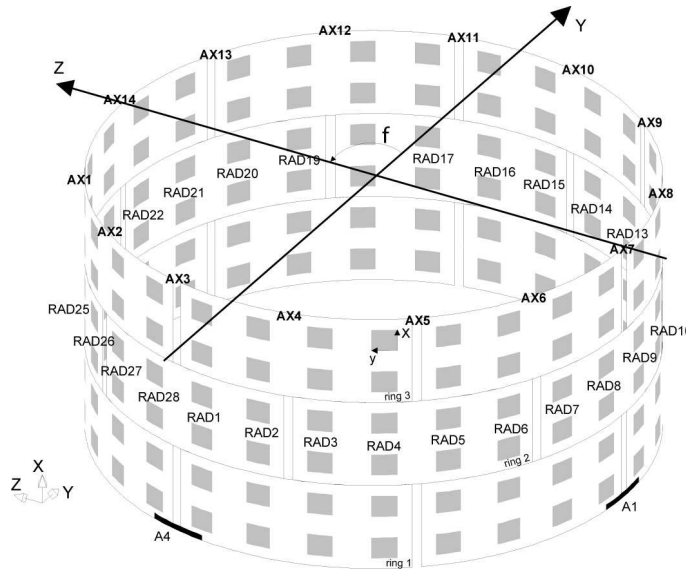
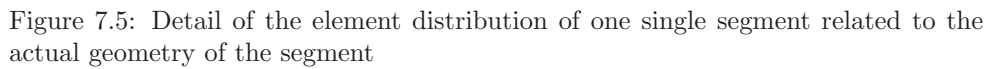


Figure 7.4: Schematic view of the outlines of the finite element model

integration points over the height of the shell elements was adopted. A detail of the element distribution of a single segment is given in Figure 7.5 on the next page. Moreover, the figure gives the cross-sections of the segments, including the positions of the segment and ring joints. In the joints between the segments and one single rings, the segments are connected to each other by concrete to concrete contact. In the ring joints plywood is adopted for transferring the axial loads and shear forces.

The principle for modeling the joint behavior is elucidated in detail in §7.3.2. Moreover, in the following sections the material properties are described as well as the boundary conditions [§ 7.3.3] and the analyzed load combinations [§ 7.3.4].



### 7.3.2.1 Concrete Segments

Table 7.1: MATERIAL PROPERTIES OF THE CONCRETE SEGMENTS

### 7.3.2.2 Joint Behavior

Concrete Mechanics Applications

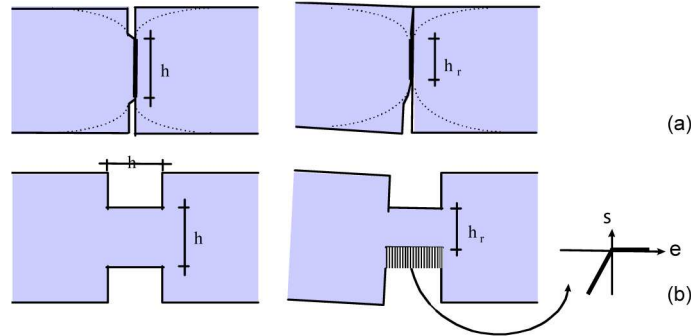


Figure 7.6: Physical joint behavior (a) and principles of modeling the joints (b), according to van Empel [74]

For modeling the joint behavior, a concept based on a model developed by Janßen [41] has been adopted. In the model the reduced (normal and bending) stiffness is obtained by a beam element between the segments. The beam element has a limited length ( $l = h$  [Fig. 7.6b]) and a reduced cross-section. The normal dependent rotational stiffness is incorporated by nonlinear material behavior of the beam ( $f_t = 0$ ).

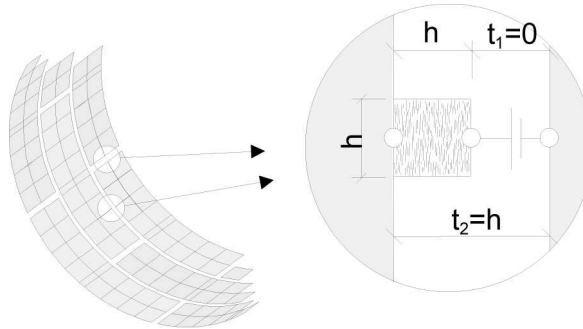


Figure 7.7: Element schematization of the joints

A schematized detail of the joints in the finite element model is given in Figure 7.7. The interface element NI6F, which is placed in series with the nonlinear beam element L7BEN, provides the slip behavior of the joint. The slip behavior also depends on the normal stress in the element.

The rotational joint behavior is characterized by the  $M$ - $N$ - $\kappa$  diagram. Figure 7.8 on the following page illustrates the rotational joint behavior for the geometry adopted in the tests and an arbitrary normal force. In the figure the theoretical solution according to Janßen [41] is compared to the numerical solution when adopting

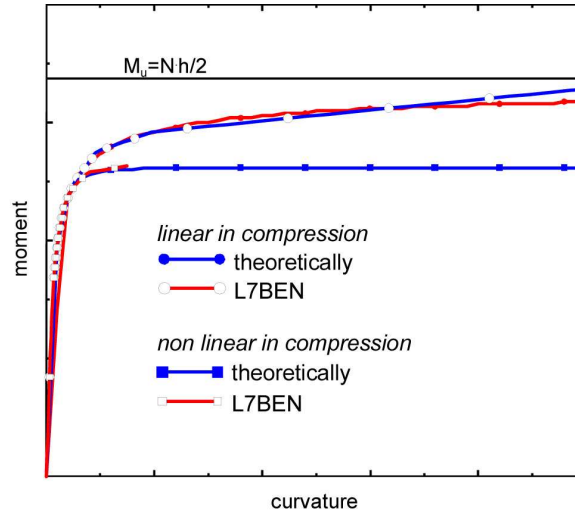


Figure 7.8: Comparison of the numerical and theoretical joint behavior, for both linear and nonlinear compression

L7BEN elements with eleven integration points over the height of one beam. Moreover, in the figure, the situation where concrete under compression behaves linear elastically is addressed as well as the situation where the compressive strength of the concrete is taken into account. In the case of linear elastic compressive behavior the ultimate moment  $M_u$  is determined by the height of the beam:  $M_u = \frac{1}{2} \times N \times h$ , where  $N$  is the normal force and  $h$  is the height of the joint. When nonlinearities with respect to the compressive concrete behavior are taken into account the ultimate moment decreases about 20%.

Moreover, it can be seen from Figure 7.8 that a good prediction is given with the numerical (beam) model. Because of the limited number of integration points (eleven) over the height, a too stiff rotational stiffness is calculated for large curvatures (when all but one interfaces are loaded in tension). In case of nonlinear compressive behavior divergence of the numerical system is obtained for large curvatures, indicating failure of the joint.

When, during construction, the segments are mounted perfectly, the joints are closed from the beginning and no initial gaps are present. Modeling the interface joint behavior for this case can be achieved by using default material models available in DIANA, i.e., Mohr–Coulomb. Nevertheless, in practice initial gaps in the joints have shown to be inevitable, resulting in local peak stresses and possible cracking of the segments.

Due to the relatively small initial gaps, contact elements have proven to be less efficient for modeling the joint behavior in such cases. For that reason, a specially developed material model (*user-supplied subroutine*) has been implemented for the interface elements.

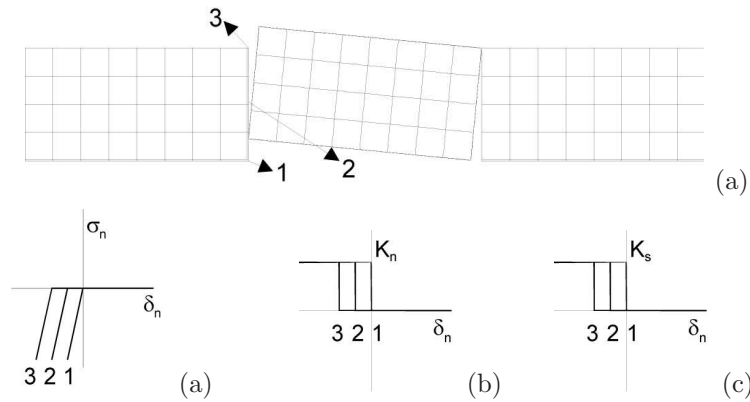


Figure 7.9: Basics of the implemented material model with respect to the joint behavior in case of initial gaps in the joints

Figure 7.9 illustrates the basics of the material model for joints with (and without) initial gaps. The relation between the normal stress and displacement is illustrated for three different positions at an oblique positioned segment [Fig. 7.9a]. Depending on the gap, the normal stiffness in compression is activated at a larger displacement. This is illustrated by the constant stiffness for two regions (tension and compression) [Fig. 7.9b-c]. Because in tension also no shear can be transferred by the joint, the shear stiffness also depends on the normal displacement in the joint as well as on the initial gap distance.

The effect of the key stones on the behavior of the lining has been modeled by assigning specific material properties to one of the segment joints in the lining.

### 7.3.3 Boundary Conditions

At the bottom of the model the lining is supported in vertical direction, circumferentially at the same angles as where the plywood (ring) joints are adopted in the model. Because the loads are symmetrically in the  $YZ$  plane, theoretically no supports are required in this plane. Nevertheless, as explained in §7.2, at four positions at the two axes of symmetry at the bottom of the model (A1 to A4 in Figure 7.4), the tangential deformations are restricted.

### 7.3.4 Performed Analyses

In the first test series the behavior of the construction under service loads has been studied (series A). The behavior due to the radial ovalization load is significantly influenced by the magnitude of the uniform axial and radial loads. These loads determine the behavior of the ring and segment joints respectively. Table 7.2 gives the combinations which refer to a high, medium and low uniform load. In this table the applied load per actuator is given. The areas at which the loads act depend on

Table 7.2: TESTED LOAD COMBINATIONS IN SERIES A

test	axial uniform	radial uniform	ovalization
A1	800	225	20
A2	1600	450	20
A3	2400	675	30

the radius of the lining ( $r = 4.525$  m), the height of the rings ( $h = 1.5$  m) and the numbers of actuators (fourteen in axial direction and per ring twenty-eight in radial direction).

In the second series of tests (series B) attention is paid to the effect of inaccurate positioning of the segments. The finite element model is used to study whether there is a relation between the width of gaps between segments and expected damage. In series B tests are foreseen with initial gaps between the second and third ring in the test specimen. At the moment this document is being prepared, the tests as well as the numerical simulations with respect to these tests are being performed. The results of the second series of tests are presented in [35].

## 7.4 Results

### 7.4.1 Introduction

In this section some results of the finite element analyses with respect to series A of the tests are presented. Moreover, some significant results are compared to the experimental measurements. Because the largest ovalization is observed in test A3, in this section attention is focused mainly upon this particular test. A detailed description of all test results is given in Vervuurt et al. [90].

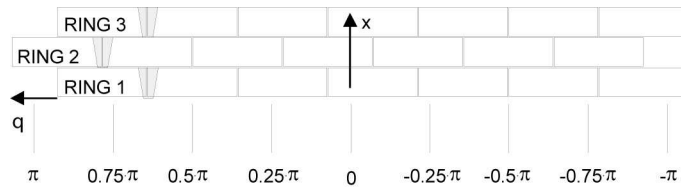


Figure 7.10: Overview of the lining seen from the inside of the set-up and the definition of the defined polar coordinate system

The results in the following sections are presented according to the polar coordinate system as illustrated in Figure 7.10. The view of the lining corresponds to the view of the lining from the inner side of the set-up. In the figure the positions of the key stones are marked by the gray areas and the dashed lines.

### 7.4.2 Deformations

The results with respect to the radial and tangential deformations in test A3 are given in Figure 7.11 ( $\delta_{\text{rad}}$  and  $\delta_{\text{tan}}$  respectively). In the figure the deformation is plotted on the vertical axis. A positive deformation refers to an increase of the diameter. On the horizontal axis the circumferential angle is given. The angle  $\theta = 0$  refers to the axis between the AX10 and AX11 in Figure 7.4. The direction of rotation of the circumferential angle is shown in Figure 7.10 as well. The position of the segments, including the key segments is shown in the inset above the figure. The deformations

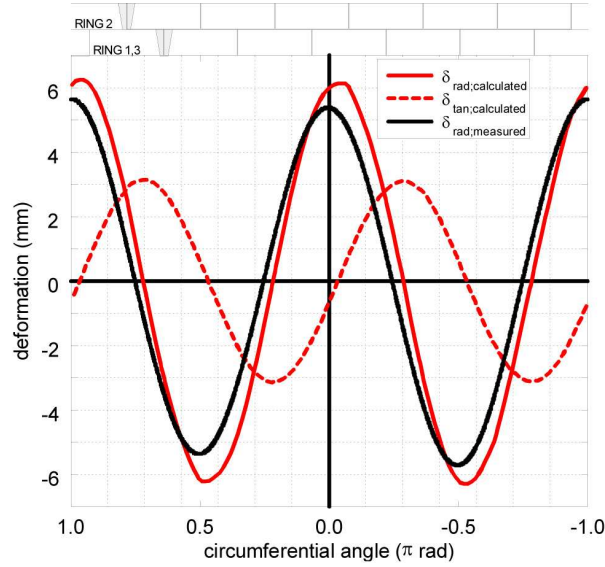


Figure 7.11: Calculated and measured average deformations (radial and tangential) in ring 2

as shown in Figure 7.11 are dominated by the radial ovalization loads [Fig. 7.2b]. Because this load is distributed uniformly over the height of the construction, it may be expected that almost no shear stresses develop in the ring joints, causing marginal differences between the deformations of the different rings. Therefore in Figure 7.11 only the results from the second ring are given. The solid black line indicates the measurements whereas the solid red line refers to the finite element calculations. In the figure, moreover, the calculated tangential displacements  $\delta_{\text{tan}}$  are given by means of the dotted red line.

From the radial deformations it can be seen that the calculated and measured average ovalization differ approximately 10% from each other. This difference is caused by either the assumed segment stiffness ( $E = 40000 \text{ N/mm}^2$ ) or the segment joint stiffness. Since the effect of the segment stiffness is considerably less than the effect of the joint stiffness, it may be expected that the latter effect is dominant for the observed differences. In the calculation a higher segment joint stiffness should be

applied. The strain measurements presented hereafter confirm these findings.

When a monolithic lining (no joints) is considered the maximum ovalization can be calculated from

$$w_{\max} = \frac{1}{9} \frac{\Delta q r^4}{EI} \quad (7.2)$$

where  $\Delta q$  is according to Figure 7.2 on page 93,  $r$  is the radius ( $r = 4.525$  m) and  $EI$  is the tangential bending stiffness of the segments. For a maximum amplitude of the load of 30 kN per actuator it follows that  $\Delta q = 19.7$  kN/m<sup>2</sup> [Table 7.2], and  $w_{\max} = 4.3$  mm. Considering the average measured amplitude in test A3 of 5.5 mm, the presence of the segment joints cause a decrease of the bending stiffness of 22% compared to a monolithic lining.

Next to the radial deformations also the calculated tangential deformations are plotted, see the dashed red line in Figure 7.11. For a monolithic lining the maximum tangential deformation is half of the radial ovalization. Moreover, the results are shifted  $\frac{1}{4}\pi$  rad.

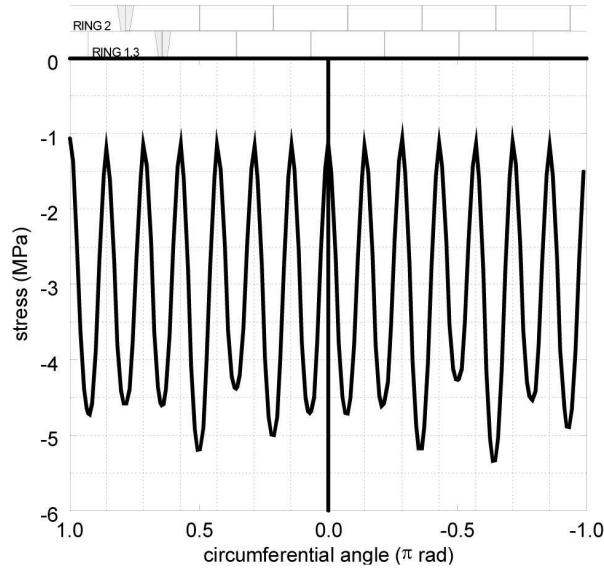


Figure 7.12: Calculated average axial stress distribution in the middle ring of the test specimen (ring 2)

### 7.4.3 Axial Strains and Stresses

In the tests the axial loads due to the TBM forces have been assumed to be uniformly distributed along the circumference of the tunnel (2400 kN per actuator for test A3). This is confirmed by the stresses obtained from the calculations [Fig. 7.12]. Consequently an average axial stress of almost 3 N/mm<sup>2</sup> may be expected.



Moreover, it can be seen from this figure that the stresses are strongly influenced by the concentrated load transfer at the joints. Close to the working lines of the axial loads (at the segment joints) large compressive stresses are observed ( $\approx 5 \text{ N/mm}^2$ ), whereas in between the segment joints (at each quarter of a segment) a rather low compressive stress is found ( $\approx 1 \text{ N/mm}^2$ ).

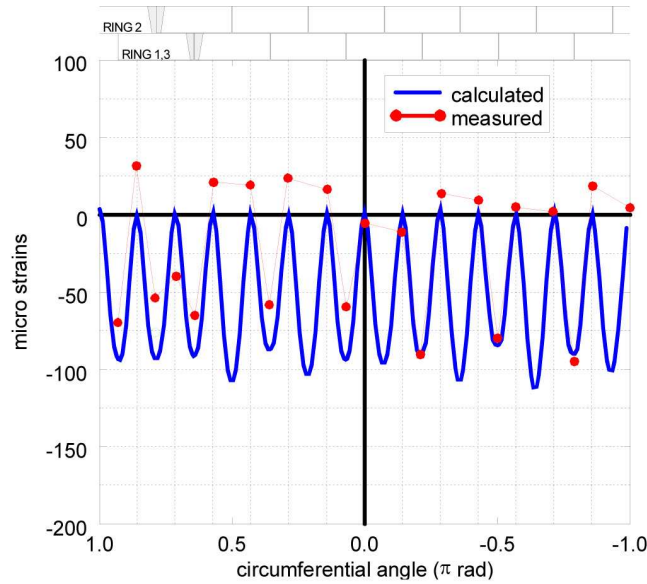


Figure 7.13: Calculated and measured average axial strain distribution in the middle ring of the test specimen (ring 2)

With respect to the axial strains [Fig. 7.13], it is found that the shape of the strain distribution equals the stress distribution (minimum at the joints and maximum at a quarter of each segment). However, the maximum strains calculated are about zero, whereas a maximum stress of  $-1 \text{ N/mm}^2$  is found. The difference is attributed to the influence of lateral contraction due to the radial compressive loads. When the calculations and the experiments are compared it is found that in the calculations the maximum strain is limited to about 0, whereas in the experiments the maximum strain varies between 0 and  $+25 \times 10^{-6}$ .

In Figure 7.14 the difference in axial strain between the inner and the outer side of the segments is shown, indicating local axial bending in the segments (due to the tapered shape of the rings). In the figure the results of the calculations are indicated by the solid lines whereas the measurements are given by dot markers in the same color connected by thin lines.

The results in Figure 7.14 show that the measurements and the calculations correspond both qualitatively and quantitatively. The influence of the segment joints is shown by the large differences between the neighboring rings. Because both the axial and the radial loads are applied symmetrically, it is expected that the observed

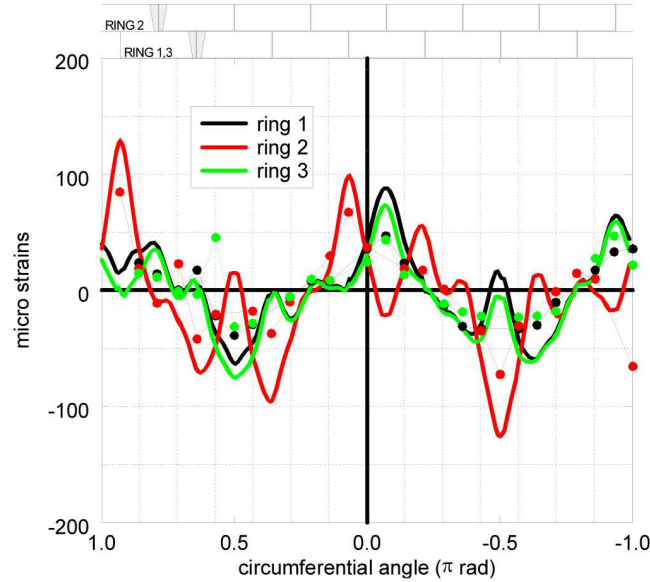


Figure 7.14: Axial strain results: difference between the inside and the outside of the segments

differences are caused by contraction effects due to the radial loads. In the calculations the differences are larger than in the experiments, indicating a too low assumed stiffness of the segment joints.

#### 7.4.4 Tangential Strains and Bending Moments

In radial direction a uniform load is applied as well as an ovalization load. In a monolithic lining a uniform radial load causes a uniform tangential stress, which can be calculated from

$$\sigma_{\text{tan}} = q \frac{r}{t} \quad (7.3)$$

where  $q$  is according to Figure 7.2a,  $r$  is the radius and  $t$  is the thickness of the segments. For tests A3, with  $q = 443 \text{ kN/m}^2$  [Table 7.2], this leads to an expected uniform stress of  $5 \text{ N/mm}^2$ . The finite element calculation yields the same conclusions, see Vervuurt et al. [92]. Similar to the axial stress and strain distribution as shown in Figure 7.12 and Figure 7.13 respectively, a considerable effect of the concentrated load introduction is found. In Vervuurt et al. [90] it is shown that the shape of the distribution is opposite to the distribution of the mean axial stress. This corresponds to the effect of lateral contraction in the segments.

The tangential bending moments are characterized by the tangential curvature in the segments. When the curvature is defined as  $\Delta\varepsilon_{\text{tan}}/t$  [Fig. 7.15], it can be seen that there are quite some differences found in the curvature between each neighboring

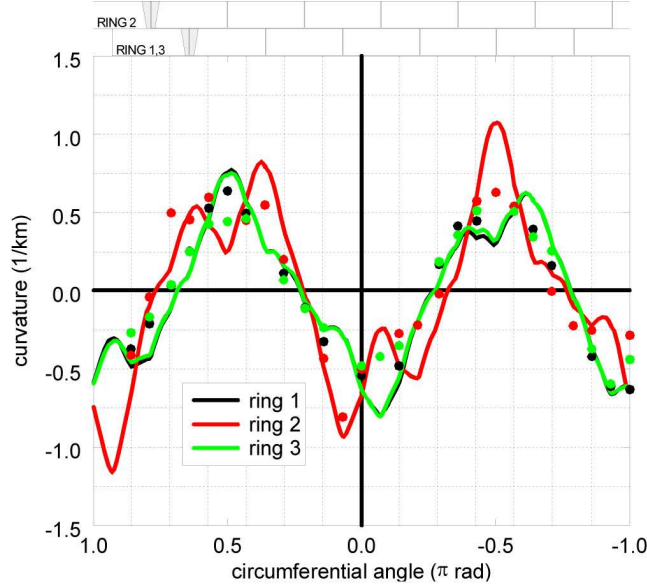


Figure 7.15: Measured and calculated tangential curvature in the segments ( $\Delta\varepsilon_{\text{tan}}/t$ )

ring. In the experiments the same tendency is found, however, less pronounced.

The differences between the measurements and the calculations are mainly attributed to the (locally) low bending stiffness of the segment (and ring) joints. For infinite stiffness of the segment joints a uniform behavior may be expected, whereas for zero stiffness  $\Delta\varepsilon_{\text{tan}}$  yields to zero. Consequently, the large differences between the subsequent rings in the calculations indicate that the bending stiffness of the segment joints is assumed too low. This corresponds to the findings considering the axial strains [Fig. 7.14].

Because the tangential curvature and the bending moment are related linearly to each other, the bending moment distribution is expected to be comparable to Figure 7.15. In Figure 7.16 the ring moments are plotted. A contour plot of the calculated bending moments is given in Figure 7.17.

The blue line in Figure 7.16 indicates the average ring moment. Because the average moment only depends on the externally applied radial loads, the distribution should be similar to the moment distribution in a monolithic lining. For a monolithic lining the moment distribution can be calculated from

$$m = \frac{1}{3} \Delta q r^2 \cos 2\theta \quad (7.4)$$

For test A3, with  $q = 19.7 \text{ kN/m}^2$  [Table 7.2], the maximum moment equals 202 kNm per ring, which corresponds to the finite element calculations.

The effect of the low bending stiffness of the segment joints is that the moment in that particular ring decreases, whereas the moment in the neighboring rings increases.

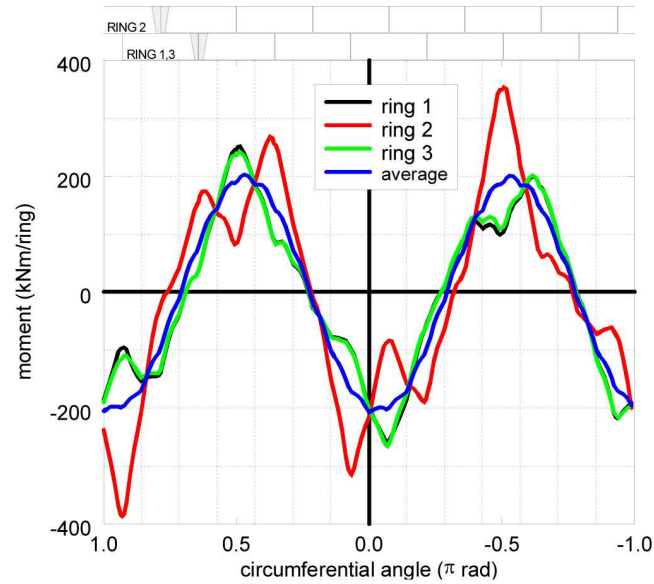


Figure 7.16: Calculated bending moments in the segments

Therefore a considerable increase of the bending moment in ring 2 is found in the case of a segment joint in ring 1 and 3, for instance for  $\theta = -\frac{1}{2}\pi$  rad. When, on the other hand, a segment joint is present in ring 2, for instance for  $\theta = +\frac{1}{2}\pi$  rad, the bending moment in ring 1 and 3 increases, however, substantially less [Fig. 7.17].

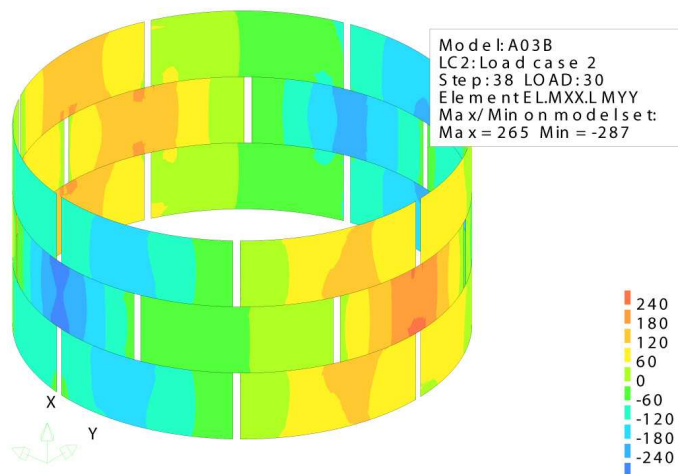


Figure 7.17: Calculated bending moments (contours)

### 7.4.5 Principal Strains

Because in series B tests are foreseen with initial gaps at the ring joint between the second and third ring of the test specimen, additional strain measurements have been performed in the third ring. By placing strain gauges at  $45^\circ$  with the tangential and axial strain gauges, the principal strains can be calculated from the results of one rosette containing three strain gauges.

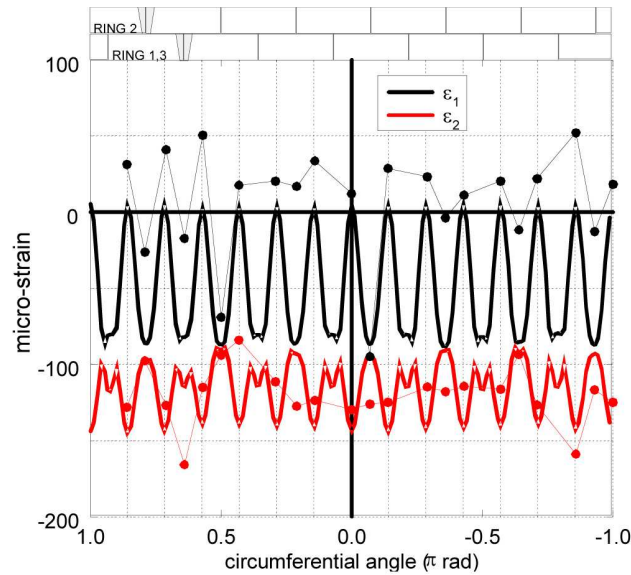


Figure 7.18: Measured and calculated average principal strains in ring 3

The results with respect to the calculated principal strains are given in Figure 7.18. It can be seen that the experiments and calculations correspond well, however, the maximum principal strain in the calculations is generally smaller than in the experiments. The principal strains correspond approximately to the axial and tangential strains ( $\varepsilon_1$  and  $\varepsilon_2$  respectively).

## 7.5 Conclusions

Finite element calculations with respect to full scale experiments of segmented shield driven tunnels have shown that the lining behavior can be predicted quite well. Differences are mainly caused by the assumed stiffness of the segment joints. The stiffness of the ring joints is of less influence in the tests carried out. Moreover, the study has shown that the comparison of the results should be carried out at the level of strains. Stresses can not be extracted directly from the strain measurements in the tests. Due to contraction effects the stress distribution differs significantly from the strain distribution.

In order to study the effect of inaccuracies in the positioning of the segments a second series of tests has been performed. In these tests initial gaps are prescribed between the second and the third ring. The results of the numerical analyses with respect to these tests have been presented at the “3rd DIANA World Conference” [35] and are also described in [91].

## Chapter 8

# Nonlinear Behavior of Joints in Bored Tunnels

W. H. N. C. van Empel and F. J. Kaalberg  
*North/Southline Consultants & Witteveen+Bos*

**Abstract.** The two bored tunnels that will be part of the North–South Metroline under the city center of Amsterdam are characterized by an innovative design of radial and circular joints. This innovative joint design calls for an innovative and advanced numerical model of the joints and the tunnel tube as a whole. While developing the three-dimensional phased model of the tunnel lining and its components, the vast array of modeling facilities offered by DIANA was optimally used. An important aspect of the development process consists of the validation regarding the behavior of the numerical components of the tunnel structure

## 8.1 Introduction

### 8.1.1 The Amsterdam North–South Metroline

Under the historic city center of Amsterdam two bored tunnels will be constructed that are part of the North–South metroline [Fig. 8.1]. These tunnels, bored with separate tunnel boring machines (TBM's), are approximately 3.6 km long and follow a route below existing streets. The bored tunnels pass through strongly varying soil layers, ranging in nature from stiff sand to soft Eem-clay. Along the proposed route of the bored tunnels, the TBM's have to be driven along narrow curvatures as low as 190 meter. The poor soil conditions at some stretches along the proposed route, combined with the locally narrow curvatures and an urban environment that is very sensitive to settlement, make the Amsterdam North–Southline a challenging project [42].

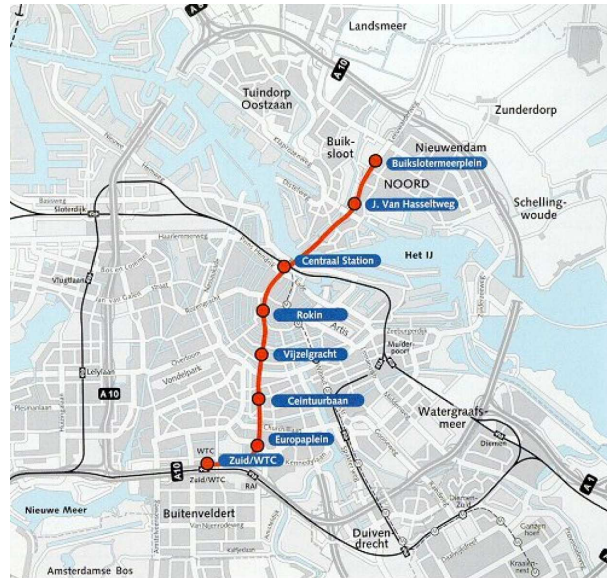


Figure 8.1: Proposed route of the North-Southline

### 8.1.2 Innovative Design of the Bored Tunnels

Because of the project specific adverse conditions encountered along the proposed route it was acknowledged in an early stage that enhancement and optimization of conventional design concepts of bored tunnels was necessary in order to minimize and control the risks regarding the structural performance of the bored tunnels during the construction phase and the serviceability phase. After thorough investigation of the theoretical and practical performance of conventional lining concepts it was concluded that conventional lining concepts in practice often give rise to structural failure in the sense of crack formation and even breaking off of ring couplers. Given the sensitive and adverse environment in which the tunnels are to be constructed a lining concept has been developed which ensures a conditional behavior of the lining, which can be managed by design and design calculations.

The innovative lining concept is characterized by a centrally placed elastomer profile in both the radial joints and the circular joints through which the normal forces at the joint are mainly transferred [Fig.8.2]. The elastomer profile not only has a structural function but also ensures a watertight joint. At several locations at the joints elastic plates are applied in order to transfer bending moments and shear forces at the joint.



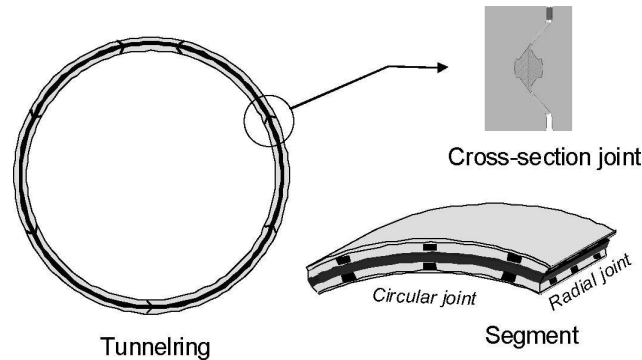


Figure 8.2: Lining concept

### 8.1.3 Numerical Modeling of the Behavior of the Tunnel Lining and its Components

Creating a lining concept that results in a defined structural behavior of the lining and its components is the first step in the direction managing and minimizing the risks regarding the structural performance of tunnel lining.

The second important step comprises realistic and state of the art numerical modeling of the behavior of the tunnel lining, its segments and its joints. Because of the fact that the detailed design (for example the stiffness of the joint plates) of the tunnel lining and its components have to be determined in the same phase where the models are applied. The models not only serve a purely predictive goal but are also used to determine the optimal constellation of design parameters, which gives the design and calculation process an additional dimension.

This is a major difference with standard tunnel design practice where (numerical) models are mostly used to predict the behavior of a lining according to a given conventional concept and detailed design, and therefore given, but mainly assumed mechanical parameters of the tunnel lining like joint stiffnesses. In the conventional design practice the behavior of the tunnel lining solely depends on boundary conditions like soil pressures acting on the lining. In the conventional situation (numerical) models are therefore only used to determine the (given) loads on, or force in the lining components in order to determine the strength of the components needed to withstand these loads and forces.

Because of the fact that the stiffnesses of the lining components in the North-South line lining concept are open and designable parameters, the distribution of the forces among these components can be manipulated by design which makes the design and calculation process regarding the North-South line lining concept differ from a conventional design and calculation process applied in bored tunnel engineering.

The fact that the North-South line lining concept has not been applied in a bored tunnel project before, and therefore no empirical data is available, calls for sophisticated and extensive modeling of all relevant mechanisms combined with an extensive test program, which also is an important aspect of the design process.

## 8.2 Conceptual Numerical Model of the Bored Tunnel

### 8.2.1 General

The behavior of a bored tunnel, consisting of several segments, is strongly determined by the interaction of these segments at the circular and radial joints. In order to predict the global behavior of the tunnel lining the individual behavior of these circular and radial joints has to be modeled in a realistic and accurate way. This joint behavior is determined by the geometrical layout of the joint and the mechanical properties of the joint components (elastomer profile and elastic plates). Globally the external loads in the tunnel lining will be distributed among circular and radial joints according to their relative stiffness.

### 8.2.2 Designing the Numerical Model

Globally the tunnel lining can be regarded as a thin walled structure. Modeling of the segments by means of curved shell elements is therefore appropriate. In order to model the joint a spring system is used [Fig.8.3a]. The centrally placed profile

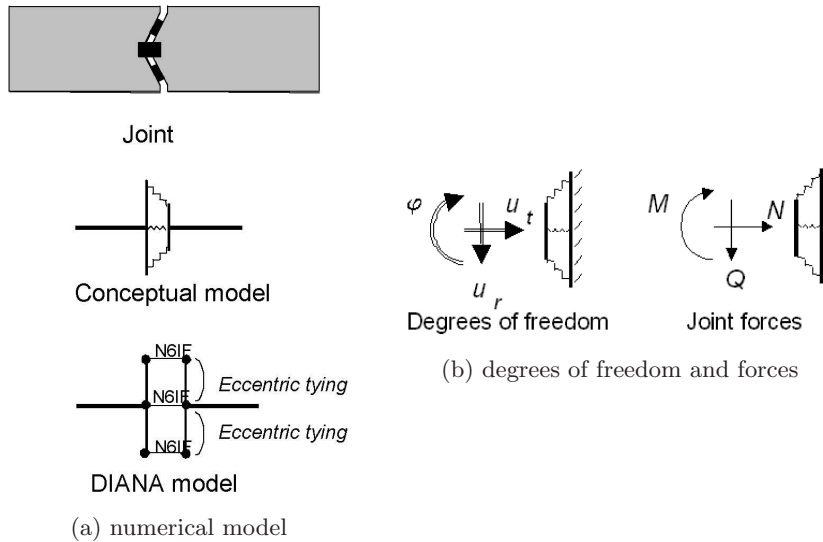


Figure 8.3: Model of a joint

is modeled by means of an N6IF interface element, oriented along the normal axis of the joint. The plates in the joint are modeled by eccentrically placed N6IF interface elements with an orientation conform the inclination of the actual plates. The two nodes that are part of the N6IF element are both eccentrically tied to the respective nodes of the shell element.

The joint and its model have three degrees of freedom corresponding to three types of loads, acting on the joint [Fig. 8.3b]. Degrees of freedom and forces are related by a stiffness matrix according to

$$\begin{Bmatrix} M \\ N \\ Q \end{Bmatrix} = \begin{bmatrix} k_{11} & k_{12} & k_{13} \\ k_{21} & k_{22} & k_{23} \\ k_{31} & k_{32} & k_{33} \end{bmatrix} \cdot \begin{Bmatrix} \phi \\ u_t \\ u_r \end{Bmatrix} \quad (8.1)$$

If the joint would be modeled with separate springs for transfer of bending moment, normal force and shear force, then a model as shown in Figure 8.4a would arise. In

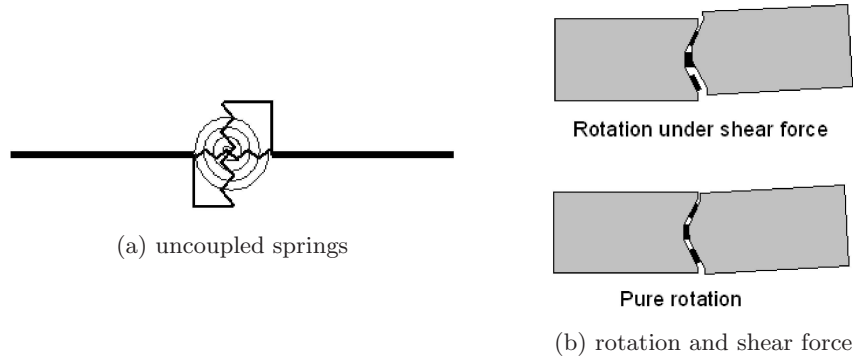


Figure 8.4: Joint model with springs

case of this model, the relationship between degrees of freedom and forces in the joint would be

$$\begin{Bmatrix} M \\ N \\ Q \end{Bmatrix} = \begin{bmatrix} k_{11} & 0 & 0 \\ 0 & k_{22} & 0 \\ 0 & 0 & k_{33} \end{bmatrix} \cdot \begin{Bmatrix} \phi \\ u_t \\ u_r \end{Bmatrix} \quad (8.2)$$

A joint model as shown in Figure 8.4a would not take into account any interaction between the three different degrees of freedom of the joint. In reality this interaction exists, which is illustrated in Figure 8.4b. If the joint is subjected to a combined shear force and bending moment, the rotation will differ from the case where the joint is purely subjected to a bending moment. Based on the considerations above, a joint model conform Figure 8.3 on the preceding page is applied, instead of the model shown in Figure 8.4a.

In Figure 8.5 on the following page the circular joint and radial joint are shown in a three-dimensional perspective. The centrally placed elastomer profile at the joint is modeled by means of a row of N6IF interface elements because no three-dimensional line interface elements are offered by DIANA at this moment. By means of lumping the individual stiffness of each interface element is assigned in such a way that the row of individual springs will act as if it were a continuous line interface element.

At the locations of the joint plates the eccentrically placed N6IF elements are applied and oriented according to the individual orientation of the plates. The nodes

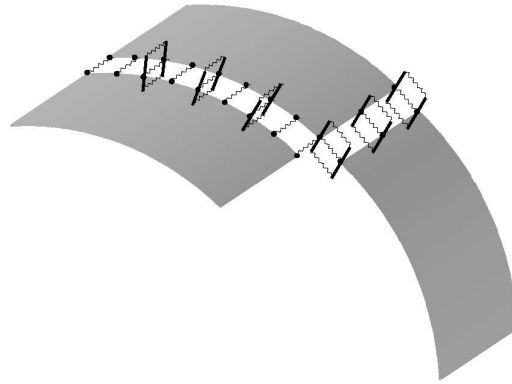


Figure 8.5: Three-dimensional view of joint model

of these interface elements are eccentrically tied to the corresponding nodes of the shell elements representing the segments.

### 8.3 Validation of the Numerical Model

The joint model to be applied in the macro model of the tunnel rings is to be validated in order to assure a correct prediction of the response of the tunnel lining and its components under the governing boundary conditions [Fig.8.6]. Also the behavior

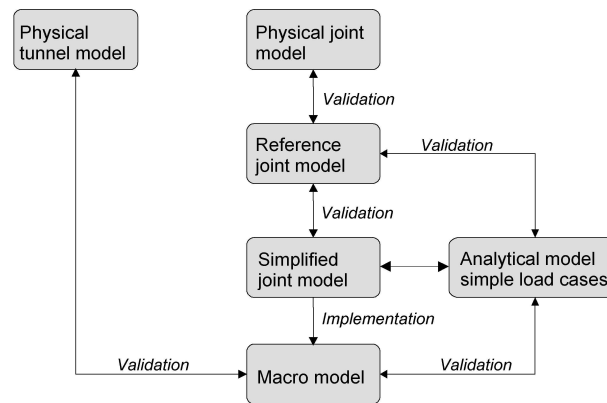


Figure 8.6: Validation procedure

of the macro model is to be validated by means of a number of benchmark studies based on simple load cases leading to a response of the tunnel lining that can be predicted analytically.

In order to validate the simplified spring joint model applied in the joints, this simplified model is to be validated based on a higher order reference model (two-

dimensional continuum model) which will be discussed later on. The behavior of the reference model can be validated on its turn by means of a full scale physical model of the joint to be tested in a laboratory. In the ultimate case the behavior of the macro model can be validated based on a full scale physical model consisting of several rings.

### 8.3.1 Simplified Spring Model – 2D Joint

In order to validate the simplified spring model to be applied in the macro model of the tunnel lining, a two-dimensional continuum model has been used as a reference [Fig.8.7]. Compared to the reference model the simplified spring model has

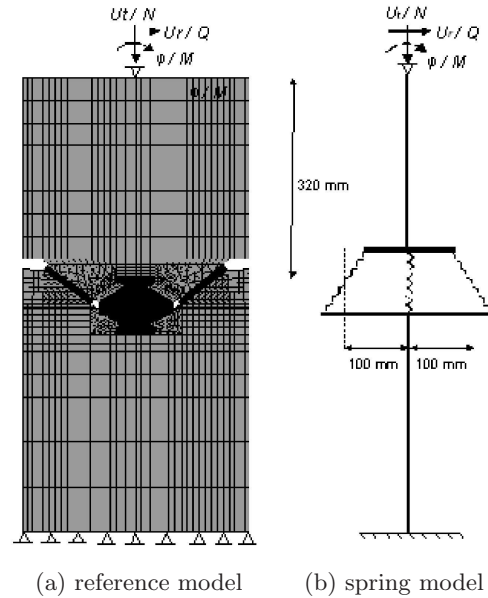


Figure 8.7: Validation of the spring model

one limitation. The springs in the simplified model do not have dimensions and represent the net behavior of the corresponding plate or elastomer profile. In order to assess the implications of this simplification several benchmark calculations have been performed. During one calculation the normal compression of the joint was set at 10 mm and a transverse offset of 2 mm was applied. Under these conditions and realistic stiffnesses of the elastomer profile and joint plates the rotation  $\phi$  of the joint was varied between  $-0.030$  rad and  $+0.030$  rad and the  $M-\phi$ ,  $N-\phi$ , and  $Q-\phi$  relationships were determined for both the reference model and the simplified spring model. In Figure 8.8 on the next page the  $M-\phi$  diagram is shown as an example.

This particular benchmark calculation, and also the other calculations showed an outstanding resemblance between the behavior of the reference model and the simplified spring model. It can therefore be concluded that the simplified spring

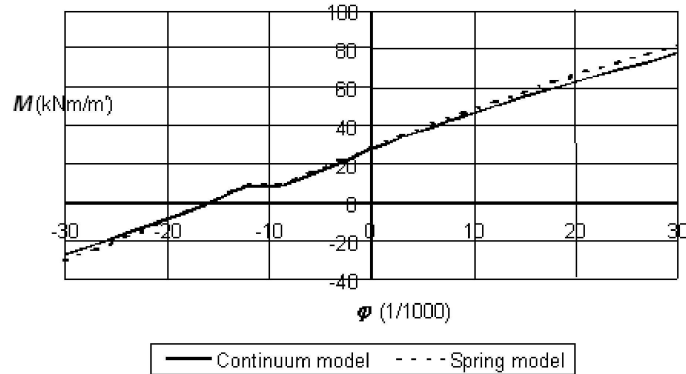


Figure 8.8: Rotational behavior of reference and spring model

model is able to behave in a way that is equal to the behavior of a more complex two-dimensional continuum model.

### 8.3.2 Macro Model of the Lining – Simple Load Cases

By applying a simple load case with regard to the macro model of the lining, and predicting the distributions of stresses and forces in the circular and radial joints, the global behavior of the macro model and the integral three-dimensional joint behavior can be validated. In this chapter the validation of the numerically predicted behavior of the circular joint will be discussed.

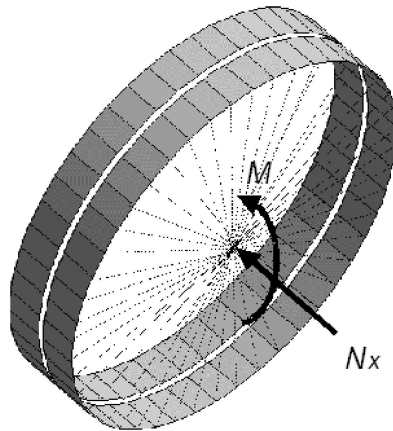


Figure 8.9: Macro model, axially loaded

The model used consisted of two tunnel rings, loaded by a resulting normal force acting in the direction of the tunnel axis [Fig. 8.9]. In order to apply these global

loads a master node was used. The nodes of the shell elements along the tunnel perimeter were eccentrically tied to this master node. In this way the global loads were automatically distributed along the tunnel perimeter on a proper way.

For a given set of material properties of elastomer profile and joint plates the distribution of the normal force along the elastomer profile in the the circular joint was determined. These material properties were chosen in such a way that the normal load was partially transferred by the joint plates. In Figure 8.10 the distribution of

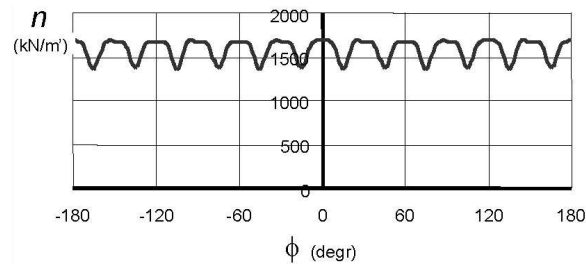


Figure 8.10: Distributed normal force in elastomer profile

the normal distributed force along the elastomer profile is shown. The diagram shows that at the locations of the plates the normal load is partially taken over by the joint plates, thus leading to a local reduction of the distributed force in the elastomer profile. Figure 8.11 shows how the global axial force is transferred in the circular joint.

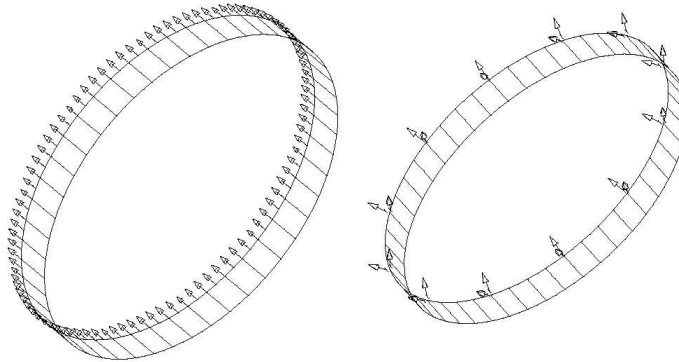


Figure 8.11: Vector representation of forces in circular joints

Qualitative and quantitative comparison of the output of the numerical model with the analytical predictions showed that the model predicts the global behavior of the lining in a proper way.

### 8.3.3 Simplified Spring Model – Results of Physical Model

After determination of the optimal constellation of design parameters based on evaluation of the output of the applied (numerical) models [§ 8.4], the abstract numerical elements and the accordingly desired behavior have to be translated into physical elements. For example, the desired stiffness of the plates (interface elements) in radial and circular joints are deduced from the model results, resulting in functional specification for the real physical plates to be produced. Once these plates have been produced, testing of the characteristics of these plates is to be performed in a laboratory.

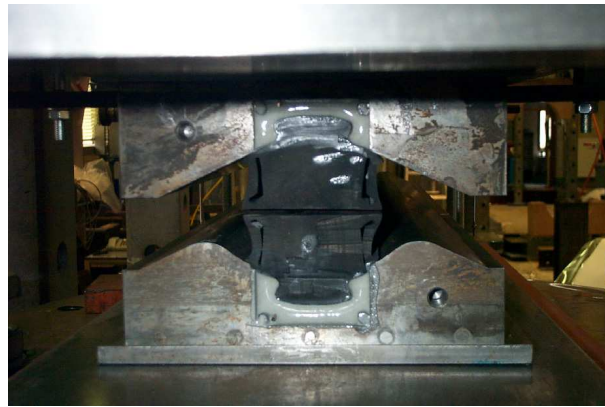


Figure 8.12: Elastomer profile placed in steel cavity

At this moment a number of tests has been performed on the elastomer profile in order to determine the normal characteristic of this profile. Figure 8.12 shows the profile as it was tested in a laboratory. Figure 8.13 shows the characteristic of the elastomer profile that was measured. This characteristic can be approximated with

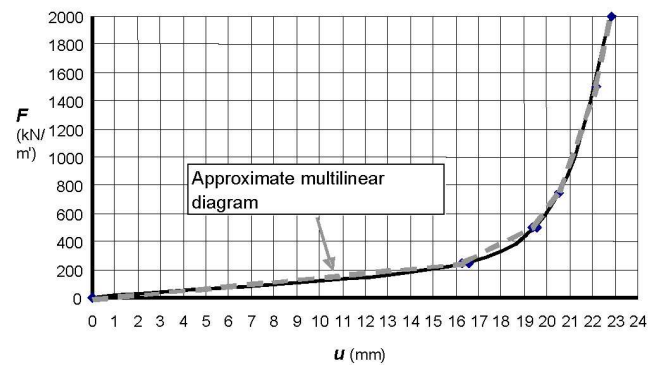


Figure 8.13: Measured normal force characteristic elastomer profile and accordingly approximated multi-linear diagram



a multi-linear diagram that serves as material input for the used interface element. The same procedure can, and will be performed in the nearby future for the elastic plates, thus resulting in input for interface elements representing these plates.

Once the properties of elastomer profile and elastic plates are known, the constitutive input for the joint model is present. The final step lies in validation of the numerically predicted kinematics of the joint as a whole, based on a 1:1 test specimen of the joint [Fig. 8.14]. Once the behavior of the numerical joint model is validated

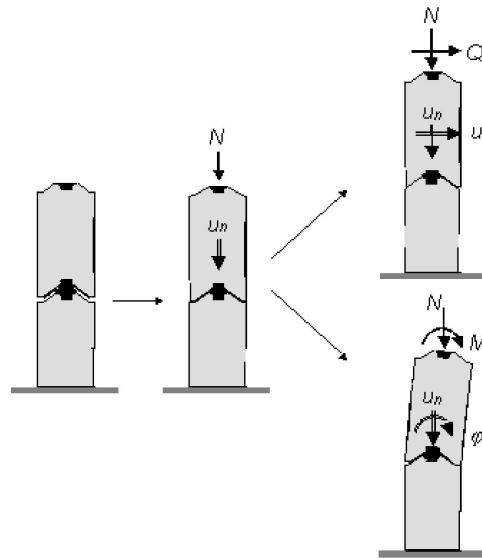


Figure 8.14: Specimen as to be tested in a laboratory

based on the physical joint model, one can be sure that the behavior of the joints in the numerical macro model is accurately simulated.

## 8.4 Application of the Model in Practice

### 8.4.1 Modeling of the Construction Phase

The construction phase during which the bored tunnel is being constructed by erecting individual segments and forming a tunnel ring is commonly recognized as a phase to be more critical than the serviceability phase of the tunnel lining. During the construction phase [Fig. 8.15], the segments are loaded by strongly varying jack forces, applied by the TBM thrust jacks. Once a tunnel ring has been completed, the TBM will continue boring and gradually the tunnel ring will leave the shelter of the TBM-shield and will be subjected to pressures, present in the grout suspension injected in the tail void.

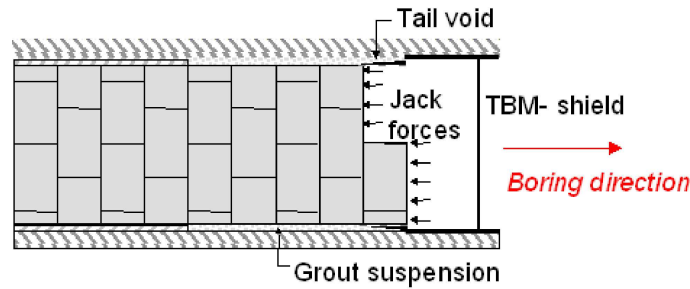


Figure 8.15: Construction of a shield driven tunnel

The complex succession of strongly varying load cases calls for a sophisticated phased three-dimensional model, commonly known as a *four-dimensional* model [Fig. 8.16]. At one side of the model the thrust jacks are modeled. Also the con-

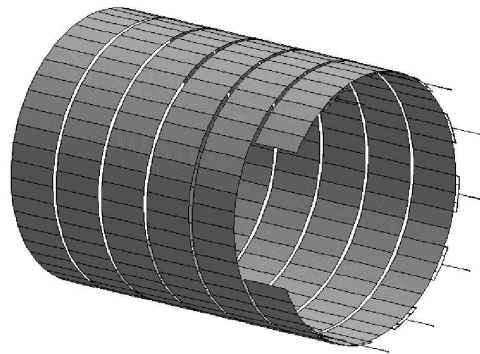


Figure 8.16: Phased three-dimensional numerical model of the tunnel lining

ical keystone has been modeled. The gradual construction of the tunnel lining can be modeled by means of a ring-by-ring or even segment-by-segment phasing of the calculation.

#### 8.4.2 Modeling of the Serviceability Phase

During the serviceability phase no significant changes in the boundary conditions regarding the tunnel occur within a limited distance along the tunnel axis. Therefore a semi three-dimensional model is used, consisting of two adjacent tunnel rings (shell elements) and a continuum model of the surrounding layered soil [Fig. 8.17]. The soil has been modeled with a Modified Mohr–Coulomb material model. Before application this material model has been successfully validated based on laboratory results of specimen of the soil layers encountered.

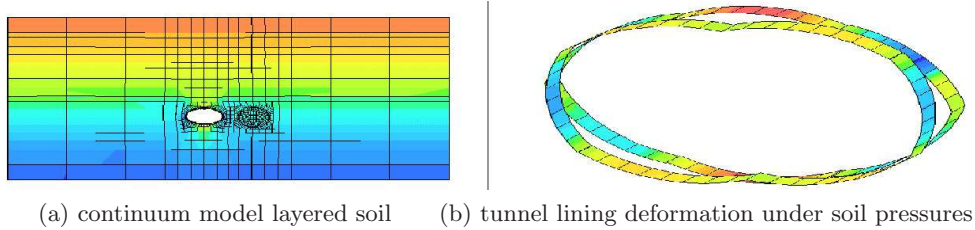


Figure 8.17: Soil model

### 8.4.3 Parameter Study

Besides performing a parameter study in order to determine the most critical configuration of conditions or parameters which can't be manipulated by design (boundary conditions like stiffnesses of soil layers, external loads etc.) a separate parameter study is performed in order to determine the optimal individual stiffness of the elastic plates in radial and circular joints. The design, and therefore the mechanical properties of these plates are not determined in advance but are to be determined based on a prediction of the behavior of the lining and its components as a function of these mechanical properties.

Once the impact of the mechanical properties of the elastic joint plates on the response of the tunnel lining and its components is quantified by means of a parameter study, the optimal joint plate design can be selected. This procedure is illustrated by a

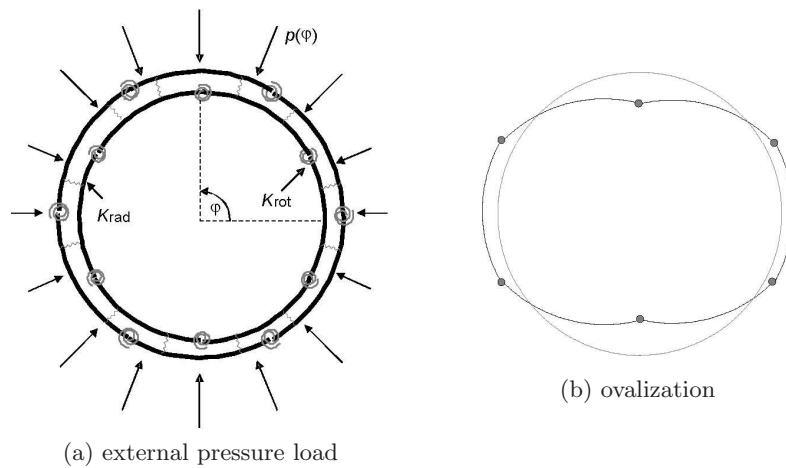


Figure 8.18: Model of tunnel ring

case regarding two tunnel rings, loaded by an external pressure distribution  $p(\phi)$  (soil-grout pressures) [Fig. 8.18a]. The behavior of the tunnel as coupled rings is commonly referred to as ring action which results in an oval deformation, or ovalization, of the tunnel rings [Fig. 8.18b].

In the case of ring action the radial joints globally act as rotational springs with an equivalent rotational stiffness depending on the stiffness of the plates applied and their eccentricity. The plates in the circular joint will merely act as translational springs with an equivalent radial stiffness depending on the stiffness of the plates applied.

For a given distribution of the external pressure along the perimeter of the tunnel rings and a selected combination of rotational stiffness of the radial joints and a stiffness of the plates in the circular joints, a calculation can be performed and the relevant loads on, and the deformation of the lining components determined. As an illustration a qualitative distribution of bending moments in both tunnel rings is shown in Figure 8.19. Depending on the ratio of rotational stiffness of the radial

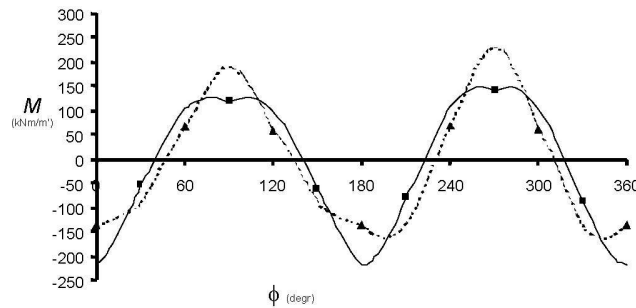


Figure 8.19: Illustrative distribution of bending moments in two tunnel rings

joints and radial stiffness of the plates in the circular joints, the external load will be distributed among radial and circular joints. The stiffer the plates in radial joints are designed relative to the plates in the circular joints, the higher the bending moments acting on the radial joints will become and the lower the forces acting on the plates in the circular joints will become. The loads acting on radial and circular joints can therefore be manipulated by manipulating the relative stiffness of these joints.

As an illustration, the maximum force acting on the plates in the circular joint is qualitatively shown as a function of the radial stiffness  $K_{rad}$  of the plates in the circular joint and the tangential (along ring perimeter) stiffness  $K_{tan}$  of the plates in the radial joints [Fig. 8.20]. It shows that the maximum load on the plates in the circular joint decreases with increasing  $K_{rad}/K_{tan}$  ratio.

The maximum load on the plates in the circular joint is only one design parameter to be taken into account. Other design parameters like deformation of the tunnel ring, forces in the segments and loads on the plates in the radial joint also have to be taken into account. The optimal  $K_{rad}/K_{tan}$  ratio is that ratio which leads to to minimal reinforcement needed for the transfer of internal forces in the tunnel lining and its components combined with an acceptably small deformation or ovalization of the lining.

Besides the ring action mechanism discussed in this chapter, other mechanisms also play a role of importance [Fig. 8.21]. Each mechanism results in a range of acceptable or preferred stiffnesses regarding the elastic plates in the radial and circular

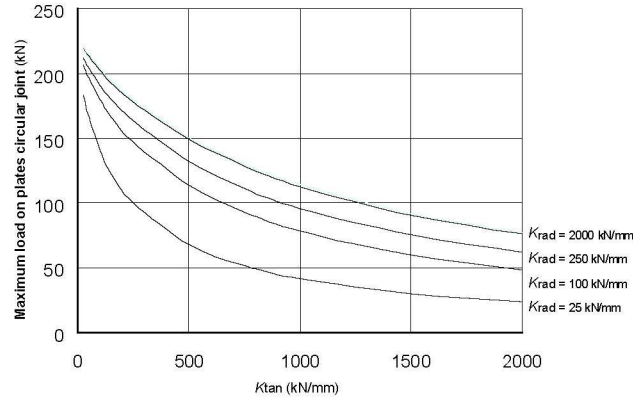


Figure 8.20: Maximum load on plates in circular joint as function of  $K_{tan}$  for four values of  $K_{rad}$

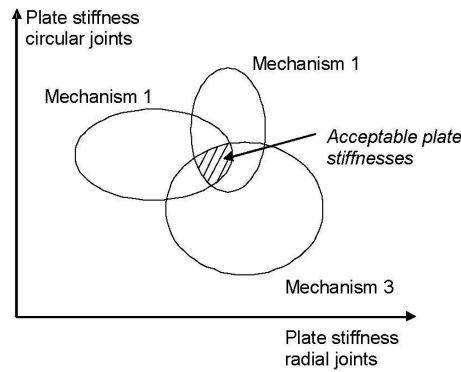


Figure 8.21: Determination of range of acceptable plate stiffnesses

joints. Integral evaluation of all ranging will eventually result in one range of plate stiffnesses which will meet all design criteria.

## 8.5 Detailed Modeling of the Elastomer Profile

### 8.5.1 General

In the preceding sections the implementation of the behavior of elastomer profile and elastic plates in the joint- and tunnel ring model has been discussed. The input for the material models (multi-linear characteristics) is eventually obtained from laboratory test results. Before production and successive testing of elastomer profile and elastic plates these components have to be designed based on the defined specifications.

Practice shows that the production and testing of custom made products, like the

needed joint components, is costly and time consuming. Therefore DIANA also has been used to predict the behavior of the elastomer profile and elastic plates. In this section the modeling of the elastomer profile will be briefly discussed.

### 8.5.2 Modeling of the Elastomer Profile

DIANA offers a number of hyperelastic material models, which can be used to model rubber-like materials. In order to model the behavior of the elastomer profile a Mooney–Rivlin material model has been used which makes use of two material constants  $C_1$  and  $C_2$  and a bulk modulus. Because of the fact that elastomer is almost incompressible, the bulk modulus was set to a high value. The material constants  $C_1$  and  $C_2$  were obtained from formulae that describe the relationship between these constants and the shore stiffness  $SH$ .

Because of the fact that strong compressions of the elastomer profile lead to numerical instability the numerical model was eventually used to semi-quantitatively assess the deformation mode of the profile under small compression. Figure 8.22 shows the deformation mode of a profile which was considered as a design candidate.

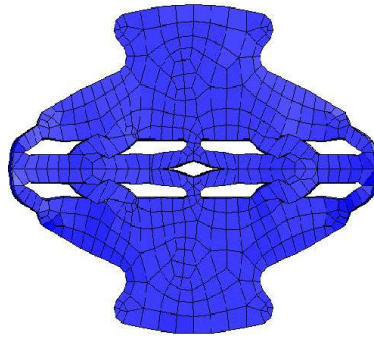


Figure 8.22: Deformation mode of an elastomer profile

## 8.6 Conclusions

The complex action of radial and circular joints in the tunnel lining has successfully been modeled by means of a simplified system of interface elements, resulting in a macro tunnel model with minimal size and complexity. Successful validation of these simplified joint models, based in higher order models and test results, guarantees a realistic prediction of the joint action in the macro model of the tunnel lining and therefore a correct prediction of the response of the tunnel lining itself.

## Chapter 9

# How to Avoid Cracking in Young Concrete

E. Schlangen

*INTRON BV & Delft University of Technology, CITG, Microlab*

P. E. Roelfstra

*FEMMASSE BV*

### 9.1 Introduction

Large concrete structures, like tunnels and bridges, are often built in phases. The most important factors that determine the risk of crack formation in the young concrete are the dimensions of the adjacent parts, the maximum temperature difference during hardening, and the extent of displacement obstruction. With the HEAT program [31] of FEMMASSE BV the building process can be simulated and predictions can be made about the development of temperatures and stresses during the hardening process.

If the tensile stresses should ever exceed the tensile strength, then HEAT can be applied to investigate whether any precautions must be taken to reduce the risk of crack formation. Various precautions are possible; the most usual ones are the following:

- Application of insulation on the formwork to decelerate the cooling down process such that the thermal strain can be followed by the viscous strain (creep) of the young concrete.
- Warming up (partially) the adjacent parts of a previous phase.
- Optimizing the concrete mixture to decrease the temperature difference and/or to accelerate the development of the tensile strength.

- Reducing the initial temperature of the mixture.
- Application of cooling pipes to control the hardening process.

Considering economical topics and fixed data, like the tempo of the building process, one or more of the possible precautions can be chosen.

As an example, the control of temperature and stress in the access roads of the Western Scheldt tunnel in Zeeland/the Netherlands have been analyzed. This project has been executed for KMW ('Kombinatie Middelplaat Westerschelde v.o.f.'). The analyses for this project have been performed by INTRON BV with the HEAT program.

## 9.2 Problem Description

The problem involves the access roads at the northern side of the Western Scheldt tunnel. These access roads are subdivided in fifteen segments of which Figure 9.1 shows a characteristic cross-section. The floors of the access road are little more

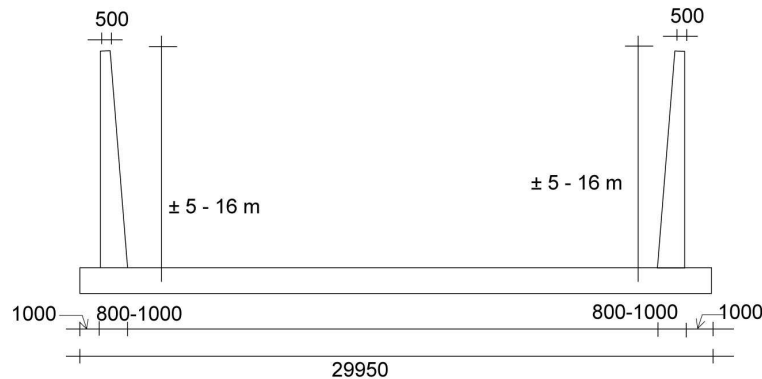


Figure 9.1: Characteristic cross-section of access road

than 30 meters wide, about 20 meters long, and about 1.30 meter thick. The floors of sections 2 up to and including 11 are being poured on top of an underwater concrete layer of little more than 1 meter thick, founded on piles. On top of the floor, walls are being poured with a height varying from 4.9 to 14 meters. The walls are tapered: their thickness varies from about 1000 mm at the bottom up to 500 mm at the top.

It is generally known that in walls thicker than 700 mm cracks may form in the young phase. Therefore, for this project the highest allowable tensile stress in the young phase was restricted to 50% of the existing tensile strength. By means of the HEAT program a number of analyses have been performed to determine effective precautions to meet this restriction.



## 9.3 Required Analysis Data

The input data for the calculations comprises the following.

- I. geometry of the structure phasing;
- II. material properties of the concrete;
- III. kinematic boundary conditions;
- IV. physical boundary conditions (climatic conditions).

The next sections further elucidate the input data required for the calculation.

### 9.3.1 Geometry and Phasing of the Structure

Figure 9.2 shows the subdivision in macro elements of the concrete pours to be performed. For simplification, because the analysis only involves the wall–floor connection, the underwater concrete floor and the structural floor have been modeled as

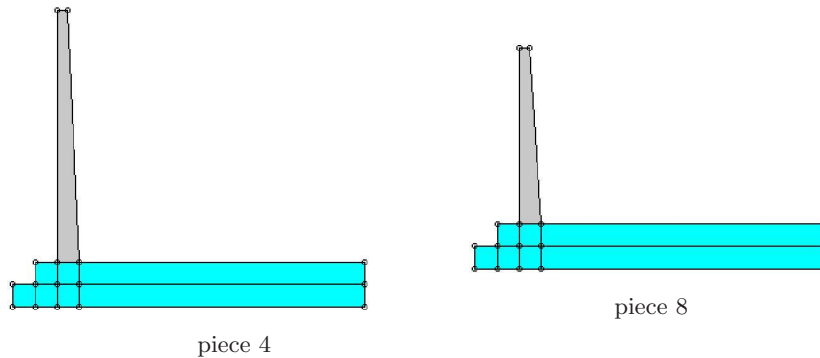


Figure 9.2: Finite element models for walls, sections 2–11

one single structural part. The walls will be poured at least four weeks later than the floors. In the calculation it is assumed that the walls at the left- and right-hand sides will be poured simultaneously which allows the application of a vertical axis of symmetry. The further subdivision of the macro elements into finite elements can be realized by means of the graphical interface of HEAT.

### 9.3.2 Material Properties of the Concrete

On the basis of the concrete composition, as prescribed by KMW, the required material properties have been determined via the material database of FEMMASSE BV. Table 9.1 on the next page summarizes the required material properties. Figure 9.3 on page 129 depicts the course of the adiabatic heat development.

Relaxation of young concrete has been accounted for via an aging Maxwell Chain, which comprises six elements. The input of the Maxwell Chain is based on creep functions from the CEB-FIP Model Code 1990 [13], and also on measured results of

Table 9.1: MATERIAL PROPERTIES

Composition			
Quality class	B35		
Cement type	CEM III/B 42.5 LH HS		
Cement proportion	340 kg/m <sup>3</sup>		
Auxiliary materials	BV/FM and LP-Bildner		
Aggregate	river sand and shingle (nominal 32 mm)		
Water-cement ratio	0.45		
Thermal properties			
Density	2500 kg/m <sup>3</sup>		
Specific heat	1.0 kJ/(kg · °C)		
Conduction coefficient	2.4 W/(m <sup>2</sup> · K)		
Total heat production	105000 kJ/m <sup>3</sup>		
Velocity coefficient	0.04		
Dormant period	7 h		
Ratio Activating energy / Universal gas constant	4700		
Thermal expansion coefficient	1.2 × 10 <sup>−5</sup>		
Poisson's ratio	0.20		
Mechanical properties			
Age [maturity days <sup>†</sup> ]	Compressive strength [MPa]	Tensile strength <sup>‡</sup> [MPa]	<i>E</i> -modulus <sup>‡</sup> [MPa]
0.75	1.4	0.37	8699
1	6.2	1.02	10833
2	15.9	1.87	16222
3	22.5	2.38	19572
7	35.3	3.28	24109
14	42.9	3.80	28996
28	48.0	4.17	32506

<sup>†</sup>One maturity day corresponds to one day of age at 20 °C.

<sup>‡</sup>Determined with CEB formulas [13] from compressive strength and fitting data.

relaxation tests performed on young concrete, by order of third parties, and extensively checked on the basis of practical experience. The temperature dependency of the relaxation is described with the Arrhenius equation.

### 9.3.3 Kinematic Boundary Conditions

Figure 9.4a shows the axes system as chosen for the structure. In the  $2\frac{1}{2}$  dimensional analysis only strains in the *XY* plane ( $\varepsilon_{xx}$ ,  $\varepsilon_{yy}$ , and  $\gamma_{xy}$ ) and perpendicular to this

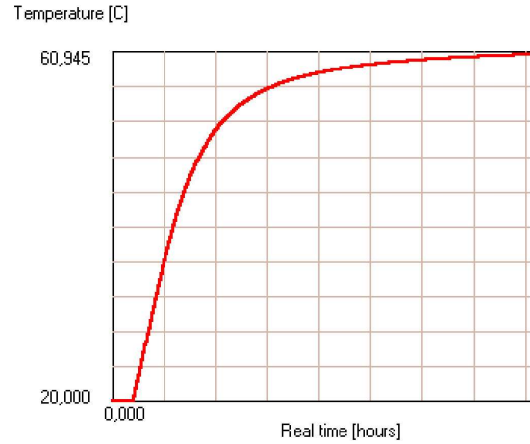


Figure 9.3: Adiabatic heat development

plane ( $\varepsilon_{zz}$ ) are considered. The strain  $\varepsilon_{zz}$  is defined as follows.

$$\varepsilon_{zz}(x, y) = \varepsilon(0, 0) + \kappa_x y + \kappa_y x \quad (9.1)$$

Where  $\kappa_x$  denotes the curvature around the  $X$  axis and  $\kappa_y$  the curvature around the  $Y$  axis. Because of symmetry the curvature around the  $Y$  axis has been constrained. Preliminary analyses showed that the extent of obstruction of the curvature  $\kappa_x$  and the dilatation  $\varepsilon(0, 0)$  was minor. Therefore, it was not necessary to constraint these strains. Figure 9.4b shows the applied kinematic boundary conditions in the  $XY$  plane.

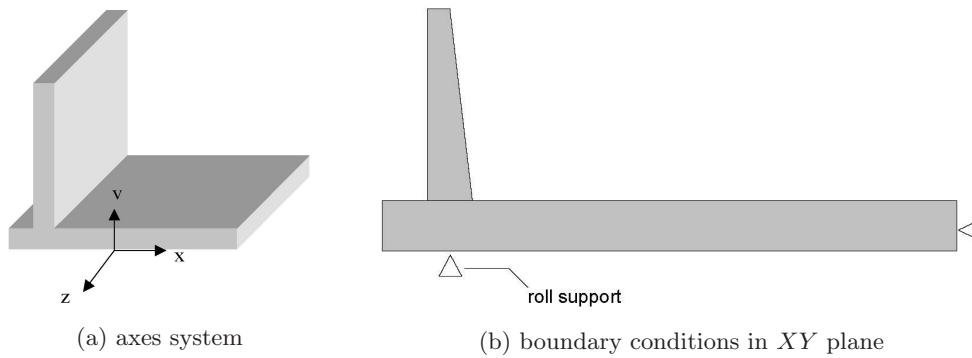


Figure 9.4: Kinematic boundary conditions

### 9.3.4 Physical Boundary Conditions

**Climatic conditions.** The average ambient temperature has been taken as 15 °C. The day and night cycle has been approximated with a sine curve with an amplitude

of 3 °C [Fig. 9.5]. The presumed wind speed is 5 m/s.

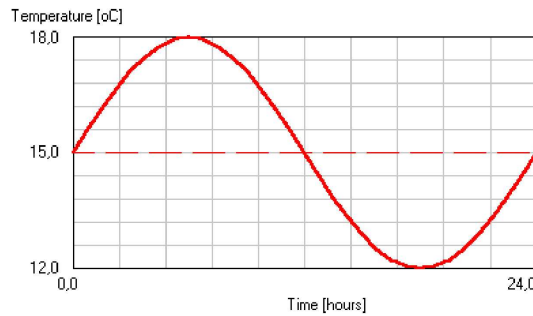


Figure 9.5: Course of the assumed ambient temperature

**Initial temperature.** The initial temperature of the concrete in the wall and in the floor has been taken respectively as 20 °C and 15 °C.

**Formwork and insulation.** In the analyses for the wall it is assumed that the formwork will be removed four days after the pour. KMW has chosen 18 mm plywood for the formwork. For a wind speed of 5 m/s the heat transfer coefficient between the wall and this formwork is 7 W/(m<sup>2</sup> · K). After removal of the formwork this transfer is 25 W/(m<sup>2</sup> · K).

## 9.4 Analysis for Situation Without Precautions

Figures 9.6 to 9.10 summarize the analysis results for the situation without precautions. Figure 9.9 and Figure 9.10 clearly show that the stress ( $\sigma_{zz}$ ) in the wall is

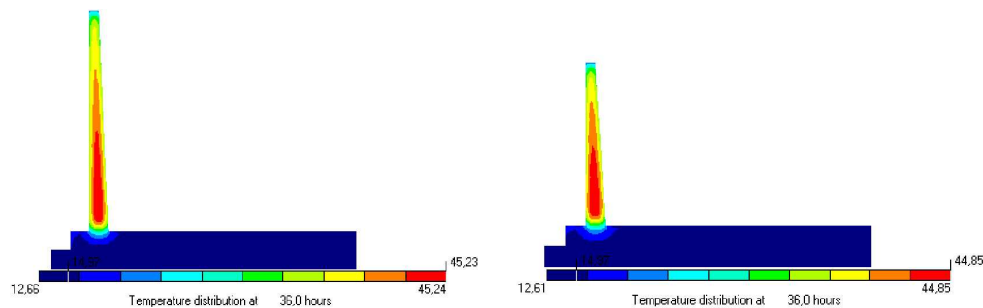


Figure 9.6: Temperature distribution at occurrence of peak temperature

well over the allowable limit of 50% of the tensile strength. The problem is largely due to the magnitude of the average temperature difference between the wall and the floor during the hydration process. Hence, precautions must be taken to reduce this

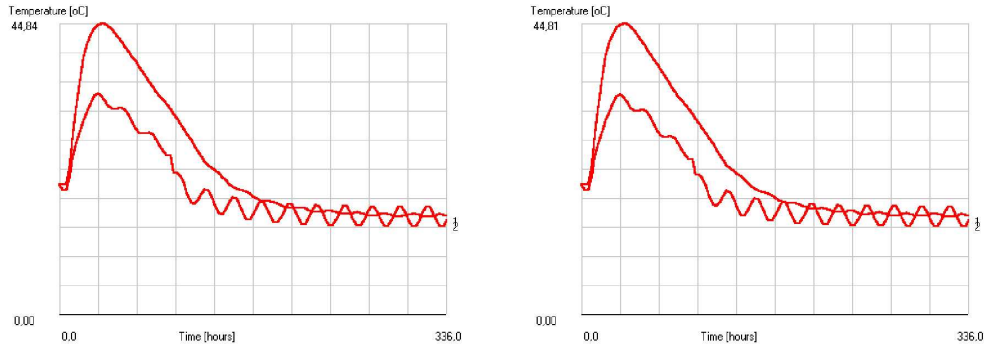


Figure 9.7: Temperature development in the center and at the surface of the wall (with a period of 24 hours)

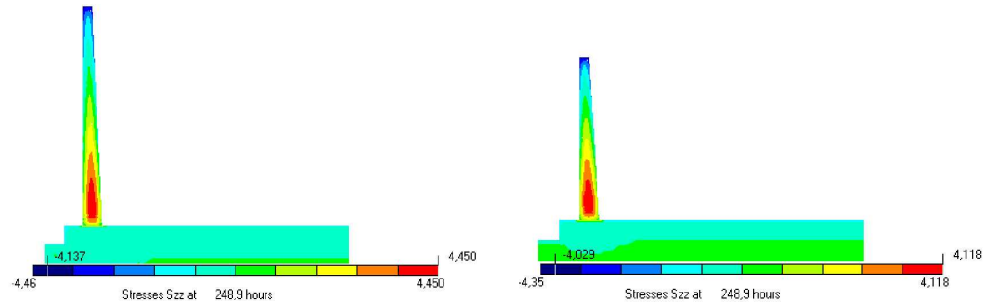


Figure 9.8: Stress distribution ( $\sigma_{zz}$ ) in the wall at occurrence of peak stress

difference. Because of the following reasons cooling turned out to be a useful and economically sensible solution.

- Pouring the floor and the walls simultaneously, like applied for the Øresund tunnel, could have been a solution. However, for reasons of construction practice the phasing of the pour could not be changed.
- Application of less insulating formwork, for instance steel, is not useful in this case because of the large wall thickness. In this situation the temperature is hardly reduced, while the local gradient from center to surface increases adversely.
- Reinforcement to reduce the crack width could not be applied usefully because of requirements with respect to waterproofness.
- Other precautions, like warming up the floor, reducing the initial temperature of the concrete mixture, and adaptation of the mixture, turned out to be technically impossible or economically infeasible.

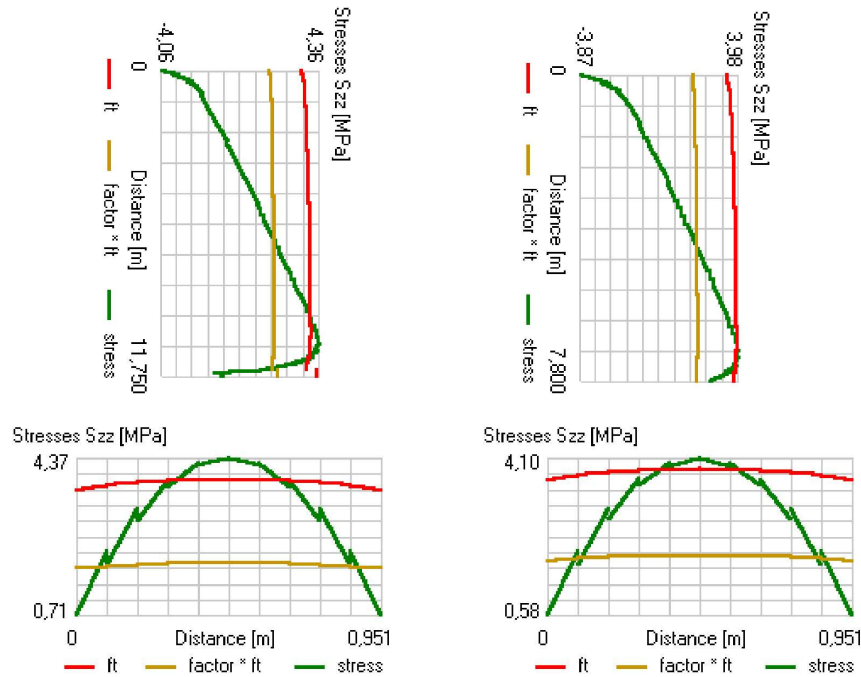


Figure 9.9: Stress distribution ( $\sigma_{zz}$ ) for vertical and horizontal section along the wall (extreme situation); the factor in the figure is 0.5.

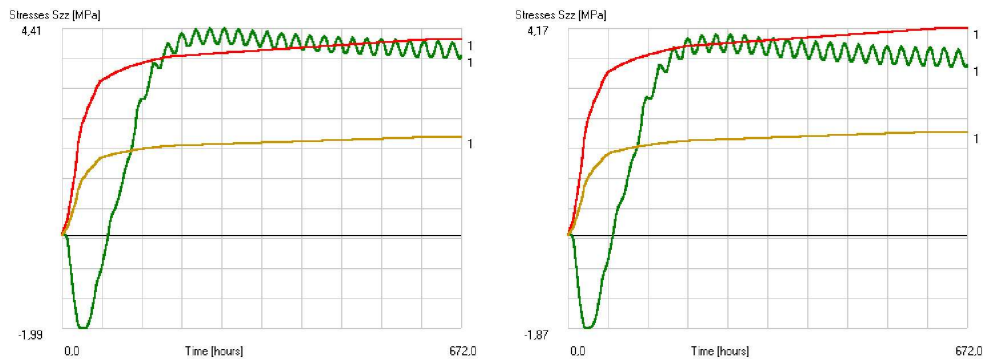


Figure 9.10: Development of tensile strength ( $f_t$ ) and stress ( $\sigma_{zz}$ ) in the center of the wall; the orange line represents 50% of the tensile strength.

## 9.5 Analysis for Situation With Cooling

### 9.5.1 Design of the Cooling Plan

If for a floor-wall construction rotation can occur around the  $X$  axis, then the highest tensile stresses will appear at the base of the wall. Therefore it is not necessary to

cool down the wall along its entire height. In most cases a cooling plan with a varying pipe distance gives the best results [Fig. 9.11]. It must be noted that the most perfect

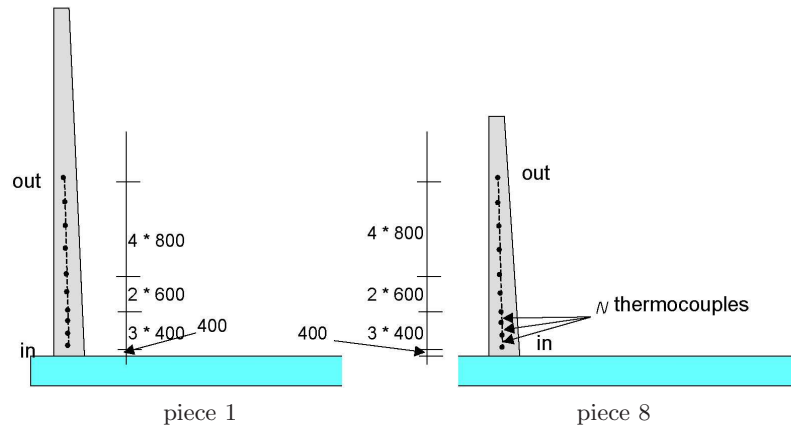


Figure 9.11: Positions of cooling pipes and thermocouples in the wall

cool plan, i.e., practicable and with optimal stress distribution, must be found in an iterative process. The number of pipes, the pipe distance, the temperature of the cooling-water, the flow rate, and the duration of the cooling must be varied systematically. Through the years, the HEAT users have developed practical schemes and applied them successfully for many types of structures.

In this case the iteration process, and consultation with KMW about practical feasibility, have resulted in the following scenario and details.

- Application of the required number of cooling pipes in the center of the wall in accordance with Figure 9.11.
- The cooling pipes are made of plastic and have an external diameter of 32 mm and a wall thickness of 3 mm.
- The cooling pipes are divided in one single cooling group per wall, with the inlet at the bottom and the outlet at the top.
- The inlet temperature is 10 °C during the entire cooling period.
- The flow rate of the cooling-water is 1.0 m<sup>3</sup>/h.
- The cooling lasts 50 hours.

### 9.5.2 Analysis Results

Figures 9.12 to 9.16 summarize the analysis results for the situation with cooling. Figure 9.15 and Figure 9.16 clearly show that the stress ( $\sigma_{zz}$ ) in the wall does not exceed the allowable limit of 50% of the tensile strength.

Actually, the analytical part is finished at this point. However, a detailed execution protocol must still be made to achieve that the precautions as determined with

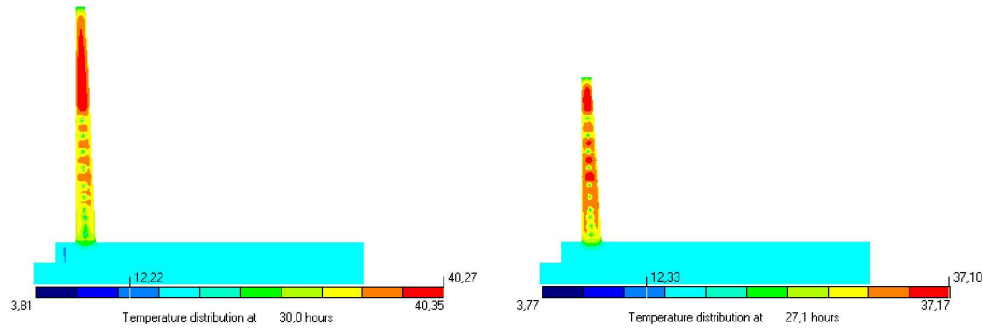


Figure 9.12: Temperature distribution at occurrence of peak temperature

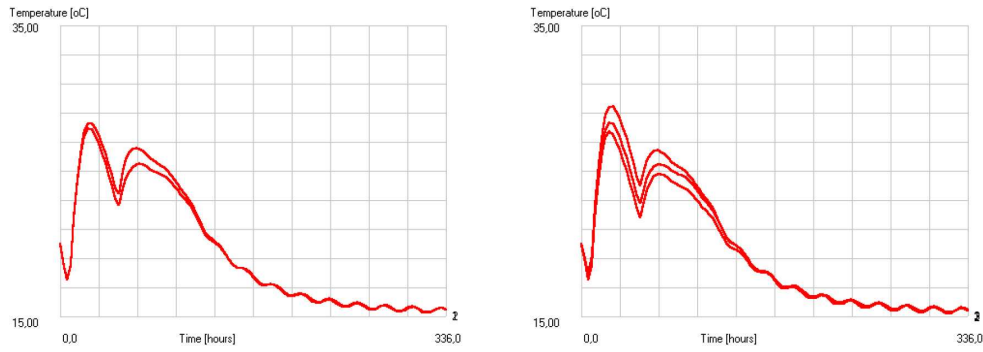
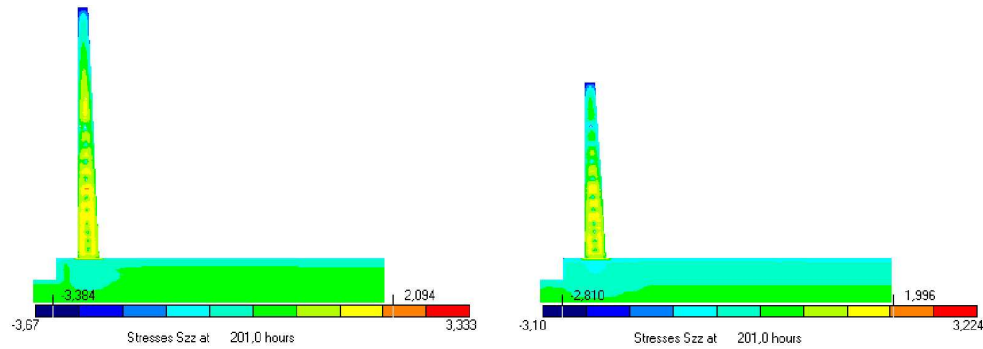


Figure 9.13: Temperature development at the thermocouples in the wall

Figure 9.14: Stress distribution ( $\sigma_{zz}$ ) in the wall at occurrence of peak stress

the analysis are successfully indeed. It is also very important to perform various checks. For reasons of completeness we will describe the protocol as formulated for the access roads of the Western Scheldt tunnel in the next section.



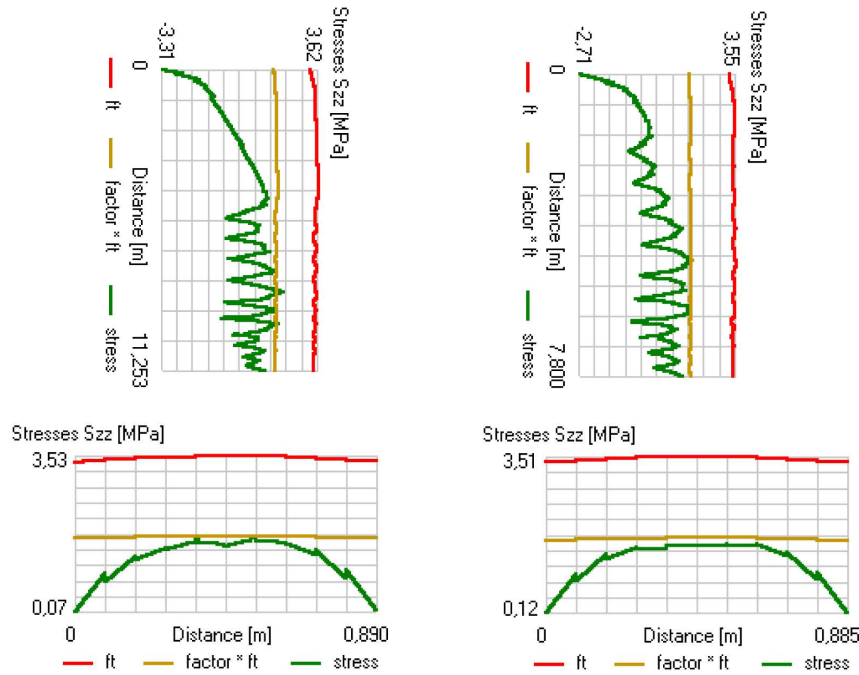


Figure 9.15: Stress distribution ( $\sigma_{zz}$ ) for vertical and horizontal section along the wall (extreme situation); the factor in the figure is 0.5.

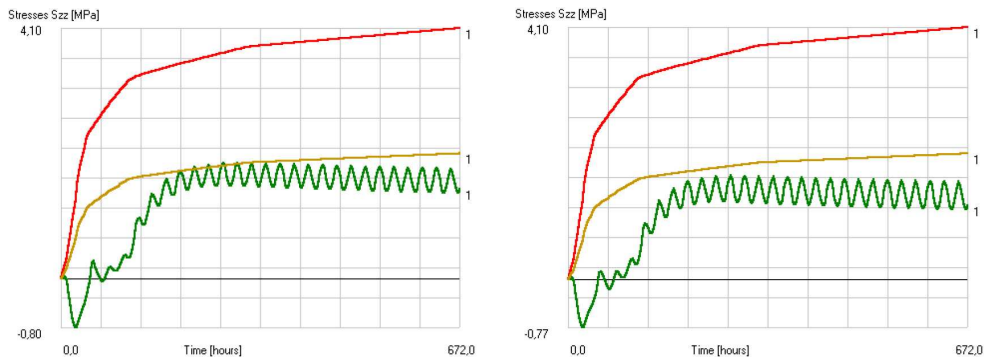


Figure 9.16: Development of tensile strength ( $f_t$ ) and stress ( $\sigma_{zz}$ ) in the center of the wall; the orange line represents 50% of the tensile strength.

### 9.5.3 Protocol for the Western Scheldt Tunnel Access Roads

#### Installation of the cooling system:

- Preferably the distance of the supports should be less than 3 m. In the longi-

tudinal direction the pipes will continue up to about 0.50 m from the end of each wall.

- Thermocouples must be applied at the positions indicated in Figure 9.11. It is advised to record the temperature of the cooling-water at the inlet and outlet of a cooling group. The temperature of the in- and outgoing water may also be recorded with devices other than thermocouples, provided that the accuracy is of the order of 1 °C. In all cases the thermocouples in the concrete must be positioned at suitable distance from an end-face to prevent distracting temperature influences.
- Thermocouples must be connected to the temperature recorder or to the maturity computer.
- The ambient temperature must be recorded.

#### Checks to be made during cooling:

- Preliminary to the pour, the cooling system must be checked for leakage by means of water with a pressure of approximately 3 bar, or so much higher as required to guarantee a flow rate of at most 2 m<sup>3</sup>/h.
- Thermocouples must be calibrated with ice water (0 °C) or a calibrated maturity computer must be applied. During the calibration the thermocouples must be connected to electric wire with the same length as applied in reality.
- Preliminary to the pour, the signal of the individual thermocouples and flow rate gauges must be checked.
- Preliminary to the pour, the temperature of the mixture and the temperature of the cooling-water must be checked. At the inlet the temperature of the cooling-water must be approximately 10 °C throughout the cooling period. The initial temperature of the mixture may be at most 5 °C higher than the average of day and night temperature. Any deviation to a higher temperature must be reported concerning the validity check of the cooling plan.
- Informatively it is indicated that the maximum required cooling capacity is about 19.7 kW for each wall.
- The moment of starting of the cooling depends on the initial temperature of the mixture:
  1. If the temperature of the mixture, at arrival on the site, is higher than the inlet temperature, then the cooling must be started at the same time as the pour of the first mortar in the wall.
  2. If the temperature of the mixture is lower than or equal to the inlet temperature then the cooling must be started at the moment that the concrete temperature has reached the inlet temperature.
- The flow rate must be set to 1.0 m<sup>3</sup>/h and, if necessary, it must be adjusted as soon as the difference between in- and outgoing water becomes more than

1.0 °C/h during the first 32 hours of the active cooling period. However, the raising of the flow rate must be performed well-controlled with maximum increments of 2.0 m<sup>3</sup>/h up to a highest pressure that has been guaranteed during the preliminary checks. The flow rate may never be reduced!

**Termination of the cooling:**

- The termination of the cooling period is determined via the temperature of the middle thermocouple. If this thermocouple is defective, the average temperature of the upper and lower thermocouple may be applied alternatively.
- After the maximum temperature of the middle thermocouple has been reached, the cooling can be brought to a stop as soon as the temperature of this thermocouple has fallen at least 4 and at most 6 °C. Both longer and shorter cooling periods increase the risk of crack formation. Indicatively, the calculations expect an active cooling period of 50 hours.

## 9.6 Conclusions

In this chapter we have outlined an example which demonstrates that problems may arise during a building process due to exothermal hardening of young concrete. KMW has recognized these problems in an early stage and has developed precautions which minimize the risk of crack formation in the young phase. It has been demonstrated that numerical methods are a perfect tool, not only to predict potential problems in the hardening process but also to develop suitable precautions. HEAT is an example of a program which offers such numerical methods. Measurements of temperatures and stresses in real-life situations of various projects have demonstrated that the predictions from HEAT are very reliable [31, 59, 63].

The number of material properties that must be specified to make a useful prediction seems extensive. Moreover, certain physical variables are not part of the practical knowledge of a civil engineer. Therefore, FEMMASSE BV has developed a database for the most prevailing concrete classes. Comprehensive information on the physical and mechanical models in HEAT, and in similar programs, can be found in [31, 59, 63, 66, 71].

**Acknowledgment.** The analyses for the cooling have been performed by ir. B. Baetens of INTRON BV under the authority of KMW. The permission of KMW to publish this illustrative example is gratefully acknowledged.



## Chapter 10

# Design of Concrete Deep Beams

P. C. J. Hoogenboom and J. Blaauwendraad

*Delft University of Technology, Faculty of Civil Engineering and Geosciences*

**Abstract.** An interactive design tool for shear walls and D-regions in beams of structural concrete is described. The PC-oriented program is based on just two elements: a stringer (straight bar) and a panel (rectangle or quadrilateral). These elements are used to build models of concrete structures. The design is done in three distinct steps: the first one is full linear elastic, the second nonlinear step accounts for cracking of concrete and yielding of panel reinforcement while the stringer reinforcement is still kept elastic and the final third step is a full nonlinear simulation of the structural behavior. Thus, the interactive procedure accounts for redistribution of stresses. The result is a final scheme of reinforcement and information on deformations and crack widths in the serviceability state. A design example is included.

### 10.1 Focus on D-Regions

The design of shear walls and beams of complicated geometry is a subject of interest for structural engineers. In international design circles for structural concrete one meanwhile is used to the distinction between B-regions and D-regions. B-regions are the parts of a structure in which the classic beam theory applies and for which we can think in terms of the familiar bending moments and shear forces (Bending). On this subject we have plenty of knowledge. The remaining part of the structure consists of D-regions in which the aforementioned classic state is disturbed (Disturbance). Examples are joints between beams and columns, zones around holes in the web of a beam, dented beam ends, and so on. In case a shear wall has an irregular shape it even has to be considered as one large D-region. The design software SPANCAD

has been set up for the design of such D-regions. It is based on AUTOCAD for its drafting functions [4].

### 10.1.1 Pro's and Con's of Existing Methods

In current design practice two methods have been accepted. Either one uses the Strut-and-Tie method or the Finite Element Method. The big advantage of the Strut-and-Tie method is its simplicity and transparency. The force transfer to the supports is clear and the details can be designed safely. However, a complication is that a different strut-and-tie scheme is optimal for different load cases and load combinations. The complication becomes even worse if load reversals must be considered and forces can reverse sign.

If one applies the Finite Element Method it is being done elastically and a post-processing program can be used which determines the required reinforcement automatically. This method is fast and simple and one can easily take into consideration several load cases and combinations, however, not the most economic reinforcement may be found. We will find that with the Strut-and-Tie method, but that method also has its drawbacks.

We already mentioned the dependency on the load combinations. Apart of that, questions can be raised in case of statically undetermined structures. Then several different strut-and-tie schemes might be applied and one can run into debates with certifying authorities, which one should be chosen. Also the question quickly arises how to control the crack widths in the serviceability state. It occurs that structural designers, who intend to apply the Strut-and-Tie method, start making an elastic Finite Element Analysis to understand the directions of the principal compression and tensile stresses. That can be a substantial support. Gradually even programs come at disposal of structural designers, which take into account the real stiffness of the struts and ties and permit to compute displacements.

### 10.1.2 An Alternative: SPanCAD

This introduction brings us naturally to the program SPANCAD. The aim of this new software is to offer an alternative design tool, which combines a number of advantages and releases a number of drawbacks. It aims for:

- applicability in an early stage of the design process,
- PC environment, under Windows, ready while you wait,
- the same model for elastic state and failure state,
- the same model for different load combinations,
- for shear walls, (deep) beams and cellular structures,
- information about crack widths and displacements,
- interactive design tool; the designer is on the lead.

## 10.2 Stringer–Panel Theory

The program SPANCAD is based on a special type of element method. In the standard Finite Element Method it is practice to apply a mesh as fine as possible, but SPANCAD is made to apply the coarsest mesh for a given geometry. This has been obtained by feeding much concrete mechanics intelligence into the elements. The second special feature of SPANCAD is the type of elements. Only two types exist, a stringer element (straight bar) and a panel element (rectangle or quadrilateral) [Fig. 10.1]. This resulted from observation of several structural designs for shear

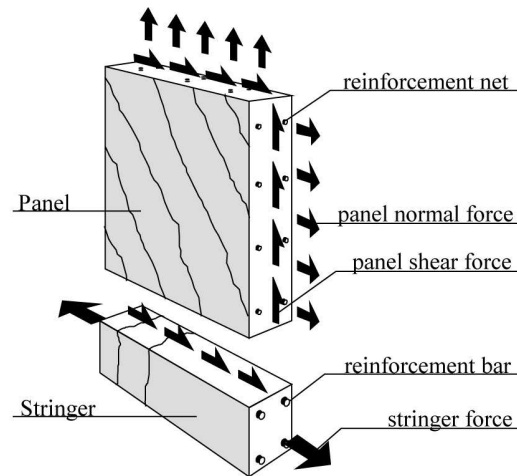


Figure 10.1: Stringers and panels are building blocks of a structural wall model

walls and D-regions in beams. It was noticed that main reinforcement often occurs in bundles at the edges and around holes (*tensile stringers* in SPANCAD). Between those stringers, wall parts occur in which distributed net reinforcement is applied (*panels* in SPANCAD).

Two versions of the stringer–panel model have been developed: a realistic nonlinear version and a simplified linear version. In the linear version the material behavior of stringers and panels is linear elastic and the panels carry only shear forces at the edges. Thus, all normal forces in the model are transferred by the stringers. Since stringers are normally positioned at the edges of a model, this gives a large lever arm for the moment in a section and an efficient force distribution.

In the nonlinear version of the stringer–panel model, the reinforced concrete material can both crack and crush, and the reinforcement can yield and break. In addition, normal forces are included at the panel edges. The latter showed to be necessary for accurate computation of crack widths, force distribution and strength. The nonlinear stringer behavior is based on the Eurocode [68] and the nonlinear panel behavior on the modified compression field theory as developed in the University of Toronto [89]. The crack spacing and crack widths are computed according to the Eurocode [68].

## 10.3 A Three-step Design Procedure

### 10.3.1 Step One: Elastic Analysis

The structural design is made in three steps. The first one is an elastic approach. In this step the simplified linear model is used. Thus, all normal forces are carried by the stringers and all shear is carried by the panels. This is fine for the elastic phase and SPANCAD will always start so. For this first step it does not matter so much what sizes of cross-sections are assigned to the stringers. It appears that a first rough estimate is sufficient for the purpose. We can just use experience and rules of thumbs. The panels have the wall thickness. The software performs a linear elastic analysis for all load combinations. The force distribution achieved in this way is a first indication for the determination of the reinforcement in the tensile stringers and the mesh reinforcement in the panels. No reinforcement in panels is needed outside tension regions.

### 10.3.2 Second Step: Nonlinear

Now we can prepare for a nonlinear analysis in which we will account for cracking of the tensile stringers and cracking and yielding in the panels. In this second step the accurate nonlinear model is used. Thus, the stress state in the panels is extended to shear *and* normal stresses. In the nonlinear step it does matter that we enter the correct cross-sections of the stringers. In compressed stringers the cross-section determines the compressive force, which has to be compared with the ultimate design strength. In tensile stringers the assigned concrete area determines the contribution of the concrete to the tension-stiffening of the stringer. For this the result from the elastic step is used as a first estimate.

All input quantities being determined now and fed into the program, we can start the nonlinear run. The nonlinear analysis is successively made for each load combination. The engineer can follow the progress of the analysis on the screen where a load–displacement graph is being drawn. The load is controlled by a load factor on the vertical axis, which starts with zero and has at least to reach the value 1 at failure. The displacement is on the horizontal axis. Which displacement should be considered is a decision of the designer. Because we now allow for cracks and yielding the graph will not be linear anymore. One thing we do not allow for in this step: yielding of the main reinforcement in tensile stringers. We found that this decision increased the robustness of the design tool remarkably. In case a tensile stringer would reach its tensile yield strength SPANCAD will artificially extend the cracked branch in the force–strain diagram of the stringer. From the analysis results it will become clear whether or not the ultimate tensile strength of a stringer has been surpassed for any of the load combinations and the designing engineer has to increase the reinforcement. He or she immediately also knows to which extent. We also can inspect the crack widths at service loads and react adequately with reinforcement adaptations if needed. Due to redistribution of stresses and the enriched capacity of the panels in this second step it also may occur that the reinforcement in a tensile



stringer can be reduced, however it is the decision of the engineer whether or not to make use of this possibility. He or she may be happy to have some reserve capacity and leave it as it is, if he does not like to strip the structure to the bone.

### 10.3.3 Third Step: Final Simulation

The third step is intended as a final check. All decisions made on basis of the analysis results of the second step must be entered into SPANCAD and then the final simulation can be started. Now no restriction on the nonlinear responses does exist anymore. If everything has been done well the result of this analysis will satisfy the structural designer and the job is finished. If he or she is not content with some details it may be needed to restart either a new step 2 or directly a new final step 3 for further improvement.

It appears that SPANCAD, if applied in this way, is a robust and fast program. The elastic analysis is done more or less instantaneously as all elastic programs and the nonlinear analysis and final simulation only require a couple of minutes. In fact the time involved with the initial modeling of the structure and the professional decisions to be made by the engineer are determining for the duration of the design process.

The final thing still to be done is detailing. Particular attention must be paid to the anchoring of the main reinforcement. At free edges the force in the stringers will be zero while we yet want to anchor them carefully.

### 10.3.4 Classical Cases Covered

SPANCAD has been designed for complicated D-regions but it should do the right things if applied to the familiar classic B-regions. It may be clear that it easily does so. Figure 10.2 shows a simply supported statically determinate example. In

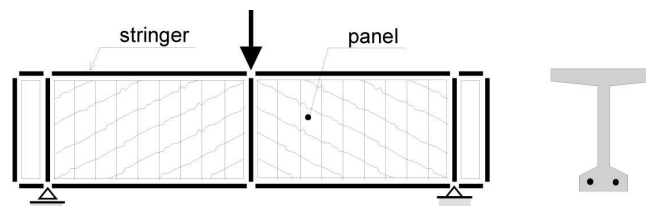


Figure 10.2: Simply supported beam model

the shown beam we have horizontal top stringers and bottom stringers to carry the bending moment (compression zone and tension zone) and panels in the web between the stringers to carry the shear force. Above the two supports and where the point load is introduced also vertical stringers are needed.

If the main reinforcement in the bottom stringer is decisive, the behavior the structure will fail in bending. If the stirrups are decisive, the beam will fail in shear. In that case SPANCAD will produce inclined principal compressive stresses that are in good agreement with the predictions from the classic theory of plasticity [9, 55].

Shear is also the dominant phenomenon in cellular structures under torsion loading. Figure 10.3 shows an example of such a structure. Again, SPANCAD produces

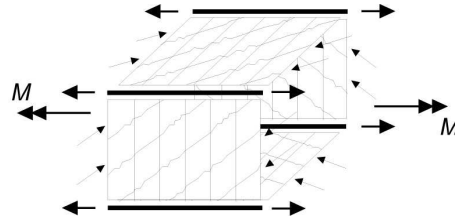


Figure 10.3: SPANCAD can also be used for torsion in box girder beams

inclined cracks in accordance with the theory of plasticity for torsion in structural concrete and both the longitudinal reinforcement and the transverse reinforcement are in tension. This could not have come into being if the panels only would carry shear stresses, as is the case in the first elastic step.

## 10.4 Design Example

SPANCAD is used here to design reinforcement for a deep beam shown in Figure 10.4. The reinforcement for this beam has also been designed by Despot and published in his PhD thesis on plastic optimization at the ETH in Zürich [21].

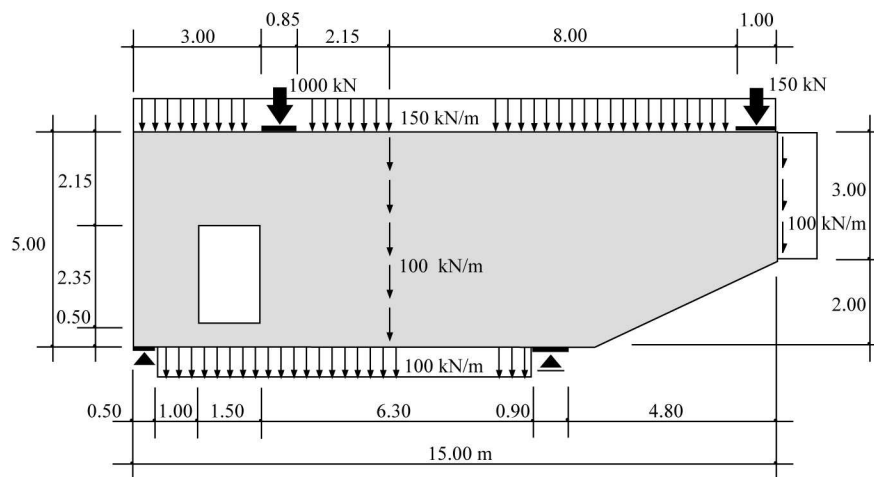


Figure 10.4: Design example of Despot in ETH Zürich. Shown are design loads for the ultimate limit state. The beam thickness is 250 mm

### 10.4.1 First Step

First the stringer–panel model has been drawn and the loading has been entered in SPANCAD [Fig. 10.5]. For the moment every stringer has a cross-section area of

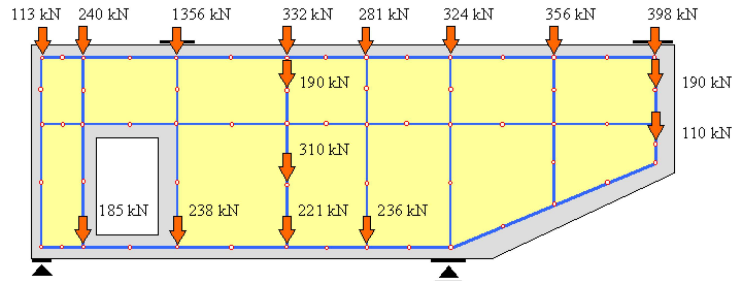


Figure 10.5: Stringer–panel model of the deep beam

250 × 300 mm. The panels have a thickness of 250 mm. The stringers and panels do not have reinforcement yet. SPANCAD computes the deformation of the model and the force flow in the model [Fig. 10.6]. In this step the stringers and panels behave linear-elastically. The stringers carry normal forces only and the panels carry shear forces only.

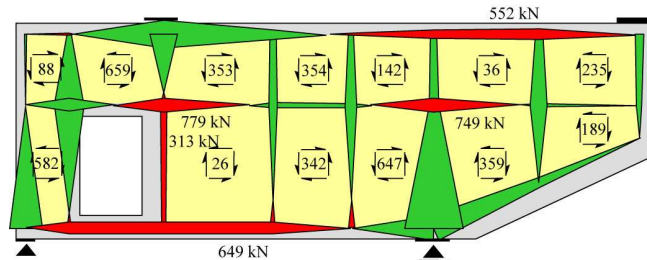


Figure 10.6: Stringer forces [kN] and panel forces [kN/m]. The width of a line is proportional to the size of the force in a stringer. Tensile forces are red and compressive forces are green.

### 10.4.2 Second Step

A standard reinforcing net  $\varnothing 7$ –150 in both directions is placed at both sides of the beam. This provides 0.20% reinforcement. The stringer and panel forces are used to select further reinforcement [Fig. 10.7]. We choose to remove some of the tensioned horizontal stringers in the deep beam. Later we will see whether the distributed reinforcement can carry this force. The dimensions of the stringers are 250 mm thick and 140 to 900 mm wide. The panels still are 250 mm thick. The material properties are shown in Table 10.1 on the next page. SPANCAD computes the force flow in the

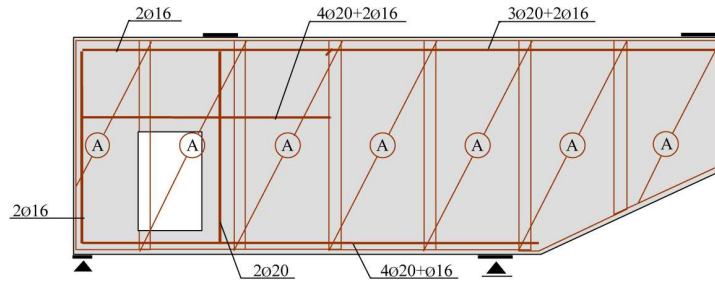


Figure 10.7: Selected reinforcement

Table 10.1: DESIGN VALUES OF THE MATERIALS FOR THE ULTIMATE LIMIT STATE

Concrete			Reinforcing steel	
Compressive strength	–19.5	MPa	Yield strength	460 MPa
Young's modulus	30000	MPa	Young's modulus	200000 MPa
Tensile strength	2.2	MPa	Hardening modulus	0 MPa
Ultimate strain	–0.0035		Ultimate strain	0.05

nonlinear model due to the load of the ultimate limit state [Fig.10.8]. In this the panels do not only carry shear forces but normal forces as well. The principal stress is drawn in the middle of each panel. A considerable redistribution of the force flow occurs compared to the linear elastic computation.

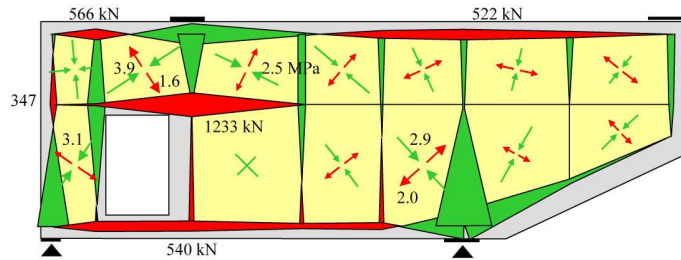


Figure 10.8: Force flow due to the ultimate load

### 10.4.3 Third Step

The reinforcement is adapted to the nonlinear force flow [Fig.10.9]. Subsequently, SPANCAD simulates the beam behavior including all nonlinear properties. Figure 10.10 shows the load–displacement diagram. Plotted is the vertical displacement of the top of the beam at the concentrated load just right of the hole. Figure 10.11 shows the crack pattern for the serviceability load at 70% of the ultimate load. The crack widths appear to be below 0.30 mm and the cracks mainly occur around the

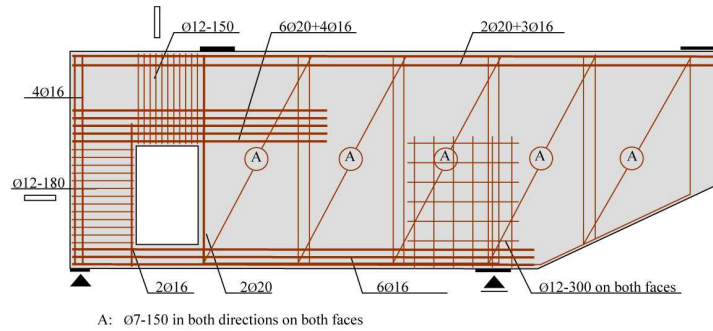


Figure 10.9: Final reinforcement layout

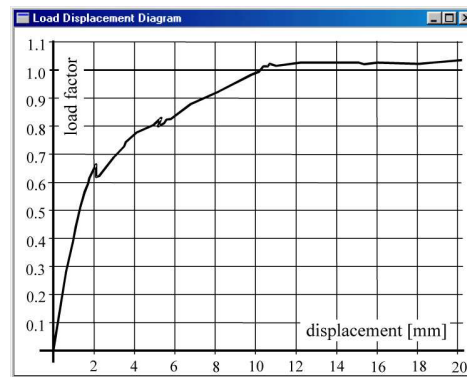


Figure 10.10: Load-displacement diagram of the deep beam

opening in the wall. They distribute over a far larger area for the ultimate load, which is not shown here.

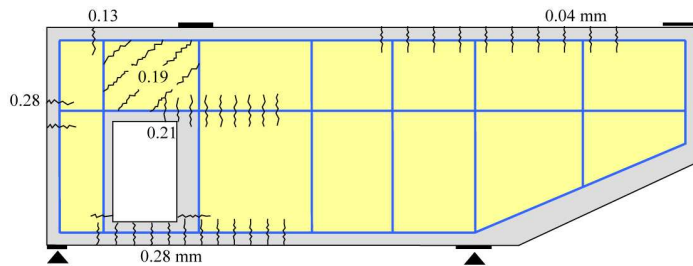


Figure 10.11: Cracks at service load (70% of ultimate load)

The amount of reinforcement is 884 kg (detailing reinforcement not included). The panels contain 483 kg and the stringers 401 kg. It appears that the selected

minimum reinforcement is quite important for the final result. In the shown design 0.20% was chosen. That is less than the minimum reinforcement that is needed if the strength of the panel should not drop after cracking. If that were the criterion, we would need 0.58%, which will result in a total amount of 1220 kg reinforcement. The minimum reinforcement can be less because the panel is capable to describe localized fracture. For comparison we mention that Despot selected 0.27% minimum net reinforcement in his plastic design of this deep beam [21]. This resulted in 1070 kg reinforcement.

## Chapter 11

# Restrengthening of Brickwork to Reduce Crack Width

L. G. W. Verhoef

*Delft University of Technology, Faculty of Architecture*

G. P. A. G. van Zijl

*Stellenbosch University, Dept. of Civil Engineering*

P. A. de Vries

*Delft University of Technology, Faculty of Civil Engineering and Geosciences*

### 11.1 Mixed Building Techniques: ‘De Adelaar’

Throughout the centuries the design and methods of construction has been related to economic circumstances, the development of techniques and materials. At one stage in this development came the brick building with wooden floors. Later, after the discovery of cement, people were able to produce concrete. First came an experimental period in which slowly but surely more and more of the structural parts of buildings were made of concrete. In the intermediate period many buildings combined the use of both materials. The walls were still erected in brickwork while the columns, beams and floors in the building were made of concrete. Such a building is ‘De Adelaar’ (The Eagle) [Fig. 11.1].

It was built in 1906 to the design of the architect Vuyk. The building was originally designed to produce soap and had an eagle on top to give a strong signal drawing attention to it. Now it is a listed building. One of the essential qualities of the building is its visual impact, which must therefore be retained. The condition of the building is poor; there are cracks in the brick walls; the concrete inside the building is very seriously carbonated and was aggressively attacked by the soap producing process.

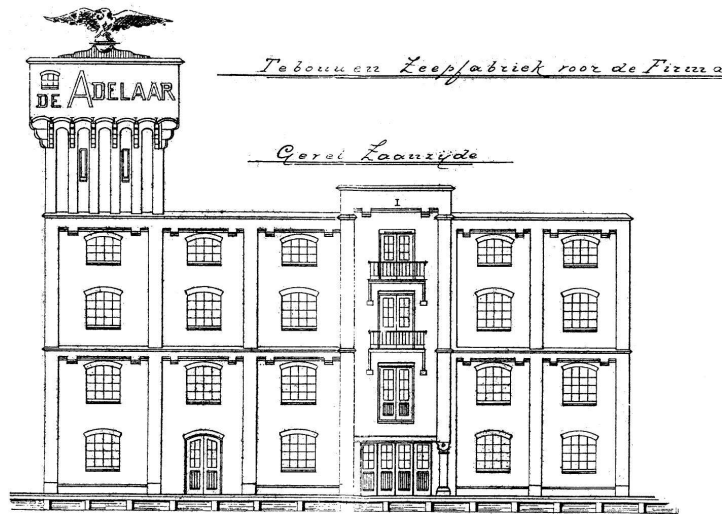


Figure 11.1: ‘De Adelaar’ backside, facing the river Zaan

With our contemporary knowledge it is not difficult to improve the quality of the brick walls, for example by replacing cracked bricks by new ones that are the same in color and texture. Another solution could be to move bricks from the inside of the wall to replace those on the outside. In this case the original material is used and the mortar pointing can be renewed. Despite the poor condition of the concrete structure, restrengthening of the original structure can be carried out, but in this case the amount of money is the determining factor.

If there is not sufficient money to pay for restoration or renovation this automatically results in the end of the existence of the building. The only alternative is that the new function itself will generate the money to earn back the investments. The quality of the building remains important to the new function, as also does the guarantee that the causes of the cracking of the brick walls can be stopped by the renovation measurements.

## 11.2 The Main Problem

The main problems of buildings with a traditional outside bearing wall of brickwork and a concrete inner bearing structure are caused by the differences in temperature movement of brickwork and concrete and the movement of moisture. Of these the movement caused by changes in temperature plays by far the biggest role, leading to vertical cracks at the weakest points – the windows. Horizontal cracks also occur, but these are clearly due to the extension of the corroded bars in the concrete floors resting in the brick walls. In any case, solutions have to be found. The fact that this kind of damage is repairable does not diminish the question whether the differential



thermal expansion and contraction will lead to cracking or, after repair, to new cracking.

The new function for ‘De Adelaar’ will be that of an office building. People have to work close to the outer walls, which will have quite a low temperature in winter. This means that the workers will radiate heat to the wall and will feel chilled or may become ill. Insulation of the wall on the outside would solve all the problems and, technically speaking, it is the only good solution. However such a solution is out of the question because of its effect on the visual impact of the building and the fact that it is a listed building. Insulation placed against the inside of the brick outer facade wall will make the difference in temperature-induced movement practically twice that in the original situation. However, under these circumstances with a wall made of bricks and a lime mortar, which is more elastic than a cement-lime mortar, the repaired wall may not crack as a result of movement resulting from temperature fluctuations.

## 11.3 Basic Interventions

The basic intervention considered is insulation, either directly on the inside, or in the form of an internal climate façade. To control the wall cracking, dilatations in the walls, or glued carbon fiber plastic reinforcement on the wall inside faces are considered.

### 11.3.1 Insulation on the Inside

Within the group of using insulation on the inside, several variations are possible [38]. Calculations for each of these have been made to determine whether condensation will occur on the under surface of the floors or inner sides of the walls. For the temperature-induced movement the maximum difference will occur if we choose the method shown in Figure 11.2a. The movement of the brick wall is initiated by the outside conditions, with peaks for the summer and the winter. The concrete structure stays more or less unchanged at a conditioned air temperature on the inside of  $20\text{ °C} < T_i < 24\text{ °C}$  in winter and  $23\text{ °C} < T_i < 26\text{ °C}$  in summer.

### 11.3.2 Adding a Climate Façade on the Inside

The idea behind the climate façade [Fig. 11.2b], is the fact that air from the inside can be led through the cavity between it and the wall. This will have a positive influence on the physical behavior of the working areas and will have a minimal technical effect on the building as a whole. Despite the greater loss of energy this seems to be one of the best solutions one can choose. To date this solution has not really been used as an option in the renovation field. A problem foreseen is that a thermal gradient will occur through the wall [Fig. 11.2b], which will cause wall bending between the concrete floors. However, it is believed that this effect will not lead to cracking, which makes this insulation option interesting, because the (average) wall temperature drop is half of the  $\Delta T = -32\text{ °C}$  in the case of direct internal insulation.

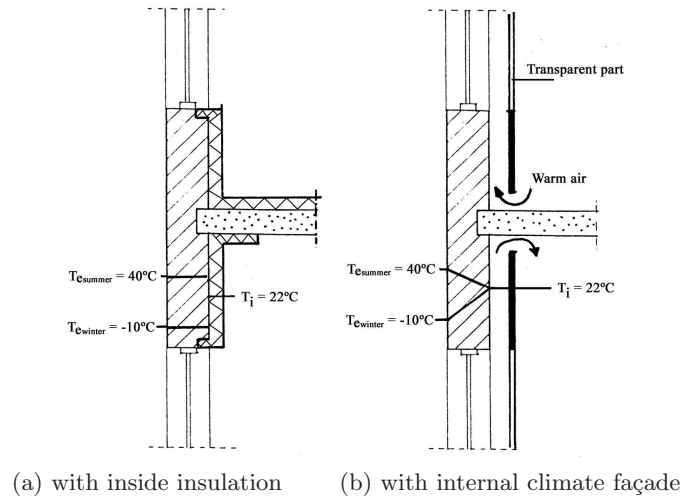


Figure 11.2: Schematic temperature flow

### 11.3.3 Dilatation Joints in the Outside Wall

From a restoration point of view this is not really an advisable option. On the other hand, interventions sometimes have to be made to prevent cracking. As a compromise, only a small number of dilatations will be allowed. Calculations are needed to establish whether a large spacing of such dilatations will limit crack widths to an acceptable level.

### 11.3.4 Reinforcement

Carbon fiber reinforced plastic (CFRP) sheets have been employed successfully to increase the earthquake resistance of masonry buildings (see Schwegler [64, 65]). This concept may also limit crack widths to an acceptable level in masonry walls. As in reinforced concrete, the reinforcement may spread the total crack width in a damaged area over several cracks of smaller width.

## 11.4 Numerical Simulation of Interventions

To study the effect of the interventions on the structural performance, numerical simulations are made. A numerical (finite element) model is employed to study the impact of the interventions on the masonry walls in particular. This model was recently developed by van Zijl [82] for the analysis of creep, shrinkage and cracking in cementitious materials, like concrete and masonry. The model employs an orthotropic Rankine plasticity model to capture cracking. Creep is simulated with viscoelasticity, as represented by an aging Maxwell Chain. The model has been shown to simulate

concrete and masonry behavior with reasonable accuracy by the verification and validation analyses of experiments [82, 83].

### 11.4.1 Modeling Strategy

The main consequence of the proposed interventions is the greater restraint to the shrinkage movement of the brickwork by the concrete floors. With the insulation the floors will be kept at an approximately constant temperature ( $T_i = 22^\circ\text{C}$ ), while they currently undergo the same temperature variation, albeit with some delay, as the brickwork, which is exposed to the varying climatic conditions. The large temperature difference between the floors and the brickwork of up to  $32^\circ\text{C}$  for the case of full insulation on the inner side of the walls will cause tensile stresses in the walls, which may lead to cracks of unacceptable width. To investigate this, the rear wall of ‘De Adelaar’ is studied. This wall is 42.1 m long, 0.33 m thick and has piers (total 0.44 m thick) on which the concrete beams rest. A one-story high wall part is modeled [Fig. 11.3].

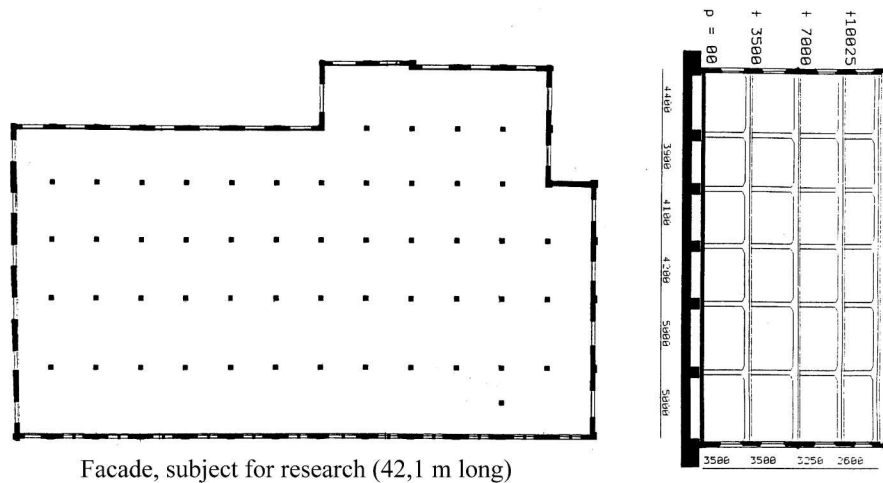


Figure 11.3: Floor plan and cross-section of ‘De Adelaar’

To limit the extent of the problem, the wall is modeled as a two-dimensional plane, which implies that only an average of the wall through-thickness temperature acts. This approach ignores bending due to temperature gradients through the wall, but this is assumed to be negligible. Symmetry is also assumed and only one half of the 42 m long wall is modeled. To further reduce the total size of the problem, the wall is considered as a homogeneous continuum. This means that the bricks and mortar are not modeled separately, but as a homogenized composite, which behaves as if bricks and mortar are modeled separately.

As indicated in Figure 11.4 on the following page, the temperature variation is assumed to have the largest impact on the fired clay type of masonry, with only negli-

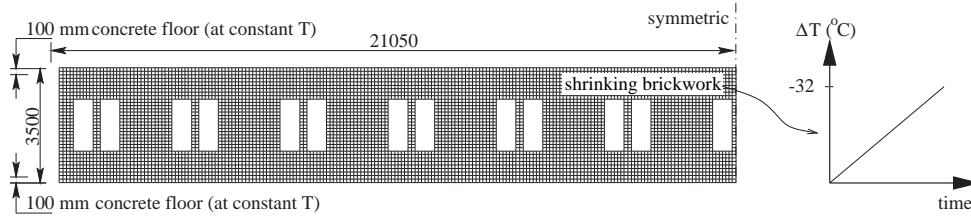


Figure 11.4: Schematization of the envisaged structural impact of the interventions (dimensions in mm)

gible hygral shrinkage. The linear temperature drop of the masonry is considered as a simplified, worst case half-day cycle. Owing to the uncertainty of the environmental processes, a sophisticated calculation of the thermal evolution is unjustified.

#### 11.4.2 Results without Restrengthening

The results from an earlier sensitivity study [87] allow some conclusions to be drawn about the proposed interventions. It is very probable that fully developed cracks of unacceptable width will occur in ‘De Adelaar’ if the walls cool down by 32 °C relative to the concrete floors. This will be the case even in the scenario of no lateral restraint

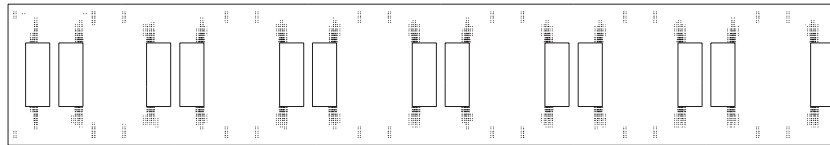


Figure 11.5: Cracking due to shrinkage restraint (crack strains shown for bound 2)

by the perpendicular connecting wall [Fig. 11.5], a high tensile strength, as well as the stress relaxation if the temperature difference evolves over 12 hours [Fig. 11.6b]. From previous studies on restrained shrinkage of masonry walls built of masonry similar to that of ‘De Adelaar’ [82], this masonry can be classified as brittle, which implies that the snap-through behavior seen for brittle masonry will also occur in ‘De Adelaar’. The introduction of two dilation joints in the brickwork is no remedy. It merely relieves the brickwork in close range of the dilation joint, while the cracks further away remain [86].

If a lower temperature difference between the brickwork and the floors can be realized, the probability of unacceptable cracking is reduced. A difference of  $\Delta T = -16$  °C in the case of an internal climate wall will cause no cracking for boundary condition 2,  $f_{t,x} = 0.4$  MPa and a 12 hour temperature cycle half-period [Fig. 11.6-b]. However, it is likely that weak spots exist ( $f_{t,x} < 0.4$  MPa). Cracks may already initiate at these weak spots and, if the cooling down occurs fast (in less than 12 hours), the cracks in the weak spots will snap through.

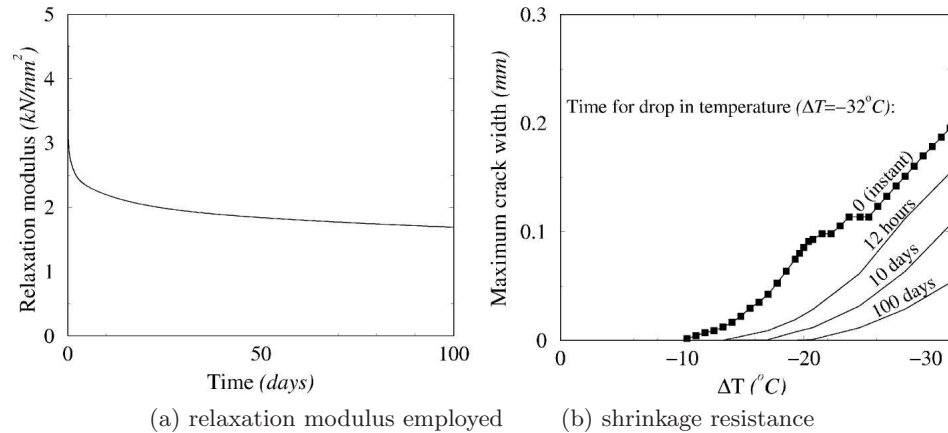


Figure 11.6: Relaxation and shrinkage

The lower level of cracking in the case of a flexible (timber), which will be even lower if the temperature drops in 12 hours instead of instantly [87], goes a long way towards explaining the non-occurrence of significant cracking in the ‘Oranje Nassau Kazerne’, another Dutch building. However, a timber floor is undesirable for ‘De Adelaar’. A pragmatic solution may be sought in the CFRP-sheet reinforcement of the walls to prevent cracks from snapping through to undesirable widths.

### 11.4.3 Brickwork with CFRP-Sheet Reinforcement

CFRP-sheet reinforcement glued onto masonry walls has been shown to strengthen masonry walls [64, 65]. Here, it is investigated whether it can avoid the serviceability limit-state of ‘De Adelaar’ being breached. Due to its high stiffness  $E = 155$  GPa and strength  $f_t = 2400$  Mpa [65], the CFRP-sheet should reduce the predicted crack widths in the restrained shrinking masonry walls by transferring stress from damaged areas to undamaged areas. In this manner more cracks, but of smaller, acceptable width will arise.

The CFRP-sheets have been modeled by overlapping horizontal rows of existing quadrilateral elements, with which the walls have been modeled, with additional quadrilateral elements. Strips of 0.8 mm thick and 106 mm wide have been modeled continuously over the whole wall length. To avoid the aesthetic impact of external CFRP-sheets on the walls, only the inside faces should be reinforced. This will increase the bending effect caused by thermal gradients. However, this is assumed to be negligible and not considered here in the two-dimensional analyses. The glue has not been modeled, which implies that perfect bond has been assumed. From private discussions with the author of [64, 65] a bond length of up to 1 m is required to develop the CFRP strength. By applying the strips continuously over the whole length this requirement is met, except at the wall ends, where the distance to the first window opening is only 600 mm. Depending on the stress level in the reinforcement

there, additional strips may be applied locally to reduce the bond length requirement.

Two cases have been considered. In the first case a single strip was applied directly below and above the window openings respectively. In the second case, two more strips were applied, each half-way between the first strip and the concrete floor. The responses are shown in Figure 11.7 in terms of the maximum crack width in the wall at a given temperature difference between the wall and the floors, as

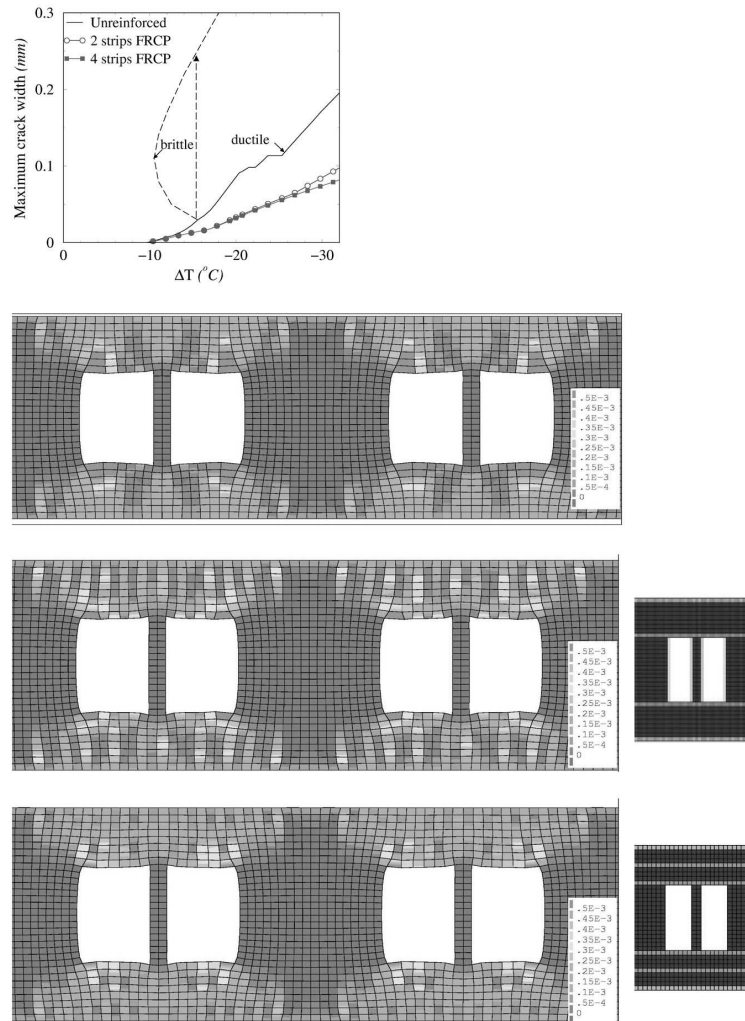


Figure 11.7: ‘De Adelaar’ unreinforced and CFRP-sheet reinforced wall responses to restrained shrinkage. Top: Maximum crack width evolution with temperature difference increase. Bottom: Crack strain contours for unreinforced wall, wall reinforced with two strips and wall reinforced with four strips CFRP-sheets.

well as cracking strain contours. For the latter, only two window openings have been zoomed out for clarity. Instead of a single, wide crack at each corner of each window opening when unreinforced, several vertical cracks occur, spread over the total window width. The maximum crack width is reduced to approximately 0.1 mm for both cases of reinforcement. Note that for the reinforced walls, the true brittle masonry fracture energy values were employed. Despite this fact, no snap-through of cracks occurred in the reinforced walls. It is recalled that ductile behavior had to be modeled to avoid snap-through in the unreinforced wall, indicated by the dashed line in Figure 11.7.<sup>1</sup>

The non-shrinking CFRP-sheets are forced into compression by the shrinking wall between the cracks. At the cracks they are stretched to bridge the cracks, causing tension. A maximum tensile stress of 65 Mpa occurs, well below their strength. This does not imply over-reinforcement, because the stiffness is required to keep the crack widths small. Also, the low stress is favorable for the bond length requirement.

#### 11.4.4 Conclusions

By finite element analyses it has been predicted that the introduction of insulation on the inner wall of ‘De Adelaar’ will lead to unacceptable cracking of the brickwork. The introduction of dilation joints in the walls at 14 m intervals does not solve the problem. A reduction in the temperature difference between the restraining concrete floors and the brickwork by an internal climate façade does not sufficiently reduce the danger of large cracks snapping through at the window openings.

CFRP-sheet reinforcement may be applied to reduce the predicted crack widths to acceptable levels. Two continuous sheets directly above and below the window openings have been shown to prevent crack snap-through. Instead of a single, wide crack as in the case of no reinforcement, several vertical cracks of small width arise. Furthermore, it has been shown that the application of two more strips produces a slight reduction in the maximum crack width and prevents crack snap-through in the wall parts between the first strips and the concrete floors at high temperature differences. Action is currently undertaken for the practical application of CFRP-sheet reinforcement in ‘De Adelaar’.

### 11.5 The Laboratory Test

Desk research as described before, give trust in a solution of strengthening of brickwork with carbon fiber reinforced plastics. This counts in general but especial for buildings with a mixed technology of concrete and brickwork. Instead of locally snapping through of some cracks, a lot of fine cracks will occur mainly in the weakest elements of the brickwork, the joints. Before introducing the technique in practice, a laboratory test, now, is under execution to check the numeric calculations. The

<sup>1</sup>Please note that this is a mere indication of the snap behavior, as the brittle case was not analyzed for the unreinforced ‘De Adelaar’ wall.

laboratory test has to simulate the desk research and both have to be as close as possible with the reality.

Nevertheless desk research and laboratory tests are not equal with the real situation. In the real situation a continuous movement of all building elements is taking place. In calculation models we are looking to the extremes and notice the brick facade becomes in wintertime shorter and in summertime longer than the concrete structure in the building. Shear forces between the concrete structure and the brick facade introduce tension and cracking in the brick facade. Furthermore the length of a facade is long while in a laboratory test a set up has to be realized with limited length and nevertheless shear forces have to be initiated leading to cracking of the brickwork.

For realization a set up has been chosen of two aluminum beams with a brickwork wall of 22 cm thickness and overall measurements of 1.3 m height and 1.5 m length [Fig.11.8]. In the middle an opening is kept to weaken the wall, as an image of a

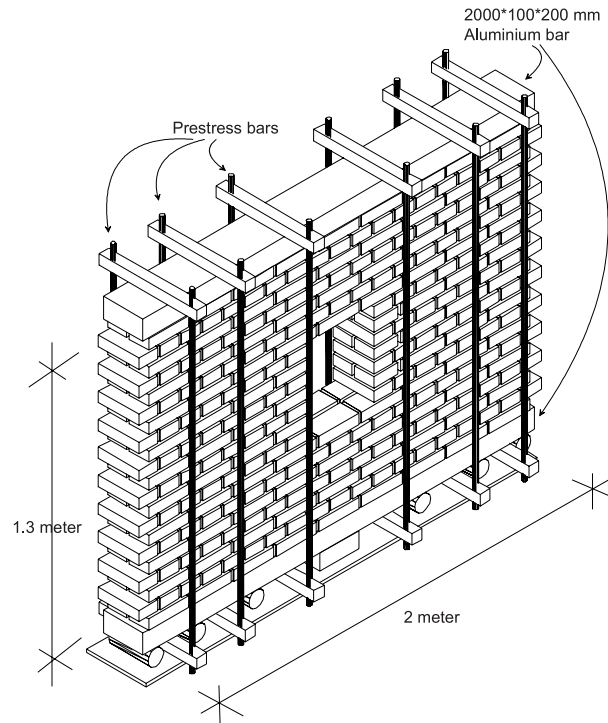


Figure 11.8: The laboratory situation

window, and to introduce snapping through of the brickwork. For the quality of the bricks Rijswaard has been chosen and for the mortar 1 cement : 1 lime : 6 sand. For old brickwork often only hydraulic lime and sand has been used but for the laboratory test it would take too much time. An adaptation for the mortar with cement and lime was necessary.



The set up is realized in a climate room. After hardening of four weeks under conditions of 20 °C and a relative humidity of 70 % the temperature in the climate room is increased with 25 °C. Aluminum and brickwork have quite different temperature moduli causing the aluminum to expand more than the brickwork. If no slip occurs between brickwork and aluminum beam, the difference in deformation will lead to tension forces in the brickwork. To prevent shock-wise deformation, the aluminum beam under and above the brickwork will be cladded with polyurethane. In this way the increase of energy will be steered by heating up the brickwork. To prevent slip the brickwork is loaded in a vertical direction with a constant load of approximately 1 N/mm<sup>2</sup>. Furthermore the first bedjoint will be made of resin instead of mortar to be sure that the forces in the brickwork are comparable with the situation in practice.

After measuring the deformation till snap through cracking occurs the temperature of the climate room will be lowered till 20 °C. The broken bricks will be removed and replaced with new bricks and new mortar as it would have been done in practice. After one week, when the mortar is dry, the CFRP strips will be glued with a resin. Two weeks later the original vertical load will be applied to the structure and the temperature in the climate room will be increased again with 25 °C.

### 11.5.1 Numerical Analysis Results

The calculations following the desk research show the principle stresses in the unreinforced wall before cracking, after 25 °C temperature increase, in the aluminum beam, and with the CFRP strips. Figure 11.9 shows the calculated stress diagrams for the laboratory tests for the unreinforced model and for the model reinforced with

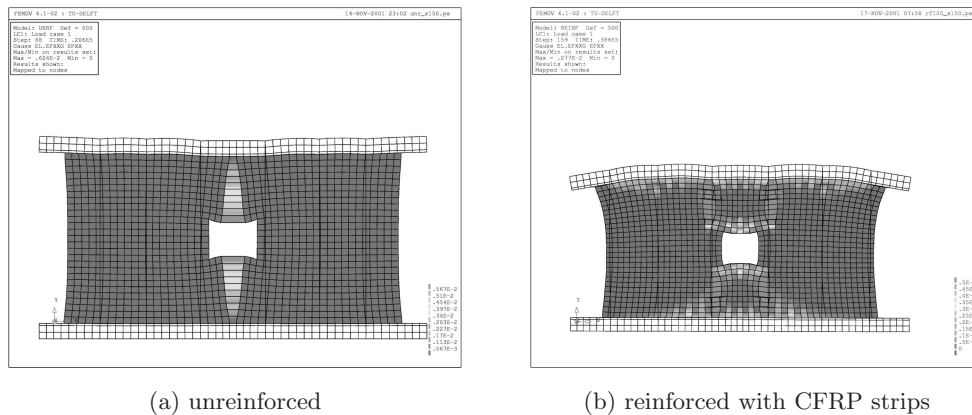


Figure 11.9: Stress diagrams of the laboratory test

4 × 100 mm CFRP strips. The laboratory situation for these models included aluminum beams of 200×100 mm, prestressed vertically by 12 × 48 kN (say reinforcing steel of 20 mm diameter up to 150 MPa prestress). For the case of low shear resistance on aluminum interface and high masonry strength the following assumptions were made for the interface: adhesion  $c_0 = 0.3$  MPa, friction coefficient  $\phi = 0.4$ ; and

for the masonry: horizontal tensile strength  $f_{t.x} = 1.0$  MPa, vertical tensile strength (joint strength)  $f_{t.y} = 0.2$  MPa.

Also a model with lower strength masonry ( $f_{t.x} = 0.5$  MPa,  $f_{t.y} = 0.2$  MPa) was analyzed. The results are shown in Figure 11.10.

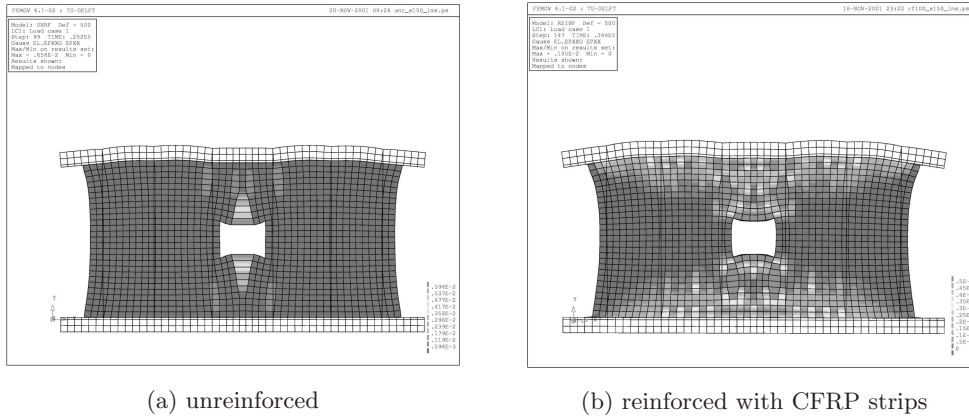


Figure 11.10: Stress diagrams of the laboratory test on lower strength masonry

### 11.5.2 Epilogue

Meanwhile, laboratory tests have been performed. The results match the previously performed numerical simulations. Detailed information about the laboratory experiments, with the obtained values and the correlation, is given in the proceedings of the I.C.P.C.M. conference “A New Era of Building”, see Van Zijl et al. [84, 85].

**Sponsors:** TU Delft, SIKA Nederland, and Spanstaal Soest.

## Chapter 12

# FEM Models Applied for Unreinforced Underwater Concrete

C. van der Veen

*Delft University of Technology, Faculty of Civil Engineering and Geosciences*

A. de Boer

*Ministry of Transport, Public Works and Water Management – The Netherlands*

### 12.1 Introduction

In the Netherlands a deep building pit can be created by sheetpile walls, tensile piles and underwater concrete. Creating a building site with underwater concrete is necessary because of the high groundwater level; otherwise an excessive amount of water must be drained. Furthermore, the permitted drainage of water is limited in the Netherlands. The building of such a site can be explained as follows [Fig. 12.1]. It starts with the ramming of steel sheetpile walls into the ground. These walls consist of steel sheetpiles of the Hoesch type, or consist of combi-walls. The type of wall used depends on the depth of excavation. After the ramming of the sheetpile walls, the excavation and anchoring starts. For the anchoring, screw-injections and strand-anchors are used. After the excavation the ramming of the foundation piles starts and mostly separate building pits are created by ramming partitions. When the ramming of the foundation piles is finished, underwater concrete is poured into each building pit. As soon as the underwater concrete has hardened, the water in the building pit is pumped away and the concrete work starts.

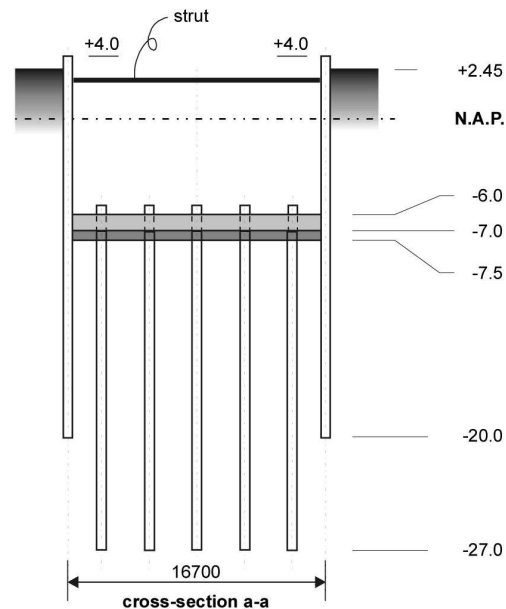


Figure 12.1: Cross-section of a building pit

### 12.1.1 Flow of Forces

The foundation, which consists of the underwater concrete floor and the piles, will be loaded by the hydraulic water pressure (buoyancy of the building pit), resulting in tensile forces in the piles.

In the horizontal direction the underwater concrete floor acts as a compression strut between the opposite steel sheetpile walls. The sheetpile walls are loaded by the water pressure and the effective soil pressure. As a result of the tensile forces in the piles and sheetpile walls the underwater concrete floor lifts upwards. However, the axial stiffness of the piles and sheer walls differs. Consequently, a different elongation occurs which affects the moment distribution in the underwater concrete floor [Fig. 12.2]. Two different building pits are shown, a small one of 19.3 m and a wide building pit. Clamping moments develop in the connection between concrete floor and sheetpile wall, because the sheetpile wall has a higher stiffness than the piles.

The moment distribution is comparable to a floor on an elastic foundation. In the small building pit the clamping moments enlarged the field moments. However, in the wider building pit, represented by the dotted line in Figure 12.2, no effect on the moment was noticed in the midspan. The bottom panel of Figure 12.2 shows the displacements of both building pits. Up till now cracking of the concrete floor was not allowed and only limited flexural tensile stresses were possible. The distribution of forces was based on a linear elastic distribution. Recently, a new design code for underwater concrete was presented, which allowed cracking in the unreinforced concrete floor. Thus, the carrying capacity of the concrete floor made use of the

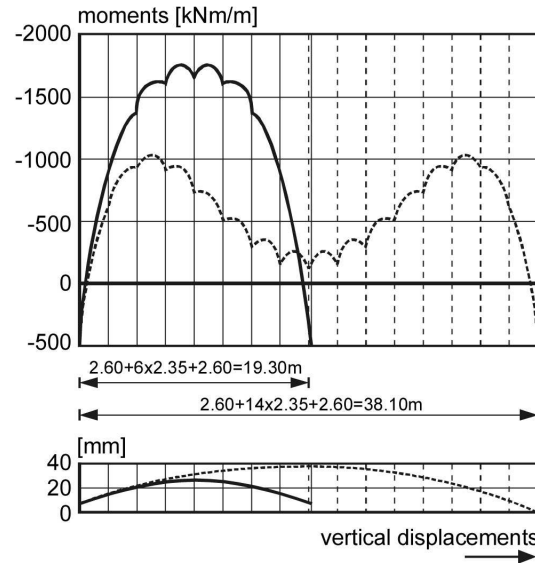


Figure 12.2: Distribution of the displacements and moments

compressive membrane force, which acts in the floor.

In order to investigate the flow of forces in more detail, different FEM models have been used. In the models, which respectively consist of beam, shell or solid elements, special attention has been paid to the interaction between the steel sheetpiles and concrete floor. With the aid of a physical nonlinear analysis features like cracking and plasticity have been included in the calculations.

## 12.2 Case Study

The different models used will be explained. We start with the most simple model. First the beam model has been used. The use of the models are demonstrated by a case. We investigate a concrete floor of 16.7 m wide and 40.0 m long. The point of departure is a beam of 1.0 m wide which represents a strip of the underwater concrete floor. It has a length of 16.7 m (this is the short direction of the building pit) and a depth of 1.0 m. The floor is supported by foundation piles with a  $450 \times 450 \text{ mm}^2$  cross-section. A concrete strength for the underwater concrete and the piles of C25 and C55 respectively was used. The floor was loaded by 7 m of water pressure.

The supports of the concrete floor from the sheetpile wall and piles are translated into translation spring elements. A spring constant has been calculated [Table 12.1].

Table 12.1: SPRING CONSTANTS

Sheet wall			Piles
$K_{\text{vert}} =$	60,000	kN/m per m <sup>1</sup>	$K_{\text{p,vert}} =$ 130,000 kN/m per pile
$K_{\text{hor}} =$	4,000	kN/m per m <sup>1</sup>	

## 12.3 Linear Elastic Calculations

### 12.3.1 Beam Model

The compressive force in the concrete floor is calculated with a load factor 1 and amounts 550 kN/m<sup>1</sup>.

As a result a clamping moment between the sheetpile wall and concrete floor is generated. This moment equals 137.5 kN/m<sup>1</sup>, and is applied on the model by an external constant moment (load case). After calculation, the moment distribution as shown in Figure 12.3a has been found. It is shown from the figure that the clamping

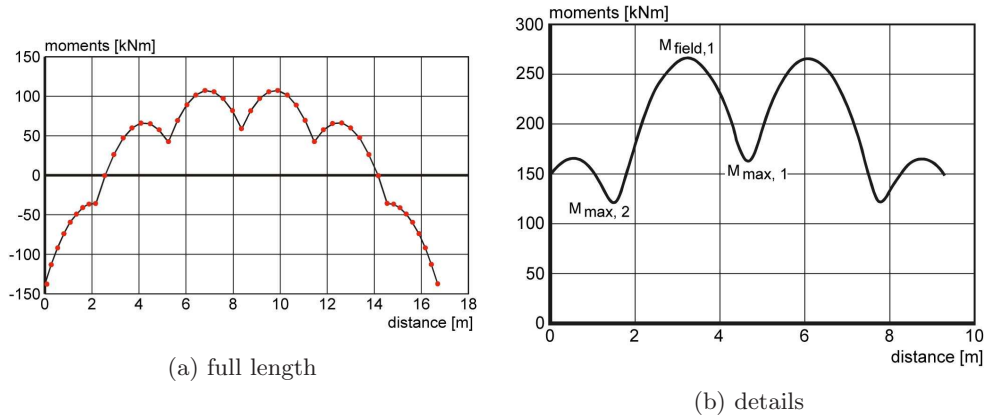


Figure 12.3: Moment distribution  $M_z$  over the length of the beam model

moment is 138 kNm. We can check the sum of moments between the pile distance, which is 3.1 m. Thus  $\frac{1}{8} \times 47 \times 3.1^2 = 56.4$  kNm and this equals the moment values found.

In order to simulate the real structure better an advanced beam model has been used. Firstly, the piles are no longer modeled with an axial spring but with CL12I line interface elements. Consequently, the wideness of the pile gets its own dimension. Thus a surface (cross-section of the pile) can be modeled. Secondly, the sheetpile wall will be modeled as a surface in the horizontal direction. Again a line interface element CL12I has been used for this purpose. In this way the concrete floor is fully supported over the depth. For the concrete floor three-dimensional CL18B beam elements have been used. By using the 'zone' option, the wideness of the concrete floor is increased

to 2.5 m (distance of the piles). The calculation has been made again. Some details about the results of the moment distribution in the short direction of the building pit are shown in Figure 12.3b.

It is clearly shown that the sharp changes in moment above the piles are now smoother. The moments above the piles are about 10 to 15 % larger than in the first beam model. The moments in the midspans between the piles are lower. This phenomenon is caused by the thickness of the piles. It is expected that the advanced model describes reality more appropriate than the first beam model.

### 12.3.2 Advanced Shell Model

In this model the concrete floor has been modeled with two-dimensional CQ40S shell elements. The intersections with the piles and concrete floor are modeled with three-dimensional volume interface elements CQ48I. The same volume interface elements have been used for the sheetpile walls both in horizontal and vertical direction. Consequently, the external moments should be translated to an equivalent surface loading [Fig. 12.4].

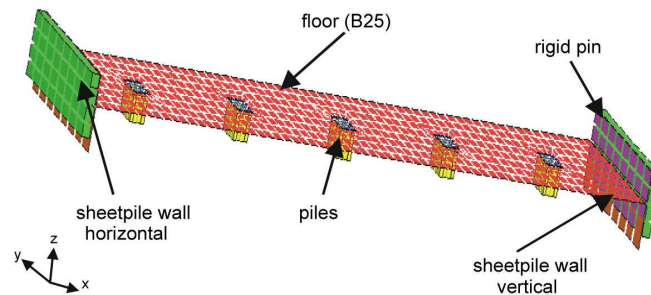


Figure 12.4: Shell model

Some results will be explained. Because the moments and displacements vary along the wideness of the model results in different cross-sections are explained [Fig. 12.5]. The distribution of the moments over the wideness of the model above

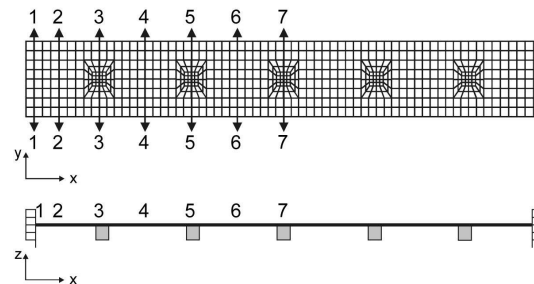


Figure 12.5: Cross-sections 1 and 7 in the shell model

and between the piles respectively is shown in Figure 12.6. Based on these results an effective widthness of 2.0 m can be derived. The area below the moment diagram is 126 kNm and the maximum moment is 65 kNm. Thus, an effective width of 2 m yields a comparable moment ( $2 \times 65 = 130$  kNm). This is less than the pile distance of 2.5 m. Comparison of the moment distribution in the cross-sections 1 to 7 with the results of the beam models, shows only small differences.

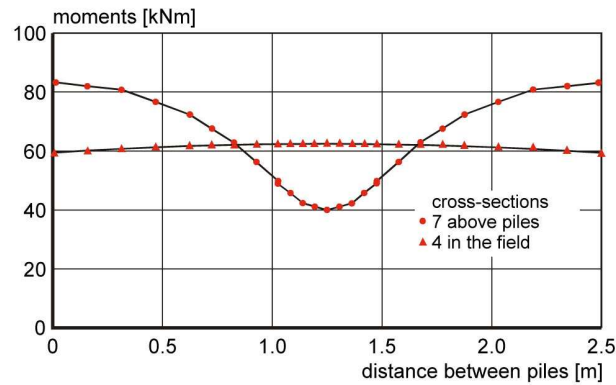


Figure 12.6: Moment distribution in cross-section 5 and 6

### 12.3.3 Three-dimensional Model

The three-dimensional model is the most complete one. The sheetpile wall and the piles have been modeled like in the shell model. The concrete floor has been modeled with quadrilateral quadratic solid elements. In DIANA these type of elements are called 'Bricks' (CHX60 element) [Fig. 12.7]. Only the supports along the sides of the

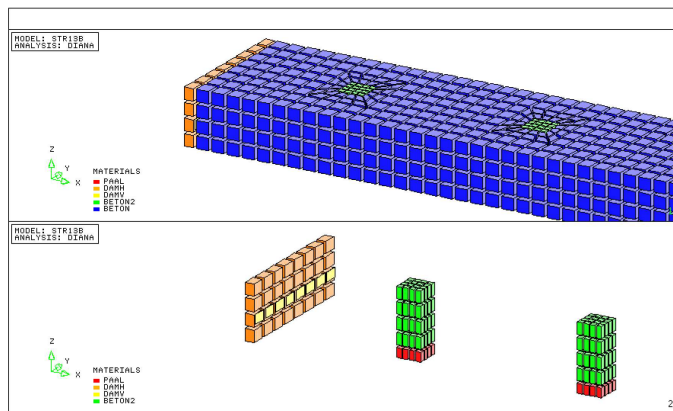


Figure 12.7: Geometry of the floor model



floor have been modified. Still, the displacements in the horizontal face have been suppressed, with this distinction that the supports are not attached to a line but to the lateral surface of the floor.

Table 12.2 shows the vertical displacements in cross-sections 1 and 7 for the three models. The mutual differences turn out to be 2 or 3% smaller.

Table 12.2: VERTICAL DISPLACEMENTS AS FOUND FOR VARIOUS MODELS

Cross-section	Model		
	solid (mm)	shell (mm)	beam (mm)
7	2.53	2.60	2.61
1	1.61	1.63	1.63

## 12.4 Nonlinear Analysis

In all models, the options of cracking and plasticity have been added. The cracking and ultimate load are compared and discussed. The different load factors are summarized in Table 12.3. The differences in the beam and shell models are small. Much

Table 12.3: LOAD FACTORS

		element type		
		beam	shell	solid
first cracking	load factor	1.4	1.4	0.6
	crack position	midspan	midspan	around pile
ultimate	load factor	4.6	3.7	2.7
	crack depth [m]	0.67	0.67	0.75

lower load factors were found with the three-dimensional solid model: 0.6 and 2.7 against 1.4 and 4.6 (3.7) [Fig. 12.8]. Furthermore, the position of first cracking differs with the three-dimensional models. In the solid model, cracking started around the pile at the underside of the concrete floor. The cracks almost reach the top of the floor, the crack depth is 0.75 m for a floor thickness of 1 m. Despite the fact that these cracks are micro cracks, problems could occur with the bond between the pile and concrete floor. This is the topic for a new research currently being performed. Further, water tightness of the concrete floor could be a problem. In general a concrete compressive zone of 200 mm insured a watertight floor. Because the crack depth at the ultimate load is 0.75 m, enough compression depth is left ( $1.00 - 0.75 = 0.25$  m) to ensure watertightness.

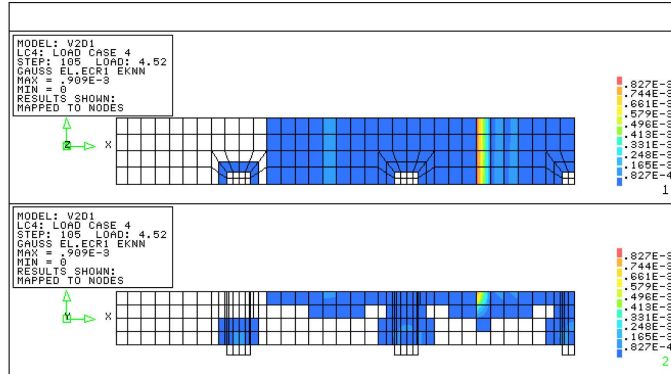


Figure 12.8: Top- and side-view crack propagation around pile at load factor 2.7

## 12.5 Conclusions

1. The results of the three different models, beam, shell and solid, are close to each other if the structure is analyzed linear elastic.
2. A nonlinear analysis gives comparable results for the beam and shell model. The results of the three-dimensional model differ. Not only the ultimate load factor is much lower but also the load factor at first cracking is lower.
3. In a three-dimensional analysis the position of the cracks are different from the one-dimensional and two-dimensional analysis. More research is needed to control the connection between the pile and the concrete floor. We have to be sure that no punching shear will occur before failure in bending of the concrete floor occurs.

**Acknowledgement.** The research reported was carried out in cooperation with the members of CUR-committee VC-61 [17]. Computational work was done by Mr. G. Kwaaitaal [47]. The practical help of Mr. A. Zeilmaker was very much appreciated.

## Chapter 13

# Structural Safety of Concrete Structures

P. H. Waarts

*TNO Building and Construction Research*

A. de Boer and A. Zeilmaker

*Ministry of Transport, Public Works and Water Management – The Netherlands*

### 13.1 Introduction

The structural behavior of building structures is often analyzed with the Finite Element Method. Given the (deterministic) parameters like loading, geometry and material behavior, stresses and deformations of the structure can be calculated. Building regulations prescribe the required reliability of structures (probability of failure). In the regulations, this safety requirement is often translated into partial safety factors. The loading on the structure is then to be multiplied by this factor and the parameters which determine the strength of the structure are to be divided by this factor.

The parameter values, obtained via the safety factor, can be applied as input for a Finite Element Analysis. The structure is considered to be sufficiently safe if the results of the Finite Element Analysis show that the ultimate states (like failure or maximum deflection) have not been reached. For small buildings, or for components of buildings with a known structural system, the approach as outlined above is likely to be adequate. With other types of buildings such a method possibly leads to a substantial over- or underestimation of the structural safety.

In this chapter we will first discuss some probabilistic methods in general [§ 13.1.1], and then the DARS method in some more detail [§ 13.1.2]. Next we will elaborate a case study which has already been discussed in a more general way in Chapter 12: the unreinforced underwater concrete floor [§ 13.2]. The underwater concrete floor is an

excellent candidate for this because some uncertainties exist with respect to loading on the floor, and to thickness and material properties of the floor. Within this case study we will only apply the advanced shell model, and subject it to a linear elastic and to a nonlinear analysis. Finally we will discuss the differences in the number of stochastic variables.

### 13.1.1 Probabilistic Methods

Generally, it is not easy to determine the real probability of failure. The TGB 1990 6700 series [53] require a building structure to be analyzed in a probabilistic way. Three levels of analysis are generally to be considered.

Level III: fully probabilistic,

Level II: like Level III, but with a few approximations,

Level I: semi-probabilistic, or the method of partial factors.

The current TGB regulations, and also the TGB regulations for geotechnics (NEN 6740 [52]), have been set up according to Level I. The Norm Committee has settled the corresponding partial safety factors based on Level II and calibrated these with respect to the regulations from the 1970's. Calculations based on Level I apply safety factors, which for concrete structures is not quite easy. In most cases it is not immediately obvious whether a parameter has a favorable or unfavorable effect. Therefore, two values have to be applied for each parameter. For  $n$  variables this leads to at most  $2^n$  calculations. The amount of calculations increases tremendously: assumed that there are 10 variables then the number of calculations becomes  $2^{10} = 1024$ . However, based on understanding of structural behavior, the number of calculations can often be reduced to  $3 \times n$ .

For building structures, the general TGB regulations require a reliability index  $\beta = 3.6$ . This conforms to a probability of failure during the life span of about  $10^{-4} = \frac{1}{10000}$ . This demands a strong certainty of the understanding of the structural behavior before the number of calculations can be reduced. On the other hand, an alternative is hardly available. Appendix A of the TGB Technical Principles [53] gives requirements regarding Level III calculations, *especially for a significant number of variables, such a calculation is comprehensive and almost impracticable*. The structural engineer has to choose between a practical but unsafe procedure, and a safe but impracticable procedure.

The TGB Technical Principles have been formulated in the beginning of the 1980's. In recent years, numerical methods for reliability analysis and structural behavior have been developed. Furthermore, computers have become tremendously more powerful. The proposition that Level III calculations with a substantial number of variables are infeasible seems to be largely superseded.

### 13.1.2 DARS Method

At the Delft University of Technology (in cooperation with TNO Building and Construction Research and with the Dutch Ministry of Transport, Public Works and

Water Management), it has been investigated whether it would be possible to determine structural safety via a combination of the Finite Element Method and probabilistic methods. Application of the Finite Element Method (FEM) to determine the behavior of a complex building structure is rather obvious in design practice. After the input of geometry data, material properties and loading, the FEM calculates the deformations, stresses and strains. If the input data has been supplied as calculation values (including safety factors) the user has only to check whether the stresses, strains and deformations do not exceed a certain limit value. If so, then the building structure is assumed to meet the safety requirements. If necessary, the FEM analyses can be repeated for other combinations of safety factors. Evidently this is a Level I approach.

The research at TU Delft has ended in a Level III analysis called ‘DARS’ which stands for ‘Directional Addaptive Response surface Sampling’. Jointly used with FEM, the DARS method leads to a FEM analysis with as input parameters the statistic indicators (mean value, standard deviation and type of partitioning) instead of the (deterministic) calculation values. Furthermore, correlations between variables can be specified. Basically, all FEM input parameters can be considered as stochastic variables, for instance:

- Geometry: coordinates, dimensions (thickness, height).
- Material properties:  $E$ -modulus.
- Loading: forces, enforced deformations.

In addition to this input data the ultimate states must be specified. This can be failure of the structure, but also the excess of a required deflection limit. The DARS method then directly determines the reliability of the structure. Typically, the required computing time can be compared to  $3 \times n$  to  $8 \times n$  deterministic analyses. For 100 stochastic variables this conforms to 300 to 800 deterministic analyses.

The DARS method goes as follows. Each stochastic variable is individually increased or decreased until failure occurs. The other variables are kept constant at their average value. Then an analytical function (response surface) is chosen such that this gives about the same results as the FEM analyses. Next ‘directional sampling’ is performed, this resembles Monte Carlo simulation where variables are randomly sampled before the check of limit state excess. Directional sampling also involves random sampling but then followed by proportional increment of the variables until failure. The DARS method performs the directional sampling on the response surface, instead of applying the actual reliability function (FEM analyses). Only if the response surface samples are of great significance a FEM analysis is still performed and, if necessary, followed by adaptation of the response surface.

## 13.2 Example Analysis – Underwater Concrete

In civil engineering practice most of the parameters may seem to be deterministic, but the opposite may be true. Usually, the subjects of non-deterministic behavior

are geotechnical constructions. However, concrete structures can be analyzed non-deterministically as well, as shown in this example. It involves the analysis of an underwater concrete floor, like discussed in Chapter 12, however here we will demonstrate a deterministic approach. Various models will come up. First we will discuss the advanced shell model with attention for some modeling aspects. Next we will present some probabilistic analyses, including the number of stochastic variables.

### 13.2.1 Finite Element Model

**Geometry.** The dimensions of the unreinforced underwater concrete floor of the ‘Advanced shell model’ [§ 12.3.2] are:

Length:  $l = 16.7$  m, measured along the shortest direction of the excavation.

Width:  $b = 2.5$  m, being the center-to-center distance between the piles, measured along the long direction of the excavation.

Thickness:  $t = 1.00$  m.

Figure 13.1 shows the finite element model of the floor only, viewed from above (top) and from aside (bottom). The floor is shown in red and the pile that goes through it

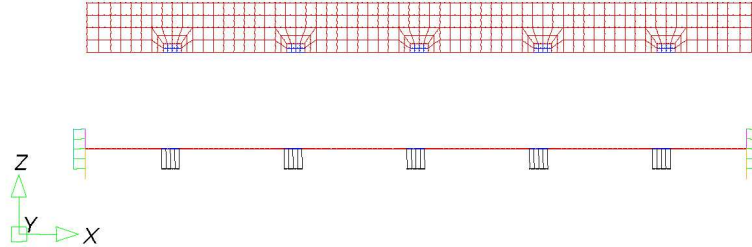


Figure 13.1: Floor FE model

in black with blue on top. The floor will be modeled with quadratic elements. Due to symmetry in longitudinal direction of the floor and the loading, only one half of the width will do. The CUR Committee VC61 has investigated the sensitivity of the floor for omission of the sheet piling and the associated soil layers. Based on this investigation the committee has decided to leave the adjoining sheet piling, and the soil layers behind, out of the analysis model and to consider only the underwater concrete floor. That is why the sheet piling and the soil layers have also been omitted in this analysis model for determination of the reliability index.

**Floor–sheet piling connection.** The thickness of the concrete floor induced the modeling of a so-called ‘spine’ at both sides of the underwater concrete floor. This spine enables the modeling of the connecting face between the floor and the sheet piling at both sides of the analysis model. The thickness of the underwater concrete floor influences the transfer of forces between floor and wall: the presence or absence of sideways pressure  $R$  from the sheet piling onto the floor [Fig.13.2]. See also

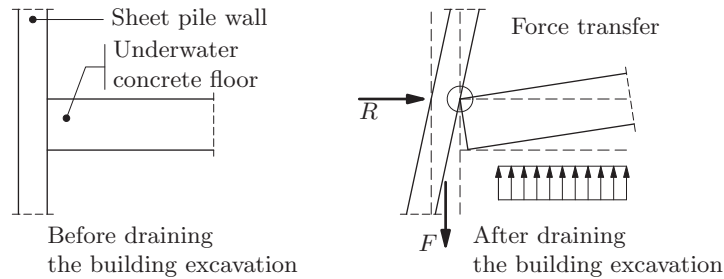


Figure 13.2: Connection sheet piling–concrete floor underwater

article 9 of the CUR Recommendation 77 [17]. The application of spines justifies the designation ‘advanced’ for the shell model of this study. When a tension stress between spine and sheet piling coincides with a puffing up of the floor due to upward water pressure, then the floor will partly come loose from the sheet piling. The spine in the analysis model can simulate this behavior.

**Connection interfaces.** In the advanced shell model the stiffness of the piles has been modeled with interface elements instead of the usually applied translation and rotation springs. This has the advantage that the rotation is implicitly modeled and that the geometry of the pile surface as such is a part of the model. To simulate the connection of the sheet piling to the floor the interface elements have stiffness in both the horizontal and vertical directions, derived from the horizontal and vertical stiffnesses of the sheet piling. Also the connection between piles and floor have been simulated with interface elements, with the stiffness derived from the length and the normal stiffness of the piles. Figure 13.3 shows the two connection details as included in the analysis model. The CUR Committee VC61 has also determined the

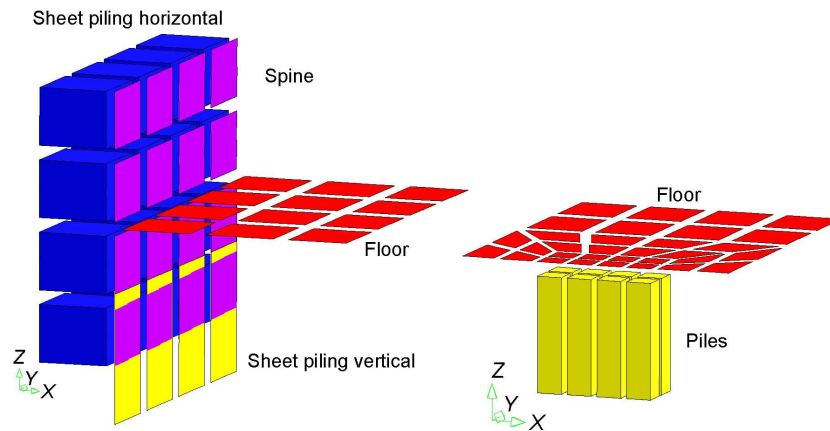


Figure 13.3: Model for connection sheet piling–floor and floor–piles

material properties with respect to the horizontal and vertical springs that simulate the connections in the CUR beam model.

**Material properties.** Table 13.1 shows the material properties as applied for the various parts of the construction. It's true that concrete quality C40 for the piles is

Table 13.1: MATERIAL PROPERTIES

Part	property	value
Floor	concrete quality	C20
	mass density	$\rho$ 2300 kg/m <sup>3</sup>
	modulus of elasticity	$E_c$ 28.5 kN/mm <sup>2</sup>
Sheet piling	moment of inertia	$I_z$ 44450 cm <sup>4</sup> /m <sup>1</sup>
	vertical spring stiffness	$K_v$ 60000 kN/m/m <sup>1</sup>
	horizontal spring stiffness	$K_h$ 4000 kN/m/m <sup>1</sup>
Piles	concrete quality	C40 <sup>†</sup>
	area	$A_x$ 0.45 × 0.45 m <sup>2</sup>
	modulus of elasticity	$E_c$ 20.0 kN/mm <sup>2</sup>

<sup>†</sup> CUR Rec. 77 → C20

rather low, during the formulation of the calculation examples for CUR Recommendation 77 the quality C20 has been assumed with the associated modulus of elasticity  $E_c = 20.0$  kN/mm<sup>2</sup>.

**Supports.** The underwater concrete floor is supported at the sides of the sheet piling and at the piles. The tips of the interface elements that simulate the piles and the sheet piling have been fully supported, that is in all directions.

**Loadings.** Three basic loads form the loading on the analysis model:

1. Horizontal pressure loads of 550 kN/m<sup>1</sup> on the floor. These pressures come from the sheet piling and point in opposite directions.
2. An eccentricity of 0.25 m of load 1 above the so-called system plane of the plate field. This introduces a bending moment of 137.5 kN/m<sup>1</sup> on both sides of the floor.
3. An upward load of +47 kN/m<sup>2</sup>, resulting from a downward dead weight load of −23 kN/m<sup>2</sup> and an upward water pressure of +70 kN/m<sup>2</sup>.

### 13.2.2 Choosing the Number of Stochastic Variables

To get a first impression of the probabilistic analysis of the underwater concrete floor the number of stochastic variables must be chosen. The geometry, material



properties, loads and supports must be considered in this choice. Consideration of stochastic values of for instance the coordinates of the nodes would be superfluous. Regarding the geometry it is obvious to make the floor thickness stochastic. After all, also the CUR Recommendation 77 concerning calculation rules indicates in article 7.1 a variable thickness.

Still open to question is the direction of the force transmission at the connection of the sheet piling and the floor. However, considering modeling of this detail in the advanced model, no stochastic variable will be introduced for this force direction. The modulus of elasticity of the underwater concrete floor is a stochastic variable, just like the five basic load cases. This gives a total of seven stochastic variables [Table 13.2]. Note that the shift parameter has only been applied for the floor thickness and

Table 13.2: STOCHASTIC VARIABLES FOR A SINGLE CASE

Stochastic func.	Symbol	Unit	Mean value	Standard dev.	Shift	Distribution
Modulus of elasticity	$E_{\text{floor}}$	$\text{kN/m}^2$	$2.85 \times 10^7$	$0.285 \times 10^7$	1000.	Log-normal
Floor thickness	$t_{\text{floor}}$	m	1.0	0.1	0.1	Log-normal
Hor. edge force left	$F_{\text{HL}}$	kN	550.	55.0	0.0	Log-normal
Hor. edge force right	$F_{\text{HR}}$	kN	550.	55.0	0.0	Log-normal
Moment edge left	$M_{\text{HL}}$	$\text{kN} \cdot \text{m}$	137.5	13.75	0.0	Log-normal
Moment edge right	$M_{\text{HR}}$	$\text{kN} \cdot \text{m}$	137.5	13.75	0.0	Log-normal
Water – dead weight	$Q_{\text{wa-dw}}$	$\text{kN/m}^2$	47.0	4.7	0.0	Log-normal

the modulus of elasticity. This is done to avoid numerical problems, because in an analysis these parameters must always be positive. For loadings this is not required.

The floor thickness is expected to be the most important parameter with respect to structural reliability. Therefore we will go into more details about this thickness. For simplification reasons we have skipped possible correlations in these considerations. The concrete slurry is applied on the bottom of the excavation by means of a lance. This induces us to subdivide the plan of the underwater concrete floor in the following zones.

- zones around the piles,
- zones adjacent to both sheetpile walls,
- zones in the field, in longitudinal and transverse direction.

Figure 13.4 on the following page shows this subdivision. In total this yields twenty-four stochastic variables: one for material and five for loading as mentioned before, and eighteen additional ones for the thickness of the underwater concrete floor. Also the material properties of the floor may be considered to depend on the location of the underwater concrete. This brings in another variant: further subdivision of the number of stochastic variables for material parameters. To make things easy, the same eighteen zones as used for the thickness will also be applied for the material.

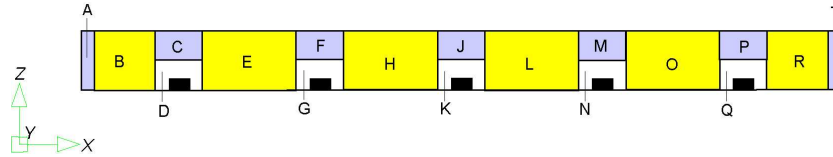


Figure 13.4: Floor subdivided in zones

### 13.2.3 Probabilistic Analysis

**Based on linear elastic analysis.** A probabilistic analysis is stand-alone, i.e., it does not depend on any analysis previously performed. Therefore, we will now discuss the type of probabilistic analysis. In daily practice of structural design, a start with a linear elastic analysis is very common. At any stage in the design process the current structural safety may be asked for. A probabilistic analysis, based on a linear static analysis, is then obvious. Based on certain understandings and checks, related to the final design stage, additional analyses may be performed. Such additional analyses may typically involve buckling, wrinkling, and physical and geometrical nonlinear phenomena. Ultimately, a probabilistic analysis may also be based on dynamic effects. In this case study we will restrict ourselves to a probabilistic analysis based on a linear elastic analysis with one deepening: toward a nonlinear analysis.

**Based on nonlinear analysis.** Control via a nonlinear analysis may be performed, for instance,

- to get an impression of a nonlinear load–displacement diagram,
- to investigate whether the sheetpile wall separates from the underwater concrete floor,
- to assess the distribution of the reaction force at the point where the pile sticks through the concrete floor.

It can be seen that the bottom has no longer stresses, i.e., the floor has no contact with the sheetpile wall due to upward bending of the floor. The presentation of a nonlinear load–displacement diagram is less relevant in this case. The two other aspects mentioned are of more importance, where the fact that the sheetpile wall peels of the concrete floor is shown in Figure 13.5. This figure depicts the normal stress of the attachment of the sheetpile wall to the floor. The connection of the stick-through part of the pile to the concrete floor is not discussed here, neither was it discussed within the aforementioned CUR Recommendation 77.

A physical nonlinear analysis naturally includes the specification of the physical nonlinear material properties. For the model in this case study we must extend the material properties for the various structural parts as indicated in Table 13.3 on the next page.

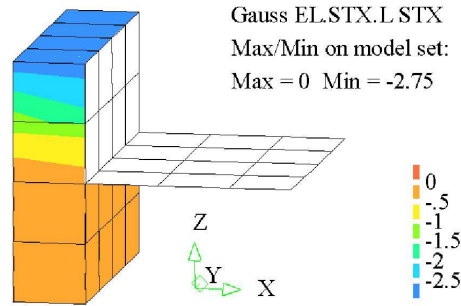


Figure 13.5: Stress distribution along spine at left floor-sheetpile wall connection

Table 13.3: NONLINEAR MATERIAL PROPERTIES

Structural part	Physical non-linear option	Type	Relevant parameters	Value
Floor	Plasticity criterion	Drucker	Cohesion	$6.3 \times 10^3$
			Friction angle	$30^\circ$
			Dilatancy angle	$30^\circ$
	Softening	Linear	$\epsilon_{ult}$	$1.7 \times 10^{-3}$
	Cracking	Constant	Ultimate tension stress in principal direction	$1.15 \times 10^3$
Connection sheetpile wall-floor	Shear	Total		
	Friction	Coulomb	Cohesion	0
			Friction angle	$0.1 \times 10^{-3^\circ}$
			Dilatancy angle	$0^\circ$
	Opening		Ultimate displacement	0

### 13.2.4 Choosing the Limit States

In addition to the type and number of the stochastic variables, also the limit states must be chosen. The displacements, strains and stresses are the most obvious limit states. For the probabilistic analysis based on the linear elastic analysis we have chosen for one single limit: the ultimate concrete stress for which no cracks occur in the floor. This means that for concrete quality C20 of the underwater concrete floor the allowable concrete stress is  $1.15 \text{ N/mm}^2$ .

For the limit states in a probabilistic analysis based on a nonlinear analysis we have chosen an ultimate strain: the strain where a micro crack changes into an open crack. An associated stress limit can not be given here, as this is zero at that stage. This means that no relevant value is available to determine the structural safety. Therefore, the determination of the chance to failure migrates from an initial crack to a real open crack. The value of the real open crack involves the additional specification of a single material parameter for the underwater concrete floor: the

ultimate strain limit  $\varepsilon_{\text{ult}} = 1.7 \times 10^{-3}$ .

### 13.2.5 Parameters for Probabilistic Analysis

The following parameters drive the probabilistic analysis:

- number of iteration steps  $n_{\text{steps}}$  is variable,
- minimum distance between response surface and limit state  $p_{\text{cond}} = 5.0$ ,
- maximum number of iterations to find the limit states  $p_{\text{max}} = 15$ ,
- convergence criterion for termination of the calculation process  $p_{\text{norm}} = 0.05$ ,
- required variation of the reliability index  $p_{\text{vari}} = 0.2$ .

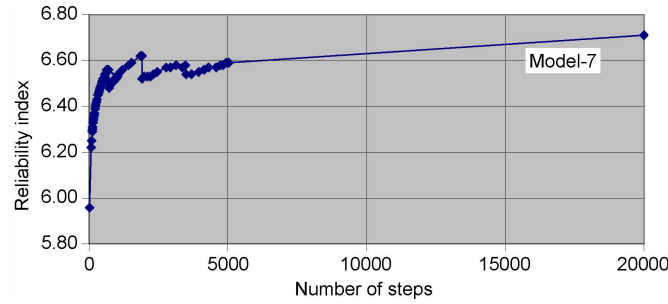
The number of analyses subsequently to the basic analysis varies as follows. The number of basic cases is equal to  $2 \times$  the number of stochastic variables, plus one. This yields 15 analyses for the simple case and respectively 49 and 83 analyses for the subsequent variations. After that, the response surface can be set up and then the analysis process proceeds depending on the direction. Usually at least 15 additional samples are required to get a first indication of the value of the reliability index. Certainty about the accuracy of the reliability index may be related to the value of the variation of the reliability index. Hence the additional parameter  $p_{\text{vari}}$ , with in this case a value of 0.2.

### 13.2.6 Probabilistic Results Based on Linear Elastic Analysis

The reliability index  $\beta$  is given as direct output, in this case  $\beta = 6.71$  for the most simple analysis model. At first sight, the design as chosen for this underwater concrete floor seems appropriate. Indeed, generally speaking a reliability index with a  $\beta > 3.6$  is OK (see the Dutch building code TGB NEN 6700 [53]). Also the minimum value of the reliability index,  $\beta = 6.4$ , does not give rise to concern. Thus, the variation in the  $\beta$  factor is small:  $V(\mathcal{P}_f) = 0.277$ . It is true that the driving parameters have not reached a value of 0.2, however the value is sufficiently small and therefore acceptable at a reliability index as high as  $\beta = 6.71$ .

This analysis reached 28636 limit state evaluations, which is fairly high. The number of samples is 375 in total which should be more than enough considering the number of stochastic variables (7). This is also proven by the low variation of the reliability index. The total number of FE analyses for this version is 9975. This is also high, considering the number of 375 samples. Indeed, a large number of FE analyses are still required, that did not directly cause a lower reliability index. However, the number of analyses is only half that of a full Monte Carlo analysis. This already demonstrates the first gain of computing time.

Of course, the relation between the reliability index  $\beta$  and the number of steps can also be indicated, like shown in Figure 13.6 on the facing page. In this figure, the last step has been interrupted at a maximum of 20000. This means that the

Figure 13.6: Relation reliability index  $\beta$  and number of steps for simple model

corresponding reliability index,  $\beta = 6.71$ , is not yet the maximum value. Nevertheless, the development between steps 5000 and 20000 shows a slight increment of the reliability index of 0.12, which is small and inspires confidence sufficiently.

Also the variation of the reliability index  $V(\mathcal{P}_f)$  can be graphed against the number of steps, which we do not show here. In stead, we may report that  $V(\mathcal{P}_f)$  decreases from 1.0 to 0.277 at 20000 steps. Once more we note that in this situation the required convergence criterion  $p_{\text{vari}} = 0.2$  has not yet been achieved.

Table 13.4: INFLUENCE FACTORS FOR RELEVANT STOCHASTIC VARIABLES

Stochastic variable	Symbol	No.	Contribution [%]
Modulus of elasticity	$E_{\text{floor}}$	1	1.5
Floor thickness	$t_{\text{floor}}$	2	53.1
Horizontal edge load left	$F_{\text{HL}}$	3	45.0

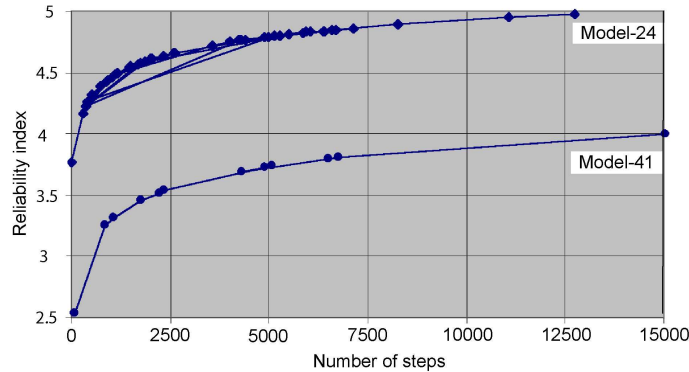
In addition to the reliability indices and the limits, also the influence factors can be output. This is of interest to determine the extent to which a certain stochastic variable has influenced the reliability index  $\beta$ . Table 13.4 shows this influence for the relevant stochastic variables, i.e., with an influence factor greater than 1%. This table clearly shows that the floor thickness and the horizontal force that acts on the left side of the underwater concrete floor affect the determination of the reliability index at most. With respect to the work on the building project we may already indicate that the floor thickness must be checked carefully.

When discussing the choice of the number of stochastic variables we have already indicated that there are two variations. Firstly the extension of the number of stochastic variables via subdivision of the floor thicknesses in various zones [Fig. 13.4 p. 176], each of these with a specific thickness. The second variation also subdivides the applied material for each of these zones. This implies an extension of the number of stochastic variables from 24 to 41. Table 13.5 on the following page gives the specific probabilistic output. This table shows that the reliability index decreases when the number of stochastic variables increases. The number of steps varies from 15000 to 200000.

Table 13.5: RESULTS OF PROBABILISTIC ANALYSES BASED ON LINEAR ELASTIC ANALYSES

Result	Symbol	Model-7	Model-24	Model-41
Reliability index	$\beta$	6.71	5.009	4.577
Minimum reliability index	$\beta_{\min}$	6.4	4.842	4.129
Variation reliability index	$V(\mathcal{P}_f)$	0.277	0.692	3.45
Number of steps	$n_{\text{steps}}$	20000	15000	200000
Number of limit state evaluations	$n_{\text{limit}}$	28636	467	344
Number of samples	$n_{\text{samples}}$	375	54	23
Number of FE runs	$n_{\text{FE}}$	9975	104	108

The model with seven stochastic variables, Model-7, showed convergence of the reliability index for 20000 steps [Fig. 13.6]. The other graphs [Fig. 13.7], show an excellent convergence for the models with 24 and 41 stochastic variables. However,

Figure 13.7: Relation reliability index  $\beta$  and number of steps for other models

this requires at most 54 FE analyses. On the other hand, the model with 41 stochastic variables only requires 23 FE analyses, which also yields a considerable reduction of the analysis time. The maximum of 200000 steps causes a substantial change in the reliability index. Between 15000 and 200000 steps the reliability index increases a bit with a value of 0.13 (from 4.0 to 4.129). However, the variation of the reliability index shows a strange discontinuity which we provisionally will attribute to the pilot version as applied to analyze the construction.

A similar table can apparently be given for the relevant influence factors [Table 13.6]. Here we only give the stochastic variables which cause an influence of more than 5%. Also this table shows that the reliability index mainly depends on the thicknesses of the floor parts, positioned close to the left-side sheetpile wall, and on the horizontal force acting from the sheetpile wall onto this part of the floor.

Table 13.6: INFLUENCE FACTORS FOR PROBABILISTIC ANALYSES BASED ON LINEAR ELASTIC ANALYSES

Stochastic variable	Symbol	Model-7	Model-24	Model-41
Modulus of elasticity	$E_{\text{floor}}$	1.5	–	–
Floor thickness	$t_{\text{floor}}$	53.1	–	–
Thickness sheet piling–floor left	$t_{\text{HA}}$	n.a.	24.9	25.9
Thickness floor first zone	$t_{\text{HB}}$	n.a.	25.3	26.3
Horizontal edge load left	$F_{\text{HL}}$	45.0	49.4	47.6

### 13.2.7 Probabilistic Results Based on Nonlinear Analysis

After the probabilistic analysis based on linear elastic analyses we will now discuss the probabilistic analysis based on nonlinear analyses. In this case the appearance of cracks is of major importance. For this variant the material indeed is an important parameter for the determination of the reliability index  $\beta$ . Also in this analysis we will apply the floor zones with specific material properties for each zone which yields a maximum of 41 stochastic variables.

Table 13.7: RESULTS OF PROBABILISTIC ANALYSES BASED ON NONLINEAR ANALYSES

Result	Symbol	Model-7	Model-24	Model-41
Reliability index	$\beta$	5.351	4.106	3.494
Minimum reliability index	$\beta_{\text{min}}$	5.220	3.932	3.358
Variation reliability index	$V(\mathcal{P}_f)$	0.815	0.599	0.508
Number of steps	$n_{\text{steps}}$	230	10000	10000
Number of limit state evaluations	$n_{\text{limit}}$	710	667	702
Number of samples	$n_{\text{samples}}$	51	53	14
Number of FE runs	$n_{\text{FE}}$	31	131	158

The results of the probabilistic analysis [Table 13.7], show that for the simplest model 230 steps have been executed. This is not sufficiently, however the current software fails here which we again attribute to the applied pilot version of the probabilistic module. If we nevertheless consider the convergence behavior of the reliability index then the results turn out to be not that bad. After all, the convergence of the reliability index is reasonably good. Notably, the number of FE analyses has considerably decreased: from 9975 to 31, which pleasingly decreases the total analysis time.

The two models with more stochastic variables have been analyzed until 10000 steps. It must be noted that the model with 41 stochastic variables has a mere 14 samples. Nevertheless, the variation of the reliability index has well decreased until 0.508, albeit that again the initially specified  $p_{\text{vari}} = 0.2$  has not been reached.

The 230 steps for the simplest model already distinctly indicate the reliability index, based on the 7 stochastic variables chosen [Fig. 13.8]. Also we can see that sometimes the analysis reverts to a previously determined reliability level. Obviously

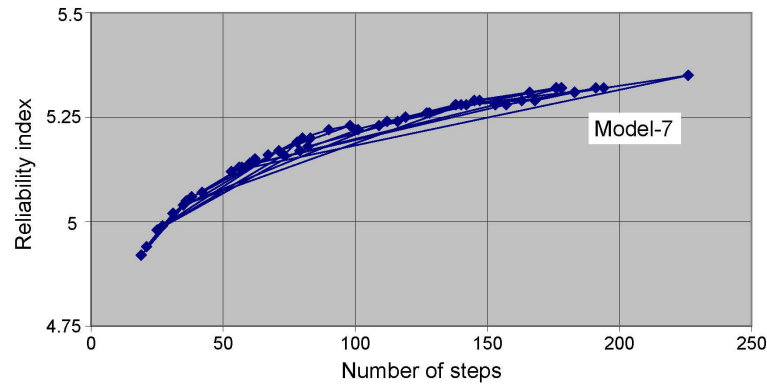


Figure 13.8: Relation reliability index  $\beta$  and number of steps for simple model based on nonlinear analyses

the analysis does not directly deliver a smooth curve. On some places the reliability index decreases in such a way that the response surface must be set up once again. This also happened a few times in the linear elastic analysis, but it predominates the nonlinear analysis. In an analysis with a large number of steps the returning lines in the graphs will of course be wiped out by one thick line, however, the phenomenon can still be observed.

Figure 13.9 on the next page shows the relation between the reliability index and the number of steps of the other models. Again we observe a good convergence. Even the 13 steps of the model with 41 stochastic variables can all be distinguished in the graph. Again we can tabulate the relevant influence factors. Table 13.8 shows this influence for the relevant stochastic variables, i.e., with an influence factor greater than 5%. We can clearly observe that the thicknesses of the specific floor zones

Table 13.8: INFLUENCE FACTORS FOR PROBABILISTIC ANALYSES BASED ON NON-LINEAR ANALYSES

Stochastic variable	Symbol	Model-7	Model-24	Model-41
Modulus of elasticity	$E_{\text{floor}}$	7.6	18.5	n.a.
Modulus of elasticity sheet p. left	$E_{\text{floorA}}$	n.a.	n.a.	7.4
Modulus of elasticity sheet p. right	$E_{\text{floorT}}$	n.a.	n.a.	7.4
Floor thickness	$t_{\text{floor}}$	49.4	n.a.	n.a.
Thickness sheet piling-floor left	$t_{\text{HA}}$	n.a.	26.4	25.2
Thickness floor first zone	$t_{\text{HB}}$	n.a.	12.6	12.0
Thickness floor last zone	$t_{\text{HR}}$	n.a.	12.6	12.0
Thickness sheet piling-floor right	$t_{\text{HT}}$	n.a.	26.4	25.2
Horizontal edge load left	$F_{\text{HL}}$	10.6	—	—
Moment edge load left	$M_{\text{HL}}$	12.9	—	—
Moment edge load right	$M_{\text{HR}}$	14.8	—	—

close to the left-hand sheet piling still have the major influence. Also the modulus



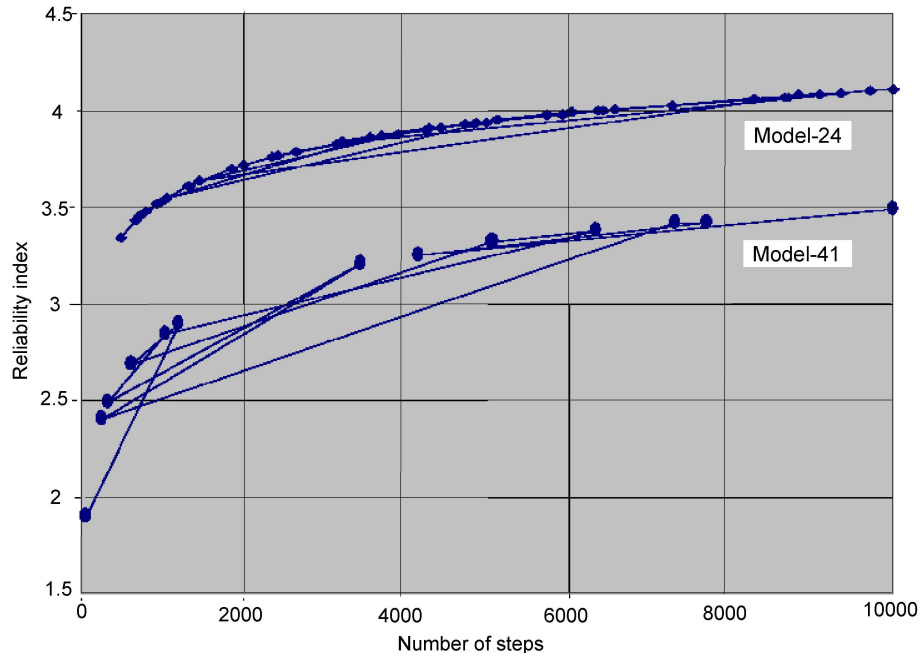


Figure 13.9: Relation reliability index  $\beta$  and number of steps for other models based on nonlinear analyses

of elasticity influences the value of the reliability index, however not to the same extent as the floor thicknesses. It also turns out that the influence of the force load decreases below 5%. Hence, we may once more conclude that the floor thickness must be checked carefully during the work on the building project.

### 13.3 Conclusions

1. The DARS method is a Level III reliability method which requires a relatively low analysis time, especially compared to the full Monte Carlo method.
2. The case study of the underwater concrete floor demonstrates the benefits of the DARS method when compared to the prevailing practice (reliability index and influence factors).
3. Already for a small number of steps the DARS method shows a reasonable convergence of the the reliability index.
4. With the DARS method, an increasing number of stochastic variables in the analysis model always yields a decreasing reliability index.
5. With the DARS method, an increasing number of stochastic variables in the analysis model always yields a decreasing variation of the reliability index.

6. For the linear elastic analyses, the influence factors of the various stochastic variables chosen are particularly concentrated around the left-side sheet piling. For the nonlinear analyses a symmetric pattern shows up.

### Litterature

- The PhD thesis of Waarts [94].
- CUR Recommendation 77 [17].
- Calculation examples by Hagaraars and Saveur [34].
- The MSc thesis of Kwaaitaal [47].
- The DIANA User's Manual [70].
- The Dutch building code TGB NEN 6700 [53].

# Bibliography

- [1] *Int. Conf. of Building Officials* (Whittier, 1997), vol. Uniform Building Code 1997.
- [2] ACI. Building code requirements for reinforced concrete. Tech. Rep. ACI 318M, American Concrete Institution, Farmington Hills, 1997.
- [3] ATTIOGBE, E. K., AND DARWIN, D. Submicrocracking in cement paste and mortar. *ACI Journal* 6 (1987), 491–500.
- [4] AUTODESK CORPORATION. *AutoCAD Version 13 for PCs c4a*. San Francisco, July 23 1998. Online: <http://www.autodesk.com>.
- [5] BARENBLATT, G. I. The mathematical theory of equilibrium cracks in brittle fracture. *Adv. Appl. Mech.* 7 (1962), 55–129.
- [6] BAŽANT, Z. P., AND OH, B. H. Crack band theory for fracture of concrete. *Mater. & Struct. (RILEM)* 16 (1983), 155–177.
- [7] BILLINGTON, S. L., AND KWAN, W.-P. Simulation strategies for structural concrete members under cyclic load. *J. Struct. Eng., ASCE* 127, 12 (2001), 1391–1401.
- [8] BLAAUWENDRAAD, J., AND HOOGENBOOM, P. C. J. Stringer panel model for structural concrete design. *ACI Structural Journal* 93, 3 (May–June 1996), 295–305.
- [9] BRÆSTRUP, M. W., NIELSEN, M. P., AND BACH, F. Rational Analysis and Design of Stirrups in Reinforced Concrete Beams. Tech. Rep. R 79, Technical University of Denmark – Structural Research Laboratory, March 1977.
- [10] BSI. Flat-bottomed, vertical, cylindrical storage tanks for low temperature service. Tech. Rep. BS 7777, British Standards Institution, London, 1993.
- [11] BSI. Structural use of concrete. Tech. Rep. BS 8110-1/2/3, British Standards Institution, London, 1997, 1985/1989, 1985/1989.
- [12] CEB. Fire Design of Concrete Structures in accordance with CEB-FIP Model Code 1990. Bulletin d’Information No. 208, Comité Euro-International du Béton, 1991.

- [13] CEB-FIP. *CEB-FIP Model Code 1990*. Comité Euro-International du Béton, 1993.
- [14] CHEN, W. F. *Plasticity in Reinforced Concrete*. McGraw-Hill, New York, 1982.
- [15] CUR. Betonmechanica voorbeelden van niet-lineaire berekeningen met DIANA. Report 134, CUR Research Committee A26, Gouda, 1987.
- [16] CUR. Aanbeveling 37 – Hoge Sterkte Beton. *Cement*, 5 (1994).
- [17] CUR. Design rules for unreinforced underwater concrete floors. Recommendation 77, CUR Research Committee VC61, Gouda, 2001. In Dutch.
- [18] CUR. Geavanceerd rekenen voor civiele constructies. Report 2003-3, CUR Research Committee A36, Gouda, 2003.
- [19] DE BORST, R. Smeared cracking, plasticity, creep and thermal loading – a unified approach. *Comp. Meth. Appl. Mech. Eng.* 62 (1987), 89–110.
- [20] DE BORST, R., AND NAUTA, P. Non-orthogonal cracks in a smeared finite element model. *Eng. Comp.* 2 (1985), 35–46.
- [21] DESPOT, Z. *Methode der finiten Elemente und Plastizitätstheorie zur Bemessung von Stahlbetonscheiben*. PhD thesis (IBK Bericht 215), Institut für Baustatik und Konstruktion, ETH, Zürich, 1995.
- [22] DROSTE, S. W. H. Voorgespannen HSB-liggers belast op dwarskracht en of wringing. Tech. Rep. TUE/CCO/98.11, Technische Universiteit Eindhoven, 1998.
- [23] DUGDALE, D. S. Yielding of steel sheets containing slits. *J. Mech. Phys. Solids* 8 (1960), 100–108.
- [24] ELFGREN, L. *Fracture Mechanics of Concrete Structures – Applications*. E & FN Spon, London/New York, 1989.
- [25] EVANS, R. H., AND MARATHE, M. S. Microcracking and stress-strain curves for concrete in tension. *Mater. & Struct., Research and Testing (RILEM)* 1, 1 (1968), 61–64.
- [26] FEENSTRA, P. H. *Computational Aspects of Biaxial Stress in Plain and Reinforced Concrete*. PhD thesis, Delft University of Technology, 1993.
- [27] FEENSTRA, P. H., AND DE BORST, R. A plasticity model and algorithm for model-I cracking in concrete. *Int. J. Num. Meth. Eng.* 38 (1995), 2509–2530.
- [28] FEENSTRA, P. H., AND DE BORST, R. A survey of plasticity and damage-based crack models for FE analysis of fracture in concrete. In *Computational Plasticity*, D. R. J. Owen et al., Ed. CIMNE, Barcelona, 1995, pp. 1535–1546.

- [29] FEENSTRA, P. H., AND ROTS, J. G. Comparison of concrete models for cyclic loading. In *Modeling of Inelastic Behavior of RC Structures under Seismic Loading*, P. Benson Shing and Tada-aki Tanabe, Eds. ASCE, 2001, pp. 38–55.
- [30] FEENSTRA, P. H., ROTS, J. G., ARNESEN, A., TEIGEN, J. G., AND HØISETH, K. V. A 3D constitutive model for concrete based on a co-rotational concept. In *Computational Modeling of Concrete Structures*, R. de Borst, N. Bićanić, H. Mang, and G. Meschke, Eds., vol. 1. A. A. Balkema, Rotterdam, 1998, pp. 13–22.
- [31] FEMMASSE BV. *On-line Help/Manual Module HEAT of FEMMASSE*, 1990–2000. Available on [www.femmasse.nl](http://www.femmasse.nl).
- [32] FIP/CEB. *Report on Methods of Assessment of the Fire Resistance of Concrete Structural Members*. Fédération Internationale de la Précontrainte, Wexham Springs/Slough, 1978.
- [33] FRISSEN, C. M. Numerieke Analyse Kokerbalkviaduct. Tech. Rep. 1999-MIT-NM-R0013, TNO Building and Construction Research, 2000.
- [34] HAGENAARS, P. A., AND SAVEUR, J. Toepassing van CUR Aanbeveling 77. *Cement*, 4 (2001).
- [35] HENDRIKS, M. A. N., AND ROTS, J. G., Eds. *Finite Elements in Civil Engineering Applications* (Rotterdam, 2002), Proc. 3rd DIANA World Conference, Tokyo 2002, Balkema.
- [36] HILLERBORG, A. Fracture mechanics concepts applied to moment capacity and rotational capacity of reinforced concrete beams. *Eng. Fract. Mech.* 35, 1/2/3 (1990), 233–240.
- [37] HILLERBORG, A., MODEER, M., AND PETERSSON, P.-E. Analysis of crack formation and crack growth in concrete by means of fracture mechanics and finite elements. *Cem. Concr. Res.* 6, 6 (1976), 773–782.
- [38] HOGESLAG, A. J., AND VERHOEF, L. G. W. Onderzoek bouwtechnische staat van de draagconstructie van bedrijfsgebouw ‘De Adelaar’ te Wormerveer. Research Report for the province North Holland, 1989.
- [39] HOOGENBOOM, P. C. J. *Discrete Elements and Nonlinearity in Design of Structural Concrete Walls*. PhD thesis, Delft University of Technology, Delft University Press, 1998.
- [40] HOOGENBOOM, P. C. J., AND BLAAUWENDRAAD, J. Quadrilateral shear panel. *Engineering Structures* 22, 12 (2000), 1690–1698.
- [41] JANSSEN, P. *Tragverhalten von Tunnelausbauten mit Gelenktübingen*. PhD thesis, Technische Universität Carolo-Wilhelmina, Braunschweig, 1983.

- [42] KAALBERG, F. J., AND HENTSCHEL, V. Tunneling in Soft Soil with a High Water Level and Pile Foundations: Towards the development of settlement-oriented and settlement-minimizing TBM operation. In *Proc. ITA World Tunnel Congress* (Oslo, 1999).
- [43] KÖNIG, G., MEYER, J., AND SINT, A. Round robin analysis on modelling of over-reinforced concrete beams – calculation of the load–deformation behavior of concrete beams with the BDZ model. In *Proc. FraMCoS-3* (Freiburg, 1998), H. Mihashi and K. Rokugo, Eds., AEDIFICATIO Publishers, pp. 1241–1252.
- [44] KOTSOVOS, M. D. Effect of testing technique on the post-ultimate behavior of concrete in compression. *Mater. & Struct. (RILEM)* 16, 92 (1983), 3–12.
- [45] KUPFER, H. Das Verhalten des Betons unter mehrachsiger Kurzzeitbelastung unter besonderer Berücksichtigung der zweiachsiger Beanspruchung. Heft 229, Deutscher Ausschuß für Stahlbeton, Berlin, 1973.
- [46] KUPFER, H. B., AND GERSTLE, K. H. Behavior of concrete under biaxial stresses. *J. Eng. Mech. Div., ASCE* 99, 4 (1973), 853–866.
- [47] KWAAITAAL, G. J. J. Flow of forces and cracking in underwater concrete floors. Tech. Rep. BSRAP-R-01023-B, Ministry of Transport, Public Works and Water Management, The Hague, July 2001. In Dutch.
- [48] MAIER, J., AND THÜRLIMAN, B. Bruchversuche an Stahlbetonscheiben. Tech. Rep. 8003-1, Eidgenössische Technische Hochschule, Zürich, 1985.
- [49] MARKESET, G. *Failure of Concrete under Compressive Strain Gradients*. PhD thesis, Norges Tekniske Hogskole, Trondheim, 1993.
- [50] MARKESET, G. Strain softening and structural analysis of beams failing in compression. In *Proc. FraMCoS-3* (Freiburg, 1998), H. Mihashi and K. Rokugo, Eds., AEDIFICATIO Publishers, pp. 1183–1194.
- [51] MESCHKE, G. Consideration of aging of shotcrete in the context of a 3D viscoplastic material model. *Int. J. Num. Meth. Eng.* 39 (1996), 3123–3143.
- [52] NEN. TGB 1990 – Geotechnics; Basic requirements and loads. Tech. Rep. NEN 6740, Nederlands Normalisatie-instituut, 1991. in Dutch.
- [53] NEN. TGB 1990 – Technical Principles for Building Structures. Tech. Rep. NEN 6700, Nederlands Normalisatie-instituut, 1991. in Dutch.
- [54] NEN. TGB 1990 – Voorschriften Beton (VBC 1995) (Regulations for concrete. Structural requirements and calculation methods). Tech. Rep. NEN 6720, Nederlands Normalisatie-instituut, 1995.
- [55] NIELSEN, M. P. *Limit Analysis and Concrete Plasticity*. Prentice-Hall, London, 1984.

- [56] RAISS, M. E., DOUGILL, J. W., AND NEWMAN, J. B. Observation of the development of fracture process zones in concrete. In *Fracture of Concrete and Rock – Recent Developments*, S. P. Shah, S. E. Swartz, and B. Barr, Eds. Elsevier, London/New York, 1989, pp. 243–253.
- [57] RIGGS, H. R., AND POWEL, G. H. Tangent constitutive matrices for inelastic finite element analyses. *Int. J. Num. Meth. Eng.* 29 (1990), 1193–1203.
- [58] RILEM. Test method for measurement of the strain-softening behaviour of concrete under uniaxial compression. *Mater. & Struct. (RILEM)* 33, 230 (2000), 347–351. Test recommendation, RILEM TC 148-SSC.
- [59] ROELFSTRA, P. E., SALET, T. A. M., AND KUIKS, J. E. Defining an application of stress-analysis-based temperature difference limits to prevent early-age cracking in concrete structures. In *Thermal Cracking in Concrete at Early Ages*, R. Springenschmid, Ed., RILEM Proc. 25. E & FN Spon, London, 1994, pp. 273–280.
- [60] ROTS, J. G. *Computational Modeling of Concrete Fracture*. PhD thesis, Delft University of Technology, 1988.
- [61] ROTS, J. G. The smeared crack model for localized mode-I tensile failure. In *Numerical Models in Fracture Mechanics of Concrete*, F. H. Wittmann, Ed. A. A. Balkema, Rotterdam, 1993, pp. 101–113.
- [62] SCHICKERT, G. Schwellenwerte beim Betondruckversuch. Heft 312, Deutscher Ausschluß für Stahlbeton, Berlin, 1977.
- [63] SCHLANGEN, E., AND SALET, T. A. M. Early-age crack control in concrete structures. In *Proc. 13th FIP Congress on Challenges for Concrete in the Next Millennium* (Rotterdam, 1998), D. Stoelhorst and G. P. L. den Boer, Eds., FIP, Balkema.
- [64] SCHWEGLER, G. *Verstärken von Mauerwerk mit Faserverbunwerkstoffen*. PhD thesis, Eidgenössische Technische Hochschule, Zürich, 1994.
- [65] SCHWEGLER, G. Earthquake resistance of masonry structures strengthened with CFRP-sheets. In *Proc. Symp. on Maintenance and Restrengthening of Materials and Structures: Brick and Brickwork* (Zürich, 2000), L. G. W. Verhoef and F. H. Wittman, Eds., pp. 105–110.
- [66] SPRINGENSCHMID, R., Ed. *Prevention of Thermal Cracking in Concrete at Early Ages*. RILEM TC 119. E & FN Spon, London, 1998.
- [67] STROBAND. Experimenteel onderzoek naar het afschuifdraagvermogen van HSB. Tech. Rep. 1st concept, Delft University of Technology, Delft, May 1996.
- [68] EUROCODE. *Common Unified Rules for Concrete Structures*. No. ENV1992-1-1. 1991, pp. 171–174.

- [69] TIMOSHENKO, S. P., AND WOINOWSKY-KRIEGER, S. *Theory of Plates and Shells*, 2nd ed. McGraw-Hill, 1970.
- [70] TNO BUILDING AND CONSTRUCTION RESEARCH. *DIANA User's Manual – Release 7*. Delft, August 1998.
- [71] VAN BREUGEL, K. (Ed.) Het grijze gebied van jong beton. *Cement* (1995-1996).
- [72] VAN DER VEEN, C. *Cryogenic Bond Stress-Slip Relationship*. PhD thesis, Delft University of Technology, Delft University Press, 1990.
- [73] VAN DER VLIET, C., ROS, P., AND ZIJLMAKER, A. Postdictierapport, Analyse van de 3-D reken-resultaten en vergelijking met de meetresultaten. Tech. Rep. NOH/77506, HSL-Zuid, 2000.
- [74] VAN EMPEL, W. H. N. C. Liggerwerking van gesegmenteerde boortunnels. Master's thesis, Delft University of Technology, Delft, 1997.
- [75] VAN MIER, J. G. M. *Strain-Softening of Concrete under Multiaxial Loading Conditions*. PhD thesis, Eindhoven University of Technology, 1984.
- [76] VAN MIER, J. G. M. Crack face bridging in normal high strength and lytag concrete. In *Fracture Processes in Concrete, Rock and Ceramics*, J. G. M. van Mier, J. G. Rots, and A. Bakker, Eds. Chapman & Hall, London/New York, 1991, pp. 27–40.
- [77] VAN MIER, J. G. M. Mode I fracture of concrete: discontinuous crack growth and crack interface grain binding. *Cem. Conc. Res.* 21, 1 (1991), 1–15.
- [78] VAN MIER, J. G. M. *Fracture Processes of Concrete*. CRC Press, Boca Raton (Fla.), USA, 1997.
- [79] VAN MIER, J. G. M. Measurement of damage parameters of brittle disordered media like concrete and rock. In *Damage and Fracture of Disordered Materials*, D. Krajcinovic and J. G. M. van Mier, Eds. Springer Verlag, Wien/New York, 2000, ch. 4, pp. 135–178. CISM courses and lectures no. 410.
- [80] VAN MIER, J. G. M., AND NOORU-MOHAMED, M. B. Geometrical and structural aspects of concrete fracture. *Eng. Fract. Mech.* 35, 4/5 (1990), 617–628. Special issue conf. FDCR-1, July 1988.
- [81] VAN VLIET, M. R. A., AND VAN MIER, J. G. M. Effect of strain gradients on the size effect of concrete in uniaxial tension. *Int. J. Fract.* 95 (1999), 195–219.
- [82] VAN ZIJL, G. P. A. G. *Computational Modelling of Masonry Creep and Shrinkage*. PhD thesis, Delft University of Technology, Delft University Press, 2000.
- [83] VAN ZIJL, G. P. A. G. Time-dependent behaviour of masonry: a numerical approach. In *Proc. 12th Int. Brick and Block Masonry Conf.* (2000), pp. 1877–1887.



- [84] VAN ZIJL, G. P. A. G., DE VRIES, P. A., VERHOEF, L. G. W., AND GROOT, C. J. W. P. Experimental confirmation of predicted restrained shrinkage damage in masonry walls. In *Proc. I.C.P.C.M. Conf. "A New Era of Building"* (Cairo, Feb. 18–20 2003).
- [85] VAN ZIJL, G. P. A. G., DE VRIES, P. A., VERHOEF, L. G. W., AND GROOT, C. J. W. P. Laboratory testing of efficiency of crack control in brickwork by epoxy bounded CFRP. In *Proc. I.C.P.C.M. Conf. "A New Era of Building"* (Cairo, Feb. 18–20 2003).
- [86] VAN ZIJL, G. P. A. G., AND VERHOEF, L. G. W. Collaboration between brickwork and concrete. In *Proc. Symp. on Maintenance and Restrengthening of Materials and Structures: Brick and Brickwork* (Zürich, 2000), L. G. W. Verhoef and F. H. Wittman, Eds., pp. 83–96.
- [87] VAN ZIJL, G. P. A. G., AND VERHOEF, L. G. W. Restrengthening of brickwork to reduce crack width. *Advances in Engineering Software* 33, 1 (2002).
- [88] VECCHIO, F. J. Analysis of shear-critical reinforced concrete beams. *ACI Str. J.* 97, 1 (2000), 102–110.
- [89] VECCHIO, F. J., AND COLLINS, M. P. The modified compression field theory for reinforced concrete elements subjected to shear. *ACI Journal* 83, 2 (March–April 1986), 219–231.
- [90] VERVUURT, A. H. J. M., DEN UIJL, J. A., GIJSBERS, F. B. J., AND VAN DER VEEN, C. Aanvullende Proeven in de Tunnelproefopstelling: Constructiegedrag onder Gebruiksbelastingen en het Effect van Plaatsingson nauwkeurigheden. (Deel 1: Opzet en Resultaten van Serie A). Tech. Rep. DC 01.06.02-01, Delft Cluster, 2002.
- [91] VERVUURT, A. H. J. M., DEN UIJL, J. A., GIJSBERS, F. B. J., AND VAN DER VEEN, C. Aanvullende Proeven in de Tunnelproefopstelling: Constructiegedrag onder Gebruiksbelastingen en het Effect van Plaatsingson nauwkeurigheden. (Deel 2: Resultaten van Serie B). Tech. Rep. DC 01.06.02-02, Delft Cluster, 2002.
- [92] VERVUURT, A. H. J. M., DEN UIJL, J. A., GIJSBERS, F. B. J., AND VAN DER VEEN, C. Full scale tests on a segmented tunnel lining. In *Proc. 1st FIB Congress* (Osaka, 2002).
- [93] VONK, R. A. *Softening of Concrete under Compression*. PhD thesis, Eindhoven University of Technology, 1992.
- [94] WAARTS, P. H. *Structural Reliability using Finite Element Analysis*. PhD thesis, Delft University of Technology, Delft University Press, 2000.
- [95] WILLIAM, K. J., AND WARNKE, E. P. Constitutive models for the triaxial behaviour of concrete. *IABSE Proc.* 19 (1975), 1–20. Proc. IABSE Seminar ‘Concrete Subjected to Triaxial Stresses’, Bergamo, Italy.



# Index

- ABAQUS package, 2
- ANSYS package, 2
- ATENA package, 3
- AUTOCAD package, 140
  
- B-regions, 139
- BDZ model, 19
- Beam elements, 97
- Box girder, 2, 61
- Brickwork, 149
- Brittle material, 2, 12
- Bulk modulus, 124
  
- Carbon fiber reinforcement, 152
- CDZ model, 19
- CEB-FIB Model Code, 53
- CFRP-sheet, 152, 155
- CHX60 element, 55, 67, 166
- CL12I element, 164
- CL18B element, 164
- Clay, 109
- Climate façade, 151
- Compression angle, 58
- Compressive strength, 36, 56
- Confinement, 26
- Convergence, 84, 85
- Cooling, 132
- Cooling pipes, 126
- CQ24P element, 68
- CQ40S element, 67, 81, 95, 165
- CQ48I element, 82, 165
- Crack Band Model, 6, 9
- Crack pattern, 58
- Crack strain, 27
- Crack width, 149
  - limitation, 152
- Cracking, 5, 25, 71, 84, 125, 142, 152
- Creep, 152
- Crushing, 26, 27, 29, 141
- CT30S element, 67, 82
  
- CUR Research Committee A36, xi
- Cyclic loading, 25, 36, 41
  
- D-regions, 139
- Damage, 2
- Damage-based cracking, 27
- DARS method, 171
- Decomposed Strain cracking, 26
- Deep beam, 139
- DIANA package, xi, 2, 3, 6, 14, 55, 71, 80, 95, 109
- DIANA User's Association, xi
- Dilatation joints, 152
- Discrete cracking, 6
- Drucker–Prager plasticity, 26
- Drying, 14
- Dugdale–Barenblatt crack models, 9
  
- Earthquake, 26
- Elastomer, 110, 124
- Elastoplasticity, 56
  
- Failure, 6
  - chance of, 169
  - compression, 15
  - tension, 18
- FEMVIEW package, 83
- Fictitious Crack Model, 9
- Fire load, 75
- Fixed crack model, 26, 35
- Formwork, 130
- Fracture energy, 12
- Fracture mechanics, 5
- Full containment tank, 76
  
- HEAT package, 3, 125
- High strength concrete, 43
- Hillerborg model, 6
- HSC beam, 43

- Influence field, 69  
Interface elements, 14, 82, 97, 112, 164, 173  
Joint, 61  
Kuhn–Tucker conditions, 30  
L7BEN element, 97  
Laboratory test, 45, 157  
Light concrete, 43  
LNG tank, 75  
Load–displacement graph, 142, 146  
Lumping, 113  
MARC package, 2  
Masonry, 152  
Maxwell Chain model, 127, 152  
Mohr–Coulomb plasticity, 98  
    Modified, 120  
Mooney–Rivlin hyperelasticity, 124  
Multiple-fixed crack model, 26, 27, 35  
N6IF element, 97, 112  
Nonlinear analysis, 69, 142  
North–South Metroline, 109  
Panel element, 141  
Phased analysis, 120  
Plastic Crack Tip Model, 8  
Plasticity, 1, 56, 71, 84, 152  
Plasticity-based cracking, 31  
Plate bending elements, 68  
Prestressed reinforcement, 62  
Probabilistic methods, 170  
Rankine plasticity, 26, 31, 152  
Rankine–Von Mises plasticity, 31  
Reinforcement, 26, 55  
    carbon fiber, 152  
    panel, 141  
    stringer, 141  
Relaxation, 127  
Reliability, 169  
Return-mapping, 30, 32  
Rotating crack model, 27, 33, 56  
RUAUMOKO package, 4  
Sand, 109  
SBETA package, 3  
Shear capacity, 26  
Shear retention, 36  
    constant, 28  
Shear wall, 3, 26, 34  
Sheet piling, 161, 172  
Shell elements, 165  
    curved, 67, 81, 95, 112  
Shrinkage, 14, 153  
Slip of reinforcement, 14  
Smeared crack model, 71  
Smeared cracking, 6, 9, 25, 26, 38  
Softening, 5, 9  
Solid elements, 67, 166  
SPANCAD package, 3, 140  
Strain decomposition, 27, 32  
Stress intensity factor, 7  
Stress locking, 27, 36  
Stress–strain relation, 12, 16  
Stringer element, 141  
Stringer–panel theory, 141  
Strut-and-Tie method, 1, 140  
Tension softening  
    linear, 28  
Tension stiffening, 14, 71, 84  
TILLY package, 4  
Timber floor, 155  
Total Strain cracking, 26, 32, 35  
Tunnel boring, 109  
Tunnel lining, 2, 91  
Underwater concrete, 161, 171  
Unreinforced concrete, 162  
User-supplied subroutine, 92  
VBC Model Code, 52  
Viscoelasticity, 152  
Von Mises plasticity, 26, 56, 71  
Yielding, 142  
Zone in beam element, 164